Single-molecule–resolved imaging of ultracold ^{87}Rb^{133}Cs molecules in an optical lattice

Adarsh Prasad Raghuram

A Thesis presented for the degree of
Doctor of Philosophy

Department of Physics
Durham University
March 2025

Abstract

This thesis presents the construction of a spin resolved quantum gas microscope for ultracold molecules of $^{87}Rb^{133}Cs$. Ultracold polar molecules in a lattice, with their long-range dipolar interactions, are a promising platform for quantum simulation of many-body systems quantum simulation. The ability to resolve single sites of the lattice, and measure the molecules rotational states opens up many interesting research possibilities. Such systems could be used to simulate a variety of many-body systems, investigating anisotropic spin models like the XXZ model, simulating the t-J model and realising exotic phases such as spin glasses and spin liquids. This work demonstrates the imaging of ultracold molecules in an optical lattice with single-molecule resolution, and spin-state resolution.

We prepare our molecules by associating high phase-space density (PSD) clouds of Rb and Cs. The clouds are prepared using a sequential loading scheme, where each species is loaded, cooled and evaporated separately, before the atom clouds are merged for association. In this thesis, we present and characterise the scheme used, whereby we can achieve the required high PSD mixture. This involves the use of a moving dimple trap and an evaporation sequence, which allows us to achieve a dual-species BEC. We then detail the association a cloud of weakly-bound Feshbach molecules and their transfer to the ground state using Stimulated Raman Adiabatic Passage (STIRAP). We discuss the characterisation of the Feshbach association process and the setup and optimisation of the STIRAP setup, including the laser system that locks to a high-finesse cavity, including the use optical feedforward to reduce the high frequency phase noise. This allows us to improve the STIRAP efficiency to $98.7 \pm 0.1\%$, a record for RbCs.

We then introduce the microscopy setup used in the experiment, with the optical lattice and light sheet used to trap the atoms and molecules and the optical molasses used to image atoms of Rb and Cs while they are confined to a lattice site. We optimise and characterise the performance of this setup, for both Rb and Cs atoms, presenting a dual-species quantum gas microscope. We also discuss the methods used to identify single atoms in the lattice, and reconstruct the lattice using a

neural-network to deconvolve the images. We finally load our molecular cloud into the optical lattice and dissociate the molecules into atoms, which act as a marker for each molecule, and are able to image the cloud with single-molecule resolution. We further leverage our ability to perform microscopy on both Rb and Cs to implement a sequence that maps the molecular rotational state to a specific species to be imaged, and realise a spin-resolved molecular microscope, where $N = 0$ state is mapped to Rb, and the $N = 1$ state to Cs.

Declaration

The work in this thesis is based on research carried out at the Department of Physics, Durham University, United Kingdom. No part of this thesis has been submitted elsewhere for any other degree or qualification and it is all my own work unless referenced to the contrary in the text.

Adarsh Prasad Raghuram

March 2025

Amended September 2025

Acknowledgements

First I thank my supervisor, Simon for his constant support and help throughout my PhD. His innate ability to instantly recognise experimental problems and issues that I have spent a week breaking my head is incredible. He has always been happy to provide good advice and guidance over the past few years. As all ultracold molecule experiments, our experiment has been a team effort, and I express my deepest gratitude to my lab mates in the past 4 years. Jonathan has been a constant fount of wisdom in the lab, first as a PhD student, and more recently as a postdoc. His calm and methodical approach to science, vast knowledge have been irreplaceable[1]. Ben has existed[2]. I also thank Sarah, the postdoc in the lab when I first joined, whose patience and skill with a clueless student will never be forgotten. I must also thank Andrew and Alex (Dr. Transport?) who was always happy to have a cheerful chat and a kind word[3]. It has also been incredible to work with Phil, whose absolutely unflappable demeanour and ridiculously deep knowledge of molecular physics have been impressive. While I have not worked much with them, I am certain that the future of the experiment is in good hands with Chris and Francesca. I must thank everyone for their friendship and help these past few years[4]

Here, I also thank the rest of the Cornish group - Dan, Tom, Alex, Arpita, Albert, Luke, Joe, Jack, and Tobias. It has been great working with them (and borrowing optics from them). Dan, Tobias and Tom in particular, for their friendship, advice and always being ready to have a chat when I need to escape the lab. QLM in general has also provided a fantastic atmosphere to work in, and has made the PhD far more fun than I may have imagined. I particular, I'd like to thank the Friday 'seminar' attendees, and the QLM supremo Ifan in particular, for always being ready

[1] And his unique brand of pragmatic pessimism

[2] It has been great working with Ben and witnessing his constant drive and enthusiasm for science, the gym and lifting washing machines.

[3] And a whiff of 'coffee' (read hell in a thermos).

[4] And putting up with the puns

to offer his sage wisdom on any topic and at any time.

The friends I have made in Durham outside the lab have also been extremely helpful. A shout out to them: - Michael (*redacted*), Ally (short), Ali (tall), Tom (tweezer**), Dan (Pumpkin), Joe (two-shoes), Sam, Bex, Emma, Rollo (Tall-o), Jack, Keerthi and Vis, particularly to the board game lot for the chaos, betrayals and many evil plans. I must thank Dan in particular for his constant friendship and good vibes (and evil grins) throughout my time at Durham - I am also contractually obliged to thank Katie without whom I would have probably been roadkill. Sam and Vis also get a special mention for being solid friends and a shared passion for board games, whiskey, climbing and the Vic.

Of course I must also thank the people who I met in my time as an undergrad in Oxford (The Raging Eagles?), who have been a constant source of friendship, support and amusement for the past 8 years. Keith who thought me to embrace the chaos in life (board games) and that there is no such thing as incorrectly fried. Nicolai (Nicky) for his incredible insanity, hundreds of history facts and a shared spirit for shenanigans. Cameron for his overwhelmingly positive presence (and use of his room) as well as for teaching me how to walk, talk and grow a beard (by being a shining counter-example). Ella for her aggressive niceness and kindness as well as a persistent cheerfulness. JJ - I am not only thanking you here because I have to. You have actually been a Fanta-stic friend. Jess, you've always kept me down to earth, and inspired me to reach high (sorry, I am hoping for one of your legendary eye-rolls if you read this). Bryony I am *only* thanking you here because have to (Just joking, you're great!!!). I also mention Calvin, Sarah, Alvin, PDC, Ayush, Kamya and Richa here, particularly PDC for her friendship (and always being happy to listen to my PhD rants)!

Last and not the least, I thank all my friends from Bangalore, particularly Mani, Pranav and Rahul for nearly two decades of putting up with me. Thatha, Paati and Ammamma[5], thank you for your love, support and encouragement. Aditi, you are by far my favourite sibling[6] (and would be even if I had another one). Amma[7] and Appa, I love you and thank you so much for everything over the past 26 (and a bit) years.

[5]Also for the best food ever and the best couches.

[6]Here only will I acknowledge that you are not adopted

[7]First person I ever met as a matter of fact

Contents

List of Figures

List of Tables

Dedication

To my family

CHAPTER 1

Introduction

1.1 Ultracold atoms

Ultracold quantum gases of atoms are currently one of the most exciting areas in modern AMO physics, having progressed tremendously in the past 40 years. There have been constant advances from the initial experiments involved in laser cooling and trapping atoms [1–3] to the production of Bose-Einstein Condensates [4–6] and degenerate Fermi gases [7,8], and to their current implementation in the construction of quantum computers [9,10] and quantum simulators [11,12]. The use of atoms for quantum simulation is of particular interest for this thesis, as we discuss the design of a molecular quantum gas microscope.

1.1.1 Quantum gas microscopes

An important advance in recent years in quantum simulation with ultracold atoms has been the development of quantum gas microscopes (QGMs) [13]. QGM experiments load ultracold atoms into single planes of optical lattices, and then image the atoms in the lattice with single-site resolution, allowing an investigation of the microscopic properties of the system. In the years since the development of the initial

quantum gas microscopes [14, 15] with Rb, multiple groups around the world have succeeded in realising QGMs with other alkali species [16–22] as well as Yb [23, 24], Er [25] and Sr [26].

These experiments have observed various interesting phenomena such as Mott insulators [15, 27, 28], antiferromagnetic correlations [29, 30] and Pauli blocking [19]. The single-site-resolved imaging has allowed one to probe phenomena that would be otherwise undetectable such as hidden correlations [31], entanglement entropy [32] and magnetic polarons [33]. A more thorough overview of QGMs can be found in review articles like [13, 34].

1.2 Ultracold molecules

While much work has gone into controlling atoms, the interaction between atoms is usually limited to short ranged contact interactions. An extension of these experiments has been to investigate systems with long-range dipole interactions. The strength of the dipole-dipole interaction (V_{dd}) between two identical molecules (or particles in general) with parallel dipole moments is given by.

$$V_{dd}(r,\theta) = \frac{d^2}{4\pi\epsilon_0 r^3}\left(1 - 3\cos^2\theta\right), \tag{1.1}$$

where d is the electric dipole moment of the particles, r is the spacing between the two particles and θ the angle between the orientation of the dipole moments and the spacing of the particles. For an experiment such as ours, with molecules in a lattice, this leads to interaction strengths V_{dd}/h on the order of 1 kHz between nearest neighbours.

A many-body system, with long range dipolar interactions has been realised in various ways. This includes using magnetic atomic species [35] such as Erbium [36], Chromium [37] or Dysprosium [38], exciting atoms to their Rydberg states (as in much of the research into quantum computers and simulators [9–12]), or using polar molecules instead of atoms. Each of these systems has its own advantages and drawbacks. Magnetic atoms are long lived, and the formation of a Bose-Einstein Condensate (BEC) is relatively simple. However, the strength of their magnetic

dipole moments is relatively small ($\approx 10\ \mu_B$) when compared to that of the electric dipole moments of Rydberg atoms and polar molecules. So, due to the weaker interaction (≈ 10 Hz in a typical system), these experiments are often limited by the lifetime of the atoms in the system. Rydberg atoms on the other hand have large dipole moments (100 to 1000 D), which allow for quick interactions (≈ 1 MHz) between atoms in the system. However, these experiments are also limited by the short lifetime of these atoms in the excited states (usually around 10 to 100 μs) [39]. Molecules offer a middle ground between the two, with long lifetimes (experiments are often limited by trap lifetimes of order 10 s) and dipole moments of the order 1 D.

The dipole-dipole interaction has made ultracold molecules an attractive medium to work with. Control of the rotational state of the molecule allows for the engineering of the dipolar interaction strength between two molecules. There have been proposals to utilise the interaction to realise quantum gates for building a quantum computer [40, 41], conduct quantum simulation of many body systems and realise new phases [42–49]. Ultracold molecules also offer a fascinating way to probe the intricacies of chemical reactions by offering the ability to control the interaction dynamics of the interacting molecules [50].

Ultracold molecules experiments face some challenges. The experiments tend to be more complicated than atomic experiments. The creation of ultracold molecules requires either direct laser cooling of a molecular species, or the association of a molecule from a mixture of two merged ultracold atomic gases[1].A significant obstacle has been the loss of molecules to scattering with the trapping light due to the formation of short lived complexes through inelastic 'sticky' collisions with other molecules [51, 52]. Another challenge has been the short rotational coherence times of the molecules due to differential light shifts from the trapping light [53]. To successfully simulate a many-body quantum system, we require rotational coherence times significantly larger than the dipolar interaction time scale.

Some of these problems have seen solutions emerge recently, with the advent of collisional shielding, both using electric fields [54–56] and microwaves [57–61].

[1]This is discussed more in the next section.

Collision shielding prevents the loss due to inelastic collisions, by engineering a repulsive potential between the molecules, preventing them from enduring 'sticky ' collisions. This has allowed molecules to be evaporatively cooled to degeneracy, both in the fermionic [59] and in the bosonic cases [62]. Previously, degenerate molecular clouds were only produced by associating degenerate atomic species [63, 64].

The rotational state coherence has been extended using a repeated spin-echo pulse sequence and magic polarisation [65, 66], and most recently using magic wavelength traps [67, 68]. This has enabled the realisation of entanglement and two-qubit gates between molecules [68–71].

The rich internal structure of the molecules, with rovibrational energy levels offers interesting prospects. These states can be readily accessed using microwave fields. In addition to controlling the dipolar interaction strength, there have been proposals to use this complicated internal structure to realise qudits [72, 73]. There have also been some proposals to use this ladder of states as *synthetic dimensions* to simulate additional spatial dimensions in a many-body system [74].

Molecules also offer an exciting opportunity to probe fundamental physics. The strong coupling of the molecules to external electric fields, along with their large internal fields make molecules able to measure properties such as the electron Electric Dipole Moment (eEDM). This has been investigated by the ACME collaboration using ThO [75], at Imperial College London using YbF [76] and JILA using HfF^+ molecules [77]. The latter has measured the most accurate bound of the eEDM to date, applying a limit of $|d_e| < 4.1 \times 10^{-30} e$ with 90% confidence.

1.3 A molecular quantum gas microscope

Molecules in a lattice are able to realise many physical systems of interest [42, 43]. The use of a QGM to probe these systems allows for the observation and investigation of the microscopic properties and correlations of such systems. The dipole-dipole interactions could be used to simulate anisotropic Hamiltonians such as XXZ Hubbard models [44, 45] with long range interactions. The introduction of tunnelling allows the simulation of quantum magnetism, with potential for realisation of the

t-J-V-W model [46] and exotic phases of matter [78] including spin liquids [48] and spin glasses [49].

Some of these phenomena have already been observed in molecules loaded into a lattice, particularly at JILA, with recent work highlighting the tuneability of the dipole-dipole interaction with an electric field [79], Floquet-engineered XYZ Hamiltonians with two-axis twisting [80], and the realisation of a t-J spin model [81]

A molecular QGM has previously been realised only in the Bakr group at Princeton. Here, single-molecule–resolved imaging in an optical lattice was demonstrated for NaRb, with the observation of the Hanbury Brown-Twiss effect [82]. A subsequent publication showed the observation of spin correlations and a demonstration of the anisotropic dipole-dipole interaction. In addition they utilised Floquet engineering to realise the XXZ Hamiltonian in their system [83].

The goal of the experiment described in this thesis is to realise a quantum gas microscope of ^{87}Rb^{133}Cs molecules, with the view of investigating such systems in the future. A particular advantage of ^{87}Rb^{133}Cs is that both species are can be easily imaged via optical molasses cooling in the lattice, so microscopy can be performed on both species[2], allowing for readout of multiple spin states by mapping spin states to species as first detailed in [84] and implemented in this work.

1.3.1 Creation of ground state ultracold molecular gases

There are two main methods used to realise an ultracold molecular gas - the *direct* method and the *indirect* method. The direct method involves first producing the molecules, and then cooling and trapping them with lasers. The indirect method operates by first cooling the constituent atomic species, and then associating them into a molecule.

Directly cooling has been successfully implemented on a variety of diatomic molecules and polyatomic molecules [85–90]. Direct cooling is restricted to those molecules with highly diagonal Franck-Condon factors, where a suitable cycling tran-

[2]At the time of writing, quantum gas microscopes have not yet been realised for Na, likely due to the difficulty of both trapping it (it has a low polarisability at wavelength like 1064 nm) and cooling it with optical molasses

sition for the laser cooling and imaging is available. Even so, the excited states often have multiple decay pathways, so multiple repump beams (or one beam addressing multiple transitions) are required to effectively cool and image the molecules [85].

Association of diatomic hetero-nuclear molecules with the indirect method involves laser cooling both atomic species and then associating them. This association can be done using a photon: termed as photo-association [91], which associates colliding atoms into an excited bound state, from which they may decay into the molecular ground state. While conceptually simple, photo-association suffers from a large number of decay pathways available from the excited state, making it difficult to associate ground state molecules efficiently.

Magneto-association, first demonstrated in [92] is the the preferred method to associate atoms to molecules. The magnetic field is swept across a Feshbach resonance to transfer the unbound atomic state to a weakly-bound molecular state (termed the Feshbach state). The weakly-bound molecules are then transferred to their rovibrational ground state using a two-photon process - Stimulated Raman Adiabatic Passage (STIRAP). Using this method, diatomic bi-alkali hetero-nuclear ground state polar molecules of KRb [93–95], RbCs [96, 97], NaK [98–101], NaCs [102, 103], NaRb [82, 104], NaLi [105] and LiK [106] have been created. There are ongoing efforts to produce molecules with other species [107–110]. In general, these associated molecules are not imaged directly, and are instead dissociated into atoms by reversing the STIRAP and magneto-association before being imaged. While we magneto-associate RbCs molecules, we note that the first ground state RbCs molecules were photo-associated [111].

1.3.2 Ultracold ^{87}Rb^{133}Cs

In this thesis, we describe our work to associate and investigate ultracold ^{87}Rb^{133}Cs molecules (which is simply referred to as RbCs). RbCs molecules have been the focus of research both in the group at Innsbruck [112–115] and at Durham [97, 116–118]. RbCs was historically chosen due to its chemical stability[3], the dipole moment, and

[3]Of currently associated molecules, KRb, NaLi, and LiRb are not chemically stable.

the relative ease of cooling Rb and Cs atomic species. While the ease of working with Rb and Cs atoms is still a benefit, the chemical stability is in fact a moot point, as molecules trapped in optical traps see fast loss due to 'sticky collisions' where they form complexes with other molecules and are lost to the trapping light [51].

RbCs has proved a fruitful molecule to work with, and currently the pathway to the production of molecules is relatively established. The experiments at Innsbruck succeeded in associating ground state molecules in a dipole trap [119] and then Feshbach molecules in the ground band of an optical lattice [113]. At Durham, there are currently three experiments working with RbCs. The initial experiment has succeeded in associating Feshbach molecules [116] and then transferring them to the ground state via STIRAP and measuring the dipole moment of 1.225 D [97]. The experiment has since investigated and manipulated the internal state of the molecules [120, 121] and observed dipole-dipole interactions [67]. Recently two more experiments have been constructed. The first is an experiment that utilises optical tweezers to trap and manipulate individual RbCs molecules. This experiment has successfully produced and imaged single ground state molecules in tweezers [117] and recently observed long-lived entanglement of the molecules [68], as well as investigating the interaction between the molecules and Rydberg atoms [122]. The final experiment, which we describe in this thesis, aims to realise a quantum gas microscope for RbCs molecules.

When compared to other ultracold molecules, RbCs has some benefits and some disadvantages. Rb and Cs are both relatively easy atomic species to work with (even compared to other alkalis), so the initial stages of laser cooling are fairly straightforward. The association process is complicated by the immiscibility of the atomic BECs, so the molecules must be magneto-associated either at phase-space densities of ≈ 0.1 [112, 116], or associated in a lattice [113]. The $N = 0$ to $N = 1$ rotational state energy difference corresponds to a frequency of 980 MHz (or 30.6 cm wavelength). The low splitting of the levels (most other molecules have splitting of 2-5 GHz) means that we are able to access many of the high rotational levels with reasonable microwave frequencies. However, it complicates microwave shielding (which requires some polarisation control of the microwaves) [58]. With the large

wavelength, it is difficult to experimentally control the polarisation to be circular[4], as has been done in other molecules where the microwave shielding has been implemented [59–63]. However, the electric fields required to implement electric field shielding ($\approx$ 2 kV/cm) are relatively low [123], making RbCs an interesting candidate for electric field shielding. The highest rotational coherences to date have been observed in RbCs with the use of a magic wavelength lattice and tweezers, allowing for rotational coherences >10 s [67, 68], moving to the regime where this has ceased to be the limiting factor for most experiments. For comparison, in other species, the use of spin-echo pulse sequences, magic wavelength traps and magic polarisation has improved the coherence times to $\approx$100 ms [65, 66][5].

1.4 Outline

In the remainder of this thesis, I describe work done to realise single molecule resolved imaging of RbCs in an optical lattice. Chapter 2 offers a brief introduction to some theoretical concepts that motivate the experiment and are useful for understanding some of the results discussed later. Chapter 3 offers a general overview of the experiment, including the experimental setup as well as common experimental techniques used. Chapter 4 described the production of a dual-species BEC in the experiment, highlighting the challenges involved in doing so, and the sequential loading scheme utilised. Chapter 5 then moves on the detailing the production of Feshbach molecules, and then their transfer to the ground state via STIRAP. Here we also present the implementation of the optical feedforward technique used to significantly improve he STIRAP efficiency. Chapter 6 then moves on to describing the microscopy of atomic Rb and Cs in the experiment, detailing the setup used and the characterisation of the microscopy. Chapter 7 then presents the some of our initial results on microscopy of molecules, including spin-resolved microscopy by mapping spin to species. Finally, chapter 8 offers a taste of the future, discussing the future of the lab and the machine.

[4] Both because the size of the antenna required is often similar to the wavelength, and the in vacuum electrodes may act to linearly polarise the microwaves

[5] Magic wavelength traps have been attempted before with NaK, but with limited success [124]

1.5 Contributions of the author

As with all ultracold matter experiments, our experiment is a team effort. The microscope experiment has been overseen by Simon Cornish, with various PhD students and postdocs involved the setup and operation of the lab. Over the course of the labs history, there have been many postdocs and students involved in the experiment. All these people have contributed to the experiment. Here I offer a brief overview of the contributions of people to the experiment.

Significant work to set up the experiment had been completed before I arrived in Durham. The vacuum setup and laser cooling setup were designed by Phil Gregory, Sarah Bromley, Alex Alampounti, Elizabeth Bridge, Danielle Pizzey, Lewis McArd, Mew Ratkata and Andrew Innes. Jonathan Mortlock (JM), Alex Matthies (AM), Sarah and Mew had worked to implement some dipole traps in the main chamber, and make a Cs BEC. The initial calculations and setup were also completed, led by AM, working with JM and Sarah. I worked with JM to setup absorption imaging in the science cell, which was used to further characterise the transport (led by AM). The science cell coils and objective were moved into the experiment around this time, mostly by Sarah, AM and JM[6]. I worked to implement and characterise the fast rotation mount, based on a design idea from JM. Sarah and JM led the design and implementation of the first version of the science cell dipole traps and the initial optical lattice, with some help in optical alignment from AM and myself. JM then led the work to observe the Mott insulator to superfluid transition, as is described in his thesis.

I spent some time investigating options to realise a dual-species BEC in the science cell[7], before deciding on the moving dimple and sequential loading scheme described in this thesis. I worked to setup and characterise the moving dimple with Erkan Nurdurn, a summer student. Around this time, I also worked to re-optimise the experimental sequence. Working with Jonathan, I led the implementation of the moving dimple into the experiment and the characterisation of the sequences.

[6] With contributions of thematic music from myself whenever the lab flooded

[7] As with all science, there were many dead ends here, which are not presented in this work

We both worked together on the overall design and setup of the dipole traps in the science cell. Working with JM and Ben Maddox (BM), I led the effort to STIRAP molecules to the ground state and characterise the same.

Andrew and Albert Tao worked on designing the setup of the STIRAP cavity before I locked the STIRAP lasers to the cavity, and characterised the lock. I worked with BM and JM to implement the optical feedforward on the STIRAP lasers, before the experiments with the same were conducted by BM and Tom Hepworth in a neighbouring lab. Jonathan designed the new bow-tie lattice (and light-sheet) setup, and led the implementation into the experiment, with help in alignment from BM and I. Following this, we all (JM, BM and I) worked to realise a dual species quantum gas microscope. I performed the molasses characterisation described in this thesis, adapting code written by JM (who also wrote the code for the NN deconvolution).

JM, BM and I then worked to image molecules in the lattice, with all of us working together on the initial signals and microwave spectroscopy, and the initial signals of single molecules in the lattice, including Rabi flops without the spin to species mapping and simultaneous dual species microscopy. This has been improved in the last few months as I have started writing this. JM and BM have implemented the blast beam and developed the final sequence for spin to species mapping described in Chapter 7. We have also all worked towards investigating collisions in a molecular gas, which is not discussed in this thesis other than a brief section in the outlook.

1.6 List of publications

The following publications were completed during the course of this work

Enhanced quantum state transfer via feedforward cancellation of optical phase noise

Benjamin P Maddox*, Jonathan M Mortlock*, Tom R Hepworth, Adarsh P Raghuram, Philip D Gregory, Alexander Guttridge, Simon L Cornish

Phys. Rev. Lett. 133, 253202 (2024)

Long-distance optical-conveyor-belt transport of ultracold ^{133}Cs and

^{87}Rb atoms

Alex J Matthies, Jonathan M Mortlock, Lewis A McArd, Adarsh P Raghuram, Andrew D Innes, Philip D Gregory, Sarah L Bromley, Simon L Cornish

Phys. Rev. A 109, 023321 (2024)

A motorized rotation mount for the switching of an optical beam path in under 20 ms using polarization control

Adarsh P Raghuram, Jonathan M Mortlock, Sarah L Bromley, Simon L Cornish

Rev. Sci. Instrum. 94, 063201 (2023)

Multi-state detection and spatial addressing in a microscope for ultracold molecules

Jonathan M Mortlock, Adarsh P Raghuram, Benjamin P Maddox, Philip D Gregory, Simon L Cornish

arXiv:2506.12329

**These authors contributed equally to this work*

CHAPTER 2

Theory

In this chapter we provide a brief overview of the theory relevant to our experiment. First, we offer a short overview on the trapping of atoms and evaporative cooling, and detail the magnetic field parameters used to control and levitate our atoms. Next, we discuss the collisions of Rb and Cs - both inter and intra-species and comment on the significant implications this has on the formation of ultracold molecules. The atoms are associated to molecules in a weakly-bound Feshbach state, referred to as Feshbach molecules, which are transferred to the ground state using Stimulated Raman Adiabatic Passage (STIRAP). We discuss this process, and the factors effecting the efficiency of the STIRAP. Finally some of the background theory to our single atom (and later molecule) resolved imaging in an optical lattice is presented, describing the physics of atoms and molecules in a lattice and the molasses imaging.

In this thesis, familiarity of the operation of laser cooling of atomic species and optical trapping of atoms is assumed, and optical trapping is only discussed in brief, to introduce relevant terms and equations that will be used often throughout the thesis. We direct the reader to [125–127] for more details of the same.

2.1 Atoms in optical traps

An atom exposed to a laser beam has an intensity dependant potential, which can be used to exert an attractive or repulsive force on an atom. The magnitude of the interaction potential (U_0) is set by the intensity of the beam (I) and the real part of the atomic polarisability at the specific laser wavelength (α_λ) used [127], and is given by,

$$U_0 = -\frac{\alpha_\lambda I}{2\epsilon_0 c}. \tag{2.1}$$

In this thesis, trap depths are quoted often. They are calculated using Eq. 2.1, and are quoted in units of temperature (usually μK to allow for easy comparison with the temperature of the atomic clouds), converted using the Boltzmann constant k_B.

Whether a laser is attractive or repulsive to an atomic species depends on α_λ. In general, laser beams red detuned (higher wavelengths) from the nearest atomic transitions are attractive and beams that are blue detuned (lower wavelengths) are repulsive. Most of the optical trapping presented in this thesis is done with light near 1064 nm. Here, the Cs polarisability (quoted in atomic units) α_λ^{Cs} is 1162 $\pm$ 2 $a.u$ and the Rb polarisability α_λ^{Rb} is 687 $\pm$ 1 $a.u$ [128]. So, for the same light intensity, Cs is trapped at almost twice the depth as Rb. 1064 nm is far-detuned for both species (the D_1 lines for Rb and Cs are at 795 nm and 894 nm respectively), so we do not suffer significant loss from scattering of the trapping light for the atoms. When trapping molecules, the loss due to scattering from the trapping light can be more of a significant issue, due to the complicated internal structure of the molecules, and the possibility of inelastic 'sticky' collisions [51].

In general, we use Gaussian beams with waists of order 100 μm to trap the atoms. A single Gaussian beam only confines atoms well radially, while being weakly confining and often allowing expansion in the axial direction. So, to effectively trap atoms in a bulk gas, we often trap them in the intersection of two different Gaussian beams approaching at different angles, known as a crossed optical dipole

trap (xODT).[1]

2.1.1 Evaporative cooling of atoms

Evaporative cooling is often used to cool trapped atomic gases further, and realise low entropy samples [129, 130]. This was instrumental in the first realisation of a BEC [4, 5]. With atoms of a given temperature trapped in a dipole trap, the atoms (while not condensed to a BEC) have a Boltzmann energy distribution. If the trap depth is lowered slightly, we truncate this distribution by allowing the atoms with the highest energy to escape. The remaining atoms in the trap can then thermalise with each other and re-establish a thermal equilibrium at a now lower temperature. Elastic collisions are key to this thermalisation process, as they allow the atoms to redistribute the energy amongst themselves.

Inelastic collisions and three-body loss serve as detriments to evaporation. Practically, atoms are loaded into a dipole trap, and the power in the trap (and hence the depth) is slowly ramped down. While a significant fraction of the atoms are lost, if the ramp is done in conditions to allow for proper thermalisation and low enough loss, the atoms remaining in the trap can be cooled to orders of magnitude below the initial temperature. The metric we most commonly use to characterise the evaporation ramps and also describe the atoms at very low temperatures is the phase space density (PSD), given by,

$$PSD = n\left(\frac{h}{\sqrt{2\pi m k_B T}}\right)^3 \tag{2.2}$$

where n is the atomic density, m is the atomic mass and T is the temperature. We work with bosonic species, so the atoms eventually reach degeneracy, forming a Bose-Einstein Condensate, the threshold of which is often taken as occurring at a PSD of 1 (experimentally observable by a bimodal distribution in momentum space).

[1] Atoms and molecules can be trapped effectively in a single beam if it is focused to very small sizes, where the divergence of the beam axially is strong enough to trap. An example is optical tweezers, used in many experiments.

2.1.2 Magnetic levitation of atoms

The magnetic moment of the atoms and molecules allows us to exert a force on them using a magnetic-field gradient. This is an extremely useful tool as it allows us to negate the effect of gravity on the atoms by exerting an equal an opposite force to "levitate" the atoms. In particular, magnetic levitation is useful as it allows us to counteract the effects of gravity on atoms in an optical trap, and allows us to image the atoms after a larger time-of-flight (TOF) in the absorption imaging (Sec. 3.2.6)[2]. We are also able to separate a mixture of atoms and molecules in different states by applying a field gradient and have them separate vertically as a different force is exerted on the different states, a technique known as Stern-Gerlach separation.

To levitate the atoms, we must cancel the gravitational force (mg) with the magnetic force (F_{mag}). This can be written as,

$$mg = F_{\text{mag}} = \mu \frac{dB}{dz}, \tag{2.3}$$

where μ is the magnetic moment of the atom or molecule (assumed to be a constant for a given state while it is being levitated), and the field gradient in the vertical direction is given by $\frac{dB}{dz}$. For atoms, the magnetic moment depends on which state the atom is in, as $\mu = g_{\text{F}} m_{\text{F}} \mu_{\text{B}}$. For molecules, the magnetic moment is different for the different states as presented in Table 2.1. The magnetic moments and levitation gradients of Rb and Cs in their ground states, as well as various molecular states of interest is presented in Table 2.1. We call the magnetic field gradient required to levitate the atoms or molecules the levitation gradient. We are fortunate that the levitation gradient for Rb and for Cs in their atomic ground states is very similar, so both species can be levitated at the same time and at the same location[3].

[2] Without levitation, we are limited to TOF times of around 15 ms.

[3] The difference in their gradients corresponds to an acceleration of ≈ 0.2 m/s^2 for one species when the other is perfectly levitated.

Species and State	Mass (amu)	μ (μ_B)	$\frac{dB}{dz}$ (G/cm)
Cs $6^2S_{1/2}\|F=3, m_F=3\rangle$	133	-0.75	31.1
Rb $5^2S_{1/2}\|F=1, m_F=1\rangle$	87	-0.50	30.5
RbCs*$\|-1(1,3)s(1,3)\rangle$	220	-1.33	29.1
RbCs*$\|-2(1,3)s(0,3)\rangle$	220	1.50	-46.0
RbCs*$\|-6(2,4)s(2,4)\rangle$	220	-0.84	25.8
RbCs Ground State	220	0.005	7700

Table 2.1: The magnetic moments and the levitation gradient of atoms and molecules in different states relevant to the experiment

2.2 Scattering rates of atoms and atomic mixtures

In a mixture of ultracold atoms, an important parameter used to describe the interactions between atoms is the scattering length a. The scattering length describes the strength of interactions between atoms. The overall scattering properties of an atom or atomic mixture depend on the contributions of each of the partial wave scattering lengths. In the case of our experiment, with the evaporative cooling and merging of species being performed at typical temperatures $\leq 5\mu$K , we find that we only need to consider the s-wave scattering lengths for the interspecies scattering. The next lowest partial wave contributions for Rb-Cs collisions are p-wave collisions, and d-wave collisions for Rb-Rb and Cs-Cs. The barrier heights for these are 54 μK , 413 μK , and 180 μK , so we do not have to consider these effects in our experiment [115, 116, 131].

The inter- and intra-species scattering lengths for Rb and Cs are shown in Fig. 2.1. Positive scattering lengths signify a repulsive interaction, and a negative scattering length an attractive interaction. Larger scattering lengths lead to more frequent interactions.

During evaporation, it is generally desirable to have a positive scattering rate (near the BEC regime), which allows the energy to be efficiently redistributed. However, particularly as the PSD of the sample increases, three body physics and loss due to three-body recombination becomes significant. In general, the three-body loss rate increases with an increase in the scattering rate ($R_{loss} \propto a^4$) [132] as the chance of a three-body interaction increases with an increase in the scattering length. So, evaporation is often done at low positive scattering rates, where the energy can be

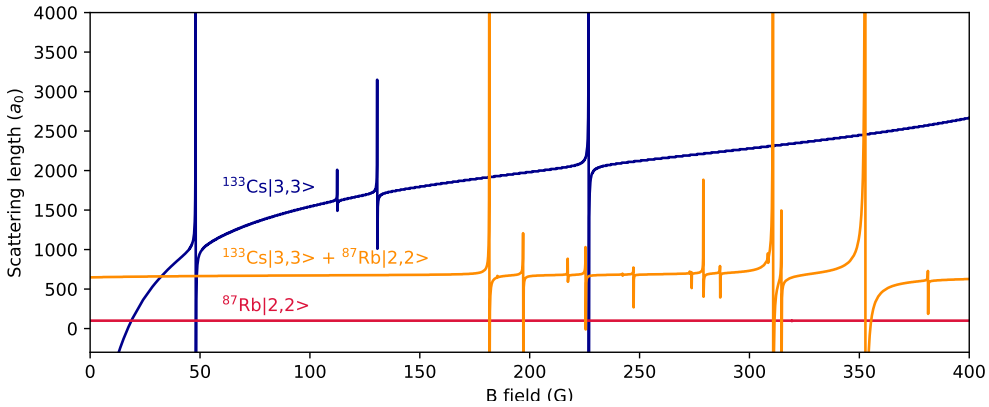

Figure 2.1: Calculated scattering lengths of Rb, Cs and Rb + Cs in the relevant states that they are present in our experiment. Calculations were performed in Jeremy Hutson's group

redistributed between atoms, but three-body loss isn't too large. Cs loss is often large, but we are aided by Efimov physics [133], which leads to Cs having a three-body loss minima where $a \approx 220a_0$, seen at a magnetic field of $B \approx 21$ G . While, the loss rate coefficient here is still significant ($\approx 3 \times 10^{-27}$ cm^2/s) [134], approximately two orders of magnitude more than that of Rb ($\approx 2 \times 10^{-29}$ cm^2/s) [135], it is low enough for us to evaporatively cool a cloud of Cs to a BEC.

The scattering lengths can be tuned by varying the magnetic field on the atoms, particularly around Feshbach resonances. Feshbach resonances occur at fields where the unbound atomic state is degenerate with a bound molecular state. This happens because the atomic and the molecular states have different magnetic moments, so experience different Zeeman shifts on application of a magnetic field. For a given combination of atoms, various molecular bound states are shifted to the same energy with the unbound atomic state at particular magnetic fields, generating avoided crossings. At the Feshbach resonance, we see poles in the scattering length. With a precise enough control of the magnetic field, the scattering length can be controlled. We make use of the Feshbach resonances to associate our molecules, as by ramping the field adiabatically over the avoided crossing, we are able to associate atoms into molecules (see Sec. 2.3).

Scattering lengths in an Rb and Cs mixture

Here, we discuss the scattering lengths of Rb and Cs in the context of associating RbCs Feshbach molecules and our experiment. For most experiments, the ideal starting point for the production of Feshbach molecules is a cloud containing a miscible mixture of degenerate atomic species to be associated. However, the scattering lengths in an Rb - Cs mixture complicate this.

The first challenge is the evaporation of Rb and Cs together to produce dual-species BEC (or even a mixture with a PSD of close to 0.1). As mentioned earlier, the evaporative cooling of an atomic species is often limited (particularly for Cs) by the three-body loss as the PSD of the gas increases. The three-body loss is related to the scattering length, with higher scattering lengths leading to greater loss. For Rb alone, this is not an issue, as the scattering length is relatively low and positive ($a_{\text{Rb-Rb}} \approx 100a_0$) across a wide range of magnetic fields. For Cs, the scattering rate is in general larger, as is the corresponding three-body loss from Cs-Cs-Cs interactions. As mentioned earlier, there is a three-body loss minima at $\approx 21\ G$, with the scattering length $a_{\text{Cs-Cs}} \approx 220a_0$, and it is possible to evaporate Cs to a BEC with the field set to the Efimov minima.

In a mixture of Rb and Cs, the inter-species three-body losses start to become a larger issue. The inter-species scattering length of $a_{\text{Cs-Rb}} \approx 645a_0$ leads to significant three-body losses from Rb-Rb-Cs and Rb-Cs-Cs interactions. Other groups working with RbCs molecules have dealt with this in different ways. The group in Innsbruck separates the species into spatially separate optical traps to evaporatively cool both species simultaneously [112, 113]. The original RbCs experiment in Durham utilises a deep magnetic trap to sympathetically cool Cs with Rb in the same trap [136]. This relies on having a large number of Rb atoms to endure the three-body loss[4]. We utilise a sequential loading scheme, where the atoms are separated temporally and spatially before they are finally overlapped to form molecules. This is discussed further in Chapter 4.

[4]Rb atoms are preferentially lost due to three-body collisions involving Cs due to their lower polarisability at 1064 nm. So, in a 1064 nm trap with both species, Rb sees a lower trap depth and is preferentially lost.

The next challenge is the miscibility of Rb and Cs BECs. The miscibility of two BECs can be inferred from their scattering length. BECs are deemed miscible if the geometric mean of the two intra-species scattering lengths is less than the inter-species scattering length (so $a_{\text{Cs-Rb}} < \sqrt{a_{\text{Rb-Rb}} a_{\text{Cs-Cs}}}$). However the background inter-species scattering length $a_{\text{Cs-Rb}}$ is large in an Rb Cs mixture as shown in Fig. 2.1. At the Efimov minimum of $\approx 21\ G$ where we conduct the evaporative cooling of Cs, $a_{\text{Cs-Cs}} \approx 220 a_0$, $a_{\text{Rb-Rb}} \approx 100 a_0$, and $a_{\text{Cs-Rb}} \approx 645 a_0$. So, a mixture of BECs here is not miscible. We refer the reader to [114] for images of a Rb and Cs BEC trapped together undergoing oscillations through each other, highlighting this immiscibility. To render the BECs miscible, we must either increase $a_{\text{Cs-Cs}}$ to $\approx 4200 a_0$ or reduce $a_{\text{Rb-Cs}}$. The Cs scattering length can be increased by tuning the field to one of many Feshbach resonances. However, at these scattering lengths, the Cs three-body loss would be catastrophic for the Cs cloud. The Feshbach resonances which allow us to tune the Rb-Cs scattering length are all at high fields, above 180 G. Here, $a_{\text{Cs-Cs}}$ is also large, and we would suffer from the Cs three body losses[5]. We follow the approach used initially in Innsbruck [112] and in the older Durham experiment [97], where we utilise a mixture that is not degenerate but still a high PSD (≈ 0.1) to associate our molecules. The drawback of this approach is that the association efficiency is lower (5%) and the associated molecules are at hotter temperatures than if we were to associate from a dual BEC. In the future, we plan to adopt a method similar to that used in [113], where the Cs three-body loss is suppressed by creating a Mott insulator state and overlapping a Rb superfluid (see Sec. 8.3 for more details). They then form a dual-species Mott insulator and associate molecules at the 352 G Feshbach resonance.

[5]The broad Feshbach resonance around 352 G in particular the most promising region for producing a miscible mixture (as has been done in [113]).

2.3 Associating molecules

2.3.1 Feshbach association

As mentioned earlier, we see Feshbach resonances at points where the energies of the unbound atomic states and bound molecular states coincide. We can use the avoided crossings here to associate the atoms into molecules. As shown in Fig. 2.2, at higher magnetic fields, the unbound state lies at a lower energy, whereas at lower fields, the bound state is at lower energy. So, we can associate molecules by sweeping the magnetic field over the Feshbach resonance, starting at a high field and adiabatically ramping down the field over the resonance. The efficiency of association depends on the PSD of the atomic mixture (if it is well overlapped) and the adiabaticity of the ramp (so the rate of the field ramp) [137].

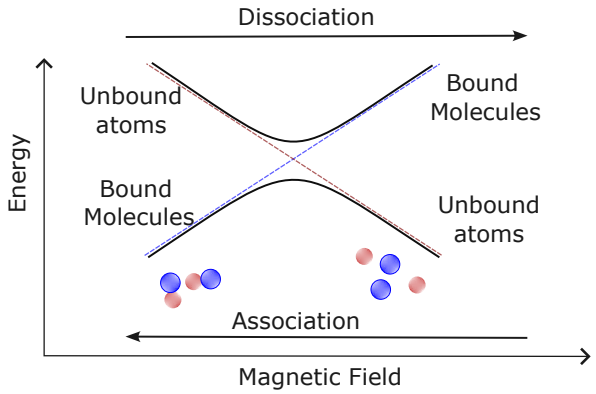

Figure 2.2: A cartoon showing how molecules are associated (dissociated) from (into) atoms pairs by ramping the magnetic field across the Feshbach resonance

In our experiment, we follow the molecule association pathway used previously in the older experiment in Durham [97, 116] and in Innsbruck [116, 119] to associate atoms into Feshbach molecules and transfer them to the ground state. We employ two Feshbach resonances - one at 197.1 G (and 90 mG wide) and another at 181.6 G (and 270 mG wide) [115] to associate and transfer the molecules into a desirable bound state. The Feshbach resonances and the energies of the relevant bound states are shown in Fig. 2.3. We note that the format used here and in the rest of the thesis for denoting Feshbach molecular states of $|n(f_{\mathrm{Rb}}, f_{\mathrm{Cs}})L(m_{f_{\mathrm{Rb}}}, m_{f_{\mathrm{Cs}}})\rangle$. Here,

n denotes the vibrational quantum number for the particular $(f_{\mathrm{Rb}}, f_{\mathrm{Cs}})$ manifold, counting down from the least bound state ($n = -1$). L denotes the quantum number corresponding to the rotational angular momentum of the atoms about their centre of mass (denoted by $s, p, d, f....$ in the usual fashion).

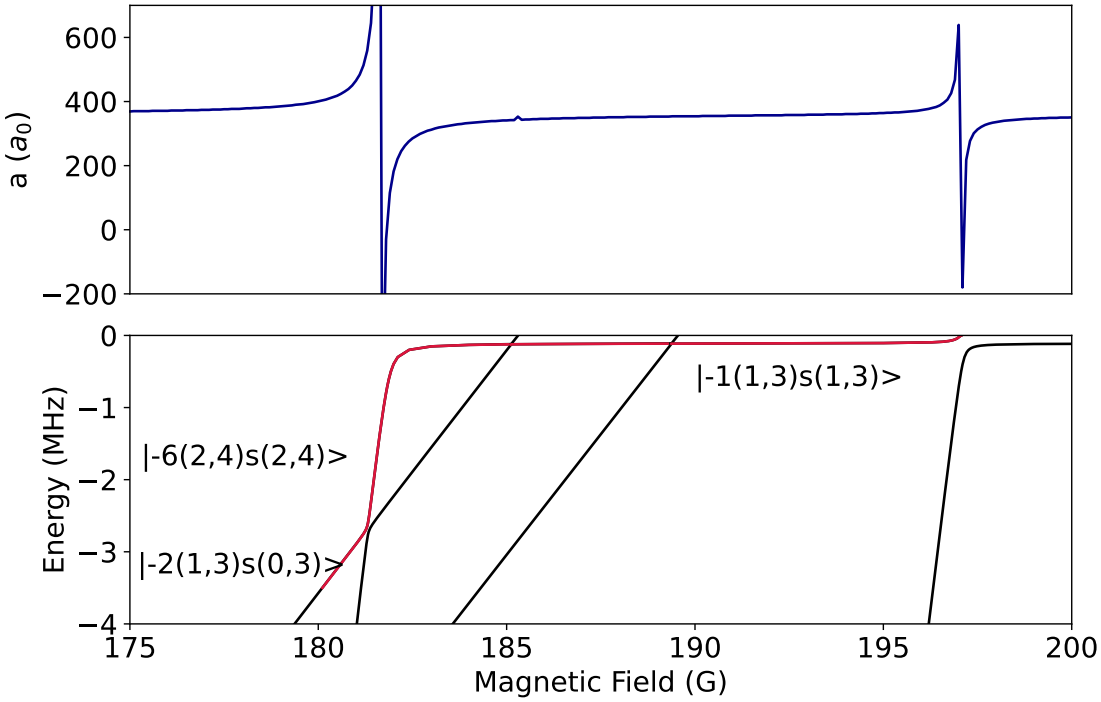

Figure 2.3: Calculated s-wave scattering lengths of Rb + Cs around the Feshbach association fields in the relevant states that they are present in our experiment (above). The binding energies of the Feshbach molecules in different states (below). The red line shows the path we take in associating molecules. Calculations done by Jeremy Hutson's group [115].

We use the Feshbach resonance at 197.1 G to initially associate our molecules. Ramping over the resonance here, we produce molecules in the weakly bound molecular state $|-1(1,3)s(1,3)\rangle$. Atoms in $|-1(1,3)s(1,3)\rangle$ are very weakly bound, with a binding energy of 110±2 kHz. We are able to transfer Feshbach molecules to different states by sweeping the magnetic field over avoided crossings with other states [116]. We transfer molecules into these fields by ramping the magnetic field over these crossings to transfer the molecules to a specific state. After associating into $|-1(1,3)s(1,3)\rangle$, we ramp down the field to transfer out of this state using

the Feshbach resonance at 181.6 G. We can transfer to the $|-6(2,4)s(2,4)\rangle$ and then the $|-2(1,3)s(0,3)\rangle$ states (both shown in Fig. 2.3), which are more strongly bound (with binding energies of a few MHz). We use both of these states in our experiment, as is discussed in Chapter 5.

2.3.2 STIRAP

From the Feshbach state, we want to transfer the molecule to the ground state via STIRAP [138]. Molecules are transferred from the Feshbach state $|F\rangle$ to the molecular ground state $|G\rangle$ via an intermediate excited state $|E\rangle$ (see Fig. 2.4). We cannot directly populate $|E\rangle$ since the excited states available have short lifetimes (decay rate $\gamma = 35$ kHz estimated previously [139]), and can decay to many other states. So molecules transferred to $|E\rangle$ are rapidly lost from the experiment. This is why we use STIRAP, where we use a two-photon Raman process to transfer from $|F\rangle$ to $|G\rangle$, without directly populating $|E\rangle$. We employ two laser beams to engineer couplings between the three states. The first beam, which we refer to as the 'pump' beam couples $|F\rangle$ to $|E\rangle$ and is at the frequency of that transition - around 1557 nm. The other beam is the 'Stokes beam' which couples the $|F\rangle$ to $|G\rangle$, and is at 977 nm.

If the system is modelled as a three state system, with $|F\rangle$,$|E\rangle$and $|G\rangle$, then one of the eigenstates [138] (which is relevant for STIRAP) is

$$|\Psi\rangle = \cos\theta|F\rangle - \sin\theta|G\rangle. \tag{2.4}$$

Here, θ is the mixing angle, which is defined as $\tan\theta = \Omega_{\text{pump}}/\Omega_{\text{Stokes}}$, where Ω_{pump} and Ω_{Stokes} are the Rabi frequencies at which the pump and the Stokes transitions are driven. It can be seen that in this description, $|\Psi\rangle$ describes a dark state with no component of the state $|E\rangle$. The other two eigenstates of the system are described by,

$$\begin{aligned} |\Psi+\rangle &= \sin\theta\sin\phi\,|F\rangle + \cos\phi|E\rangle + \cos\theta\sin\phi|G\rangle \\ |\Psi-\rangle &= \sin\theta\cos\phi|F\rangle - \sin\phi|E\rangle + \cos\theta\cos\phi|G\rangle, \end{aligned} \tag{2.5}$$

where ϕ is defined by $\tan 2\phi = \frac{\sqrt{\Omega_{\text{pump}}^2+\Omega_{\text{Stokes}}^2}}{\Delta}$, where Δ is the detuning of the beams

from resonance.

The pulse sequence used along with and illustration of the scheme is shown in Fig. 2.4. The pulse sequence to transfer from $|F\rangle$ to $|G\rangle$ involves ramping down the Stokes beam and simultaneously ramping up the pump beam. This is done so that with maximum Stokes power (and no pump power), the system is initialised in the dark state $|\Psi\rangle$, with $\cos\theta = 1$ and the two other states having no $|F\rangle$ component. We then transfer to $|G\rangle$ by adiabatically reducing the Stokes intensity while increasing the pump intensity. When the Stokes laser is off and the pump laser is at maximum intensity, $\theta = \pi/2$, and the system is completely transferred to $|G\rangle$. Theoretically, this process is 100% efficient, however in practice, it is limited by non-adiabaticity of the transfer and laser phase noise [140–142].

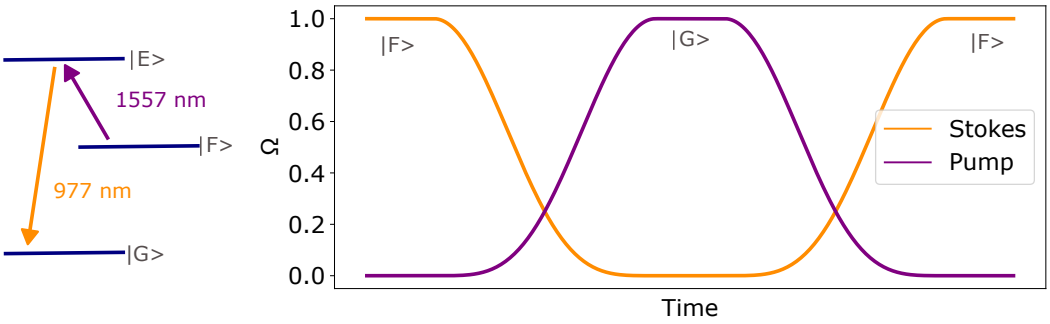

Figure 2.4: The pulse sequence used to transfer molecules from the $|F\rangle$ state to the state $|G\rangle$ and back using STIRAP. We use a $\cos^4$ pulse shape to optimise efficient transfer [138].

STIRAP efficiency

The efficiency of STIRAP is limited by two factors. The first is the non-adiabaticity of the transfer - which leads to molecules populating states other than the dark state and being lost to decays from $|E\rangle$. The second is the phase noise on the lasers when they are locked [141, 142]. The laser phase noise induces a coupling between the dark state and the bright states from which the molecules can be lost [142]. With

the laser phase noise, we can model the STIRAP efficiency (η) as,

$$\eta(t) = \exp\left(-\frac{\tau_{\text{adi}}}{t} - \frac{t}{\tau_{\text{deph}}}\right), \tag{2.6}$$

where ($\tau_{\text{adi}} \equiv \pi^2\gamma/\Omega^2$) is the timescale of adiabaticity defined in terms of the loss rate from $|E\rangle$ (γ) and $\Omega = \sqrt{\Omega_{\text{pump}}\Omega_{\text{Stokes}}}$ related to the Rabi frequencies. τ_{deph} is the dephasing timescale, which includes the effect of laser phase noise, the linewidth of the lasers, and any other noise source that causes detuning between the two lasers, changing the two-photon detuning. The maximum efficiency achievable is equal to $\eta(t) = \exp\left(-2\sqrt{\tau_{\text{adi}}/\tau_{\text{deph}}}\right)$ at a pulse time $t = \sqrt{\tau_{\text{adi}} \times \tau_{\text{deph}}}$. The peak efficiency approaches unity as $\tau_{\text{adi}} \to 0$ or $\tau_{\text{deph}} \to \infty$. So, it is desirable to maximise the Rabi frequency - or practically, maximise the intensity of the pump and the Stokes beam on the atoms and to reduce any causes of dephasing.

We find that the main contribution to τ_{deph} is from the high frequency laser phase noise. This phase noise is an unavoidable consequence of the locking of the lasers using a feedback loop. While the locking suppresses low frequency drifts and low frequency phase noise, a characteristic of any PID locking scheme is the servo bump, which introduces some high frequency phase noise into the system. We lock both the pump and the Stokes laser to the same cavity, so we expect any drifts in frequency from drifts in cavity length to be suppressed in the two-photon detuning. If the finite linewidth (Γ) of the lasers was the sole cause of the loss, the dephasing time would be $\tau_{\text{deph}} = 2/\Gamma$, which for our measured linewidths of ≈ 500 Hz corresponds to ≈ 4 ms. Experiments which have attempted RbCs STIRAP have seen dephasing times an order of magnitude lower than would be expected from the Rabi frequencies and linewidths of the beams [97, 143]. This has been attributed to additional dephasing from the high-frequency phase noise of the laser[6]. We model the efficiency and show that this is indeed the case [144] and the STIRAP efficiencies can be improved by reducing the phase noise. This is discussed further in Sec. 5.9.

[6]It was even found that the optimal STIRAP efficiency was at powers lower than the maximum available power, since increasing the laser power increased the magnitude of the phase noise

2.4 Optical lattices

We find it useful to offer a brief overview of the physics of optical lattices, and introduce terms and concepts used later in the thesis. A more thorough overview of lattice physics and its relation to ultracold matter can be found in [145–149] - particularly for discussions on the band structure and the Hubbard Model, which are left out of this thesis since we do not present any experimental work requiring a detailed knowledge of them[7].

The energy of particles in a lattice potential can be described by a band structure, whereas the interactions can be described with the Fermi-Hubbard, or the Bose-Hubbard (as in this case) model. Ultracold atoms in optical lattices are an exciting platform for the simulation of Hubbard models [150], and molecules offer some exciting avenues to be investigated [43].

An optical lattice is can created by applying a periodic intensity mask, or by a combination of two or more interfering laser beams, which create a periodic potential. We opt for the latter approach. Previous work in our experiment [148] has presented a 3D lattice potential created by three laser beams retro-reflected. This creates a potential of the form,

$$V = V_0 \cos^2(k_{\text{lat}} x), \tag{2.7}$$

where k_{lat} is the wavevector of the lattice given by $2\pi/\lambda$, and a nearest neighbour lattice spacing a_{lattice} of $\lambda/2$. Since then, we have replaced it with a bow-tie lattice configuration, where the same beam is reflected on itself for four passes. In this geometry, the lattice spacing is $a_{\text{lattice}} = \lambda/\sqrt{2}$, though the trap depth from the same power is 4 times larger.

The lattice depth V_0 is usually quoted in terms of recoil energy (E_{rec}), given by,

$$E_{\text{rec}} = \frac{\hbar k_{\text{lat}}^2}{2m} = \frac{h}{8 m a_{\text{lattice}}^2}. \tag{2.8}$$

For a lattice spaced by 752 nm, the recoil energy for Cs is $E_{\text{rec}}^{\text{Cs}} = 31.8$ nK, $E_{\text{rec}}^{\text{Rb}} = 48.6$ nK, and $E_{\text{rec}}^{\text{RbCs}}$=19.2 nK. As the recoil energy is inversely proportional to the

[7] Although the near future of the experiment will do so

mass, loading into the lowest energy bands is more difficult for particles with higher masses. We currently associate molecules from atoms at ≈ 200 nK, so the molecules populate multiple lattice bands when loaded into the lattice from a cloud. In the future, we plan to load atoms into the lattice from a BEC, and perform Feshbach association in the lattice itself, which should leave us with molecules in the ground band of the lattice. Currently, the lattice is used at high depths of >3000 $E_{\mathrm{rec}}$to pin the atoms to their sites throughout the imaging process.

2.4.1 Layer selection

Quantum gas microscope experiments typically require the preparation of a single plane of atoms. The imaging systems used to image atoms on their lattice sites typically have depths of field sufficient to image multiple lattice layers. In our case, the depth of field for imaging at 852 nm is given by $z_d = \lambda/\mathrm{NA}^2 \approx 3\mu m$. So, if we have multiple layers within this spacing, they are all imaged. It is difficult to distinguish between atoms from different layers, and the atoms stacking makes reconstruction of the lattice very difficult

There are two main strategies used to prepare a single layer of atoms for imaging in microscope experiments. The first method of layer selection involves loading a 3D lattice and then utilising some technique (such as a magnetic field gradient) to tune the available microwave transitions of adjacent layers away from each other [151–153]. With a sufficient field gradient, only a single plane of the lattice can be transferred to a different hyperfine state. The other planes can then be blasted away before returning the selected plane to the ground state. This method relies on highly stable magnetic fields, an extremely mechanically stable setup and a low level of background magnetic field fluctuation (or some active compensation thereof). For the Cs atoms spaced 532 nm apart[8], if we were to employ a magnetic field gradient of 50 G/cm and a bias field of 20 G, we would require a total field stability of 2 mG (from the coils and the background field combined), a current stability of about 70 ppm, and high mechanical stability of the experiment are required - all of

[8]The vertical lattice would be retro-reflected, and not a bow-tie lattice, so the spacing is 532 nm rather than 752 nm.

which are experimentally challenging. We find instabilities in the magnetic field of ≈ 5 to 10 mG, which enough to make the scheme infeasible for us (without improving the noise)[9].

The other approach relies on compressing a larger cloud into only a single layer - often using optical methods. Some groups [21, 154] employ a shallow angle lattice which can produce lattice spacings of ≈ 10 μm. These lattices are often employed in a configuration where the lattice spacing can be changed (an accordion lattice) [18, 24, 155]. The method we have implemented uses a beam that is tightly focused in only one axis - often referred to as a light sheet [19, 82, 156] - which compresses all the atoms into a single plane.

2.5 Fluorescence imaging

To image atoms trapped in the optical lattice, we must induce some emission of light from the atoms while they are in the lattices. The atoms must remain trapped in the lattice for many imaging cycles in order to emit enough light so that they can be reliably imaged. So, it is desirable that the light used for imaging also cools the atoms. In microscopes with alkali metals, the molecules are made to fluoresce either using a molasses cooling scheme [14, 15, 20, 21, 83, 157], EIT cooling [16, 22, 26], or with a Raman sideband cooling scheme [17–19, 155, 158, 159]. We use D_2 molasses cooling to cool and image both Rb and Cs in the optical lattice. As shown by its efficacy in the other setups (which include Rb and Cs atomic microscopes), molasses cooling is a good choice as it is relatively simple to setup, and is able to maintain the atoms at temperatures (≈ 10 μK) where they can reliably be trapped and pinned by the lattice (≈ 200 μK).

The fluorescence light is collected by a high numerical aperture (NA) objective lens, and then focused onto a camera to generate the image of atoms in the lattice. The number of photons scattered is given by the scattering rate, which is described in terms of the molasses beam detuning Δ, saturation parameter $s_0 = I/I_{sat}$ and

[9] Air conditioning cycles, rogue power supplies, AC noise from the mains, and being in a building with other experiments all have an effect.

linewidth of the transition Γ by,

$$\Gamma_{scat} = \frac{\Gamma}{2} \frac{s_0}{1 + s_0 + (\frac{2\Delta}{\Gamma})^2}. \tag{2.9}$$

With a brief overview of the relevant theory provided, we shall now proceed to describe the overall experimental setup.

CHAPTER 3

Experimental setup

In this chapter, we provide an account of the experimental setup. We provide a brief description of the vacuum setup used, and the dual-chamber design of the experiment. We present the optical setup used for the laser cooling of both species, and briefly discuss the optical setup of beams throughout the experiment. We highlight the optical transport scheme used in our lab to transfer atoms from our Main Chamber to the Science Cell. Much of the laser cooling and transport was set up before my PhD and details can be found in [148, 160, 161]. The setup of the dipole traps in the Science Cell, the STIRAP beams, and the microscopy setup are only briefly mentioned in this chapter as they are discussed in detail throughout the remainder of this thesis.

We also present some of the methods used to control the optical beams, magnetic fields and microwaves critical to our experiment, including detail of the fast rotation mount developed [162]. We finally offer an overview of some of the commonly used routines performed to characterise the setup, which are referred to throughout the rest of the thesis.

3.1 Overview of the experiment

The apparatus was designed to perform quantum gas microscopy of RbCs molecules - or single molecule resolved imaging of molecules in an optical lattice. This experimental apparatus (along with an experiment using optical tweezers) were envisioned as the next generation setup following the older RbCs molecule experiment in Durham [116, 120, 163].

The older experimental apparatus consists of a single chamber with a deep magnetic trap used to trap both atomic species and then create molecules. In our experiment, we utilise a dual-chamber design, with the MOT loads and laser cooling of the species performed in the 'Main Chamber', and the association of molecules and microscopy performed in the 'Science Cell' - a glass cell 37.2 cm away.

The use of the dual-chamber design offers many advantages, and is particularly common in quantum gas microscope experiments [14–17, 19, 22, 24, 158] where the need for a high NA objective lens placed close to the cell makes a dual-chamber design preferable. We are further motivated towards a dual-chamber design as to make ultracold associated molecules, our experiment requires the laser cooling of two different species. This adds to the complexity and the laser cooling beams take up a significant portion of the optical access available in the Main Chamber. With the use of our dual-chamber design, we gain the optical and mechanical access required for the microscope objective lens and the lattice beams. We are also able to maintain a better vacuum in the Science Cell, with the further separation from the dispensers used to load the MOT. The Science Cell was designed with four in-vacuum tungsten electrodes, to be used to apply and control the electric field on the molecules. The use of a dual-chamber design poses one obvious additional challenge - transporting the atoms from one chamber to another efficiently. To offset some of the loss in number and phase space density caused by transport, we perform Degenerate Raman Sideband Cooling (DRSC) of both species before transport. We are able to leverage the dual-chamber design and the optical transport to our advantage by employing a sequential loading sequence, where the atoms of Rb and Cs are sequentially loaded and transported to the Science Cell - where they are associated. We discuss the motivation behind the dual-species sequence, and the sequence itself, in detail in

Chapter 4.

3.2 Optical and vacuum setup

3.2.1 Vacuum setup

A rendering of the entire vacuum system is presented in Fig. 3.1. The atoms of Cs and Rb are loaded into a 3D MOT in the Main Chamber from two $2D^+$ MOTs arranged on either side of the Main Chamber. The $2D^+$ MOTs provide cold atom beams to the Main Chamber. Dispensers of Rb and Cs[1] are installed in the relevant 2D MOT vapour cells, and are used to keep a reasonable vapour pressure in the cell. The 2D MOT cells can be maintained at much higher vapour pressures than the main experiment, due to a differential pumping section of 1 mm diameter and 13.25 mm length, and are pumped by a Agilent VacIon 10 ion pump.

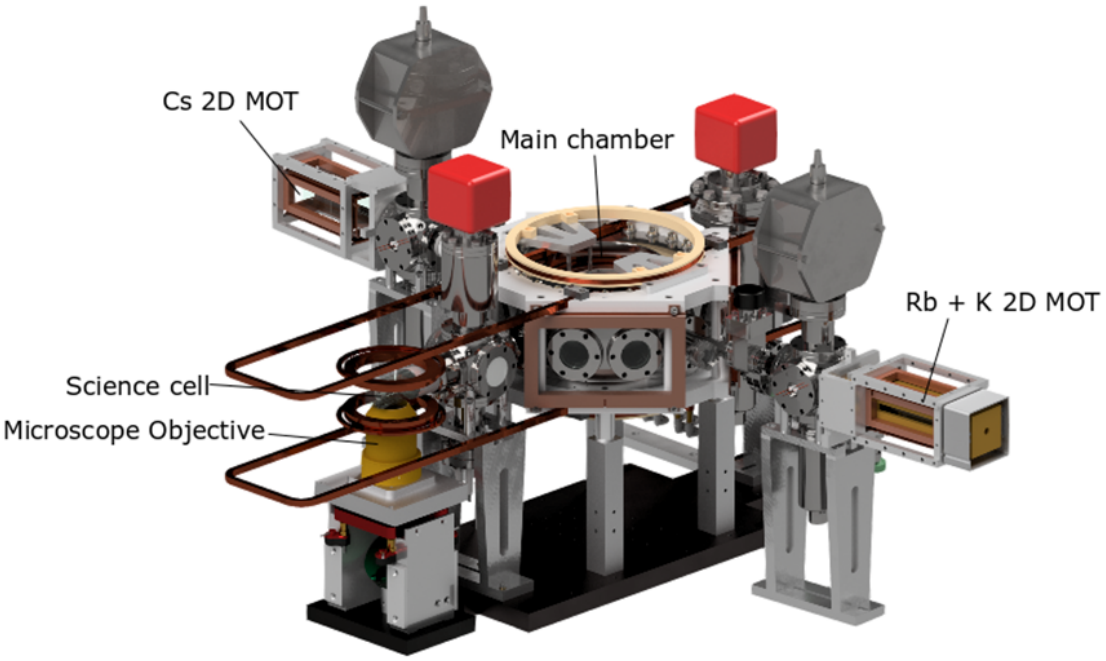

Figure 3.1: A rendering of the experiment showing the vacuum setup.

The Main Chamber consists of 12 sides, each fitted with anti-reflective (AR)

[1]We also have K dispensers fit into the experiment, in the same cell as Rb - a harkening to ambitions of producing KCs molecules. This is not discussed in this thesis

coated viewports (AR at the relevant wavelengths of 780 nm, 852 nm and 1064 nm). This is connected to the Science Cell - a Cold Quanta custom manufactured glass cell. The cell was specifically designed to have flat AR windows to reduce aberrations in imaging. We maintain an ultra-high vacuum in the Main Chamber and Science Cell using a non-evaporable getter (NEG) and a NEXTorr ion pump.

3.2.2 Laser cooling setup

We require a complex laser system to produce light at the right frequencies and powers required for laser cooling Rb and Cs atoms in the MOT and the DRSC. We utilise the D_2 line as shown in 3.2 for both species to perform the laser cooling. We use saturated absorption spectroscopy to lock lasers to the cooling and repump transitions for both species. The lasers used for this are on a dedicated table, separate from the main experimental table. We use Toptica DL Pro lasers to provide light close to the Cs and Rb repump transitions, and a Toptica TA to provide light tuned to the cooling transitions. The $2D^+$ MOT, 3D MOT, and imaging all require beams of different powers and frequencies. This is attained by splitting the beam out of the laser using a set of Polarising Beam Splitters (PBSs) and half-wave plates (HWPs). The different components of the beam are double-passed through dedicated Acousto-Optical Modulators (AOMs), which allows us to control the power and frequency of the beams individually. The light for the Cs DRSC is from the same TA used for the MOT and imaging cooling beams, but for Rb, we have a separate Toptica TA used for this. The beams are then coupled into fibres and sent to the main experimental table. A detailed account of the setup of these lasers and the frequencies and powers of all the beams used can be found in [148, 160].

3.2.3 Main Chamber setup and sequence

General setup

The optical setup in the Main Chamber is illustrated in Fig. 3.3. We operate a six-beam MOT setup for each species (three beams retro-reflected). In addition, the

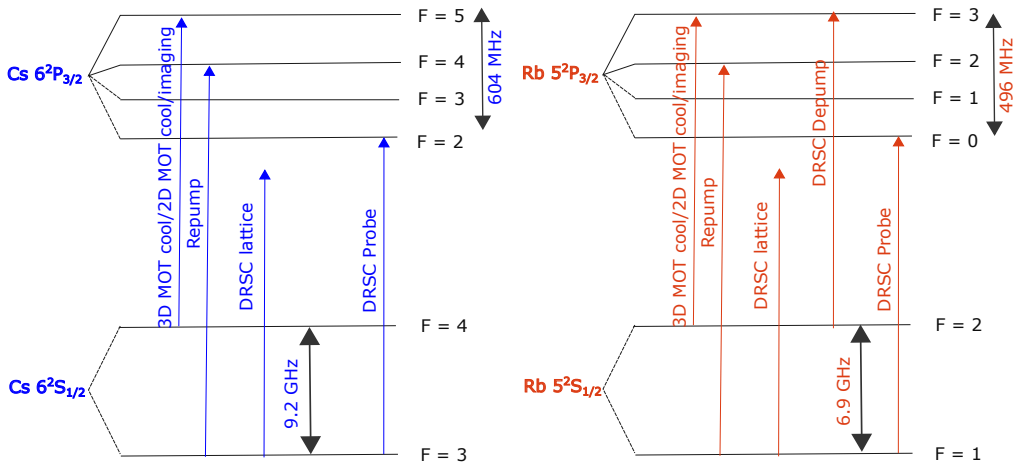

Figure 3.2: A schematic (not to scale) showing the relevant D_2 transitions used to cool Rb and Cs in our experiment.

light for the DRSC lattice and cooling is coupled into the same fibre for both species, and propagates down the same optical path. After DRSC, the beam is loaded into a large waist crossed optical dipole trap that we call the Main Chamber reservoir. From this trap, the atoms are transported to the Science Cell using an optical conveyor-belt transport in a 1D lattice. This required two counter-propagating beams as shown in Fig. 3.3. A more detailed schematic can be found in [164]

MOT load and cMOT

The sequence for both Rb and Cs starts with loading the 3D MOT. The 2D+ MOT and 3D MOT both operate using light red-detuned from the cooling and repump transitions. We require about 2 s of MOT load for Cs and 6 s for Rb to saturate the number of atoms later trapped in the reservoir[2]. After the MOT load, we utilise a 50 ms long compressed MOT (cMOT) stage where the magnetic field gradient is ramped up to 28 G/cm to compress the MOT and improve mode-matching to the DRSC lattice. We then apply 2 ms of optical molasses cooling [1, 166] to reduce the temperature of the atom clouds.

We have investigated the use of a temporal dark MOT [167] for both species to improve the MOT load in the sequence. Here, the repump light is ramped down

[2]This is currently limited by the 2D MOT vapour pressures, and we have seen a significantly quicker load using light-induced atomic desorption (LIAD) [165].

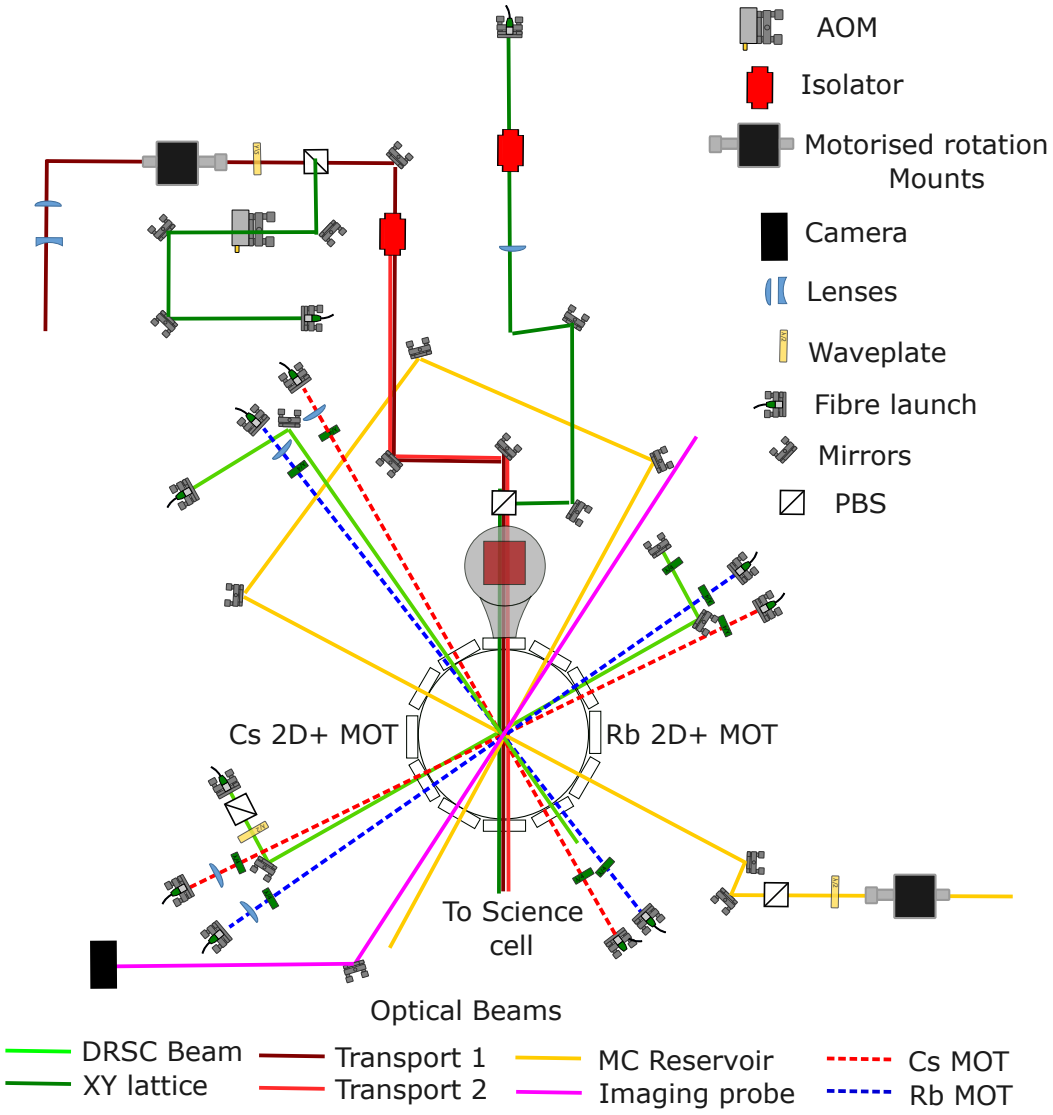

Figure 3.3: The optical setup in and around the Main Chamber. The MOT and DRSC beams originate from the laser cooling table, the setup of which is described in [160]. The remainder of the setup on the main experimental table is shown in Fig. 3.6

during the cMOT phase, so that the atoms spend more time in the lower hyperfine state, reducing loss from the MOT beams. We ramp the power of the repump beam down during the cMOT phase, and measure atom number in the reservoir trap (described below) to optimise this as shown in Fig. 3.4.

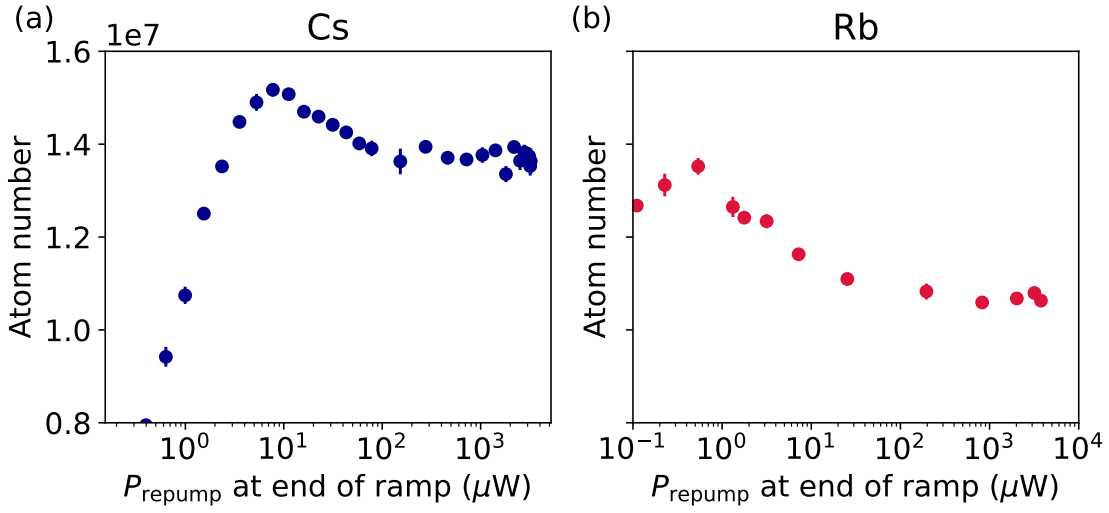

Figure 3.4: The temporal dark MOT for both Rb and Cs. The repump intensity is ramped down from the maximum intensity over the course of the 50 ms long cMOT stage. (a) and (b) show the atom number in the Main Chamber reservoir as a function of the Repump power for Cs and Rb respectively at the end of the cMOT stage for a saturated MOT load. The non ramped power that we initially start with is 320 μW for Cs and 372 μW for Rb. Both plots share a Y-axis.

Degenerate Raman Sideband Cooling

To reduce the temperature of the cloud further, and increase the phase-space density, we utilise Degenerate Raman Sideband Cooling (DRSC). DRSC is often utilised to cool atomic clouds to low temperatures (below 1 μK) without suffering a large loss in atom number. It was first demonstrated in Cs in [168] and Rb [167]. The DRSC in our experiment is based on a Cs DRSC setup in another lab in Durham detailed in [109], and details of our specific setup are presented in [148, 160].

A DRSC cooling scheme works by loading atoms into an optical lattice, and then removing energy though cycles of Raman transitions and optical pumping, where each cycle removes two quanta of the vibrational mode of the trapping lattice. We offer a brief overview as to how the DRSC works for Cs, with a similar scheme for Rb. We start with Cs atoms in the state $|F = 3, m_F = 3\rangle$. Once the lattice is turned on, the atoms populate the vibrational levels of the lattice v. Before any cooling is done, the atoms are in $|F = 3, m_F = 3, v\rangle$ where $v \gg 1$. The magnetic field is tuned to induce a Zeeman shift where the separation of adjacent m_F states is the same as the

difference in energy of additional vibrational levels. So, the state $|F = 3, m_F = 3, v\rangle$ is now degenerate with $|F = 3, m_F = 2, v - 1\rangle$ and $|F = 3, m_F = 1, v - 2\rangle$. We then cycle atoms through these states using a two photon Raman transition (driven by the lattice beams). The atoms in $|F = 3, m_F = 1, v - 2\rangle$ are then transferred to the $|F = 3, m_F = 3, v - 2\rangle$ by pumping to the $6P_{3/2}|F' = 2, m_F = 2\rangle$ state with the *polariser beam*. In this way, the atoms lose two quanta of vibrational energy every cycle until they reach $|F = 3, m_F = 3, 0\rangle$ or $|F = 3, m_F = 3, 1\rangle$. Atoms in $|F = 3, m_F = 3, 1\rangle$ are able to go to $|F = 3, m_F = 2, 0\rangle$, but can not be transferred to the $m_F = 1$ levels. This is solved by having the *polariser beam* not be completely circularly polarised, but having a small amount of linear polarisation to drive atoms to the $6P_{3/2}|F' = 2, m_F = 2\rangle$, from where they decay to $|F = 3, m_F = 3, 0\rangle$. Rb has a similar scheme but requires an additional beam combined onto the lattice known as the depumping beam[3] (resonant with the F=2 to F'=2 transition), which prevents accumulation of atoms in F=2 by driving them back into the DRSC cycle.

The initial optimisation of the DRSC was performed during the early stages of the setup of the experiment [160]. Over the course of the work presented in the thesis, we found that the performance of the DRSC was not as good as we expected, particularly for Rb. At the time, we were planning on loading and Rb and Cs simultaneously in the experiment, and the atom number we were able to load into an optical trap (the MC reservoir trap) was limited by the mismatched times required for the DRSC. Cs was optimal at 3 ms while Rb was optimal at 15 ms. The extra hold time in the lattice when the two species were cooled together lead to a significant loss in atom number. On performing a 'tune-up' of the laser cooling and DRSC system, we found that we were able to reduce the Rb DRSC time to the point where both Rb and Cs are optimal at 3 ms. We have $\approx 2 \times 10^7$ atoms of both species at 1.05 ± 0.06 μK for Cs and at 2.1 ± 0.2 μK for Rb after 3 ms of DRSC individually. While we do not currently cool the species together, it is reassuring to note that the DRSC times are similar if we were to attempt this in the future.

[3]For Cs, the lattice beam is tuned to act as the depump

Reservoir trap

After DRSC, the atoms are cold enough that they can be optically trapped as a bulk gas in an optical-dipole trap with reasonable laser intensities. The atoms are loaded into a crossed optical dipole trap (xODT) formed by a beam from a 50 W fibre laser (IPG YLR-50-LP) in a bow-tie configuration called the Main Chamber reservoir (MC reservoir) trap. The reservoir trap is formed from a 500 μm beam in a bow-tie configuration, sized to mode-match the cloud after DRSC The coherence length of this laser is short enough that we form an optical trap, and not a lattice. We are able to load 2.1×10^7 atoms of Rb and 1.8×10^7 Cs atoms into the Main Chamber reservoir, at a temperature of 3 μK for Cs and 6 μK for Rb. The atoms are levitated in the reservoir using a magnetic field gradient, as described in Sec. 3.3.2. The atom number in the experiment is measured using absorption imaging as described in Sec. 3.2.6.

3.2.4 Optical transport

The next stage in our experiment is optical transport, where the atoms are transported 37.2 cm to the Science Cell. Transport of atoms in ultracold matter experiments is not uncommon, with many experiments opting to perform some form of transport given the advantage of transferring the atoms to a different region with more optical access and better vacuum conditions. A detailed account of the setup of our optical transport is given in the following theses [148,161] and publication [118].

Transport has been achieved in a variety of manners, both optical and magnetic. Magnetic transport is performed by trapping atoms in a magnetic trapping potential, and translating it either by mechanical translation of the trapping coils [169–172], or by having multiple coils with time varying fields [173–175]. Optical transport is perhaps more common, since it requires less mechanical space and is applicable to all species (irrespective of their magnetic moments). The simplest method used is the translation of an optical dipole trap using a mechanical translation stage [176–178]. This method suffers some loss due to inherent vibrations associated with the stages used, and the clouds post transport are elongated in the direction of transport, since

the trapping confinement is weaker along that direction. In addition, this method is often relatively slow. Developments to this methods have included replacing the stage with a variable-focus lens [179, 180] to remove the mechanical vibrations. However, the thermal drift of the focal lengths and power limitations though the variable-focus lenses are significant challenges. The axial confinement has also been improved in experiments using a translation stage by forming a xODT from two beams focused by a single lens (which is then translated to move the trap) [181] or using pair of translation stages to shift the position of an optical lattice [182].

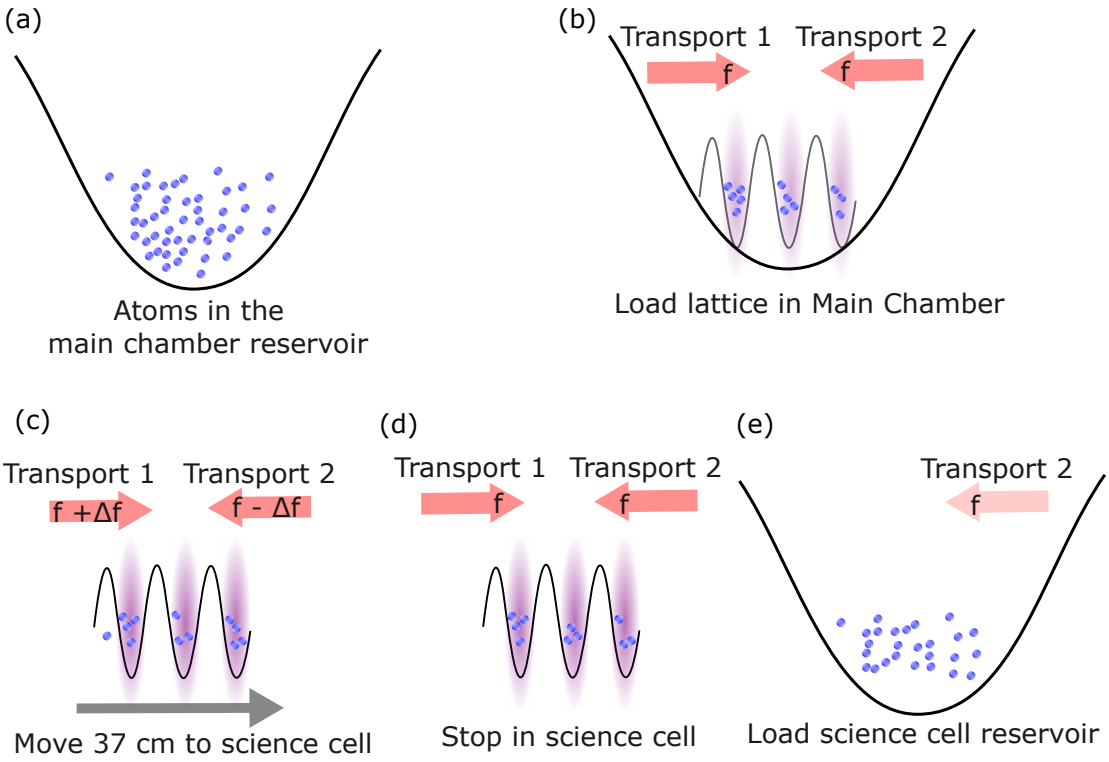

Figure 3.5: An illustration of the sequence for optical transport of one species from the Main Chamber to the Science Cell using the optical-conveyor belt technique.

We opt for a method using a moving lattice often referred to as an optical conveyor-belt as shown in [158, 183–189]. Here, the atoms are trapped in an optical lattice formed from the interference of two coherent counter-propagating beams. The lattice potential leads to a strong confinement in the direction of transport. The lattice is translated by changing the frequency of the lattice beams relative to

each other during the sequence to move the lattice. For a lattice formed of light at wavelength λ, a change in frequency of Δf results in the lattice translating with a velocity $v = \lambda \Delta f/2$. The frequency of each lattice beam is controlled during the experiment to transport the beams from the Main Chamber to the Science Cell.

While the confinement along the direction of transport is no longer an issue, the limiting factor now becomes the trap depth radially across the transport beams, as the atoms are no longer trapped at the focal point of the beams. Previous experiments have addressed this issue using a variable focus lens to synchronise the focal position of the lattice beams with the atoms [188], or by using a Bessel beam for the lattice [187]. We opt for a simpler method, using two overlapped Gaussian beams for our transport. The trapping potential is determined by the combination of both transport beams. We carefully select the focal positions and waists of each beam to maximise the minimum trap depth in the transport path as detailed in [118]. The careful selection of the focal position, along with high optical powers allows us to achieve a trap depth sufficient for transport[4]. We label the transport beam that propagates from the Main Chamber to the Science Cell as the Transport 1 beam and the beam that propagates the other way (Science Cell to Main Chamber) as Transport 2.

We require two high power phase coherent beams for the transport lattice. This is achieved by seeding two fibre amplifiers (Azurlight Systems) from a common laser (2 W, 1064 nm Mephisto-NPRO). The fibre amplifiers are run at output powers of 30 W and 40 W[5]. This configuration allows us to use light directly from the amplifier outputs, maximising the optical power on the atoms. The coupling efficiency of the AOMs and the driving frequency of the AOM does not effect the power or position of the beam on the atoms at all. Each fibre amplifier needs around 10 mW of light to output its maximum power, and as long as that amount of light is provided, we have a reliable output from the amplifiers. The frequency of each of the transport beams is controlled using a dedicated AOM driven by a DDS board programmed to

[4]The author firmly believes that there are few problems that can not be solved with the use of more optical power.

[5]The beam focused closer to the Science Cell is the 40 W beam. The beams were initially both 30 W, however one of the lasers was upgraded.

output a linear frequency ramp. This allows us to control the frequency of the two beams independently, and hence control the lattice frequency. More details of each of the beams is presented in Sec. 3.2.7.

We have previously reported single species transport efficiencies of 75% in our experiment [118]. Since then, we have made two significant changes to the transport setup - namely the replacement of one of the 30 W fibre amplifiers with a 40 W amplifier, and the use of a linear ramp over a minimum jerk ramp. While the minimum jerk trajectory is slightly more efficient than the linear ramp, we use the linear ramp as it allows us to use our DDS board to programmatically generate the ramp. This allows us to have a smooth linear ramp without using a look-up table and makes programming the DDS easier. We see a transport efficiency of ~ 70 %, and are consistently able to transport 1.4×10^7 atoms of Rb and 1.3×10^7 Cs atoms into the lattice in the Science Cell.

3.2.5 Science Cell setup

The optical setup of the beams in the Science Cell is shown in Fig. 3.6[6]. The transport beams described earlier propagate along the length of the Science Cell, transporting atoms from the Main Chamber to the Science Cell. Once the atoms are transported to the Science Cell, they are trapped in another large waist xODT called the Science Cell reservoir. In the Science Cell, we initially load into a large waisted trap (referred to as SC Reservoir trap), formed by the combination of the Transport 2 beam and a cylindrical beam (SC Reservoir beam) from the 50 W IPG laser (same laser used for the MC Reservoir, with the power redirected using a rotation mount). The beam is cylindrical (200 μm vertically and 500 μm horizontally) to match the shape of the atoms after they have been transported. We are able to load upto 8×10^6 atoms of Rb and 6×10^6 of Cs into this trap from the lattice.

The next stages of the experiment in the Science Cell use the small waist optical-dipole traps (the dimple traps) and evaporatively cool the atoms to reach the high PSD required to make molecules. The atoms are loaded from the reservoir into the

[6]Some optics and optical paths are not shown to improve readability of the figure. These are mostly pickoffs of the beams used for servoing the power and monitoring the position

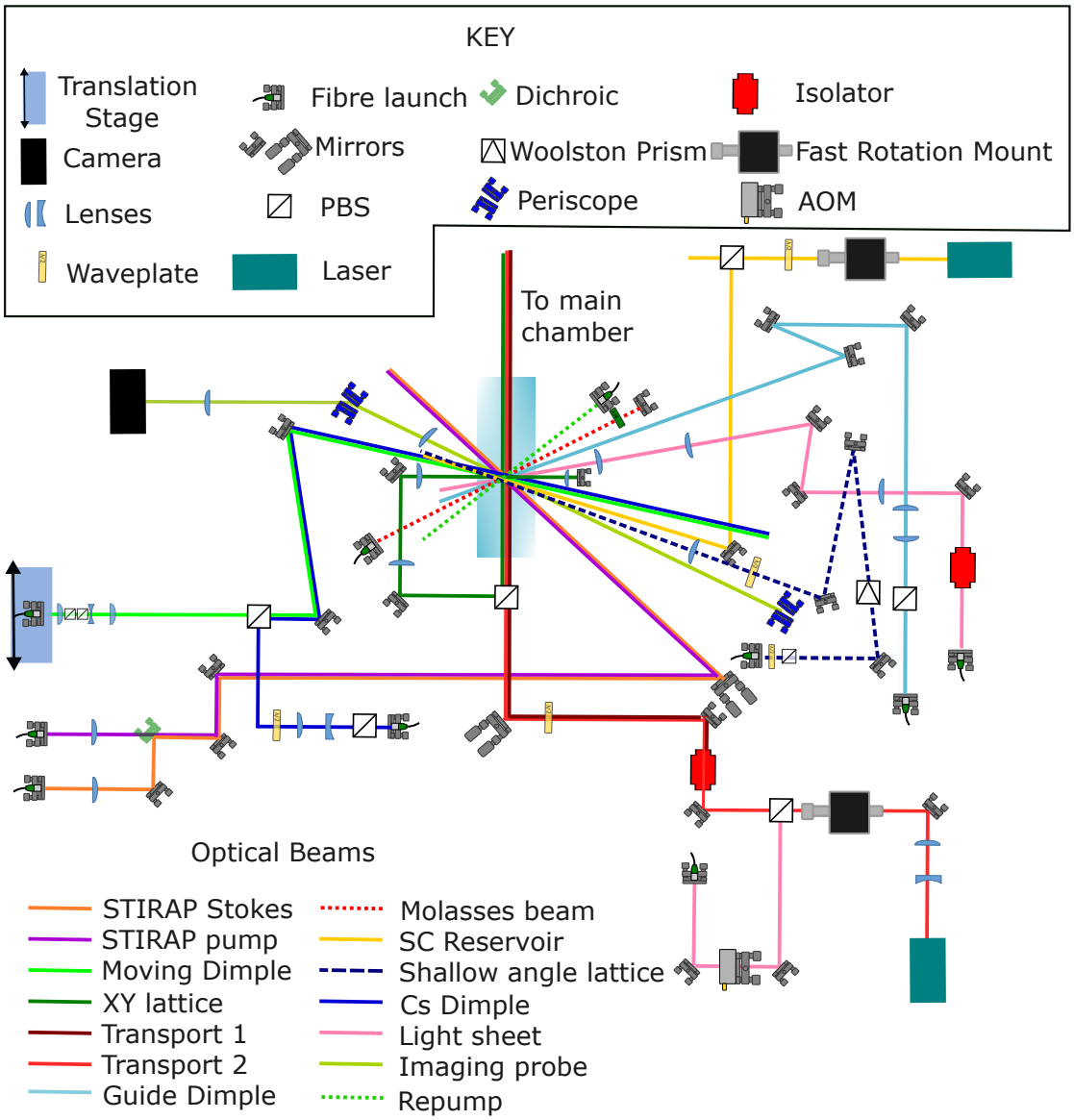

Figure 3.6: The setup of optics and beams around the Science Cell.

smaller optical traps (known as dimple traps) using the 'dimple trick' [190]. The dimple trick allows us to increase the atom density by loading the atoms into a smaller volume, which increases the thermalisation rate, with more collisions occurring between the atoms, which is necessary for efficient optical evaporation. The 'dimple trick' involves adding a smaller waist (dimple) trap overlaid to the larger waist trap. This causes the atoms to collect in the smaller dimple trap, and the reservoir beams can then be ramped off to leave atoms trapped in the dimple trap. The atomic species are levitated using a magnetic field throughout the sequence in

the Science Cell.

From here, we proceed to make molecules in the Science Cell by associating our ultracold atoms and image the atoms and molecules using the quantum gas microscope. The sequence and remainder of the setup in the Science Cell is one of the main focuses of this thesis. Put briefly, we first cool Rb then transport it to the Science Cell. The Rb is loaded into a moveable xODT, and then moved 1 mm away. Cs is then cooled and transported to the Science Cell. Both atomic clouds are evaporatively cooled before being merged into the same xODT. We then conduct magneto-association to prepare weakly-bound molecules by ramping the field over a Feshbach resonance, and transfer the Feshbach molecules to their ground state using STIRAP. Experiments can now be performed on the ground state molecules, before they are dissociated back to an atom pair for imaging. The microscopy of atoms involves ramping up the optical lattice and a light sheet to pin the atoms to their sites in a 2D plane before imaging them with the molasses imaging. The typical sequence to image molecules in the optical lattice takes around 30 s. Full details of the dual species loading and evaporation can be found in Chapter 4, the molecule formation in Chapter 5 and the atomic microscopy in Chapter 6.

3.2.6 Absorption Imaging

Many of the measurements presented in this thesis are performed by imaging the cloud using absorption imaging (apart from the microscope images). The technique of absorption imaging is very common in ultracold matter experiments, and has been detailed in [191]. The technique provides an image of the atom cloud by imaging its 'shadow'. We a probe beam of circularly polarised light to drive the σ^+ cycling transition of the atomic species on the D_2 line (so resonant with the $|F, m_F\rangle = |4, 4\rangle$ to $|F, m_F\rangle = |5, 5\rangle$ for Cs and $|F, m_F\rangle = |2, 2\rangle$ to $|F, m_F\rangle = |3, 3\rangle$ for Rb). The atoms are prepared in the required state (F=4 for Cs and F=2 for Rb) using a 500 μs pulse of repump light to drive them out of the lower hyperfine state. The absorption imaging takes three sequential images for each sequence. The first image is taken of the atoms with a 65 μs pulse of the probe beam called the *atoms* image. The second image is then taken with the 65 μs pulse of the probe beam (but no atoms

in this image) - called the *probe* image, followed by an image with no probe beam as the *background* image. The absorption of the resonant light by the atoms causes a dark shadow in the first image, and the three images can be used to determine the optical depth (OD) of the cloud as follows,

$$OD = -\log\left(\frac{atoms - background}{probe - background}\right). \tag{3.1}$$

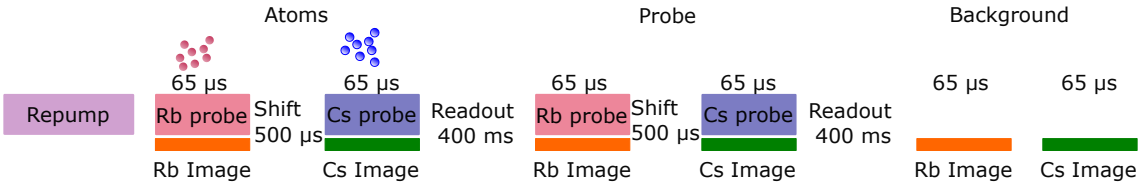

Figure 3.7: An illustration of the sequence used for absorption imaging of Rb and Cs in the same sequence. We use the Fast Kinetics mode on the camera which allows us to take two images 500 μs apart, rather than wait for the readout (which would be 400 ms, making it infeasible).

We can image both Rb and Cs in the same sequence with our absorption imaging. We do this using the 'Fast Kinetics' setting on the camera, to image Rb first and then Cs as is illustrated in Fig. 3.7. The Fast Kinetics allows for the camera to take multiple images with a very low delay, by having 'dark' areas of the camera which are shifted to the imaging area between shots without any readout. This means that the camera can take two images in a time limited by the 'shift speed' (the time needed for the camera to move the data on a pixel to a new pixel) and not the readout time. The pixels are readout after each set of Fast Kinetics images is taken.

The optical setup used for the absorption imaging is shown in Fig. 3.8. We use a two-lens system to image the atom cloud onto the camera (Andor Luca (R)). The Main Chamber and Science Cell are imaged using the same camera. The use of a twisted periscope in the path causes the image to be rotated as shown in Fig. 3.9 (which we correct for when presenting any other absorption images in this thesis).

We can infer the cloud size and atom number from these absorption images. First, to calibrate the imaging, we image the cloud under free gravitational fall, and calibrate the position of the cloud centre with the known value of acceleration due to gravity to calibrate the pixel size. The atom cloud is allowed to expand for a

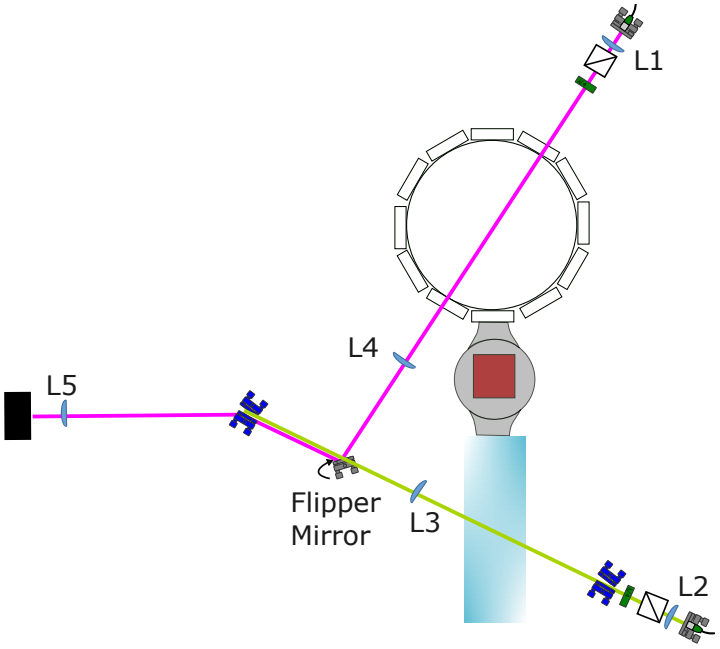

Figure 3.8: Absorption imaging setup. The imaging paths from the Main Chamber and the Science Cell are combined onto the same camera using a flipper mirror. Much of the imaging path sits above the rest of the experiment using some periscopes. The lenses used are as follows:- L1 (f=100 mm) L2 (f = 175 mm) L3 (f=150 mm) L4 (f=250 mm) L5 (f=50 mm)

known time-of-flight (TOF) before being imaged. This is done in order to have the cloud spread out and reduce the OD so that we can reliably capture an image of the entire cloud. We usually magnetically levitate the atoms during this TOF, to prevent them from falling out of the imaging region of interest.

Fringe removal

The absorption imaging setup has fringes present, likely caused by some combination of Newton's rings, small dust particles, and aberrations due to the finite size of the imaging optics. While the fringe pattern is globally constant, the pattern shifts slightly (with slight intensity and phase variations) between the different images taken in a sequence, leading to noise on the final absorption image. In our experiment, this noise is significant when we attempt to image clouds of $<$5000 atoms[7],

[7]More accurately an OD of $<$0.3. This corresponds to 5000 molecules when we are imaging atoms dissociated from Feshbach molecules in our experiment

which we require for imaging the atoms dissociated from molecules.

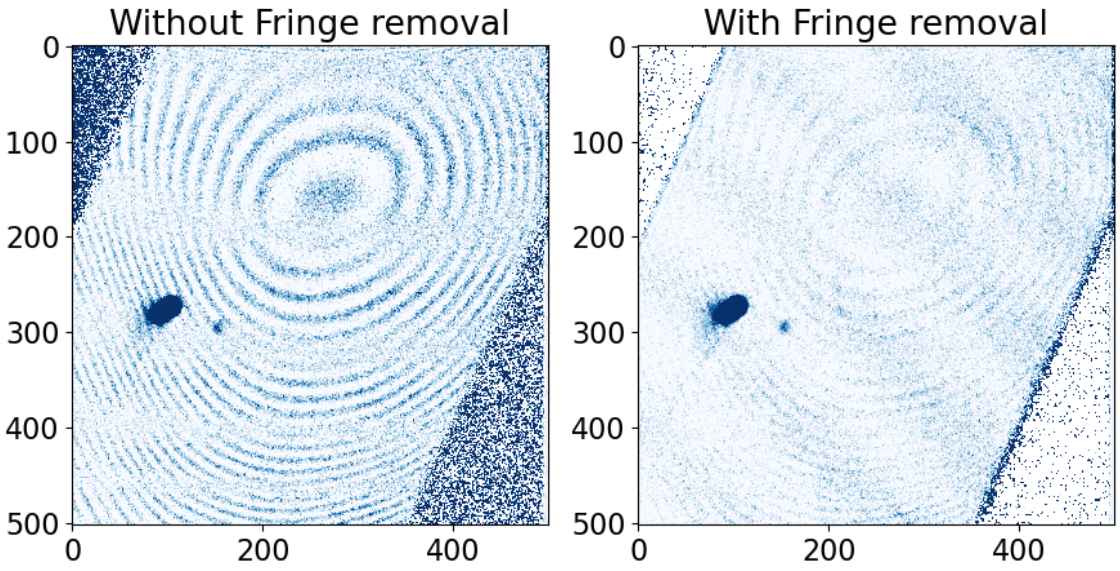

Figure 3.9: Absorption images with and without the fringe removal showing two clouds of Rb atoms. This is an image from a sequence that produces a cloud of atoms and Feshbach molecules. The larger cloud in each image contains 80,000 atoms, and the smaller one contains 4,000 atoms (which have been dissociated from Fehbach molecules). Here we show the images as they are taken. All future absorption images are presented with the fringe removal implemented, and the image rotated so that gravity acts vertically down.

In order to remove these fringes, we utilise a fringe removal algorithm, similar to those described in [192, 193]. This method takes in a series of reference *probe* images, and load them into a matrix. We then use a single value decomposition algorithm (with the function scipy.linalg.eigh) to generate a predicted *probe* image for a given *atoms* image. With enough probe images loaded for reference (typically above 10, although we usually use 50 images), the constructed *probe* image contains fringes that have an amplitude and phase matching that of the *atoms* image, and can now be successfully subtracted out. Figure 3.9 shows the effect of fringe removal, with an image displayed with and without the fringe removal applied. Without the fringe removal, we can resolve clouds of about 0.1 OD above the background (the background is not necessarily zero due to intensity variations in the probe between images in the same sequence). This reduces to around 0.03 when using the fringe

removal.[8]

3.2.7 Overview of the lasers used

We use a variety of laser in our experiment for various purposes. The trapping lasers are all listed in this section. The cooling lasers are just briefly mentioned, as the detailed setup of the cooling lasers is detailed in [148, 160]. The setup of the lasers used for trapping atoms in the Science Cell in the lattice and dipole traps is mentioned in more detail here, with an overview in Fig. 3.10.

For laser cooling, we have a separate laser to address the cooling and repump transitions of each species. For Cs, we have a Toptica DL Pro which provides repump light. The laser is locked using a vapour cell, and the power is split between the 2D+ MOT, the 3D MOT and repump for the atoms in the Science Cell (mostly used for imaging). We require more power on the cooling transition, and use a Toptica TA for this. The light from the cooling laser is split between light for the 2D+ MOT, the 3D MOT, the DRSC lattice, the light for molasses imaging in the Science Cell, and the probe for absorption imaging. The Rb setup mirrors the Cs setup, with the exception that the light for the DRSC lattice is sourced from a separate Toptica TA.

The light for optical trapping in the Main Chamber and the Science Cell (including the lattices and the dipole traps) is sourced from from a combination of lasers as described in Fig. 3.10. A major consideration in the setup of the lasers is the accidental formation of a lattice by two lasers at the same frequency that are on the atoms at the same time[9]. This can cause rapid heating and loss of the atoms. The M-Squared Ti:Sapph laser used for the shallow angle lattice is often used at wavelengths substantially different (currently 830 nm) than the 1064 nm used in the other trapping beams, so a lattice is not formed with it. The IPG laser used for the reservoir traps has a short coherence length, and is not at the same frequency as the Mephisto lasers. So, we do not worry about forming a lattice with this laser.

[8] We take probe images in every sequence we run and constantly update a bank of probe images used for the fringe removal.

[9] For an experiment that images atoms and molecules in optical lattices, we have spent a surprising amount of time avoiding the formation of optical lattices.

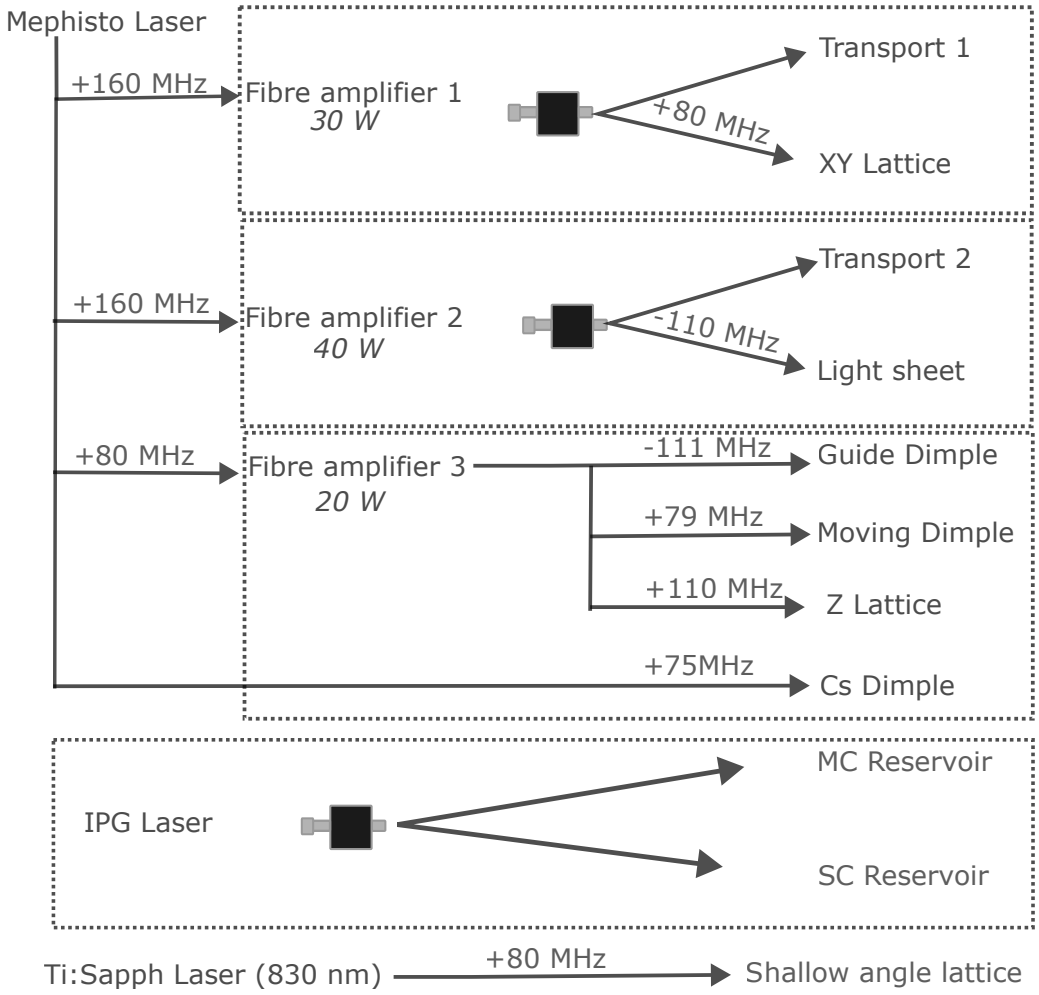

Figure 3.10: A list of all the trapping 1064 nm lasers (and the Ti:Sapph used for some optical trapping) used and a schematic of the offset frequencies used to ensure that we do not form a lattice accidentally

In the Science Cell, the atoms are trapped in combinations of the Transport 2 beam, the Moving Dimple beam, the guide dimple beam and the Cs dimple beam[10]. We must ensure that all these beams are maintained at different frequencies to avoid any accidental optical lattice formation. All these beams are from Fibre amplifiers seeded by the same laser. The AOMs used to control and servo the beam power also apply a frequency offset, the detuning of which is enough to prevent loss of the atoms in the lattice. Fig. 3.10 shows the details of the frequency offsets of each beam.

[10]And the SC reservoir beam, but we do not worry about that as detailed previously

3.3 Experimental control

3.3.1 Fast rotation mount

Over the course of the work described in this thesis, we developed a rotation mount to rapidly switch the polarization of a beam in order to divert the power of the beam between two paths using a PBS. This has been published in [194], and further details can be found there.

In our experiment, we would like to change the polarisation of a beam to rapidly switch a beam between two different paths, as in [159, 195, 196]. The change of polarisation leads to a change in the amount of light that is reflected or transmitted by a PBS, which allows use to divert power from one incident beam to multiple paths. Dynamically changing the polarisation mid-sequence allows us to re-use the power of our trapping beams for different traps at different stages of the experiment. This method is preferred to The dynamic control of the polarisation of a beam during an experiment is often done by rotating a polariser or a wave plate using a specialised rotation mount. Common rotation mount designs use servo motors and stepper motors [197–200], where the rotation of the shaft is transmitted to a receptacle for the optic using a series of gears [199] or a belt [200]. We find this method preferable to alternate methods of beam switching such as the use of flipper mirrors or the use of AOMs. Flipper mirrors are unsuitable at the high powers (around 50 W) we operate at. AOMs have a limited diffraction efficiency, and we want to maximise the power in each beam.

This is done by rotating a half-wave plate (HWP) by 45°, which rotates the polarisation of the beam by 90°. The beam can then be split using a PBS, with the power of the transmitted beam P_{T} from an incident beam of power (P_0) is given by Malus' law, $P_{\mathrm{T}} = P_0 \cos^2(\theta)$. This allows us to reuse the power from a single laser in multiple optical beam paths - useful in experiments such as ours. In our setup currently (see Fig. 3.6 and Fig. 3.3, we have three such rotation mounts. They divert power between (i) Transport 1 and XY lattice (ii) Transport 2 and the light sheet (iii) the MC reservoir and the SC reservoir.

For use in the experiment, we desired a rotation mount that could switch the

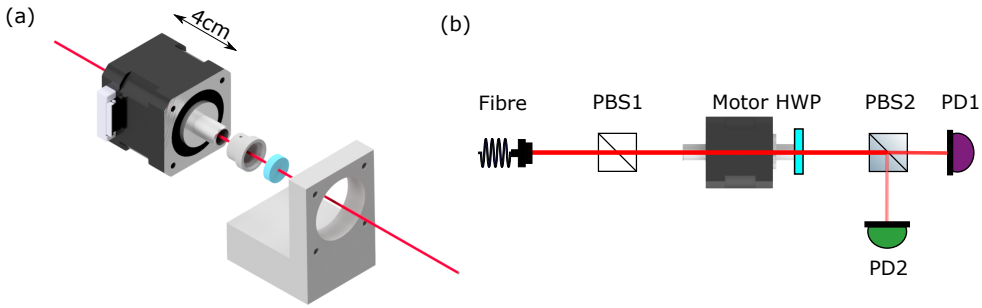

Figure 3.11: a) The hollow stepper motor along with the adapter for a half-inch diameter wave plate and an L-shaped mounting bracket. The motor shaft is hollow, with an inner diameter of 8 mm which allows a laser beam to pass through it as shown. (b) The setup used to test the rotation mount. The first PBS cube sets a well-defined polarization into the rotation mount. By measuring the power out of the two ports of a second PBS with photodiodes (PD), we can extract the angle of the half-wave plate (HWP), independent of power fluctuations of the beam. Figure adapted from [162]

HWP the required 45° rapidly (ideally in under 50 ms). Most commercial models prioritise accuracy over rotation speed, so usually take over 100 ms to turn the required 45°. In our experiment we use a stepper motor with a hollow shaft[11] as in [23]. The hollow shaft lets us attach the HWP to the motor shaft, and pass the beam through the shaft. This allows us to reduce the moment of inertia of the system to be rotated by (i) having no additional belts or gears attached to the motor (ii) having the axis of rotation passing through the centre of the wave plate.

We control the rotation of our motor using an Arduino UNO microcontroller and a TMC2208 stepper motor driver chip. They provide the correct current waveform to the motor to ensure the required motion is completed. As in all stepper motors, the motion of our motor is discretised in steps - each full step equating to 1.8° in our case. The effective resolution of a stepper motor can be reduced with control of the current in the individual motor coils, a practise commonly known as micro-stepping. In addition to improving the resolution of the motor, micro-stepping provides for smoother rotation profiles and lower vibrations. We operate the motor under half-stepping and quarter-stepping for give step sizes of 0.9 and 0.45° respectively. The

[11] SCA4218M1804-L NEMA-17

motor is driven using the current waveforms generated using the Arduino Accelstepper [201] library. We use a constant acceleration position ramp, where the motor velocity is increased at a uniform rate to a maxima, and then decreased from there to zero, bringing the rotation to a stop.

Figure 3.11 (a) shows the setup of the rotation mount. A HWP is affixed to the motor using a machined adapter. The adapter is small and compact to minimise any addition to the moment of inertia of the setup. The motor is connected to the optical breadboard using a separate adapter.

The setup used to test the rotation mount is shown in Fig. 3.11 (b). A PBS is used to set a well defined linear polarisation of light into the rotation mount. The polarisation is then rotated by the HWP, depending on the orientation of the HWP. A second PBS then splits the light between two paths, and the power in each path is measured using a photodiode to indicate the angle of the HWP.

We operate the rotation mount in two different configurations. The *testing configuration* and the *switching configuration* (highlighted in Fig. 3.12 (a)). The *testing configuration* is used to maximise the sensitivity of our measurements at the start and end of a 45 degree rotation of the HWP. The *switching configuration* is what we use to switch the beam from one path to another completely. We additionally define a switching time as the time taken for the rotation mount to complete an entire 45 degree rotation. Use of the *testing configuration* maximised our sensitivity to measuring the switching time.

Figure 3.12 shows the measurement of the switching time of the motor as a function of the acceleration of the motor used. Given that the motor operates in discrete steps, the time between the m^{th} and $(m+1)^{\text{th}}$ pulse into the stepper motor is given by [202],

$$t_{\text{m}} = 2\left(\sqrt{\frac{m+1}{a}} - \sqrt{\frac{m}{a}}\right). \tag{3.2}$$

where a is the acceleration of the motor in steps s^{-2}. From this we are able to calculate the expected switching time for a given acceleration. Figure 3.12 (a) shows the dependence of the switching time on the acceleration, which is in good agreement with our expectation. The inset shows a sample switch in 15.9 $\pm$0.3 ms

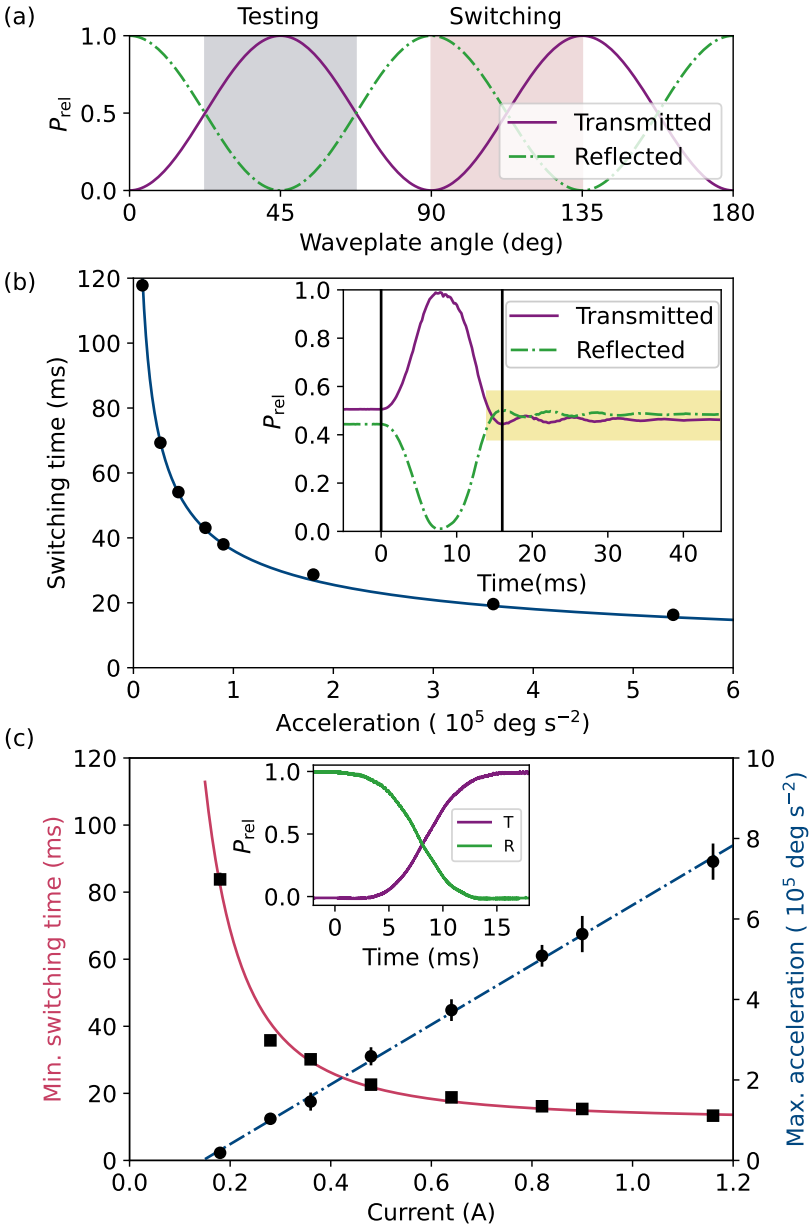

Figure 3.12: (a) The predicted beam power as a function of wave plate angle. P_{rel} refers to the power measured at a PD normalised to the full beam power. The grey and pink areas correspond to the testing and switching configurations, respectively. Typical signals associated with each configuration are shown in the insets of (b) and (c). (b) Switching time vs. acceleration using half-stepping at a motor current of 1.0 A. The blue line is the predicted behaviour, and the black points are the measured times. The black lines in the inset show the start and end of the switch. The typical uncertainty of the switching time is less than 0.4 ms. (c) Minimum switching time and maximum acceleration as functions of current. The maximum acceleration is directly proportional to the current, implying torque-limited behaviour. Inset is the signal at a current of 0.96 A, demonstrating switching in under 20 ms. Figure adapted from [162].

(the fastest observed). We measure the maximum achievable acceleration of the motor as a function of the current supplied to it. The current supplied is controlled using the TMC driver chip[12]. The maximum acceleration is defined as the maximum acceleration that can be programmed to the mount before the rotation of the HWP becomes incomplete or inconsistent (eventually failing completely). The maximum acceleration is dependant linearly on the current provided to the motor, implying torque limited behaviour, as shown in Figure 3.12 (b). The motor is limited to 1.2 A. The inset of Figure 3.12 (c) shows a switch in the switching configuration, where the power is completely diverted from one arm to another.

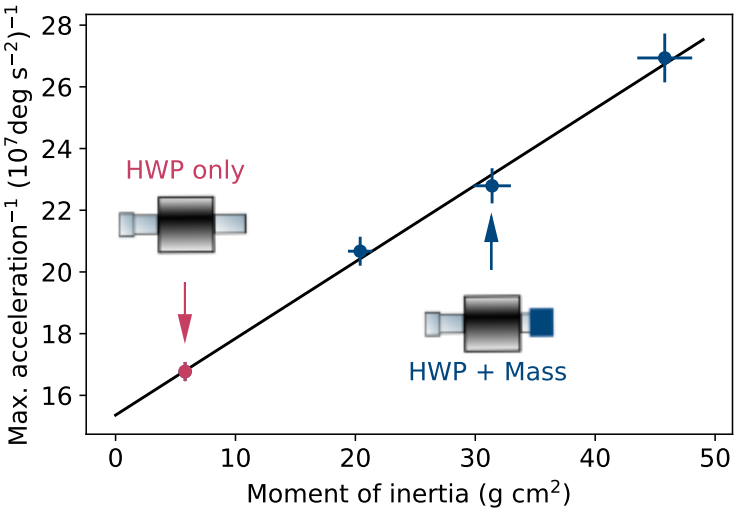

Figure 3.13: Switching time limited by torque of the motor. (b) The inverse of maximum acceleration as a function of the moment of inertia of load at a current of 0.96 A. With the HWP fixed to one end, we attach hollow cylinders of varying ,asses to the motor shaft and measure the maximum acceleration. The linear fit between acceleration and moment of inertia gives the maximum torque as 0.069(3) N m, and the moment of inertia of the shaft as 60(4) g cm^2. The red point is the acceleration with only the wave plate attached. Figure adapted from [162].

Torque limited behaviour is further confirmed by adding a mass to the motor and measuring the maximum acceleration for a fixed current of 0.96 A with different moment of inertias of the load as shown in Fig. 3.13. For a given current (I) in the motor, the maximum torque output (τ), and hence the maximum acceleration

[12]Care should be taken when using this to avoid minor shocks. Refer to the supplementary material of [162] for full details on the setup and safe operation

are related by a proportionality constant K, such that ($\tau = KI$). So, for a given moment of inertia the load, the maximum acceleration a_{max} is inversely proportional to $L_{\text{total}} = L_{\text{load}} + L_{\text{shaft}}$ as,

$$a_{\text{max}} = \frac{KI}{L_{\text{shaft}} + L_{\text{load}}}. \tag{3.3}$$

The maximum possible acceleration is set by the moment of inertia of the motor shaft itself. We estimate the moment of inertia of the HWP and the adapter to be 5.8(3) $\text{g}\,\text{cm}^2$. From here, we measure the maximum acceleration at different values of L_{load} to extrapolate L_{shaft} as 60 ± 4 $\text{g}\,\text{cm}^2$, in reasonable agreement with the manufacturers quoted value of 54 $\text{g}\,\text{cm}^2$. The fit gives the constant relating acceleration and torque as $K = 0.072 \pm 0.003$ $\text{N}\,\text{cm}\,\text{A}^{-1}$.

Stepper motors are known to endure small vibrations at the end of their rotation [202, 203]. The inset of Fig. 3.12 (b) shows these vibrations. As shown in Fig. 3.14, the vibrations are of the form of a damped oscillation, with a frequency ω dependant on the torque output by the motor $\omega = \sqrt{KI/L}$. We initially used the DRV8825 driver chip, but later switched to the TMC2208 chip to minimise the oscillations. Compared to the DRV8825, the TMC2208 chip is able to reduce the oscillations significantly by ramping off the current in the motor coils [204] as shown in Fig. 3.14.

It should be noted that the vibrations shown in Fig. 3.14 are taken in the *testing configuration*, which greatly magnifies the effect of these oscillations. When using the DRV8825 for a 39 ms switch, we see oscillations of 3% of the peak signal (or 0.4°). In the *switching configuration*, this same angular oscillation amplitude corresponds to only 0.03% of the power. So, they are generally insignificant for use in the *switching configuration*, but may have an effect if the motor is used in another manner. We note that the TMC2208 chip is effective at negating the oscillations only for switching times greater than 30 ms. For quicker switching times, the oscillations return with a similar amplitude to the DRV8825.

We find the rotation mount to be very robust and repeatable. While testing, we set the device to run 2000 switches over a period of 11 hours in a half-stepping

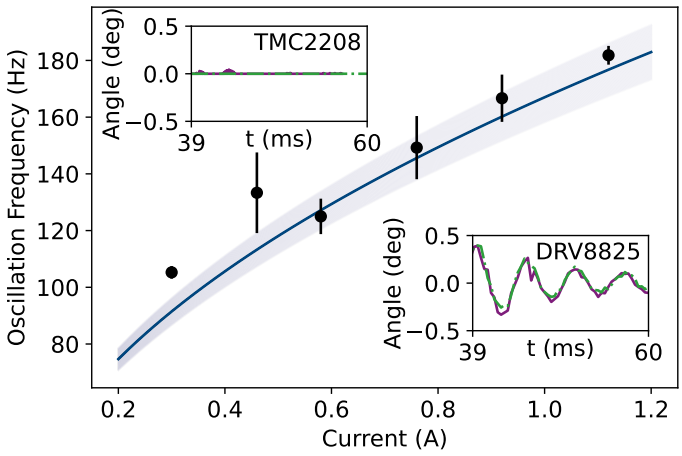

Figure 3.14: Oscillation frequency as a function of the current for a switching time of 39 ms (the switching time used in our experiment). After a switch, the stepper motor undergoes damped oscillation. The oscillation frequency is determined by the torque from the motor coils, $\omega = \sqrt{KI/L}$ where the symbols are defined in Eq. 3.3. The predicted frequency at different currents is shown by the blue region, with $\sqrt{K/L}$ taken as 167(9) Hz/$\sqrt{A}$ calculated from values obtained earlier. The inset plots show the oscillation signal when using the DRV8825 and TMC2208 chips at a current of 0.92 A, and highlight the superior performance of the TMC2208. Figure adapted from [162].

configuration at a switching time of 39 ms. Rather than operate a to-and-fro switching scheme, we set the motor to rotate 45° every 20 s in the same direction. This allows for easy identification of any error and the accumulation of error. With ideal operation, the motor would return to the same position every 8^{th} switch. A skipped step during a switch would result in an offset in the position of the motor by 1.8° for each subsequent switch.

We affix a 3D printed mask onto the rotation mount with 4 spokes, so that at the end of every switch, the mask cuts the beam in half (similar to a knife edge type measurement). We estimate a skipped step in the switch would lead to a 6% change in intensity (with the mask blocking more or less of the beam). Over the 2000 switches, we note a standard deviation of the fractional transmission over the full period of measurement as 0.12%, with the single largest deviation being 0.37%. We ascribe these differences to correspond to the uncertainty in our measurement - from changes in temperature, and electronic noise on the photodiode. So, we conclude that the motor did not miss a single step over the course of testing and deem it

reliable enough for open loop operation.

Since the design and testing of the rotation mount, we have introduced the rotation mount into our experiment, with three mounts currently in our setup. Over the past 2 years, we have not noticed any issues with reliability of these mounts. In addition, we operate the mounts in a three set-point scheme. As mentioned earlier, the SC reservoir trap is formed of the Transport 2 beam and the SC reservoir beam. The Transport 2 beam at full power has around 30 W of power on the atoms at a waist of ≈ 250 μm. In the course of our experimental sequence, it is occasionally preferable to have some control of the power of each individual beam in order to balance the trap. We thus find it advantageous to include a third set-point into the programming for the motor, where only half the power is diverted into the Transport 2 path. Generally speaking, a large number of setpoints could be encoded into the rotation mount to have an arbitrary amount of power in each path.

3.3.2 Magnetic field coils

The magnetic field on the atoms in our experiment are controlled by a series of circular coils present above and below the Science Cell and the Main Chamber. We pass a current through the coils, and the field on the atoms depends on the current in the coils. For a Helmholtz pair (anti-Helmholtz pair), the field (field gradient) is directly proportional to the current in the coils. The coils were designed to provide a maximum bias field of 400 G (with the aim of eventually addressing the Rb-Cs Feshbach resonance at 352 G), and a field gradient sufficient to levitate the atoms. The setup and characterisation of these coils has been described previously in [148, 160, 161]. The coils themselves are made of copper and are hollow to allow them to be water cooled[13]. We have a separate high current power supply for the Main Chamber (Agilent 6690A) and the Science Cell coils (Delta Elektronika SM6000). Here, we provide an overview of all of the coils present in the experiment.

In the Main Chamber, we have a coil pair connected in a Helmholtz configuration referred to as the Main Chamber bias coils. These coils provide a magnetic field for

[13]The author would like to note that a surprising amount of plumbing is required to run an ultracold matter experiment such as this

the atoms during their time in the Main Chamber, and are particularly important for Cs - as the field must be kept near the Efimov minimum near 22 G when it is trapped to prevent rapid three-body loss. To provide a magnetic field gradient for the atoms, we utilise an anti-Helmholtz configuration coil pair, which is generally used to levitate the atoms in the Main Chamber. The Main Chamber also consists of three pairs of Helmholtz configuration coils pairs to provide smaller fields (upto 5 G) - oriented in three perpendicular axes. These coils are used to adjust the location of the MOT (and cMOT), provide a quantization axis for the DRSC and the imaging, and null the field for the optical molasses cooling. There are two coils around the Main Chamber that are not used, both Helmholtz pairs. One is around the Main Chamber (initially designed for Feshbach association and field ramps in the Main Chamber) and the other is a racetrack shape that extends around both the Main Chamber and the Science Cell (designed to control the field across the transport).

The Science Cell has three main coil pairs, which we refer to as the Science Cell bias, the Science Cell jump (both Helmholtz pairs) and the Science Cell quad coils (an anti-Helmholtz pair). The bias coils are designed to generate fields of up-to 400 G, with a response of 2.07 G/A. We use these coils to control the magnetic field on the atoms throughout the sequence - notably the field on the atoms in the dipole trap (Cs at the Efimov minimum) and getting the magnetic field on the atoms close to the Feshbach resonance. For fine control of the magnetic fields however we use the jump coils, with a response of 0.27 G/A, around an order of magnitude lower than the bias coils. This allows us to have finer control of the field from these coils. We use these coils to ramp over the Feshbach resonance and control the field of the Feshbach molecules. The coils are currently operated in a range of 26 G. This is done to give them a dynamic range between 178 G to 204 G (with the bias coils providing the offset) used in the Feshbach association scheme[14].

The quad coils (response of 0.47 $\mathrm{Gcm^{-1}}A^{-1}$)[15] are used to provide a field gradient

[14]We could run them in a range of around 50 G if required, limited by the MOSFETs in our servo system. The 26 G range is set by the servo circuit, which takes inputs in the -10 to 10 V range. Having this correspond to 26 G of field maximises the accuracy with which we can operate the coils

[15]We could reach gradients of around 100 $\mathrm{Gcm^{-1}}A^{-1}$, making the levitation gradient of 31 $\mathrm{Gcm^{-1}}A^{-1}$ accessible, but the typical magnetic trap gradients of $\approx$ 300 $\mathrm{Gcm^{-1}}A^{-1}$ are out of

on the atoms. This is used to levitate both atomic species throughout the sequence, as well as to over-levitate the atomic or molecular species and to perform Stern-Gerlach experiments. We are able to provide a field gradient in only one direction (to levitate the Rb and Cs atoms against gravity).

Finally, the Science Cell also has three pairs of shim coils in three perpendicular axes, with a ≈ 5 G range. They are used to set a quantization axis during absorption imaging, null the field during the optical molasses and centre the magnetic field gradient (see Fig. 4.10) during the sequence.

Field control and noise

We require stable magnetic fields throughout the experiment. The microwave spectroscopy and microwave transfer of atoms and molecules, the Feshbach association sequence, the transfer of the Feshbach molecules to the appropriate state, and the STIRAP itself all rely on the magnetic field being stable to the $\approx$ 10 mG level. In addition, the field needs to be controlled reliably shot-to-shot, to implement the same magnetic fields every shot. We control the field using a servo circuit designed at JILA, and detailed descriptions of the servo circuit used can be found at [205,206].

The servo circuits work by measuring the current in the coils at any time, converting it to a voltage, comparing it with a reference voltage, and then servo the current to make the voltages match using a PI loop. The current in any of the coils at a given time is read out using a Hall sensor[16]. The output current from this sensor is dropped over a sense resistor[17]. The voltage across this sense resistor is compared and stabilised to a reference voltage. The reference voltage can either be provided by an external set-point controlled by Labview, or by an internal voltage generator (for better stability). The feedback is done using an array of three MOSFETs[18] in parallel. The feedback output sets the Gate voltages of the MOSFETs, controlling the current in the circuit.

Even with the servo circuit, we can measure some noise on the coils using a

reach

[16]Honeywell CSNS 300

[17]Vishay 20 Ω

[18]IXYS IXFN 180N15P FET

separate out of loop Hall sensor (LEM Ultrastab 600). We measure an AC field noise of around 20 ppm at 180 G from the bias coils (around 4 mG), and a DC field stability of 6 ppm in the coils. In addition, we measure a background field noise at 50 Hz, presumably from the mains. As I write this, work is being done in the lab to find, characterise and eliminate these sources of magnetic field noise. We can mitigate the effect of the 50 Hz noise by syncing our experimental sequence to the mains AC cycle.

3.3.3 Beam servos and control

We employ multiple Acousto-Optic Modulators (AOMs) to control both the power and the frequency of our beams in the experiment. The n^{th} order of an aligned AOM consists of light at a frequency $\omega + n\omega_{mod}$, where ω_{mod} is the RF modulation frequency of the AOM, and ω is the frequency of the beam incident on the AOM. We often use AOMs to control the frequency of a beam (particularly the beams used for laser cooling, molasses imaging and absorption imaging). This is done using a series of Voltage Controlled Oscillators, where the RF output frequency depends on the input voltage. This allows us to change the frequency of the beams during the sequence by changing the voltage into the amplifiers. The AOMs are also ideal for controlling the powers of the beams. They have short (often in the 100 ns range) rise times, controlled by changing the power of the RF input to the AOM. We use this to quickly switch on or off the beams and control the and stabilise power dynamically. The powers in the dipole trap beams, the STIRAP beams, the cooling beams, and the lattice beams are all controlled like so.

It is crucial in many parts of the experiment to have precise control of the power of the optical beams. The power of beams in our experiment is prone to drift for many reasons. The most common is a change in polarization of the beam due to the birefringence of an optical fibre it goes through. Most beams we use for dipole traps pass through a fibre and then a PBS. The PBS ensures that the trapping light is linearly polarised, but changes the polarisation noise to intensity noise. Without active feedback, we see significant drifts in intensity from the thermal drifts of the AOM's used to control the power. The power of our beams is controlled by a

feedback loop. In this case, we pick off a small fraction of the power of the beam using a glass blank or a beam sampler (or the transmission through a mirror) and align it to a photodiode. The signal from the photodiode is compared and stabilised to a reference voltage for the power. The feedback is implemented by controlling the RF power into an AOM (often by controlling the gain of an RF amplifier). This allows us to stabilise the power of the beams. This is particularly important for the dimple and the optical lattice beams. The optical lattice in particular requires good stabilisation over a range of powers. We would like to servo the lattice at a wide range of powers, spanning many orders of magnitude ($\approx 1E_{\mathrm{rec}}$ for realising a Mott insulator and $\approx 10,000E_{\mathrm{rec}}$ for imaging). This is done using a photodiode with a logarithmic response (a simplified version of Texas Instruments LOG114). We find good response over seven orders of magnitude of power using this setup [148].

3.3.4 Microwave control

As with many ultracold atomic and molecular experiments, a key tool in the control of the internal state of the atoms and molecules is the use of resonant microwave fields. We have utilised microwaves to address the $F = 3$ to $F = 4$ transition in the Cs ground state (9.2 GHz without a magnetic field), the $F = 1$ to $F = 2$ transition in the Rb ground state (6.9 GHz at no magnetic field), as well as the $N = 0$ to $N = 1$ (980 MHz), and $N = 1$ to $N = 2$ (1960 MHz) transitions in the ground state RbCs molecules. We currently have an array of microwave antennae attached close to the cell that have been tested *ex situ*. We use multiple Windfreak SynthHDs as microwave sources. The microwaves are then amplified using a microwave amplifier and sent to the antenna. While some characterisation of the various antennae was performed over the course of the work presented in this thesis, the characterisation was complicated by the presence of large amounts of metal near the Science Cell[19]. The setup of a well characterised antenna array and development of sophisticated control of the microwave field in the Science cell is planned for the near future.

[19] A well known feature of ultracold matter experiments, the metal in and around the chambers complicates microwave setups

3.4 Experimental methods

In this section, we present brief accounts of various measurements used to characterise and calibrate the experiment.

3.4.1 Temperature measurement

The temperature of the cloud can be measured from the momentum distribution of the cloud. In practice, this is done by measuring the size of an atomic cloud after a known TOF at multiple times[20]. The size of the atom cloud ($\sigma_0(t)$ is expected to evolve with time t as,

$$\sigma_0(t) = \sqrt{\frac{k_B T t^2}{m} + \sigma_0^2(0)}, \tag{3.4}$$

where T is the cloud temperature and m is the mass of the atomic species. Figure 3.15 shows a sample temperature measurement of an atomic cloud.

3.4.2 Microwave spectroscopy

A method of calibrating and measuring the magnetic field - which is of great use to us is to drive a known microwave transition in the between the $F = 3$ and $F = 4$ states of the $6^2S_{1/2}$ state for Cs[21]. The transition frequency and its dependence on the magnetic field are well known [207]. We are able to determine the field at any point in the experimental sequence by driving a Cs microwave transition. The experimental sequence consists of a pulse of the microwave light during a hold in the dipole trap. The cloud is them imaged using absorption imaging, but *without* any repump light ($F = 3$ to $F' = 4$). In the absence of repump light, atoms that started in the $6^2S_{1/2}$ $F = 3$ state are not imaged. Only the atoms in the $6^2S_{1/2}$ $F = 4$ state - which have been transferred by the microwave pulse will be imaged. The microwave frequency is then scanned to identify the entire feature.

Figure 3.16 shows sample scans of the Cs $F = 3$ to $F = 4$ transition at different

[20] In theory this could be done with a single TOF time, given a known starting size of the cloud.
[21] We could use Rb as well

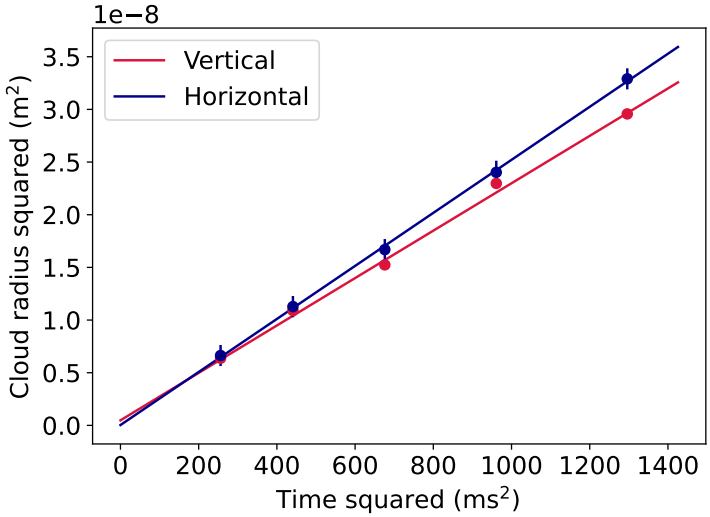

Figure 3.15: A sample measurement of the temperature of the cloud. The vertical and horizontal waists are measured after a known TOF, and fit to Eq 3.4.1 to ascertain the temperature. The plot shows a measurement of the temperature of the Rb cloud in the middle of its evaporation, with a temperature of 204 ± 6 nK measured with the vertical waist and 229 ± 6 nK measured with the horizontal waist. We generally use the evolution of the vertical waist to measure temperature, as the horizontal waist spreads out slightly due to the gradient field.

magnetic fields. We can scan for the transition at different coils setpoints to ascertain the magnetic field on the atoms. We do this by fitting a Lorentzian to the atom number distribution. The centre of the Lorentzian is converted to a field using the known splitting of the energy levels in Cs [207].

3.4.3 Trap frequency measurements

The measurement of the trap frequency of a dipole trap is crucial for the setup and characterisation of our experiment. It is particularly useful when aligning our many optical trapping beams onto the atoms - particularly in the axial direction. The trap frequency (ω_t) of a Gaussian beam of waist (w_0) is given by [208],

$$\omega_t = \frac{4\alpha P}{\epsilon_0 c m w_0^4}. \tag{3.5}$$

Here, α is the polarisability of the trapped species at the wavelength of the trapping light. For a given beam, the trap frequency thus depends strongly on the waist of

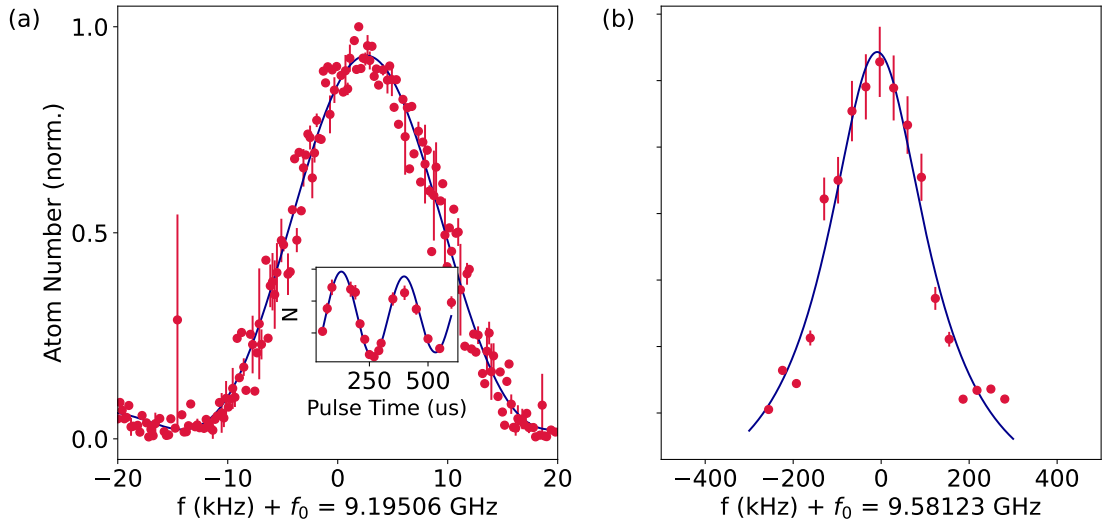

Figure 3.16: We scan the frequency of a microwave pulse onto the Cs atoms, driving the π transition while imaging without repump light. (a) shows a scan of the microwave frequency at low field, with the resultant lineshape fit to a Fourier broadened sinc^2 function. The error on each point is the error from multiple shots. The inset shows a Rabi flop of Cs driven at low field. (b) shows a scan at high field fit to a Lorentzian. The centre position is used to calculate the magnetic field. We find fields of 1.156 $\pm$ 0.003 G and 182.01 $\pm$ 0.02 G for (a) and (b) respectively

the beam at the atoms. So, we often align our beams to be focused on the atoms by maximising the trap frequency as the focal position is translated.

Two of the common methods used to measure the trap frequency of atoms in a trap are using parametric heating measurements and by measuring centre of mass oscillations of the atoms. We generally use the latter. Our measurements are done by holding the atoms in a dipole trap. The atoms are then perturbed slightly to excite oscillations and trapped only in the beam of which the trap frequency is being measured. We generally perturb the cloud in one of two ways (i) by turning down the levitation field for a brief period so the atoms fall in the trap or (ii) by releasing the atoms from the dipole trap for a few ms so they fall out of the centre of the trap. The position of the atoms is then measured as a function of the hold time in the lone beam. We fit beam waists by varying the beam power or the beam focal position and fitting to Eq. 3.5. A sample measurement is shown in Fig. 3.17

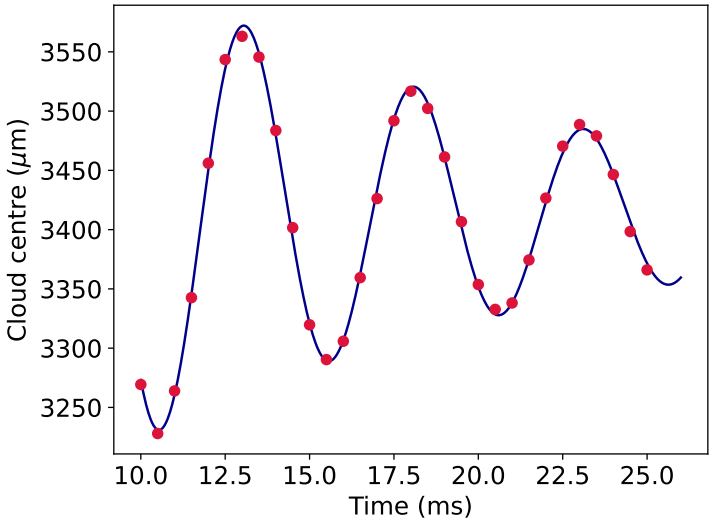

Figure 3.17: A sample measurement of the trap frequency of a beam (in this case the Moving Dimple beam). The atom cloud is released from a xODT into a single beam after a perturbation. The atoms are held in the beam for a known amount of time, and then released and imaged after a TOF. The position of the cloud when imaged oscillates with the trap frequency of the beam (see Eq. 3.5)

3.4.4 Kapitza-Dirac measurements

When aligning and measuring our optical lattices in the experiment, we measure the lattice depth using a Kapitza-Dirac scattering experiment [209]. The experiment involves pulsing the lattice on for a short time on to a prepared BEC of atoms. The atoms experience some momentum transfer, with quantised units of momentum (in multiples of $\pm 2\hbar k_{\text{lattice}}$ transferred to the atoms in the sample. The population of atoms in each of the different momentum states oscillates as a function of the lattice pulse time. When imaging after a TOF, this results in a distribution with different clouds present in the image at different positions according to their momentum. We can find the population of each of the momentum states and fit to a solution of the Hamiltonian describing atoms in a lattice,

$$H = -\frac{\hbar}{2m}\frac{d^2}{dx^2} + V_0 \sin^2(k_{\text{lattice}} x), \tag{3.6}$$

where m is the mass of the atom, and V_0 is the lattice depth. We generate numerical solutions as described in previous work from our lab in [210], and fit the population distributions in momentum space to the solutions to obtain the lattice depth.

CHAPTER 4

A dual-species high-phase-space-density mixture

In this chapter, we detail the production of a high phase space density mixture of Rb and Cs using a moving optical dipole trap and a sequential loading scheme. We will detail the need for such a sequential scheme, the design, setup and characterisation of the moving optical dipole trapping beam used. We then discuss the methods used to evaporate Rb and Cs together in a controlled manner to prepare a mixture of sufficient phase space density (PSD) and atom number suitable for association into Feshbach molecules. We are able to produce a mixture of PSD $\approx$ 0.1 for each species as well as evaporate both species to a Bose-Einstein Condensate (BEC) simultaneously.

4.1 The need for a sequential loading scheme

To provide a brief recap of the sequence in the main chamber discussed in Chapter 3, the atomic species are loaded into a MOT and then undergo some sub-Doppler cooling (Molasses and DRSC). They are then loaded into an optical dipole trap (Main Chamber Reservoir trap) from which they are transported to the Science Cell for evaporative cooling and association to molecules. Further details are available

in [118, 148].

As detailed in Chapter 2, there is a need to keep Rb and Cs separate while evaporatively cooling. The large interspecies scattering length leads to large three-body loss if the species are evaporated together. This is typically seen as loss in Rb atom number due to the lower polarisability of Rb compared to Cs at 1064 nm. We initially considered the method used in Innsbruck [112, 113], where the Rb and Cs are loaded into a common large waisted optical dipole trap, and then separated into two species specific dimples which are moved apart. The evaporation is done in these separated traps, before the species are merged for association.

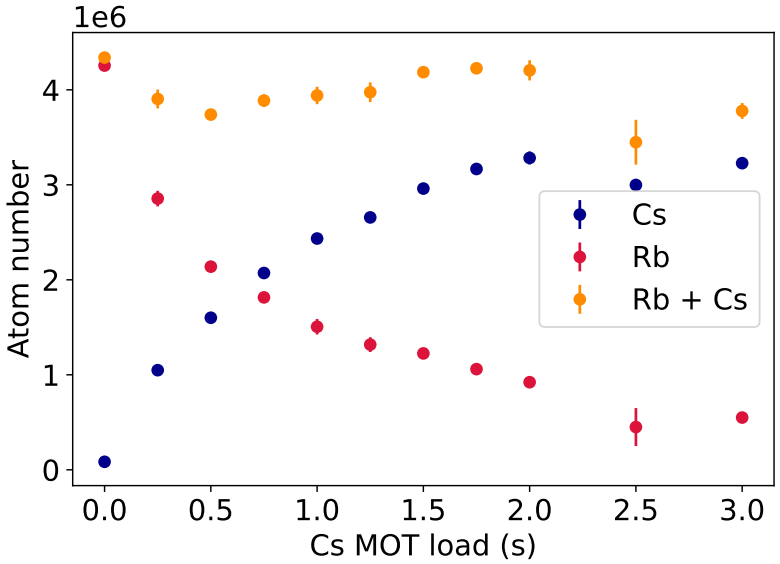

Figure 4.1: Loss in the simultaneous loading sequence. The Rb and Cs MOTs were loaded sequentially, followed by sub-Doppler cooling and transport (which was done together). The atoms of both species were then loaded into the SC reservoir together. Here, we measure the Rb and Cs atom numbers in the SC Reservoir as a function of the MOT load time for Cs. We see significant loss in Rb as Cs is introduced into the sequence

With this method, the MOT load and the sub-Doppler cooling of the two species must be done together. This requires various parameters in the sequence (particularly cooling times and magnetic fields) to be a compromise between the optimal values for each species. In addition the presence of one species leads to a loss in the number of atoms of both species, due to collisions. We can measure this by testing a simultaneous loading sequence.

Beam name	Waist (μm)	Angle of incidence (°)[1]
SC Reservoir beam	500 (horiz) and 200 (vert)	100
Guide Beam	93	70
Moving Dimple beam	47	-27
Cs Dimple beam	45	-27

Table 4.1: The parameters of the dimple beams used in the Science Cell in the experiment

Figure 4.1 shows the number of atoms loaded into the Science Cell Reservoir trap (SC Reservoir) as a function of the Cs MOT load time. This was done by first loading the Rb MOT till it was saturated, then loading the Cs MOT, and varying the Cs MOT load time to change the amount of Cs loaded. Following the dual-species MOT, the sub-Doppler cooling and transport of both species was performed simultaneously before they were loaded into the SC reservoir. As expected, we see an increase in the Cs atom number (blue points) as the Cs MOT load time is increased. We see a significant loss of Rb (red points) as Cs is loaded, with the number of Rb atoms falling as the number of Cs atoms loaded increases. We see that the total number of atoms loaded (orange) remains roughly constant. The loss increases dramatically when loading a dimple trap (formed by the Guide dimple and the Cs dimple beams) - where the trap waists are smaller and there is more confinement - with both species, where the increased density leads to much more extreme loss of atoms (after even 100 ms of Cs MOT load, we see no Rb).

4.1.1 The sequential loading sequence

To avoid this loss, we choose to leverage our optical transport and implement a sequential loading scheme. This allows us to evaporate Rb and Cs separately. This is facilitated by three beams used to form dimple traps in the Science Cell, namely the Guide dimple beam, the Moving Dimple beam and the Cs dimple beam. The beam layout used here is shown in Fig. 3.6 and in Fig. 4.2.

Figure 4.2 (a) shows the optical setup of the optical dipole trap beams in the Science Cell. All the beams are at a wavelength of $\approx$ 1064 nm, with the frequencies

[1]Measured clockwise from transport 2 going from the main chamber into the Science Cell

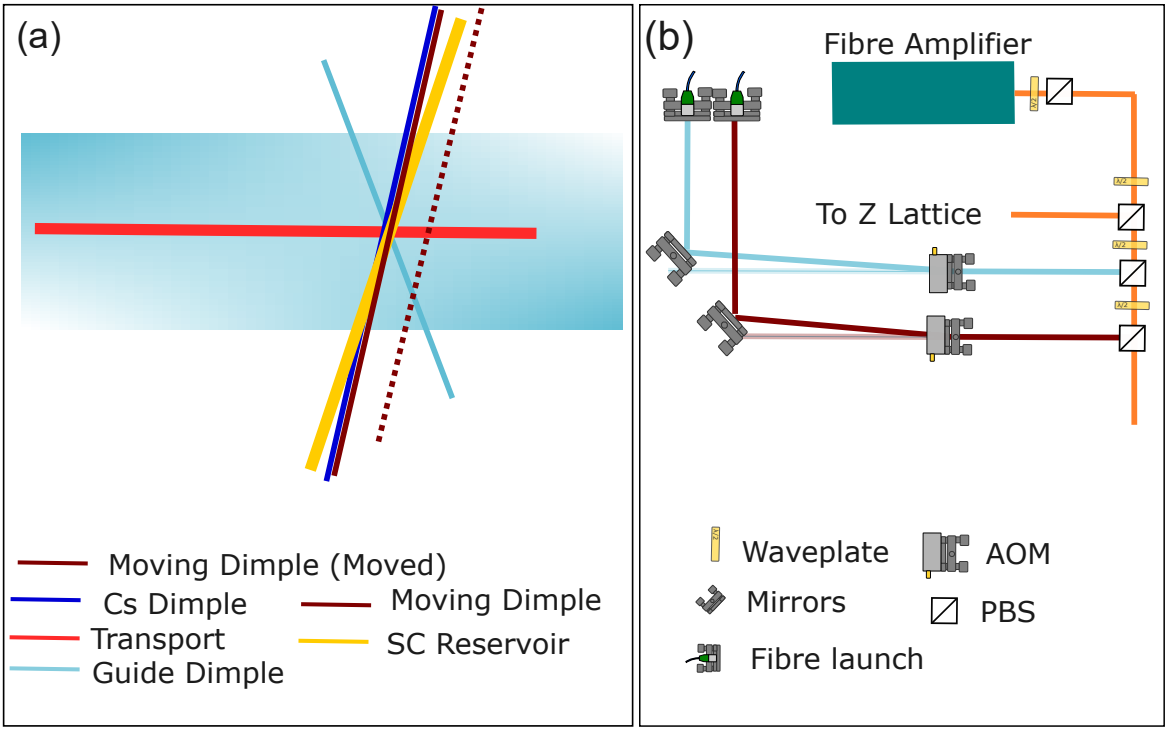

Figure 4.2: An illustration of the traps in the Science Cell. (a) shows the layout of all the trapping beams in the Science Cell. The Guide dimple and the Moving Dimple beams are sources from a fibre amplifier as shown in (b). Full details of the beam layout in the Science Cell can be found in Fig. 3.6, while full details of the Moving Dimple optical setup are presented in Fig. 4.4

set to different values using AOMs (which are also used to servo the beams) to prevent the formation of a lattice. The Guide Dimple and the Moving Dimple are sourced from one of the Azurlight 1064 nm Fibre amplifiers (Fibre Amplifier 3) as shown in Fig. 4.2 (b), while the light for the Cs Dimple originates from the Mephisto laser. Table 4.1 summarises the parameters of each beam.

We first offer a high-level description of the sequence, as illustrated in Fig. 4.3 before going into more details of the optical setup and the sequence. We first load a Rb MOT and perform the sub-Doppler cooling of Rb in the main chamber. We then load Rb into the Main Chamber Reservoir trap and transport it to the Science Cell. In the Science Cell, Rb is loaded from the transport lattice into the SC Reservoir (Fig. 4.3 (a)). From the SC reservoir, Rb is loaded into the a smaller xODT formed by the Guide dimple and the Moving Dimple beams (Fig. 4.3(b)). We refer to this

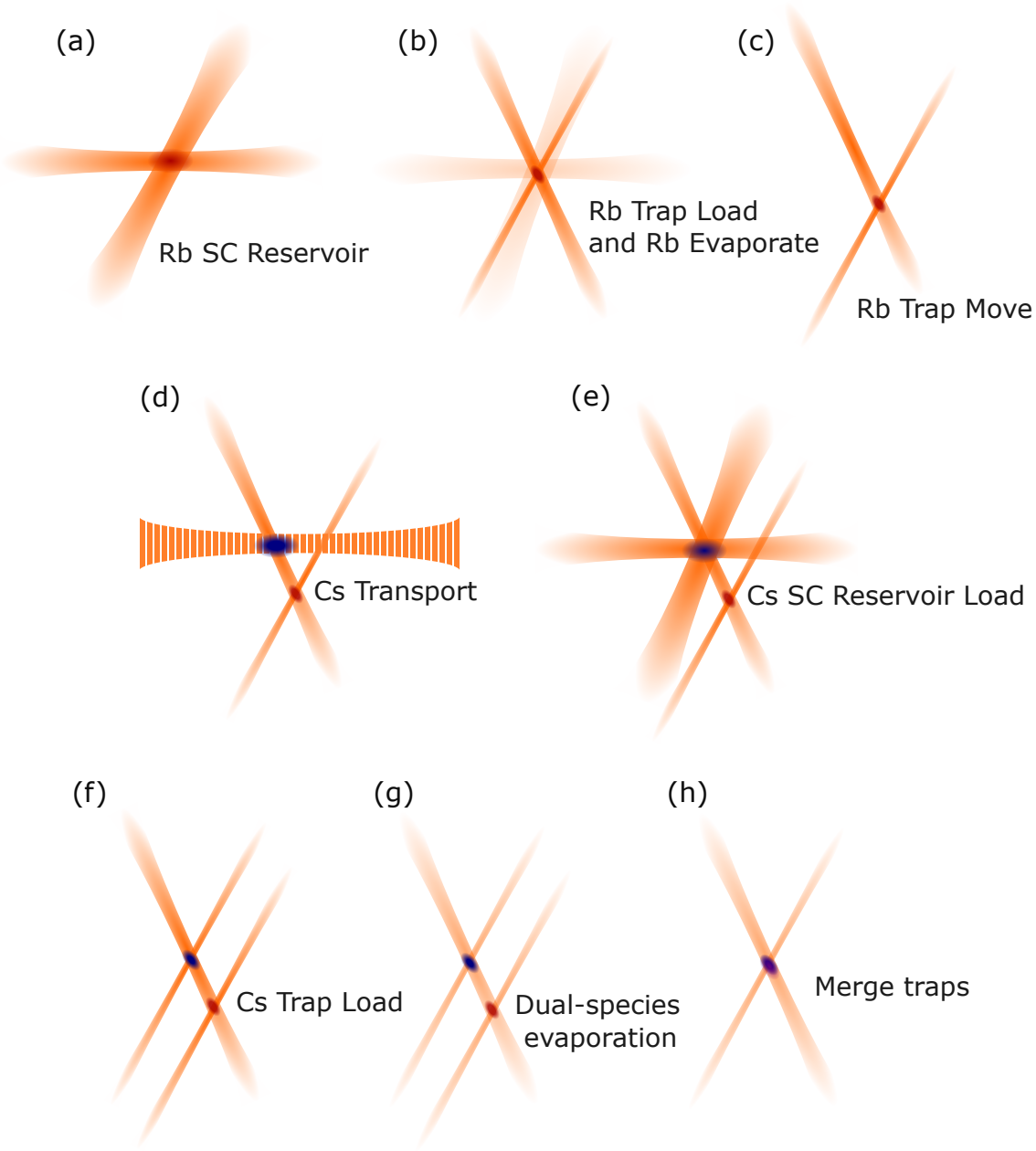

Figure 4.3: A depiction of the atoms and the trap locations in the Science Cell (as seen from above) throughout the experimental scheme, showing the sequential loading, followed by evaporation and finally merge of the two species. The Rb pre-cooling and transport occur before the depicted steps, and the Cs MOT load and pre-cooling occurs during and after the Rb trap is moved.

trap as the Rb trap. We perform some evaporative cooling of Rb in this trap before we move the position of the trap by translating the position of the Moving Dimple beam across the Guide Dimple beam. This changes the position of the intersection

of the beams, where the atoms are trapped, moving the atoms (Fig. 4.3 (c)). While the the beam is being translated, we load the Cs MOT. Rb is then held in the Rb trap while Cs undergoes DRSC and is transported to the Science Cell (Fig. 4.3 (d)). Crucially, the Rb trap has been moved away from the transport beams, so the Rb atoms are not effected by the transport. Cs is loaded into the SC Reservoir (Fig. 4.3 (e)) and then into a dimple trap we call the Cs trap (Fig. 4.3 (f)), formed by the Cs Dimple beam and the Guide beam. We now have Rb and Cs trapped at separate positions, with the Rb trap occurring at the intersection of the Moving Dimple (at its 'moved' position) and the Guide Dimple. The Cs trap is at the intersection of the Cs Dimple and the Guide Dimple. We note that the Cs Dimple beam was aligned to co-propagate with the initial ('unmoved') position of the Moving Dimple Beam. This was done to prevent the occurrence of a third trap at an intersection of the Moving Dimple and the Cs Dimple. We then evaporatively cool both Rb and Cs at the same time by ramping down the powers of all three beams in a carefully controlled manner (Fig. 4.3 (g)). The evaporation is done at $\approx$ 21 G to minimise Cs three-body losses. We can attain simultaneous BECs of Rb and Cs from this evaporation.

However, when we associate molecules, we do not evaporate all the way to BECs. As the Rb and Cs BECs are immiscible as discussed in chapter 2, we curtail the evaporation at a PSD of ≈ 0.1 for each species - where the clouds are still miscible. This means that we have dense thermal clouds rather than BECs, which suffices for production of the molecules. We do this to optimise for molecule number after magneto-association, as we must balance the association efficiency (which increases as PSD increases) with the total atom number (which decreases as we increase the PSD by evaporatively cooling the clouds). We then merge the Rb and the Cs atom clouds by translating the position of the Rb Dimple back to its initial position, where the Rb trap and Cs trap are overlapped (Fig. 4.3 (h)). We are able to create a mixture containing $\approx$ 2×10^5 atoms of each species at a PSD of ≈ 0.1, from which we associate molecules.

4.2 The Moving Dimple trap

We now discuss the design and operation of the Moving Dimple trap used to facilitate this scheme. The Moving Dimple is designed in a manner similar to that used in [113], where the trap is moved by translating the fibre tip before an aspheric lens. The motion of the dipole trap beam at the atoms is set by the magnification of the system, i.e by the ratio of the beam waists of the dipole trap and the radius of the fibre tip.

4.2.1 Design

The optical and mechanical setup of the Moving Dimple are shown in Figure 4.4[2]. The dimple consists of an optical fibre before an aspheric collimating lens. This is followed by PBSs which set a linear polarisation, followed by a telescope and focusing lens to set the beam to the required size, so that it can be focused to the desired size on the atoms (approx 50 µm). The fibre is mounted on a translation stage (Elliot Scientific - MDE 330), with a piezo-actuator (Elliot Scientific - MDE 227) affording 100 µm of motion of the fibre tip. However, we find that beyond translations of 80 µm of the fibre on the stage (1000 µm of the beam at the atoms), further motion of the beam leads to a degradation of beam shape, by enough to lead significant loss in the dipole trap. The voltage into the piezo-adjuster is supplied by amplifying the output of an Arduino Uno board using a piezo amplifier (MDT693B). A 12-bit DAC (DFR0971) is used at the output of the Arduino to allow for smooth voltage ramps.

The Moving Dimple trap is designed to be bichromatic - in addition to 1064 nm, it can also operate at 830 nm so that it could be used as a species selective trap between Rb and Cs. This is from our initial plans to utilise a sequence similar to that used in Innsbruck [112, 113]. We only operate with 1064 nm light now, as the use of the sequential loading negates the requirement of a species selective trapping potential. The lenses in the setup were chosen to balance their chromatic focal

[2] All lenses are from Thorlabs. A1: C220TMD-B - f = 11.0 mm, L1 : f=-30 mm, L2: f=60 mm, L3: f=, L4 f=, L5,f=250 mm

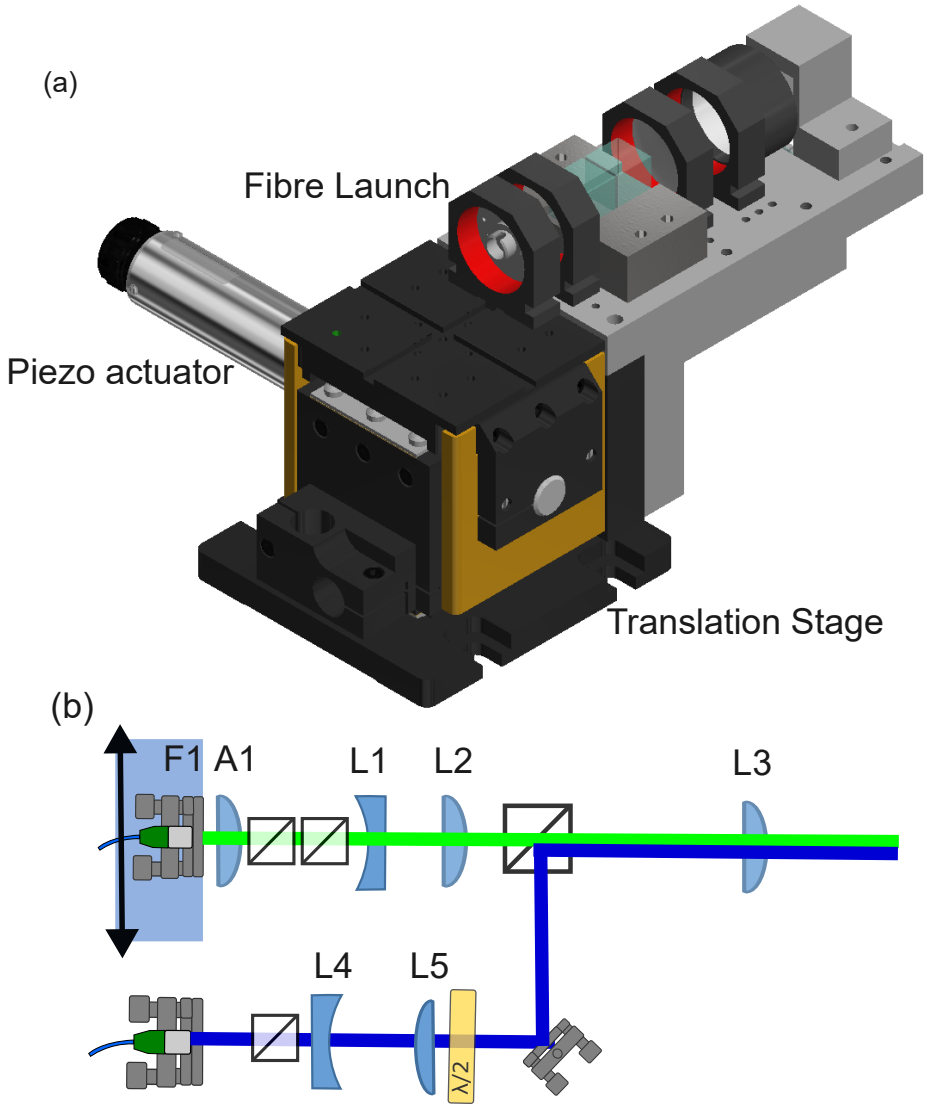

Figure 4.4: The setup of the Moving Dimple. (a) shows a render of the Moving Dimple setup. (b) shows a schematic of the corresponding optical setup and that of the Cs dimple which propagates along the same path. The fibre (F1) is mounted on a piezo-actuated translation stage. The aspheric lens (A1) and the telescope lenses (L1 and L2) are mounted on a custom machined block for stability. The block includes a periscope to change the height of the beam to that of the atoms. The Cs dimple is overlaid onto the Moving Dimple using a PBS before they are both focused at the same location in the Science Cell. The separation of F1 and A1, along with the alignment of the two pairs of telescope lenses allow for the selection of an appropriate focal length and the axial alignment of the focus for both beams.

length shifts and to ensure that the beams of different colours focus at the same axial location.

We find that the beam shape is approximately Gaussian and relatively non-aberrated (by visual inspection using a camera) for approximately 80 μm of motion of the stage away from the centre, while the beam size remains relatively constant (to within 5%). This is supported by measurements of the trap frequency with the atoms, where we find the trap frequency of of the Moving Dimple at its initial position and after a 80 μm stage movement to vary by only $\approx 10\%$. We find the movement of the stage to be stable and repeatable to ≈ 1 μm (comparable to the stability of the camera used to measure this)[3].

4.2.2 Alignment

The Moving Dimple was aligned onto the atoms using trap frequency measurements (Sec. 3.4.3). The Moving Dimple fibre tip was centred on the Aspheric lens and aligned to have the beam collimated out of the telescope. The beam was then coarsely aligned to the atoms by maximising the number of atoms able to be trapped in a xODT of the Moving Dimple beam and the Guide Dimple beam[4]. The fine alignment was conducted using the three-axis adjustment of the stage, maximising the trap frequency at a given power. The Cs Dimple beam was then overlapped with the Moving Dimple using a camera.

The optical setup was designed and tested *exsitu* to choose appropriate lenses. The size of the fibre tip was only known to rough accuracy (4$\pm$1 μm), so the optical setup was designed to achieve a waist close to 50 μm. The magnification is then measured by moving the beam, and comparing the movement at the beam focus to that on the stage. The *exsitu* measurements of the beam waist and magnification of 43 ± 2 μm and 12.5 ± 0.5 respectively are similar to the *insitu* measurements of

[3]The first run of the stage after some downtime seems to have a large hysteresis, before settling into a repeatable cycle. Practically, this results in us requiring a single warm up shot of the experiment at the start of a day.

[4]The dimple beams are aligned by forming a xODT with another dimple beam. The first dimple beam was aligned by forming a xODT with another beam in the Science Cell (a Transport beam or the Reservoir beam)

the same performed once the beam was aligned to the atoms.

We find a waist of the Moving Dimple on the atoms to be 47 ± 2 μm from a trap frequency measurement. By imaging the position of atoms trapped in the dimple before and after the beam is moved, we find that the magnification of the system is 13.5 ± 0.1. We are able to trap atoms well in the Moving Dimple trap, both at the initial position - where it loads atoms from the SC Reservoir trap, and when the trap is moved out of the way of transport. We measure a lifetime of over 20 s for Rb atoms in the Rb trap, both at the initial position, and when it is moved by ≈ 1000 μm (moving the stage 80μm).

4.3 Single-species evaporation

We first test the efficacy of the trapping scheme by loading atoms of only one species into the optical traps in the Science Cell and evaporatively cooling them to a BEC. For Rb, we evaporate in the Rb trap (Moving Dimple + Guide dimple) while for Cs we do so in the Cs trap (Cs dimple + Guide dimple). The production of a Rb BEC is a significant benchmark here, as previously, we required an additional 830 nm beam (for additional trapping and confinement) to evaporate Rb to a BEC [148, 161]. With the new trapping scheme along with some improvements from re-optimisation of the laser cooling and transport stages of the experiment, we are able to evaporate Rb to a BEC without any additional beams[5].

The momentum distribution of a BEC is not Gaussian (obeying Bose statistics instead). At any point, we assume that our cloud is a mixture of atoms that have condensed, and atoms that are still thermal. We use the fitting function described in [191] to fit our bimodal clouds and extract an atom number as well as a condensate fraction. This is done by integrating the OD counts from absorption imaging along the two axes of the image, and fitting a curve of the form $\rho(x) = \rho_{\text{thermal}} + \rho_{\text{BEC}} + c$,

[5]Re-optimisation of the cooling and transport has given us more Rb atoms, and the new trap design gives us a tighter trap to evaporate Rb in, increasing the collision rate and improving the thermalisation

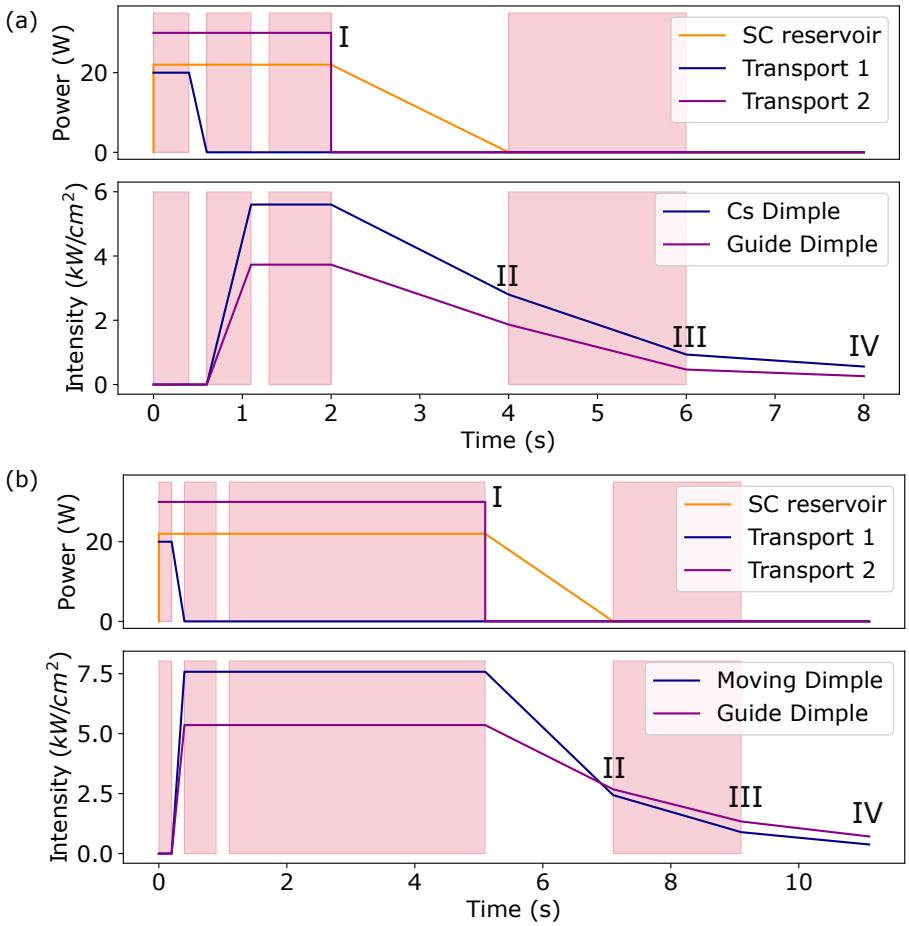

Figure 4.5: The sequence used to prepare a single-species BEC for Cs (a) and Rb (b). We note the four points (I,II,III,IV) in the sequence we measure the atom number and temperature at in order to gain an idea of the PSD during the evaporation trajectory.

where

$$\begin{aligned} \rho_{\text{thermal}}(x) &= \frac{N(1-\beta)}{\sqrt{2\pi}\sigma_{\text{thermal}}}\exp\left(-\left(\frac{x-x_0}{\sqrt{2}\sigma_{\text{thermal}}}\right)^2\right), \\ \rho_{\text{BEC}}(x) &= \frac{15}{16}\frac{N\beta}{\sigma_{\text{BEC}}}\text{Max}\left(1-\left(\frac{x-x_0}{\sigma_{\text{BEC}}}\right)^2, 0\right). \end{aligned} \tag{4.1}$$

Here, β is the BEC fraction, x_0 is the centre of the cloud, σ_{thermal} and σ_{BEC} are the widths of the thermal fraction and the BEC respectively, and c is an offset to account for the background signal in the images.

A common technique when cooling a gas evaporatively is to use multiple ramps

to optimise the cooling process. The experimental control software we use is only capable of linearly ramping the beam power, so we usually use three to four different ramps when evaporatively cooling to a BEC. This enables us to ramp down the trap at different rates throughout the sequence as shown in Fig. 4.5. The evaporation time is often in the range 5-10 s, and is a significant proportion of the total experimental cycle time.

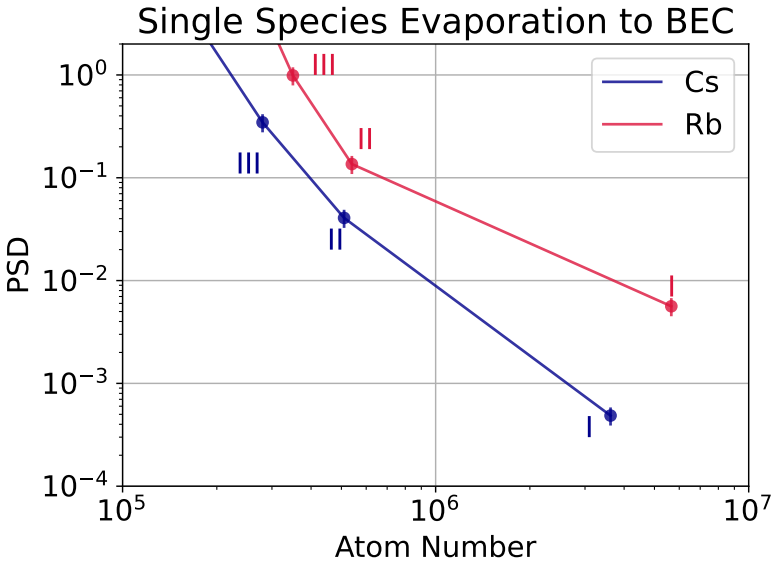

Figure 4.6: A measure of the atom number of Rb and Cs throughout the evaporation process. We see evaporation efficiencies of > 2.0 for both species. The final point of the evaporation ramp, where we have a BEC, is not shown here, as it is difficult to measure a PSD of a highly condensed cloud. We instead fit a bimodal distribution and quote a BEC fraction as shown in Fig. 4.7

We are able to achieve efficient evaporation to a BEC for both species separately as shown in Fig. 4.6. Figure 4.5 shows the powers of the beams during the evaporation ramps. We further note that the evaporation was conducted with the atoms magnetically levitated, and at a magnetic field of 21 G (to minimise the Cs loss). The optimisation of the ramp steps and the evaporation efficiency are both characterised using the PSD (defined in Eq. 2.2). The evaporation ramps were designed to maximise the atom density (for the initial ramps), and then later to maximise

the BEC number. The efficiency of the evaporation (η_{evap}) is characterised by,

$$\eta_{evap} = \frac{d\log(PSD)}{d\log(N)}, \tag{4.2}$$

where N is the atom number. The trap frequencies required to calculate the PSD are the geometric mean of the trap frequencies of the two beams ($\omega^2_{\text{trap}} = \omega_1\omega_2$) forming the dimple trap, measured using oscillations in the trap (see Sec. 3.4.3) The evaporation efficiencies we see here are similar to other experiments which produce BECs in a dimple trap [112].

Figure 4.7 shows images of the Rb and Cs BECs in the single-species sequences. With ramps optimised individually for each atomic species, we are able to achieve a cloud of 2×10^5 Rb atoms at a BEC fraction of $56 \pm 5\%$ and 5.8×10^4 Cs atoms at a BEC fraction of $76 \pm 3\%$.

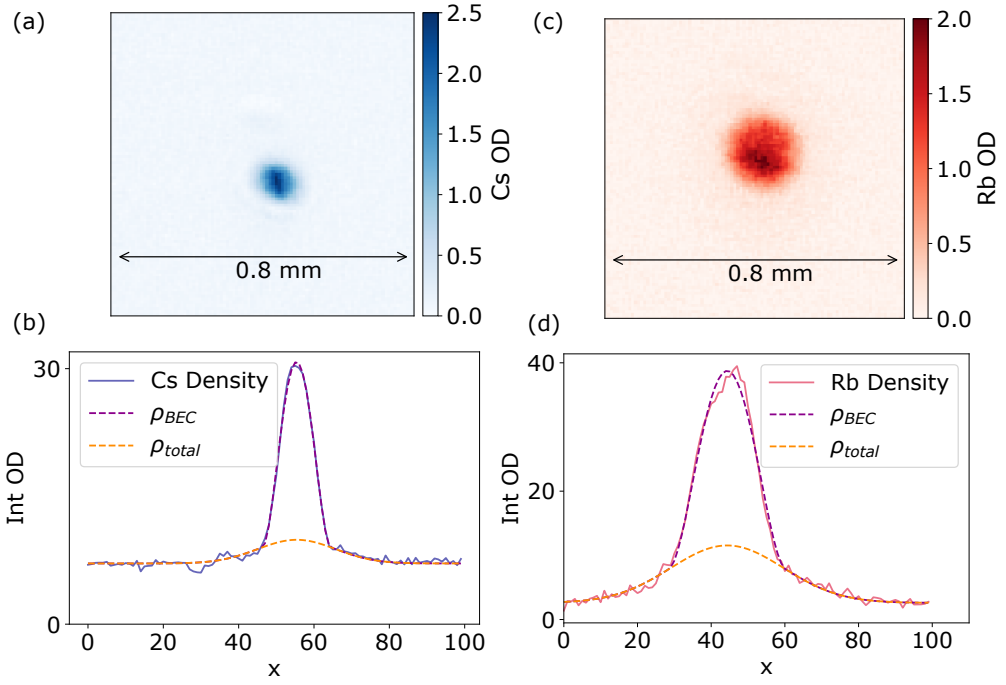

Figure 4.7: Images of the BECs of Cs and Rb in the single-species sequences optimised for the production of the BEC. Each image is from a different experimental run, and a different sequence. (a) shows and image of the Cs atom cloud, with (b) showing the integrated OD (summing vertically here), and fits to Eq. 4.3. (c) shows an image of Rb and (d) the integrated OD and similar fits. These images were taken after 60 ms of TOF, and we see that the cloud is still optically dense - indicating a BEC.

4.4 Dual-species sequence

Now that we can produce BECs of both Rb and Cs separately, we attempt to achieve the same in a single experimental run. The start of our dual-species sequence is loading the Rb trap with Rb from the SC reservoir in the same manner as the single-species sequence. Once the dimple is loaded, we translate the dimple position in 2 s between the initial and final point. The dimple follows a minimum-jerk trajectory to minimise atom loss during this motion. The distance the trap is moved is set by the following: (i) the trap must be moved far enough that the atoms are not lost when Cs is transported[6] (ii) they must be moved far apart from the initial trap to prevent Cs and Rb from mixing during the simultaneous dual-species evaporation (iii) if moved too far, the beam quality starts to degrade, and atoms are lost from the trap[7].

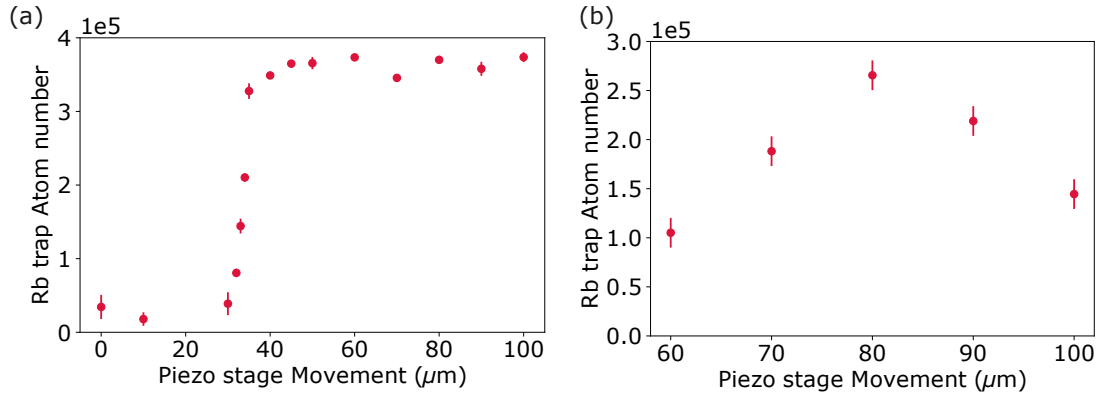

Figure 4.8: The optimisation of the Moving Dimple movement. (a) shows the dependence of atom number on the dimple movement after the transport lattice is moved. After a motion of ≈ 40 μm on the stage, the atoms are no longer perturbed by the transport lattice. (b) shows the optimisation of the move distance after evaporation. We set the Moving Dimple to move 80 μm on the stage, or ≈ 1000 μm on the atoms in the final sequence.

Figure 4.8 shows optimisation of the dimple distance moved. We first investigated the distance required to move out of the transport lattice, shown in Fig. 4.8 (a).

[6]The atoms must be moved far enough away so that the effect of the transport lattice is negligible and that they are held in the dimple trap and not transported into the wall of the Science Cell.

[7]The beam becomes bigger and non-Gaussian in shape, causing a reduction in trap depth.

This was done by loading the dimple and then moving a variable distance away in 2 s. After the move, the transport lattice was turned on, and the lattice beam detunings were ramped to mimic the optical transport, before measuring the Rb atom number in the trap. We find that there is a steep loss curve here, but stage motion greater than $\approx$ 36 μm means that we see no loss to transport. Figure 4.8 (b) shows the optimisation of the moving distance in the sequence by measuring the atom number in the trap after conducting our dual-species evaporation ramps (the details of the evaporation ramps are discussed below).

We initially load $(8.4 \pm 0.2) \times 10^5$ Rb atoms at 915 ± 4 nK. After moving, we find that we are left with $(6.4 \pm 0.2) \times 10^5$ Rb atoms at 522 ± 7 nK[8]. Once we have moved the Rb trap, we are able to transport Cs in and load it into its own dimple trap. We then face the challenge of evaporatively cooling the two species together.

4.4.1 Controlled dual-species evaporation

The evaporation of two species simultaneously faces some additional challenges when compared to the evaporation of a single-species. The scattering length and polarisability of Rb and Cs are not the same, so the evaporation ramp each species prefers is slightly different (both beam powers and ramp times). We must find a set of ramp parameters that offer a compromise between the species, which reduces the efficiency of evaporation when compared to the single-species evaporation case. The more significant challenge however comes from preventing the two species from mixing during the evaporation.

Normally during evaporation, as the trap depths are lowered, the highest energy atoms leave the trap, preferentially escaping along the beams themselves (Fig. 4.9), as the path of the beams offers a lower potential than the remaining 'dark' areas. For single-species evaporation, this is fine. To optimise the evaporation, the beams are usually ramped down in a balanced manner, with equal loss in all the directions. However, with our trap geometry, where the two traps share a beam (the Guide dimple beam), this is extremely undesirable. Atoms of Rb or Cs that are lost from

[8]The reduction in temperature could be from some preferential loss of the hottest atoms during the move step, as well as Rb having had more time to thermalise in the trap.

the trap and leave along the Guide dimple beam may reach the other trap. Here, they are able to collide with atoms of the other species and can get recaptured in the other trap. The atoms that have been lost during evaporation are relatively hot, so when they collide with the atoms of the other species, they increase the energy of the ensemble and reduce the efficiency of the evaporation process. Moreover, as the atomic clouds reach high PSDs, there is significant three-body loss from interspecies interactions. This is particularly harmful to the Rb atoms, as its lower polarisability (and hence lower trap depth) means that, when Cs atoms are recaptured by the Rb trap, they lead to loss of most of the Rb atoms due to the three body interactions. So, it is critical to minimise the interaction of Rb and Cs during the evaporative cooling process.

This was visible in our first attempts at simultaneous evaporation as shown in Fig. 4.9. When the dual-species evaporation sequence is run while blocking the MOT load of one species, we are able to load the other species into a dimple and evaporate successfully (Fig. 4.9 (b) and (c)). However, when both species are loaded, we see that there is some re-capture of atoms, which leads to large loss in atom number, especially of Rb. This is highlighted in Fig. 4.9 (d) and (e), which show images of the Rb and Cs cloud in the same dual-species sequence.

We limit the mixing of the species during evaporation by controlling the separation of the species during evaporation, preferentially evaporating along the non-shared beams (Moving Dimple and Cs Dimple), and using the magnetic field gradient to tilt the traps. The separation of the species is controlled by the amount the Moving Dimple moves, as is shown in Fig. 4.8 (b). During evaporative cooling, we keep the non-common beams - the Cs dimple and the Moving Dimple at higher intensities to the Guide Dimple. This creates a lower potential along these beams, and thus encourages selective evaporation along these beams rather than along the Guide Dimple. Finally[9], we are able to use the magnetic field quad coils to 'tilt' the trap potentials away from each other along the Guide dimple, to minimise atom loss into the traps.

[9]And perhaps most crucially. This solution is perhaps the most 'magical fix' to an issue the author has seen in the lab.

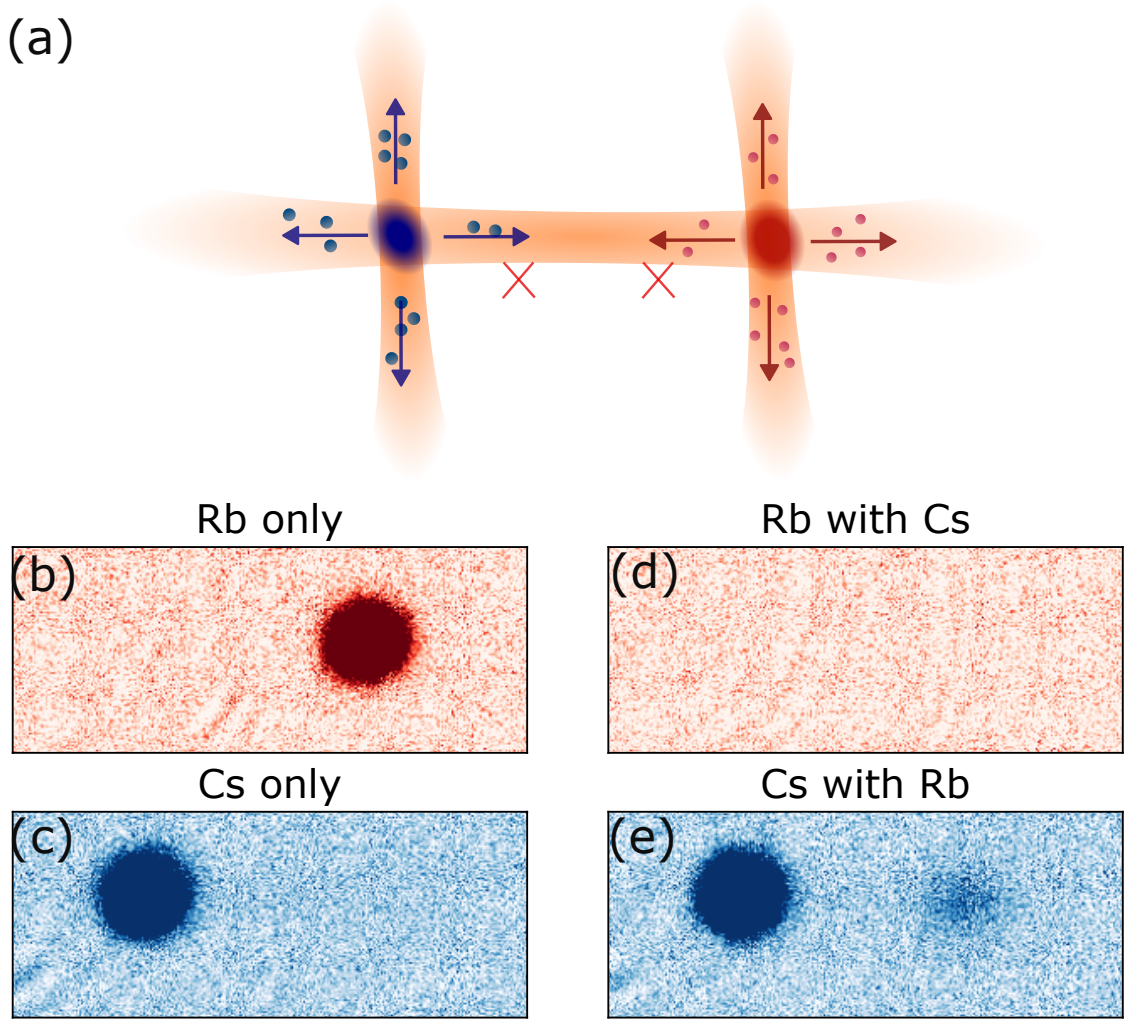

Figure 4.9: Cs and Rb mixing in dual-species dimples. On top (a), we show a cartoon of the atoms in their traps and the directions they can evaporate. Evaporation along the trap is problematic as atoms can get recaptured in the other trap and lead to loss from interspecies collisions. Below, we show images of the two species in the dimples after some evaporation, taken with and without the presence of the other species in the sequence. With only one species loaded, we are able to evaporate both species well (as shown in (b) and (c)). When we introduce the second species, we see a loss of atoms (particularly Rb). This is due to Cs atoms reaching the Rb trap and getting captured in the trap, resulting in the destruction of the Rb atom cloud from three-body loss.

The quad coils (Sec. 3.3.2) are the anti-Helmholtz coil pair designed to provide a magnetic field gradient at the atoms to levitate the atoms. Normally, we use the shim coils to position the field minima to coincide with the atoms (and maximise the field gradient on the atoms). Here, we find that if the field minima is positioned between

the Rb trap and the Cs trap, the potential is maximised between the traps, which tilts the traps away from each other[10]. With just the beam powers optimised (and not the field minima), we see that the mixing of Rb and Cs limits the atom number of each in our dual-species sequences. We optimise the field from the shim coils to centre the field minima and minimise the interspecies interaction by maximising the Rb atom number after some evaporative cooling, shown in Fig. 4.10. As shown in Fig. 4.10 we find that we are able to reduce the presence of Rb in the Cs trap (and vice versa) to a negligible value[11].

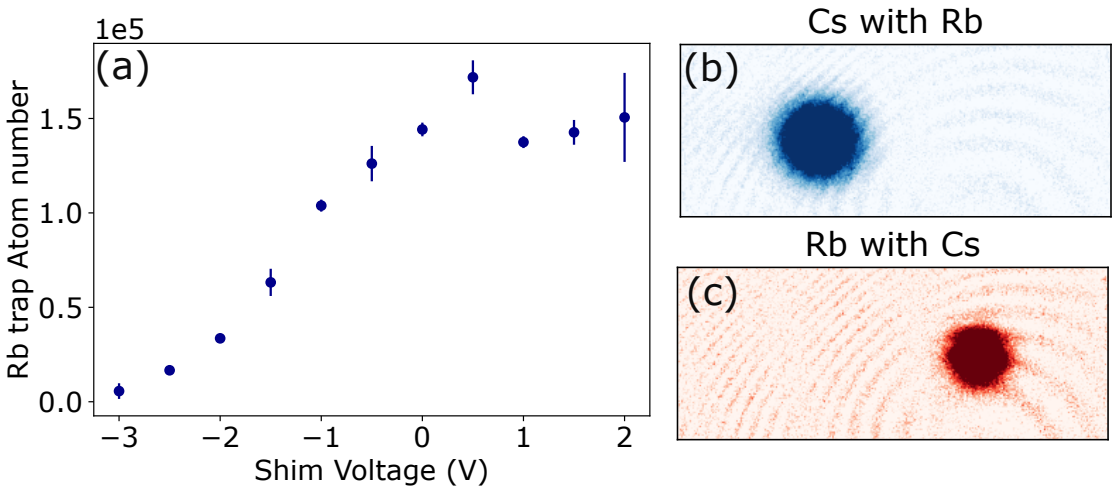

Figure 4.10: Prevention of mixing of Rb and Cs in the dimple traps using the magnetic field. (a) shows a measurement of the atom number in the Rb trap in the dual-species sequence after some evaporation as a function of the shim field used to centre the field minima (this was repeated for the other shim directions). (b) and (c) show images of Rb and Cs after some evaporation in the dimple. These are images of both the atom clouds taken in the same sequence. The sequences are similar to those used in Fig. 4.9, with the optimisation of the shim field being the main change. We note the improvement here, where we have a large Rb cloud, as we no longer see loss from its interaction with Cs atoms. (b) and (c) are presented at the same OD colour scale of Fig. 4.9.

Figure 4.11 (a) shows the potential landscape of a horizontal slice of the trapping region at one point during the optical evaporation sequence we use. As was

[10]In other words, field minima is centred between the traps, with both species in their high-field seeking states leading to the atoms being repelled away from the centre.

[11]Below what we can image

discussed, the Cs Dimple and the Moving Dimple are maintained at higher intensities than the Guide Dimple to reduce loss along the Guide Dimple. Fig. 4.11 (b), which plots the potential across the Guide Dimple, highlights the contribution from the magnetic field in tilting the traps away from each other.

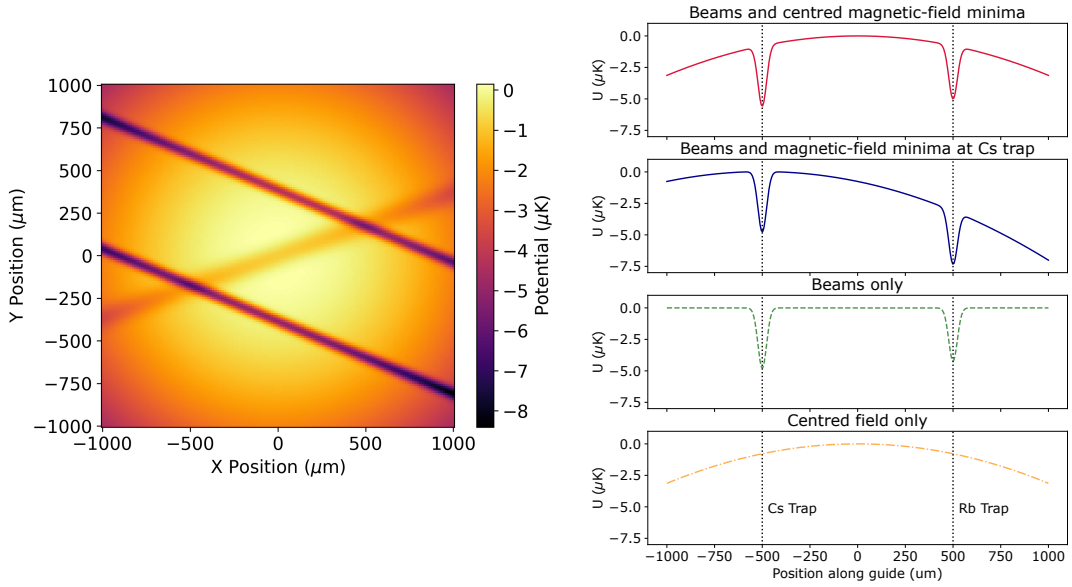

Figure 4.11: A calculation of the potential of the traps in the first stage of evaporation used in the dual-species evaporation sequence after both traps are loaded, and the field minima is centred between the traps. (a) shows the potential landscape, with the both the traps visible. We note that the guide is intentionally shallow to discourage evaporation along it. (b) shows the total potential along the guide dimple, along with the various contributions from the beams and magnetic fields. We note the effect of the magnetic field gradient on tilting the traps away from each other.

4.4.2 Characterisation of the dual-species evaporation

We find that with the two traps sufficiently separated, and the field minima centred between the atoms, we can ramp down the powers of all the dimple beams simultaneously to evaporate both species together efficiently. Figure 4.12 shows the sequence used to evaporate the two species together and then merge the traps. While we are able to evaporatively cool to a simultaneous dual-species BEC of Rb and Cs, we typically cease the evaporative cooling when the atoms have a PSD of ≈ 0.1 for

reasons described in Chapter 3. We prepare a dual-species mixture of $\approx 2 \times 10^5$ atoms of each species at temperatures of around 200 nK and a PSD of ≈ 0.1.

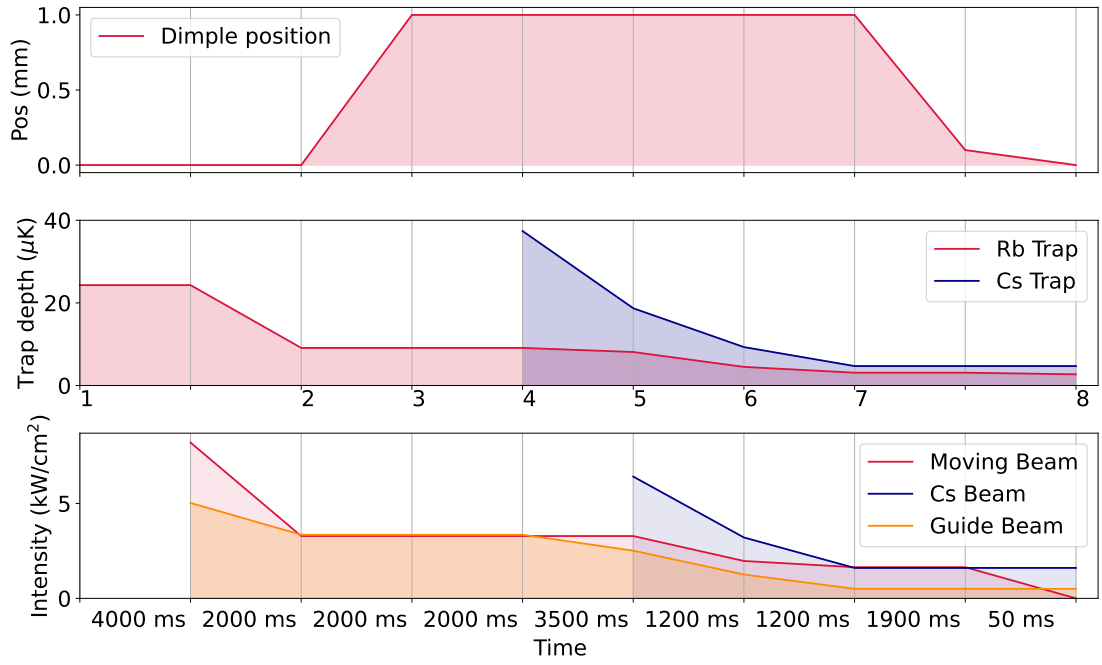

Figure 4.12: The sequence used to evaporate Rb and Cs together to create the high PSD mixture used to produce molecules. The first subplot shows the position of the Moving Dimple, with the second subplot the depths of the traps. The steps 1-8 labelled are as follows. (1) Rb Reservoir loaded (2) Rb trap loaded (3) Rb trap moved (4) Cs Reservoir loaded (5) Evaporation ramp 1 (6) Evaporation ramp 2 (7) Evaporation Ramp 3 (8) Traps Merged

The sequence is optimised for the maximum number of both atoms in the final merged trap (at the desired PSD). The evaporation trajectory of both species throughout the sequence is shown in Fig. 4.13. We investigate the effect of inter-species collisions in this sequence by running the sequences for a dual-species merge and evaporation while loading only a single-species MOT. As shown in Fig. 4.13, we find that the evaporation trajectory for both species is independent of the presence of the other species (within experimental error). This indicates that the methods used to prevent the species mixing are extremely effective.

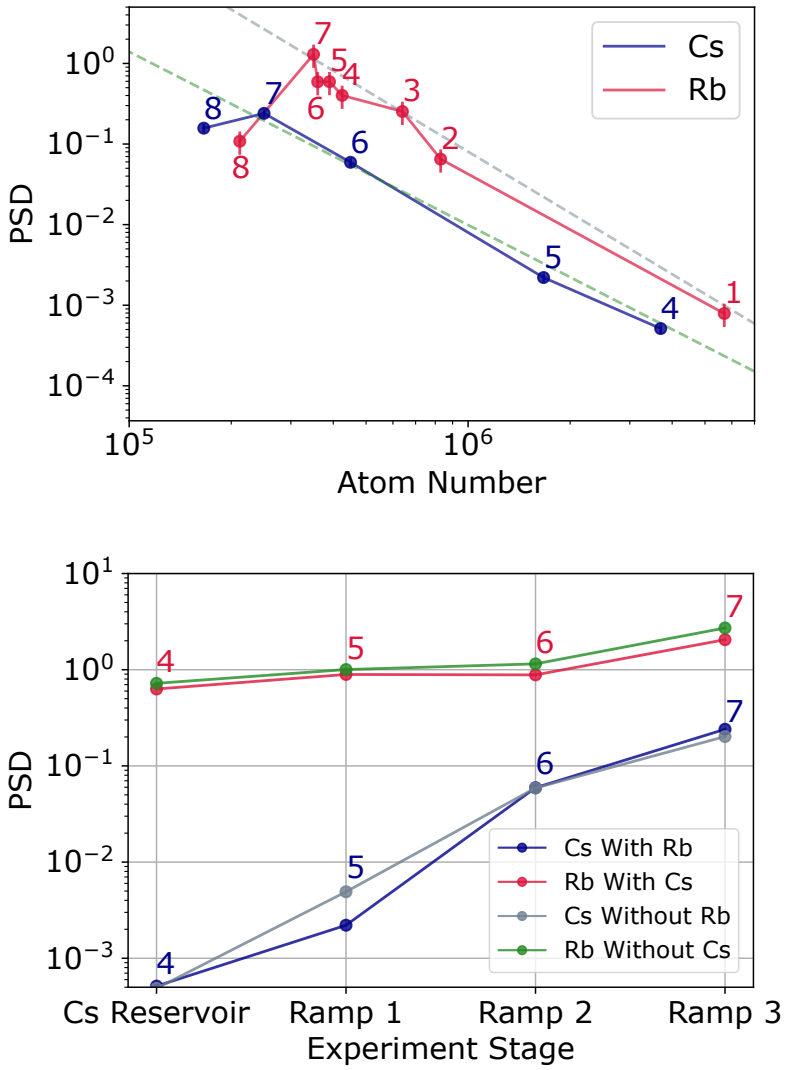

Figure 4.13: Characterisation of the evaporation ramps for Rb and Cs together. (a) shows a measurement of the PSD during the sequence. The numbers 1-8 correspond to the steps of the sequence labelled thus in Fig. 4.12. (b) shows a measurement of the PSD when the experiment is done with both species, and compares it to when the same sequence is run without the presence of one species. The PSD of both species is agnostic to the presence of the other species, which shows that we have abated collisional losses between the species during evaporation.

4.5 Dual-species BEC of Rb and Cs

We are able to produce a BEC of Rb and Cs in the Science Cell at the same time, and move them to be <200 μm apart. While in the sequences used to produce RbCs molecules, we merge clouds at PSD $\approx$ 0.1, the production of a dual-species BEC is a useful metric to benchmark the evaporation. Moreover, we plan to soon

upgrade our molecule production method to produce denser clouds of molecules in the ground band of the lattice as demonstrated in [113]. This relies on merging a superfluid cloud of Rb with a Cs Mott insulator, so it requires a dual-species BEC as its starting point.

The first steps of the evaporation to a BEC are performed as before, up to the evaporation step before the merge. Then, instead of moving the Rb trap to overlap with the Cs trap, we continue ramping down the beam powers to reach a BEC for both species.

We find that we are able to produce a BEC of Cs and Rb at the same time with atom numbers of $(4.4 \pm 0.1) \times 10^4$ with a BEC fractions of $80 \pm 3\%$ for Cs and $(1.7 \pm 0.1) \times 10^5$ with a BEC fraction of $43 \pm 4\%$ for Rb, fit using the bimodal distribution (Eqn . 4.3). The BEC size for both species is $\approx 80\%$ of that produced in a single-species shown earlier. This is likely due to the sequence now being optimised for the dual-species evaporation, and not for a single specific species. After evaporation, we are able to move these clouds 120 μm apart, and still see a dual-species BEC. We have not investigated merging the BECs in detail as of yet. In the future, we plan to extend this sequence to the merging of a Rb superfluid with a Cs Mott insulator to associate molecules in a lattice, similar to [113, 114].

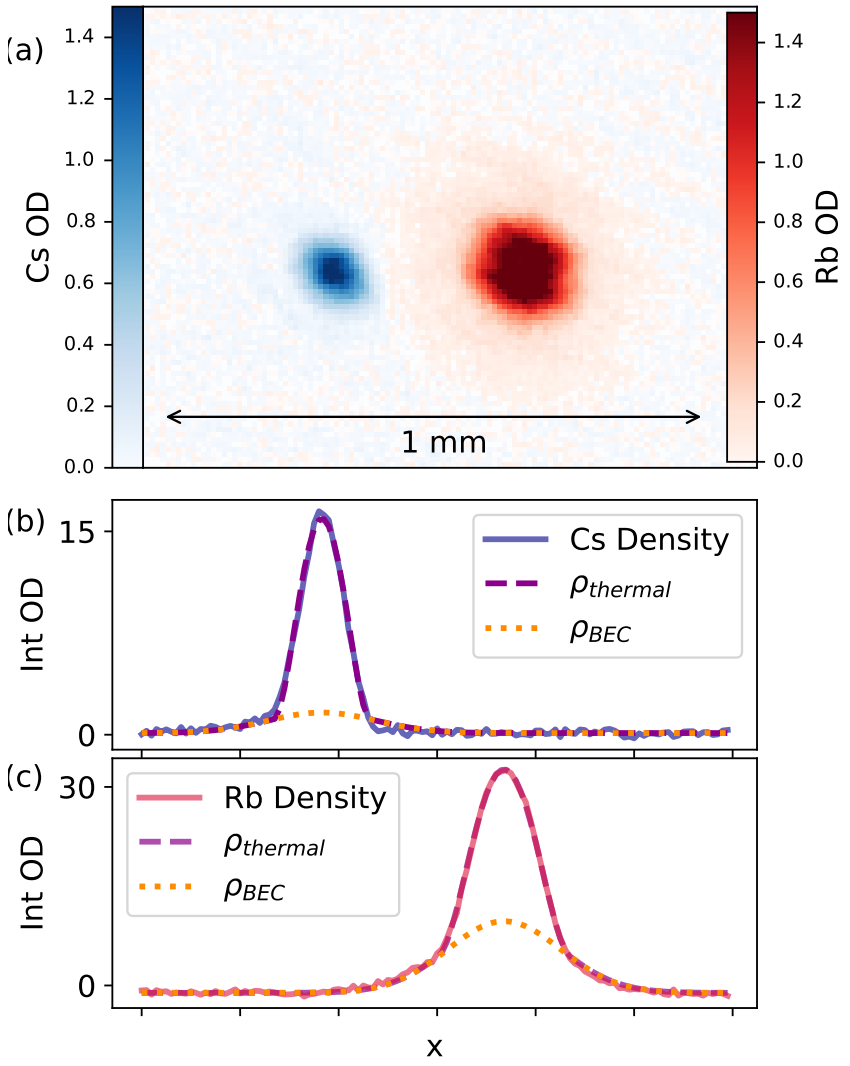

Figure 4.14: A dual-species BEC of Rb and Cs, produced in the Science Cell. The clouds are both optically dense even after 50 ms of TOF, characteristic of a BEC. We fit a bimodal distribution of the form Eq. 4.3 and find Cs and Rb atom numbers of $4.4 \pm 0.1 \times 10^4$ ($1.7 \pm 0.1 \times 10^5$) with BEC fractions of 0.80 ± 0.03 (0.43 ± 0.04)

CHAPTER 5

Production of Ground State RbCs molecules

This chapter discusses the production of ≈ 2700 ground state molecules from the dual species mixture. The molecules are first magneto-associated into the state $|n(f_{\mathrm{Rb}}, f_{\mathrm{Cs}})L(m_{f_{\mathrm{Rb}}}, m_{f_{\mathrm{Cs}}})\rangle = |-6(2,4)d(2,4)\rangle$ via the $|-1(1,3)s(1,3)\rangle$ Feshbach state by ramping the field over the Feshbach resonances at 181.6 G and 197.1 G. These molecules are then transferred to their ground state via STIRAP (Stimulated Raman Adiabatic Passage). We detail the implementation, optimisation and characterisation of the STIRAP optical setup in our lab, following similar setups detailed in [163, 211]. We finally show that we were able to use optical feedfoward to reduce the noise on our STIRAP lasers and achieve the highest STIRAP efficiency seen in RbCs of $98.7 \pm 0.1\%$ [144].

5.1 Feshbach Association

With a high phase space density dual species mixture realised, we move on to associating Feshbach molecules. Further details on the theory behind the Feshbach association can be found in Sec. 2.3.1 The scheme we use for the production of Feshbach molecules involves first sweeping the magnetic field through Feshbach res-

onance at 197 G, to prepare molecules in the $|-1(1,3)s(1,3)\rangle$ state. The molecules in this state have a similar levitation gradient to the atoms themselves, so we transfer the molecules to the $|-2(0,3)d(1,3)\rangle$ (-0.9 μ_B) or the $|-6(2,4)d(2,4)\rangle$ states to separate the molecules from the atoms using a magnetic field gradient. To make ground state molecules, we transfer molecules to the $|-2(0,3)d(1,3)\rangle$ state for separation and then prepare them in the $|-6(2,4)d(2,4)\rangle$ state for STIRAP to the ground state. The state the Feshbach molecule is in can be controlled using the magnetic field as has been discussed previously (see Fig. 2.3).

5.2 Magnetic Field Calibration

The magneto-association of atoms to molecules requires fine control of the magnetic field on the atoms. The Feshbach resonances for the molecules are at relatively high magnetic fields ($\approx$ 197 G and 181.5 G) and are relatively narrow (about 200 mG). To successfully associate, we must be able to ramp to just above the Feshbach resonance, and then ramp down over it in a controlled manner. So, before investigating the interspecies Feshbach resonance, we chose to calibrate our field more precisely using the atoms.

The magnetic field inside the science cell is controlled by the various coils as detailed in Sec. 3.3.2. The initial calibration of the coils was conducted using a Hall probe before the coils were mounted in the experiment. We rely on two methods to generate an accurate calibration of the magnetic field from the coils on the atoms - using the Cs Feshbach resonances and using microwave transitions from the Cs atomic ground state. The Cs intraspecies Feshbach resonances offer a convenient set of well defined magnetic field checkpoints to search through. In addition, we use the 11 mG wide Cs Feshbach resonance at 19.9 G to magneto-associate some Cs_2 Feshbach molecules to confirm we have the necessary control of the magnetic fields required.

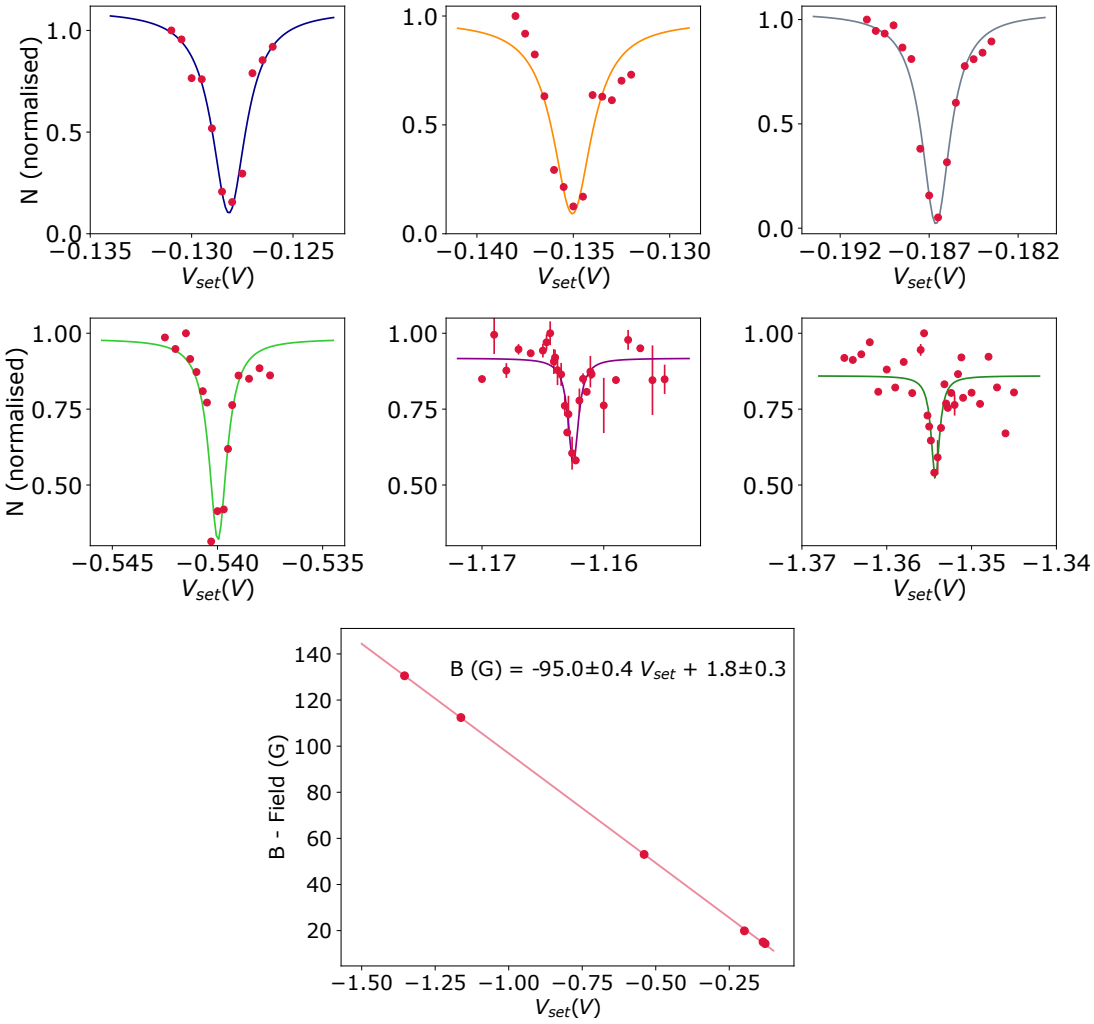

Figure 5.1: We scan the magnetic field during a 300 ms hold time where Cs is held in the dipole trap (≈ 100,000 atoms at a PSD of 0.1). We see loss in atom number at the Feshbach resonances. We fit a Lorentzian to this to find the Feshbach resonances, and use the known positions of these resonances [131, 212] to calibrate our magnetic field with a linear calibration(below).

5.2.1 Cs Feshbach resonances and Cs_2 Feshbach molecules

Cs has a rich, well characterised structure of Feshbach resonances at magnetic fields of under 200 G, which we use to calibrate our magnetic fields [131,212]. The scattering rate increases at the position of a Feshbach resonance, so the Cs three body loss rate increases significantly when the field is set to a Feshbach resonance. So, if we hold a cloud of Cs at a reasonably high density (PSD ≈ 0.1) at different magnetic fields, we expect to see a drop in atom number at the Feshbach resonances from the

increased three-body loss.

The current in the coils is set by an external analogue control voltage provided to the servo boxes. We expect the current (and thus magnetic field) to be linearly proportional to the control voltage. We load a cloud of Cs at a PSD of ≈ 0.1 into the dimple trap and then hold in the trap for 500 ms. The magnetic field is switched to different values during this hold time, and we measure the atom number after the hold. We are able to identify the various Feshbach resonances of Cs from the dips in atom number at the resonances as shown in Fig. 5.1. The magnetic field can then be calibrated against the control voltage using a linear fit shown in Fig. 5.1 - the values of the magnetic field quoted in the thesis arise from this calibration. The jump coil was calibrated similarly.

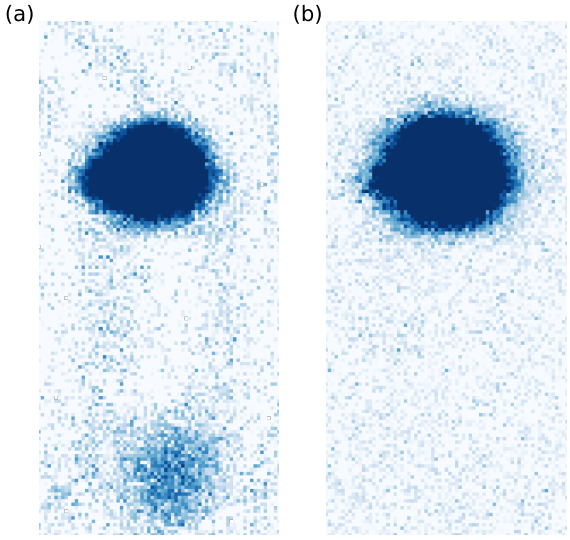

Figure 5.2: (a) An image of Cs in the sequence after producing and dissociating Cs Feshbach molecules. The large cloud on top is the main Cs atom cloud, while the lower smaller cloud shows the dissociated Cs Feshbach molecules. (b) shows the same sequence without dissociation - with the Feshbach molecule cloud no longer visible

Next, as a test of our ability to control the magnetic field ramps, we associate Cs_2 Feshbach molecules from a cloud of Cs atoms by ramping the magnetic field over the 19.9 G Feshbach resonance, followed by dissociation by rapidly ramping the field back over the Feshbach resonance as shown in Fig. 5.3. The jump coil was used for

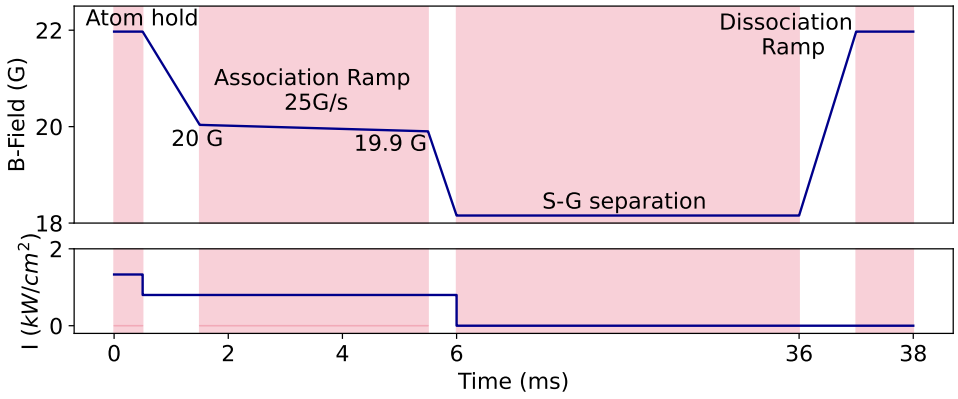

Figure 5.3: The sequence used to associate Cs_2 Feshbach molecules from a Cs atomic cloud. The atoms and molecules are separated in a 30 ms Stern-Gerlach separation at 33 G/cm (levitation field for Cs atoms). The lower panel shows the peak intensity of the trap used.

these ramps over the bias coil (see Sec. 3.3.2). This makes it both more precise and less noisy, since it operates at a larger current, where the servo performs better. The Cs_2 molecules have a magnetic moment of -0.9 μ_B, which corresponds to a levitation gradient of 52 G/cm compared to 31 G/cm for the Cs atoms [213]. Thus, the atoms and molecules can be separated with a Stern-Gerlach separation. After the Stern-Gerlach separation, the magnetic field is ramped up to dissociate the molecules, leaving two distinct atom clouds - one comprised of the dissociated molecules, and one comprised of the population that was always an atomic cloud. These are then imaged using absorption imaging. We confirm that the lower population is indeed from Feshbach molecules by taking an image without the dissociation ramp, where we do not see any signal of the second cloud as shown in Fig. 5.2. We are able to create $(1.2 \pm 0.2) \times 10^4$ Feshbach molecules[1] from a cloud of $(2.3 \pm 0.2) \times 10^5$ Cs atoms at a PSD of 0.39 ± 0.05.

[1]Note that the number of Feshbach molecules is half the number of atoms imaged in the cloud

5.2.2 Microwave spectroscopy and reduction of eddy currents

To gain an accurate measurement of the magnetic field on the atoms at different points in the sequence, we used the microwave transitions (See Sec. 3.4.2) in Cs to accurately determine the magnetic field at different points in the sequence as shown in Fig. 5.4[2]. We load Cs into an optical-dipole trap and then turn on both the jump and bias coils to reach a total magnetic field of 202.5 G. We hold the atoms in the dipole trap for a known time then apply a 100 μs microwave pulse, and fit a central frequency of the transition (from which we extract the magnetic field using the known energy level splitting). Here we drive the $|3,3\rangle$ to $|4,3\rangle$ π transition. The microwave transitions are around 300 kHz wide (corresponding to a magnetic field of $\approx$ 150 mG).

By scanning for the transition at different hold times after the magnetic field ramp, we are able to precisely trace the magnetic field as a function of time in the experiment. We find that after the current in the coils has finished ramping to its final set-point, there is still a significant drift in the magnetic field on the atoms - attributed to an eddy current. We fit this field to an equation of the form $B = B_0 - B_\mathrm{d}\ e^{-\frac{t}{\tau}}$, where B_0 is the field in the steady state, B_d gives the magnitude of the induced eddy field and τ the timescale of the exponential decay. On fitting, we get $B_0 = 202.66$ G, $B_d = 3.0$ G and $\tau = 7.2$ ms. This is a significant drift in magnetic field when compared to the 197.1 G Feshbach resonance width of 90 mG [115]. We diagnosed this as being due to a large eddy current in our experiment that was induced by the rapid change in magnetic field from 22 to $\approx$ 200 G.

A simulation using finite element analysis (on Ansys) was conducted to identify the main source of these eddy currents. The simulation included the portions of the stainless steel vacuum assembly apparatus close to the science cell, the in vacuum tungsten electrodes, the copper magnetic field coils, the aluminium mount for the objective lens, and the aluminium optical breadboards in closest proximity to the atoms. This predicted that the 'upper breadboard' had the most significant contribution to the overall field drift from the eddy currents. The upper breadboard

[2]The microwave setup was implemented after the calibration with the Cs Feshbach molecules. The values of field agree between the two after accounting for the eddy currents detailed here

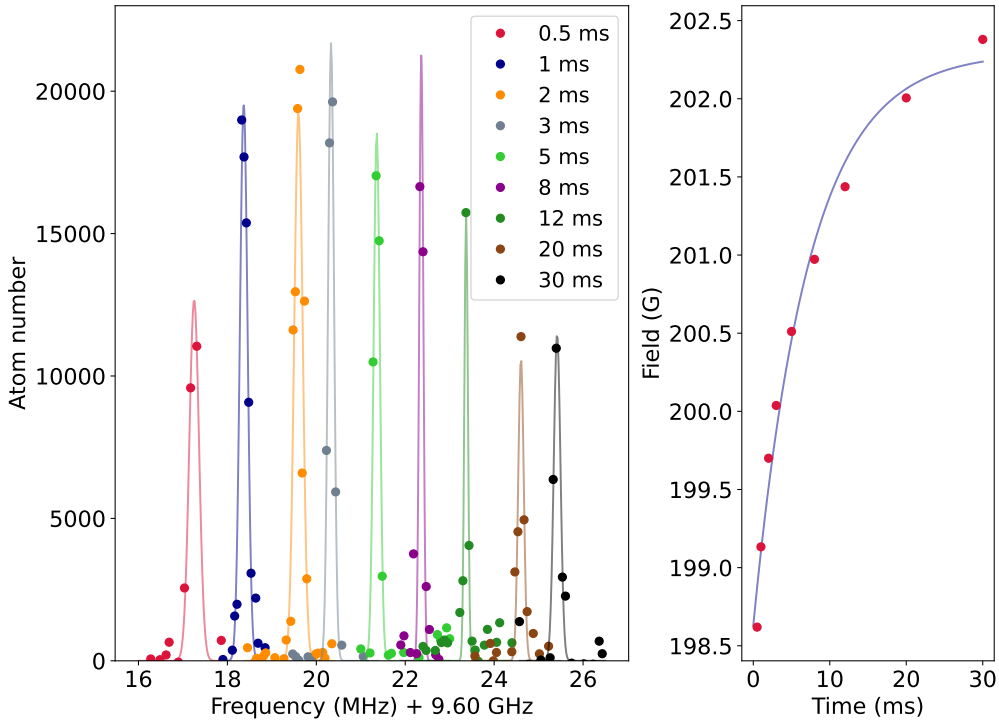

Figure 5.4: We scan the microwave field to identify the $|3,3\rangle$ to $|4,3\rangle$ π transition at different hold times after the magnetic field has ramped up to the 202.6 G setpoint from the 22 G setpoint. (a) shows the transitions moving with hold time after the field ramp as the field changes due to an eddy current. Each point here is a single shot. A Lorentzian is fit to each of the curves. From the centre of the Lorentzian, we can calculate the magnetic field at different times after the field has been ramped, as shown in (b).

is 575×525×20 mm optical breadboard located on top of the science cell, which we use to mount the vertical lattice optics. Initially, the breadboard was located 113 mm above the atoms (see Fig. 5.5).

We removed this breadboard and then repeated our earlier measurement of probing the magnetic field at different hold times after the field ramp, and find a significant reduction in the field drift. The amplitude of the field drift due to the eddy current has reduced to 0.8 ± 0.1 G with an exponential relaxation time (τ) of 9.0 ± 0.3 ms, almost a factor 4 reduction from before. This fits quantitatively with the predictions of our finite element analysis simulation, with qualitative differences in the shape of the decay curves being attributed to the simulation not being an exact

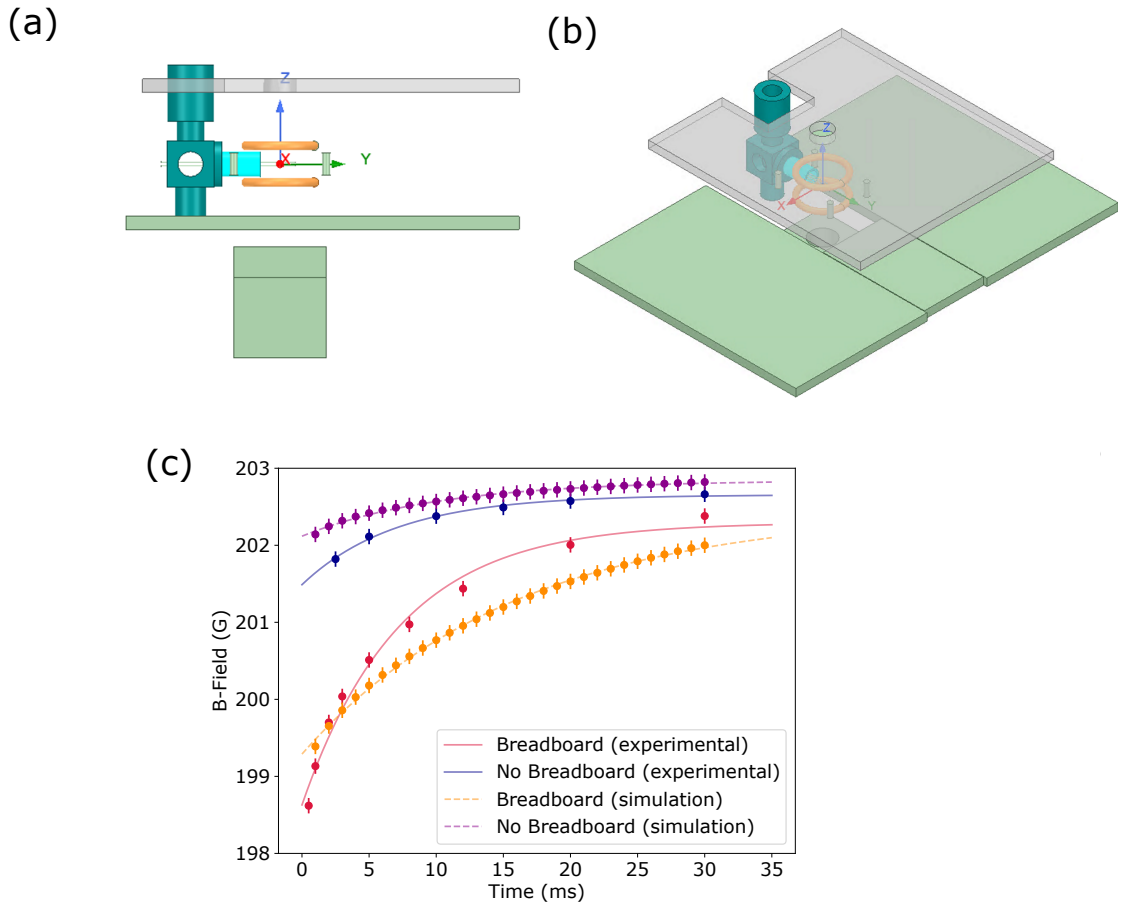

Figure 5.5: The reduction of eddy current after removing the upper breadboard. (a) and (b) show renderings of different views of the setup used to simulate effect of the eddy currents on the magnetic field at the atoms. (c) shows the measured eddy current with and without the breadboard as well as the simulated eddy currents with and without the breadboard. We find that the breadboard was in fact the main source of the eddy currents, and removing it reduced the field drift significantly.

recreation of the experimental setup. The majority of the remainder of the field drifts are predicted to be due to an eddy current induced in the mounting of our high NA objective lens. With this reduction on field drift, we proceed to associating Feshbach molecules. We reintroduced the upper breadboard with minimal effect on the current by cutting a slot in the breadboard to reduce the eddy currents and remounting it 263 mm above the atoms.

5.3 RbCs Feshbach molecules

5.3.1 Scanning for the Rb-Cs Feshbach resonance

The next step is to identify the Rb-Cs interspecies Feshbach resonances at 197.1 G and 181.6 G that we plan to use to associate and then change the state of our Feshbach molecules. In order to do this, we prepare a mixture of Rb and Cs in a dipole trap at PSD of 0.1 as detailed in Chapter 4. We are able to reliably prepare a mixture of 10^5 atoms of both species in a dipole trap. To identify the Feshbach resonances, we load the dipole trap with the mixture, then hold the mixture in the dipole trap at a set field for 300 ms before imaging both species. As shown in Fig. 5.6, we are able to identify Feshbach resonances at 181.6 $\pm$ 0.2 G and 197.1 $\pm$ 0.2 G, consistent with the previously observed values [115,214,215]. We note that while we initially load around 100,000 atoms of each species into the dipole trap, After they are held together for 300 ms, the atom number for both species drops significantly due to the large loss rates in a Rb-Cs mixture.

5.3.2 Associating RbCs Feshbach molecules

To associate the molecules and then separate the molecules from the atoms, we follow the experimental sequence described in Fig. 5.7. After merging the species, we hold in the dimple trap for 5 ms at 22 G before switching the field up to 202.5G, above the Feshbach resonance. We hold at this field set point for 4 ms to allow the field to stabilise and the eddy currents to dissipate enough to associate molecules. We then ramp the field to 198.1 G, just above the Feshbach resonance, using the jump coil, in 3 ms. The Feshbach association ramp is a 4 ms 1.2 G ramp across the Feshbach resonance. We now have a mixture of atoms and molecules in the $|-1(1,3)s(1,3)\rangle$ state. For maximum separation, we prepare the Feshbach molecules in the $|-6(2,4)d(2,4)\rangle$ low field seeking state by ramping the field down to 181.7 G, and perform a Stern-Gerlach separation experiment (a TOF in a field gradient). After the dissociation, we are able to image the two distinct clouds representing atoms and molecules separated vertically by the Stern-Gerlach experiment. We then proceed to optimise the sequence for the maximum Feshbach molecule number. It

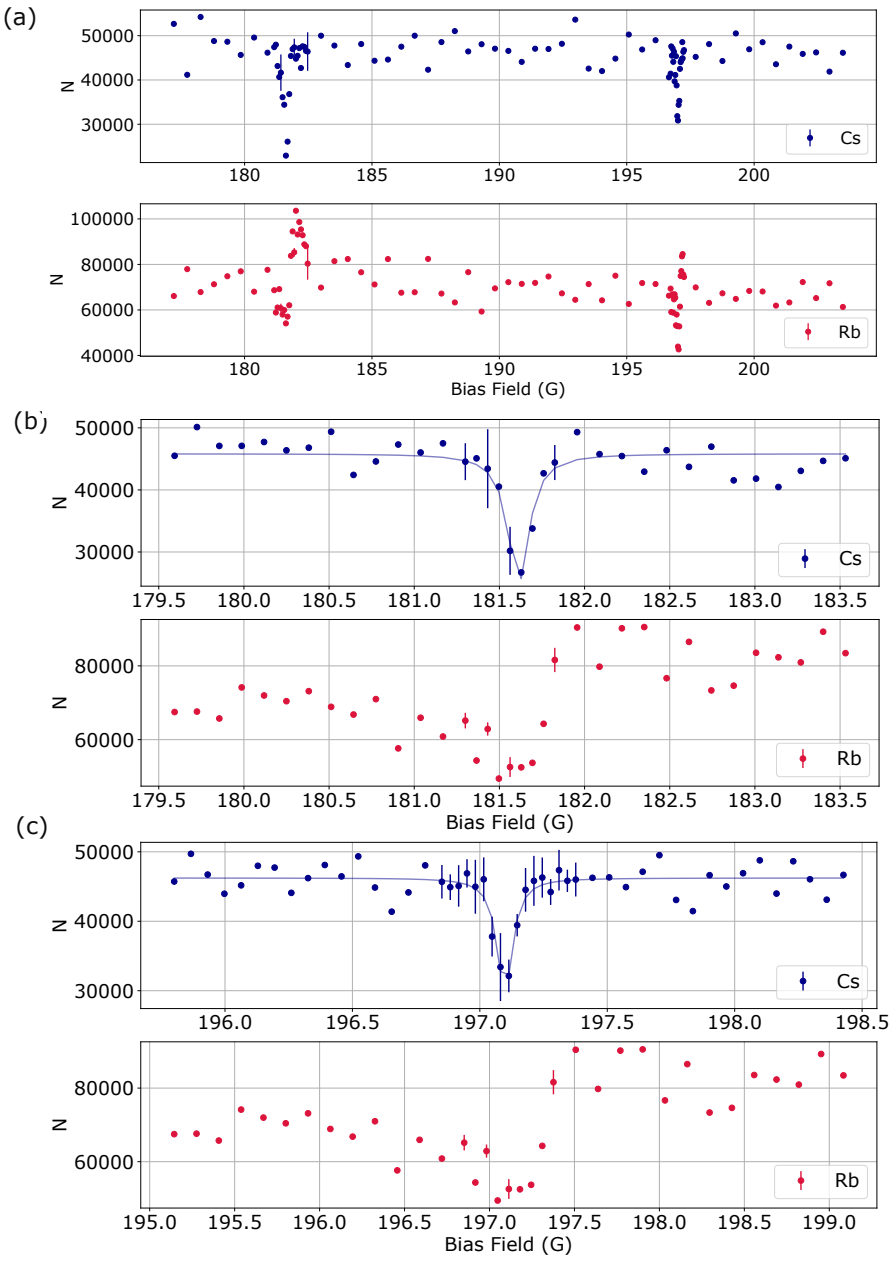

Figure 5.6: We scan the magnetic field during a 300 ms hold time where both species are held together in a dipole trap. We see loss in atom number at the Feshbach resonances. (a) shows a scan across the entire 26 G range accessible by the jump coil, with both Feshbach resonances accessible. (b) shows a scan of the the Feshbach resonance we find centred at 181.6 ± 0.2 G, while (c) shows the Feshbach resonance at 197.1 ± 0.2 G.The center positions are extracted from a Lorentzian fit to the Cs atom number, with the major source of uncertainty in field arising from the error in our calibration. It should be noted that the Cs atom number after this hold is significantly lower than the Rb atom number due to collisional loss.

should be noted that to achieve sufficient contrast to image the Feshbach molecules reliably, we must use the fringe removal algorithm detailed in Sec. 3.2.6[3]. Figure 5.8 shows some images of the atoms along with Feshbach molecules.

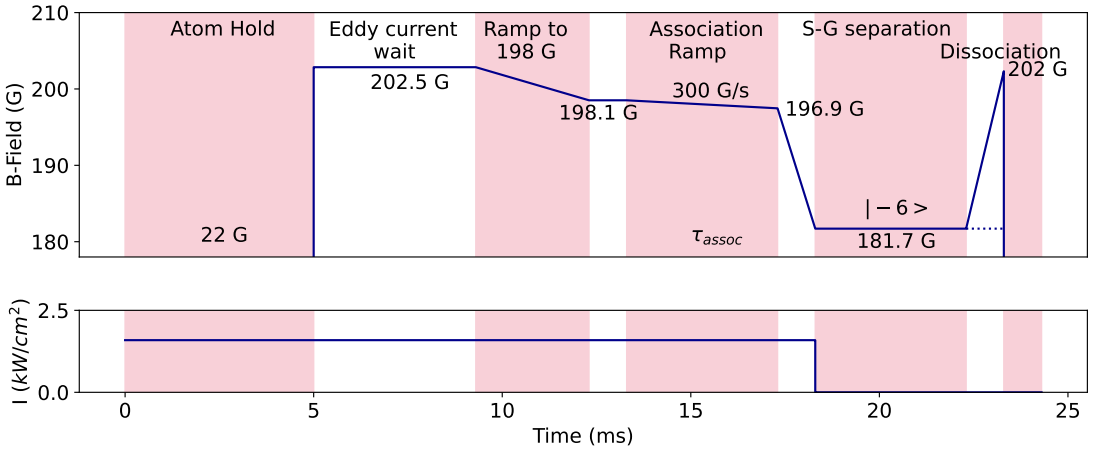

Figure 5.7: The sequence used to produce a cloud of RbCs Feshbach molecules. After merging the species at 22 G, we ramp the field up and scan over the Feshbach resonance at 197.1 G. The field is then ramped once again down to 181.7 G to put the molecules into the low field seeking $|-6\rangle$ state, where we perform Stern-Gerlach separation at 33 G/cm. The atoms are levitated while the molecules fall vertically giving us two separate clouds. The magnetic field is then ramped up to 202 to dissociate the molecules, allowing us to image the resultant atoms.

We optimise the Feshbach association ramp across the 197 G Feshbach resonance. The ramp time and the ramp endpoint both must be optimised here. For optimal Feshbach molecule production, we want to start above the resonance and ramp adiabatically over the Feshbach resonance. The ramp should cross the entire Feshbach resonance for optimal molecule production. In addition, the ramp time must balance the adiabaticity (faster ramps are less adiabatic leading to lower association efficiencies) with collisional loss (slower ramps offer more time for the molecules to collide with themselves and the atoms). Figure 5.9 shows the molecule number as a function of the magnetic field ramp endpoint for different ramp durations. We find a 1.2 G 200 G/s ramp over the resonance to be optimal, similar to [215].

It is also important to optimise for the loading and overlap of the two species in

[3]The fringes are often at a comparable OD to the atoms

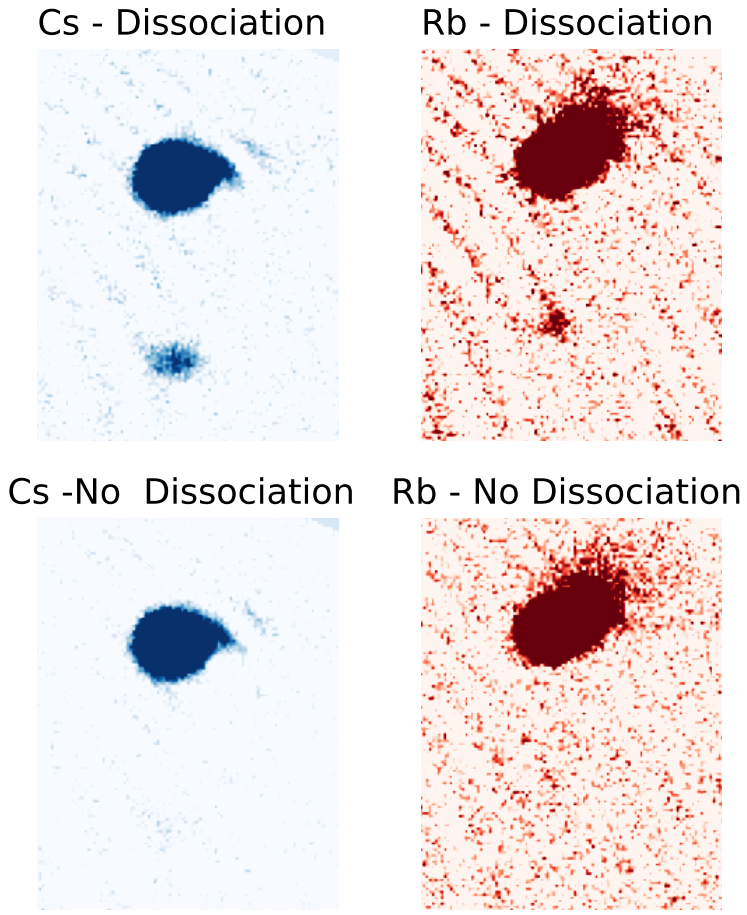

Figure 5.8: Images of Cs and Rb imaged in the sequence where molecules are associated and then allowed to fall (with the fringe removal used). We see that the large atom cloud for both species, and the smaller cloud of atoms that were dissociated from molecules. When the dissociation step is removed, we do not see this second cloud.

the dipole trap. In the sequence, the Rb atom cloud is moved back from its separated position 1 mm away to overlap with the Cs dimple. The movement trajectory is a 2 second long minimum jerk ramp. In the last 50 ms of the motion of the Rb dimple, we ramp the Rb dimple beam off linearly. This prevents the Rb dimple beam from perturbing the Cs atoms in the Cs dimple. We find that it is important to control the position at which the Rb ramps off. The Rb cloud needs to be close enough to the Cs dimple that the atoms are attracted into the Cs dimple, but not so close that the Cs cloud is perturbed by the Rb dimple beam. The movement of the beam is programmed into a ramp between two fixed points. Rather than alter the

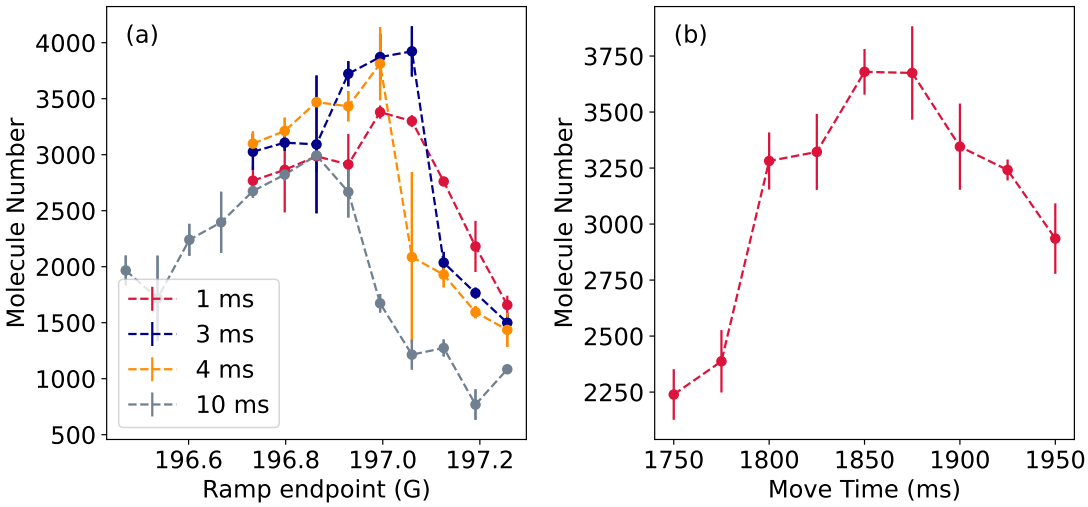

Figure 5.9: The optimisation of the sequence for production of Feshbach molecules. (a) shows the optimisation of the field ramp over the 197.1 G Feshbach resonance to produce molecules in the $|-1(1,3)s(1,3)\rangle$ state. We ramp the magnetic field from 198.0 G to different values and plot the molecule number as a function of the field ramp endpoint. As expected, the ramp is optimal when we have completely crossed the Feshbach resonance. The molecule number also depends on the field ramp time. (b) shows the Feshbach molecule number as a function of the move time, for a 3 ms ramp with 197.0 G endpoint before the dimple ramp off starts. This acts to overlap the atomic clouds well for the association step.

programming of the piezo adjuster, we find it experimentally easier to start turning the Rb dimple beam off partway through the movement of the beam. We optimise for the Feshbach molecule number as a function of the move time before the beam is ramped off as shown in Fig. 5.9. This can be considered as optimising for the position of the Rb atom cloud when Rb dimple is ramped off.

5.3.3 Purification of the Molecules

While it is easier to separate the atoms from the Feshbach molecules when the molecules are in the low field seeking $|-6(2,4)d(2,4)\rangle$ state, we can not trap the Feshbach molecules easily in this state. Our current coil setup is only able to provide a field gradient in one direction, so we are unable to levitate the molecules in the $|-6(2,4)d(2,4)\rangle$ state. We purify the Feshbach molecules by transferring them to the high field seeking $|-2(0,3)d(1,3)\rangle$ state, where they have a magnetic levitation

gradient of 44 G/cm, which differs from the atomic levitation gradient of ≈ 31G/cm for both Rb and Cs. Figure 5.10 shows the sequence used to purify the molecules in the dipole trap. After associating into the $|-1(1,3)s(1,3)\rangle$ state, we ramp the magnetic field down to 179 G, where the molecules are firmly in the $|-2(0,3)d(1,3)\rangle$ state. We then turn the magnetic field gradient up to 44 G/cm and lower the trap depth as shown in Fig. 5.10. We conduct a 18 ms Stern-Gerlach separation for

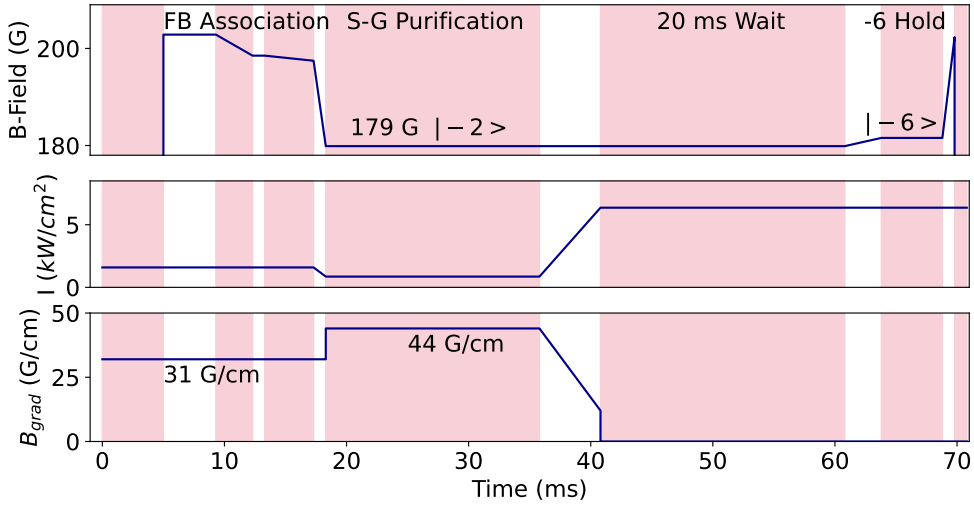

Figure 5.10: The sequence used to purify the Feshbach molecules, and achieve a cloud of Feshbach molecules in an optical trap. After producing the Feshbach molecules, we ramp the field to transfer the molecules to the $|-2\rangle$ state, where they have a levitation gradient of 44 G/cm, differing from the atomic levitation gradient of 31 G/cm. We then perform a Stern-Gerlach purification by ramping down the trap depth, and overlevitating the atoms out by switching the magnetic field gradient to 44 G/cm. We then have a 20 ms wait for the atoms to fall out of the field of view, before transferring the molecules to $|-6\rangle$ and dissociating.

purification, where the atoms are over-levitated out of the trap while the molecules remain trapped. We are able to separate the atoms from the molecules and end up with a sample of 2700 molecules (compared to 4000 Feshbach molecules produced). We attribute the lower molecule number to collisional losses of the molecules with the atoms and other molecules during the purification process. While we are unable to see any atoms left behind in the trap with absorption imaging, we later see that there are a few (≈10) atoms left behind when using the microscope later. Most of the work presented in the thesis was completed with this magnetic purification,

although we later employ a high-field blast beam to remove all the atoms as detailed in Sec. 7.2.2.

We are then able to turn the field gradient off and transfer the molecules into $|-6(2,4)d(2,4)\rangle$ while ramping the trap depth higher to keep the molecules trapped. We can measure the lifetime of the Feshbach molecules held in the trap in the $|-6(2,4)d(2,4)\rangle$ state as shown in Fig. 5.11. The loss of Feshbach molecules could occur from a combination of collisional losses with other molecules in the trap, and photo-excitation due to trapping photons from the 1064 nm trap [216]. Fitting to an exponential decay, we measure a lifetime of the molecules of 21 $\pm$ 4 ms with 1.3 kW/cm^2 of trapping light on the atoms and 17 $\pm$ 3 ms with 3.2 kW/cm^2 of light on the atoms, suggesting that the collisions are the dominant mechanism of loss in the trap. In any case, this lifetime is sufficiently large compared to the time required for STIRAP to the ground state (100 μs approximately).

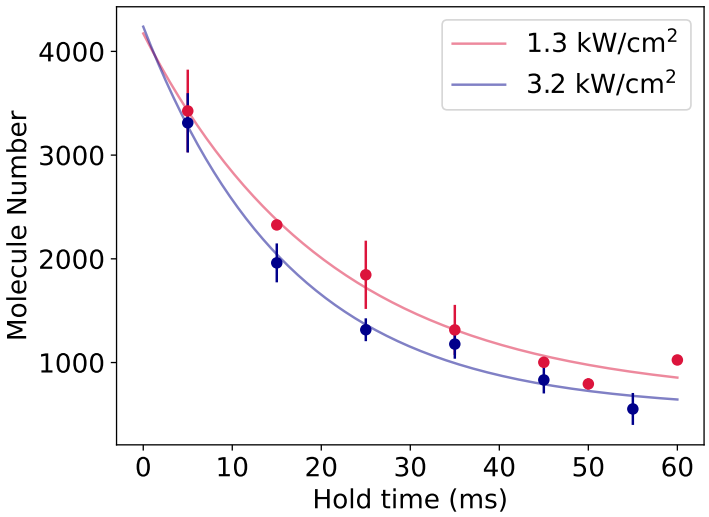

Figure 5.11: The lifetime of the Feshbach molecules measured for two different trapping intensities. After being purified and prepared in the $|-6\rangle$ state, the molecules are held in the trap for varying amounts of time before they are dissociated. We attribute the loss seen here predominantly to collisions with other molecules in the trap.

We next measure the magnetic moment of the Feshbach molecules, and confirm that we are in the correct state throughout the sequence. Once we have molecules trapped in the $|-2(0,3)d(1,3)\rangle$ state, we turn off the trap and switch the magnetic

field bias to different values with a constant field gradient of 44 G/cm. We then plot the vertical position of the molecule cloud as a function of the magnetic field. The molecule cloud undergoes ballistic motion with a given acceleration for about 2.6 ± 0.2 ms in total, before it is dissociated into an atom pair. The Cs we image undergoes further ballistic motion at a different acceleration for 2.3 ± 0.2 ms before being imaged. Fig 5.13 shows the position of the cloud as a function of the magnetic field during the free space time of flight of the Feshbach molecule. This agrees qualitatively with the calculated magnetic moment of the molecule at different fields [215]. It isn't straightforward to convert from a displacement to a magnetic moment due to variation in the magnetic moment with the field as it ramps over the resonance during the 1 ms dissociation ramp. We note that when substituting the earlier mentioned parameters into the ballistic equation of motion, assuming a constant molecular magnetic moment, and assuming that the magnetic moment switches from that of a molecule to an atom when the field crossed the Feshbach resonance, the peak 240 μm displacement of the molecules shown in Fig 5.13 at 181.8 ± 0.3 G corresponds the molecules having a magnetic moment of 1.4 ± 0.3 μ_B - consistent with the theoretical expectation of 1.5 μ_B when the molecules are in $|-6(2,4)d(2,4)\rangle$.

5.4 STIRAP overview

In order to have have long lived molecules with dipole-dipole interactions, we must transfer the Feshbach molecules to the ground state, using the STIRAP pathway detailed in [97]. More details of the STIRAP pathway and the process can be found in Sec. 2.3.2. One of the requirements for efficient STIRAP is a laser system with both pump (1557 nm) and Stokes (977 nm) narrow linewidth laser sources. The frequency of each laser should be stable and controllable to the 10 kHz level and have minimal noise across the frequency span (and particularly at the Rabi frequency of the STIRAP transition [142]). In the following sections, we detail the setup of a Pound-Drever-Hall (PDH) offset lock for the STIRAP lasers using an Ultra Low Expansion Cavity (ULE) Cavity - (Stable laser systems custom specification). Two similar setups [97, 217] have already been constructed in Durham, so we are able to

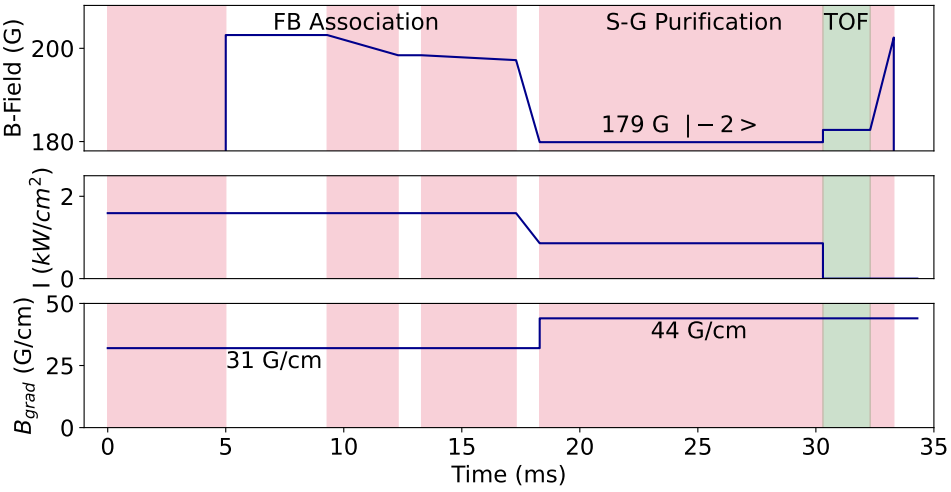

Figure 5.12: The sequence used to probe the magnetic moment of the Feshbach molecules at different magnetic fields. As before, we associate the molecules from the atomic mixture and then purify the sample to wind up with Feshbach molecules in an optical trap in $|-2(0,3)d(1,3)\rangle$. We then keep the gradient field at 44 G/cm (the levitation gradient for $|-2(0,3)d(1,3)\rangle$) and switch off the trap while switching the magnetic field to various values using the jump coil. The molecules have 2 ms of TOF in this field before we ramp up the magnetic field to 202 G to dissociate. We measure the vertical position of the atoms as a measure of their magnetic moment.

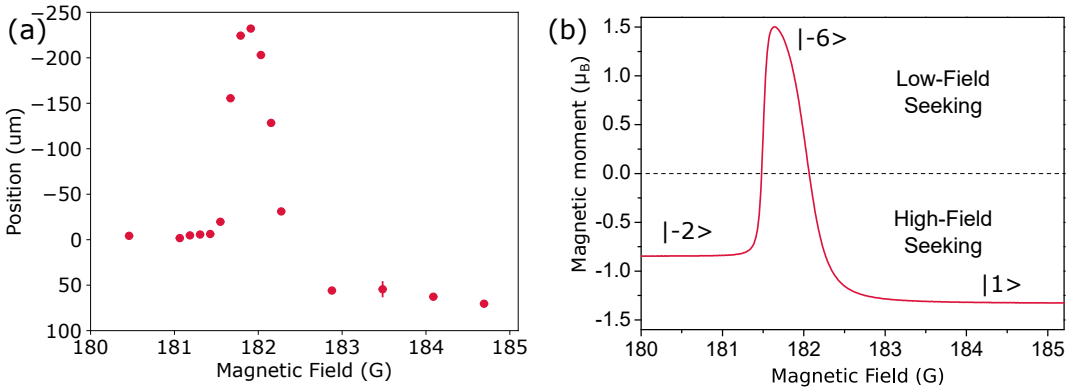

Figure 5.13: A measurement of the changing magnetic moment of the Feshbach molecules (a) the position of the Feshbach molecule cloud after a TOF at 44 G/cm displaced from the levitated position. The points are plotted with negative (downward) displacement on the positive y-axis to allow for visual comparison with the theory plot. (b) the predicted magnetic moment of the Feshbach molecules as a function of the magnetic field adapted from [215]

draw from the methods used in each of them, as well as utilising some of the light from those systems as a reference. We are able to lock the lasers to a linewidth of <1kHz and achieve efficient transfer to the rotovibrational ground state. The STIRAP efficiency is limited by the high frequency (1 MHz) phase noise on the beams as a result of the servo bumps from the PDH lock. We show that we are able to reduce this noise significantly using the feedfoward method, and further improve the STIRAP efficiency, now limited by the available power [144].

5.5 Setup of the STIRAP lasers

The optical setup used to lock both the STIRAP beams is presented in Fig. 5.14. It is based on the designs used in [163,218]. We use a diode laser (Toptica DL Pro) for both the pump and the Stokes beams. Both beams have an identical optical setup. After the output of the laser head, we use two cylindrical lenses to shape the beam to be circular. The beam is then split into two parts using a glass wedge (Thorlabs PS810). One of the reflections of the wedge (2% of the power) is coupled into a fibre Electro-Optic Modulator (EOM) and used for locking. The remainder of the beam is used for the STIRAP in the experiment. STIRAP requires pulse amplitude shaping - so fast control of the intensity of the beams. The beams are For this, we use two AOMs (ISOMET M-1205-0.6), coupling the beams to the first order of the AOMs (80 MHz), and controlling the power out of the AOMs by controlling the RF power in. After the AOMs, the beams are coupled into fibres which transfer the light to the main experimental table. We can programme arbitrary power ramps into the AOM using a DDS, and use $\cos^4$ intensity ramps for both the beams. The pulse shape is not extremely critical as long as the mixing angle varies adiabatically. The effect of different ramp shapes is discussed in [219]. Additional lenses are used in the path to shape the beam to maximise coupling through the AOM and the optical fibres.

The remainder of the beam is coupled into an AOM. We perform the amplitude shaping of both the pump and the Stokes beams by varying the RF power into the AOM. We program $\cos^4$ intensity ramps into the AOM using the DDS board. We

utilise the 1^{st} order of the AOM (80 MHz) for the STIRAP, coupling it into a fibre that goes to the experiment. We use some lenses in order to shape the beam for optimal coupling into the AOM and the fibre collimators.

The light that is coupled into the EOM is used for the PDH lock. After the necessary sidebands are added onto the beam with the EOM, the resultant beam is coupled into the cavity, with care taken to make sure that it is the TEM_{00} mode that is maximised. The Ultra-Low Expansion (ULE) cavity we use is coated for both our STIRAP wavelengths, so we can use a dichroic to overlap the beams and couple both the Stokes and pump beams into the same cavity. The reflection of the cavity is aligned onto a photodiode[4], with a fast enough frequency response to be able to resolve the PDH sidebands. This reflection is used for the PDH lock.

5.6 The PDH Lock

We use the Pound-Drever-Hall (PDH) locking scheme to lock both the lasers to the ULE cavity [220]. The ULE cavity works by reflecting light at all frequencies other than those resonant with one of the cavity modes, which occur in multiples of the Free Spectral Range (FSR) - $\nu_{FSR} = c/2L$ - specified to be 1.5 GHz for the cavity. Light at those frequencies is transmitted through the cavity. The sharp reflectance dip around the cavity modes is used to lock the lasers. For the PDH lock, the beam is phase modulated prior to the cavity using an EOM at a frequency ν_{mod}, which adds sidebands to the reflection (and transmission) signal. The reflected signal from the cavity is measured using a fast photodiode (Thorlabs PDA015C2). The signal from the photodiode is mixed with the a signal in phase with the modulation signal to produce a PDH error signal. The laser can be locked to this error signal using a PID control loop. The quality of the lock is set by the slope of the error signal, which depends on the linewidth of the cavity ν_{cavity}, often quantified using the cavity finesse $\mathcal{F} = \nu_{\text{FSR}}/\nu_{cavity}$. The stability also depends on the cavity stability - particularly the length of the cavity. This is why we use a ULE cavity stabilised to the minimum expansion temperature.

[4]PDA05CF2 - Thorlabs. 150 MHz Bandwidth

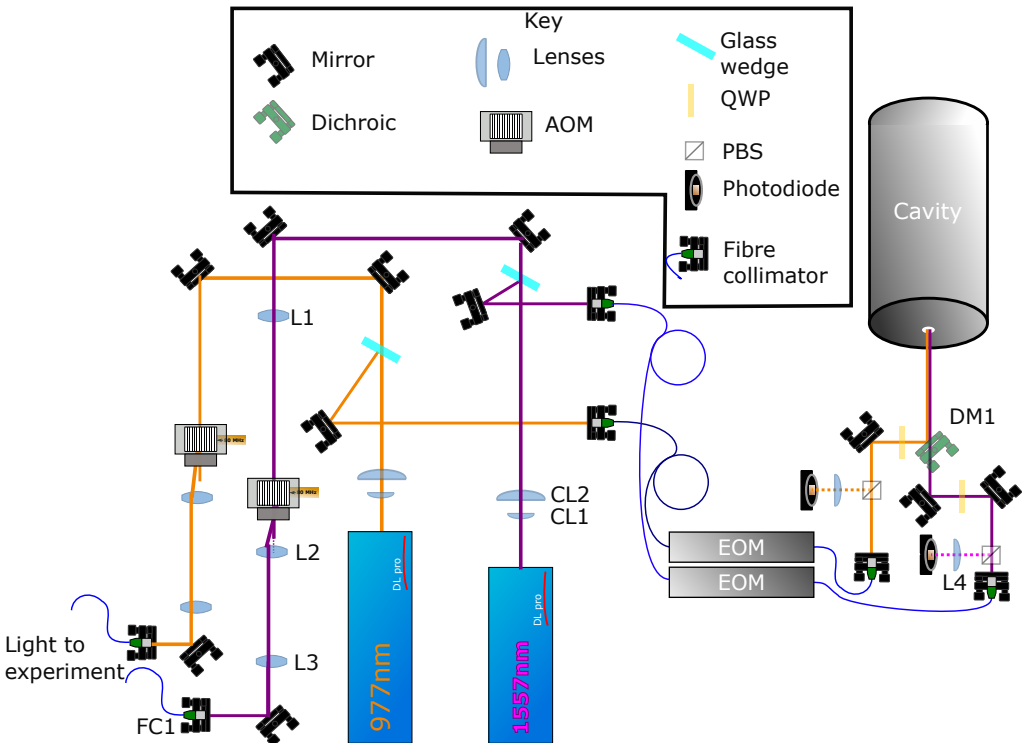

Figure 5.14: The optical setup of the STIRAP lasers. A small portion of the the pump and the Stokes beams, picked off using a blank, is used to lock the lasers to the same ULE cavity using an offset PDH lock as described in the text. The majority of the power is sent to the experiment through an AOM (used for pulse shaping) and a fibre.

The cavity provides a very stable set of frequency references, however the reflectance peaks are at set frequency points and cannot be tuned or controlled. We would like to lock the STIRAP laser to an arbitrary frequency setpoint, so must employ an offset PDH lock as detailed in [221]. The offset lock is performed by applying an additional modulation to the light into the cavity using the EOM. This additional offset modulation frequency ν_{offset} can be an arbitrary frequency - often significantly larger than ν_{mod}. As a result of this modulation, we have two additional PDH features at $\pm\ \nu_{\text{offset}}$ from the carrier, which we can lock to instead.

The schematic of the PDH locking system we use is shown in Fig. 5.15. We use a Toptica Fast Analog Controller Pro (FALC Pro) module to realise the PDH lock. An RF combiner (Minicircuits ZAPD-2-252-S+) combines two RF frequencies

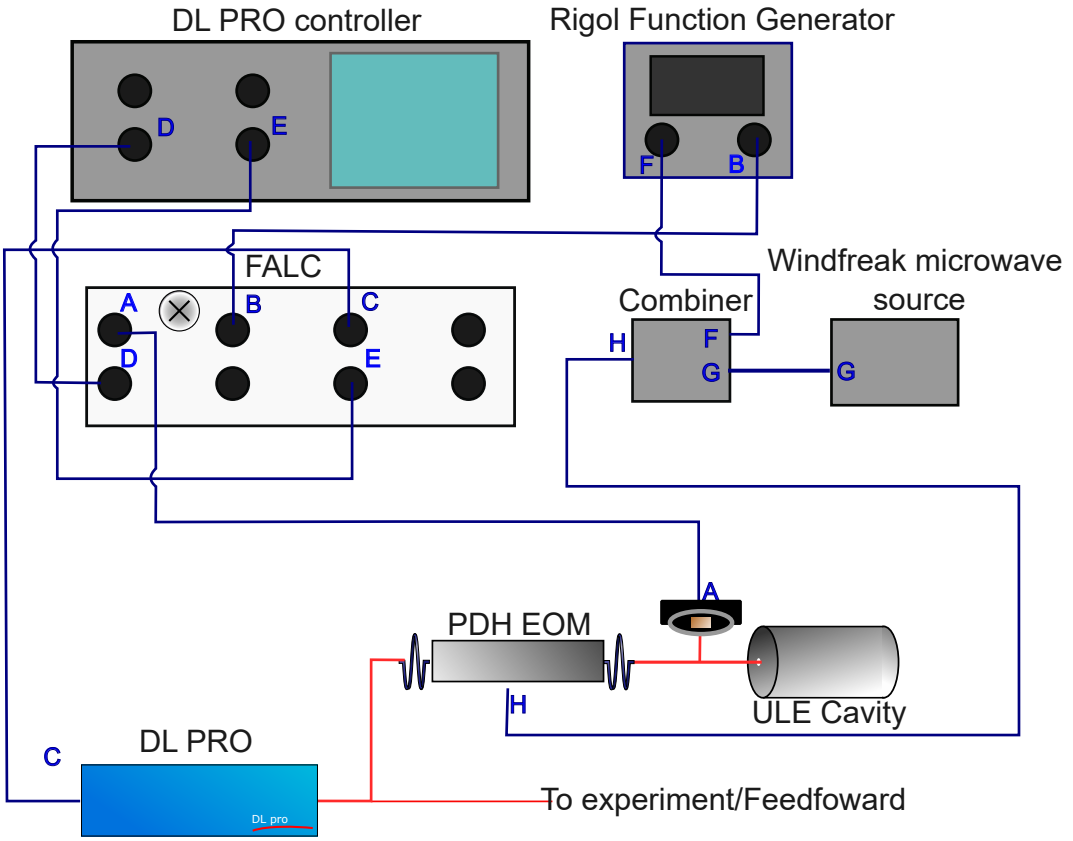

Figure 5.15: The setup of the PDH locking for the STIRAP lasers (shown here for one laser). The EOM is modulated with a RF frequency from both Rigol function generator (ν_{mod}) and the Windfreak (ν_{offset}). The reflection off the cavity is measured using a photodiode, which is sent to the FALC, where it is demodulated with a signal in phase with ν_{mod} to generate the PDH signal to lock with. The error signal is output by the FALC (channel E) and can be used to check the performance of the lock. The letters show the connections used in the figure. A - PD signal. B- Modulation signal. C - Laser input. D - Unlimited Gain input. E - Error signal Monitor. F -PDH Modulation input. G - Offset modulation. H Combined Modulation

(ν_{mod} and ν_{offset} used for the PDH offset lock. We use a Rigol arbitrary function generator for ν_{mod} and a Windfreak SynthHD for ν_{offset}. The modulation signal and photodiode signal are fed into the FALC, which has an internal mixer, and is able to output the PDH error signal. The locking is done using the PID controls inbuilt to the FALC, controlled using the Toptica TOPAS GUI.

5.6.1 Coupling the beam through the cavity

The first step in setting up a PDH lock is to couple the beams to the cavity, aligned with the TEM_{00} mode. For ease, we set up a photodiode to measure the transmission of the cavity, and couple the beam into the cavity. We ensure that the beam is coupled to the 0^{th} order in two ways. The 0^{th} order has only one transmission peak (TEM_{00}), while the higher orders have multiple transmission peaks visible close together (e.g TEM_{01} and TEM_{10} for the 1^{st} order). The TEM_{00} is also Gaussian shaped, and can be easily identified using a camera (for the 977 nm beam). The cavity is aligned to give the maximum ratio between the heights of the TEM_{00} and other modes. In addition, for optimal coupling, the curvature of the beam wavefront and focal position must be matched to the concave mirror inside the cavity. A pair of lenses on a cage mount after the fibre is used to set the beam to the correct waist size and position. Full details of this can be found in [222]. We are able to align the cavity to have a ratio of 140 between the 0^{th} and the first order peaks for the Stokes laser and 80 for the pump laser.

5.6.2 Optimising the PDH signal

For an optimal PDH lock, the strength of the RF driving signals need to be set as follows. The power in the n^{th} order sideband (P_n) is proportional to the Bessel function [223],

$$P_n \propto |J_n(\beta)|^2,$$

where β is the modulation depth of the EOM. The modulation depth is a characteristic of the specific EOM and the driving frequency used. We measure the modulation depth (β) of the EOMs at both the Rigol PDH sideband frequency ($\approx$ 20 MHz) and the offset frequency ($\approx$ 400 MHz) for both EOMs. Figure 5.16 shows a fit of the ratio between the power in the carrier and 1^{st} order sideband $|J_1(\beta)/J_0(\beta)|^2$ for different RF voltages from the Rigol (for the PDH modulation) at 16 MHz for the 977 nm EOM. Figure 5.16 (c) shows the same for different RF powers from the Windfreak (for the offset lock). Using this, we are able to calculate the optimal RF

power setpoints. The optimal setpoint for the PDH lock modulation (V_{mod}) is where the cross product of the first sideband and carrier is maximised ($|J_1(\beta)J_0(\beta)|$), which happens at $\beta = 1.081$. The optimal power setpoint for the PDH offset (P_{offset}) is where there is maximum power in the relevant 1$^{\text{st}}$ order sideband[5], so $|J_1(\beta)|^2$ is maximised at $\beta = 1.84$. The 1557 nm PDH was setup in a similar fashion. A list of all relevant frequencies and RF powers can be found in Table 5.1.

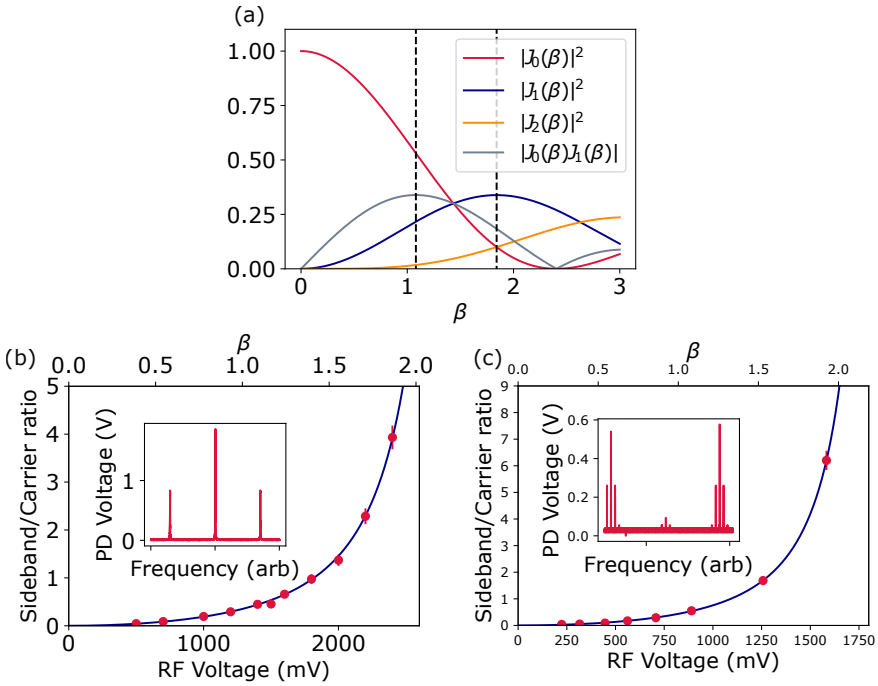

Figure 5.16: The power in the carrier and the various sidebands of a EOM is given by a Bessel function, plotted in (a). We measure the modulation depth by measuring the transmission of the cavity while scanning the laser frequency and fitting to the Bessel function. (b) shows the ratio of power in the first sideband to carrier for the 977 nm beam, as a function of the RF driving voltage at an RF frequency of 22 MHz used for the PDH error signal. The modulation depth here is found by the fit to be $\beta = 1$ at 1.3 V, and RF power is set to $\beta = 1.081$. The inset shows a sample trace of these peaks. A similar characterisation is performed as shown in (c), driving the EOM at 400 MHz with the Windfreak microwave source. The modulation depth here is found to be $\beta = 1$ at 0.8 V, and the RF offset power is set to $\beta = 1.841$. The inset shows all the transmission peaks, with the three small peaks in the centre corresponding to the 0$^{\text{th}}$ order of the offset, and the larger peaks to the left and right the $\pm 1^{\text{st}}$ order peaks

[5] P_{offset} is set to maximise the order to which the laser is to be locked, and V_{mod} is set to maximise the sensitivity of the PDH locking at this (or any) lockpoint.

$\nu_{\text{mod}}^{\text{pump}}$	15.5 MHz
$\nu_{\text{offset}}^{\text{pump}}$	$\approx$ 176 MHz[6]
$\nu_{\text{mod}}^{\text{Stokes}}$	22.0 MHz
$\nu_{\text{offset}}^{\text{Stokes}}$	$\approx$ 490 MHz
$V_{\text{mod}}^{\text{pump}}$	2.1 V
$P_{\text{offset}}^{\text{pump}}$[7]	20.0 dBm[8]
$V_{\text{mod}}^{\text{Stokes}}$	4.1 V
$P_{\text{offset}}^{\text{Stokes}}$	16.4 dBm

Table 5.1: The list of powers and frequencies used for the offset PDH lock for both STIRAP lasers

5.6.3 Characterising the cavity

The ULE cavity was quoted to have a FSR of 1.5 GHz and a finesse of 30,000. The FSR of 1.5 GHz means that we expect to see a transmission peak every 1.5 GHz of laser frequency. We are able to verify this at the STIRAP wavelengths. We first lock the lasers to the central carrier mode - not the offset generated by the Windfreak. We then set P_{offset} so that $\approx$ 20% of the power is in the sideband set by the offset frequency. The transmission of the cavity is monitored using a photodiode, and plotted as a function of the offset frequency. As the frequency is set to be a FSR, the sideband coincides with the cavity mode adjacent to that of the carrier, and the transmission of the cavity increases as both the carrier and the sideband are transmitted. Figure. 5.17 shows a scan of the offset frequency for both the 977 nm and the 1557 nm laser. From this we are able to extract the cavity specifications at 977 nm (1557 nm), namely the FSR of 1499.4249 $\pm$ 0.0003 MHz (1499.1383 $\pm$ 0.0014 MHz), cavity linewidths of 50.1 $\pm$ 0.7 kHz (50.9 $\pm$ 0.3 kHz) and Finesses of 29900 $\pm$400 (29500 $\pm$ 300). We note the small but statistically significant difference in cavity linewidths for the two wavelengths corresponds to a difference of 30 μm, likely the width of the wavelength dependent coating on the mirror.

[6]This frequency is the value used to lock to the STIRAP transition, and tells us how far away from the transition the cavity mode lies. There is a drift in this parameter over a few months as is discussed later

[7]The Windfreak power (used for the offset sideband) is set in dBm, while the Rigol (used for the PDH signal) is in volts. The values quoted here reflect that.

[8]The optimum for the pump laser would actually be 21.1 dBm, but the Windfreak has a maximum power of 20 dBm, which is sufficient to produce a good lock.

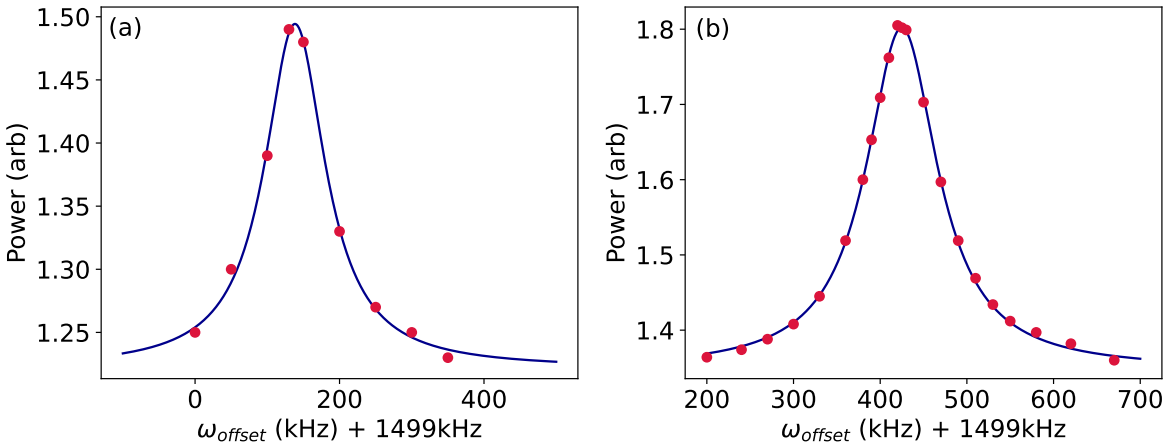

Figure 5.17: A measurement of the FSR and the linewidth of the ULE cavity at (a) 1557 nm and (b) 977 nm. The laser is locked to the cavity mode, and the Windfreak offset power is set such that around 20% of the power is in the first order sideband. The offset frequency ν_{offset} is then scanned. At the point where ν_{offset} is equal to one FSR of the cavity, we see transmission of the sideband through the cavity as it coincides with the next adjacent cavity mode to the one the laser is locked to.

5.6.4 Characterising the lock

With the PDH signal optimised, we now are able to lock the laser to a PDH sideband at an arbitrary frequency. The PID values of the lock are set using the TOPAS GUI, optimised for both a robust lock[9] and minimal high frequency noise from 'servo bumps'. The role of the high frequency noise in reducing the STIRAP efficiency has been discussed previously in Sec. 2.3.2. We measure the high frequency noise on the laser output using a self heterodyne beat note between the cavity transmission and the output of the laser. This can be measured by measuring the PDH error signal. The two beams are combined using a 2-to-1 fibre and focused onto a photodiode. The signal of the photodiode is analysed using a spectrum analyser. Figure. 5.30 shows the noise spectrum with the servo bumps of both the 977 nm and the 1557 nm laser when locked. We observe that the PID lock is stable over the course of a day, and can handle routine disturbances to the laser table.

We would like to characterise the linewidth and stability of our system. Previous

[9]The robustness of the lock was tested by generating a percussive perturbance on the table using a screwdriver in a gravitational potential

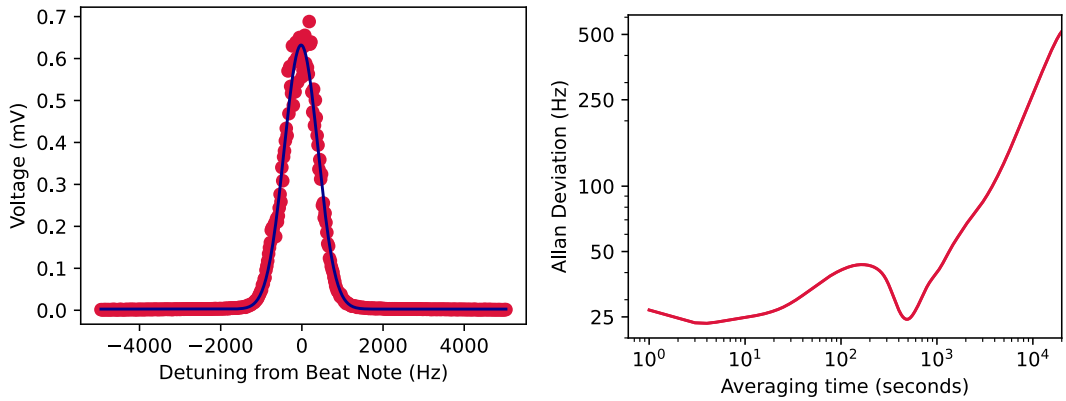

Figure 5.18: (a) A beat note between our locked Stokes laser and an identically locked laser in a neighbouring lab. The Gaussian width of the beat note is 832 ± 6 Hz, implying a linewidth of $832/\sqrt{2} \approx 600$ Hz for each laser. (b) the Allan deviation of the laser plotted with a 7 hour long measurement

work in other groups in Durham has characterised the performance of a similar offset lock system [163] in detail. There, a frequency comb and a delayed self-heterodyne beat were used to measure the long term stability and the linewidth respectively. We set up a heterodyne beat-note measurement between the our laser system and an identical setup used in another experiment in Durham [211]. We characterise the linewidth and the stability of the lasers with a heterodyne beat note measurement between the two systems. The linewidth measured is an upper limit on the linewidth of each individual locked laser - given that the linewidth of the beat note would be a convolution of the individual linewidths. Similarly, the frequency drift, measured over 7 hours using an Allan deviation measures the relative frequency drift between both beams.

We measure a linewidth of the beatnote of <1kHz and a drift of ≈ 500 Hz in frequency over 7 hours. The linewidth here is the fitted width of the beatnote, and the drift is the change in centre position of the beatnote. As we will later measure, the linewidth of the STIRAP transition is ≈ 200 kHz, significantly larger than the linewidth and the drift. We attribute the frequency drifts to changes in the lab environment - such as the external temperature effecting the cavity size. The peak at around 300 s and dip at 600 s in the Allan deviation corresponds to our known Air conditioning cycle time of 10 minutes (the temperature of the lab fluctuates

cyclically by approximately 1 degree). The larger deviation over the 7 hour time scale (from 5 pm to 12 am) likely originates from changes to the lab environment between when it is staffed and running compared to switched off. We conduct these measurements only for the 977 nm laser, and make the assumption that the performance of the 1557 nm laser lock is similar given that is has been locked in a similar manner[10].

5.7 Ground State RbCs molecules

5.7.1 Alignment of the beams

The optical setup to align the STIRAP beams onto the atoms is shown in Fig. 5.19. The pump and the Stokes beams emerge from fibres mounted on an optical cage system. A collimating lens for each beam (L1 f = 40 mm and L2 f = 25.3 mm) is also mounted on the cage on a 1-axis translation mount (Thorlabs - SM1ZA). The two beams are then combined on a dichroic (DM1 - Thorlabs DMLP1000) and then focused onto the atoms by a lens (L3 - Edmund optics f= 200 mm). The science cell is coated to be transmissive for the STIRAP wavelengths only at a 45° angle of incidence. The control of the separation between the fibre tip and the collimating lenses allows us to overlap both STIRAP beams axially, and ensure that the waist of both beams corresponds to the position of the atoms. The radial position of the beams is set by the mirrors M1 and M2, which are both mounted on a Kinematic mount with a differential adjuster (Thorlabs DM22). The pump (Stokes) beam has waist of 41 μm (38 μm) on the atoms, with a power of 8 mW (41 mW) on the atoms. For both the beams, the alignment (in the radial and axial directions) was initially conducted by trapping a Cs atom cloud in an xODT formed of the STIRAP beam and the guide dimple beam, and optimising for the atom number in the trap.

Next, we search for both the STIRAP transitions to lock the beams to. The frequency of the beams can be controlled precisely by the offset frequencies $\nu_{\text{offset}}^{\text{Stokes}}$

[10]The linewidth of the lock can be estimated from the gradient of the error signal slop, as was previously measured to be $\approx$ 1 kHz in the other setup. We find that the error signals for the pump and Stokes lasers are similar, so expect the locked linewidth to be similar.

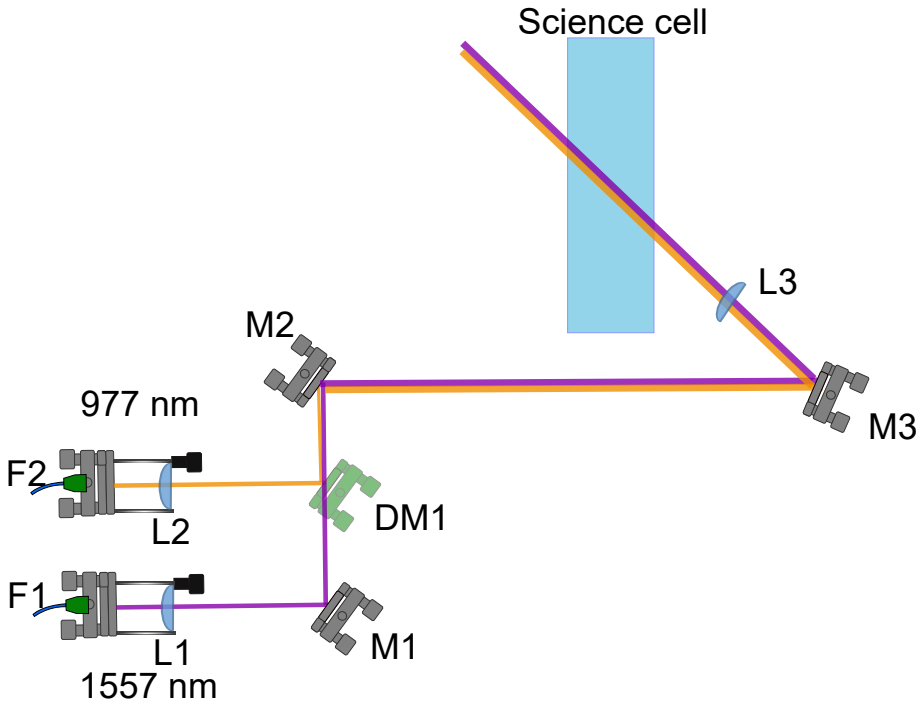

Figure 5.19: The optical setup of the STIRAP beams on the main experiment table. The beams both emerge from an optical fibre (F1 and F2) and are then collimated by a lens (L1 and L2). The waists of the beams after collimation is measured to be 4.6 mm for the Stokes and 7.4 mm for the pump. The beams are then combined on a dichroic (DM1) and steered onto the atoms with mirror (M3) through a focusing lens (L3).

and $\nu_{\text{offset}}^{\text{pump}}$ as detailed above. We find that the lock is robust to sudden changes in frequency of around 5 MHz. So, we are able to scan the frequency of the STIRAP beams in this range by changing ν_{offset} in between experimental runs, rather than changing the RF frequency of the AOM. We benefit from the previous work done in neighbouring labs, particularly from having access to light that is used for the same purpose and using the same wavemeter. This allows us to set up the offset lock very close to the transition with a beat note between the two before we conduct any experiments with the molecules. Slight changes to the transition frequencies are expected from the difference in magnetic fields during the STIRAP pulses in our experiments. We find that we are within 200 kHz of the STIRAP wavelengths used in the other lab (corresponding to around 200 mG in magnetic field).

It should be noted that for molecules in an optical trapping potential, the STIRAP transitions will be light-shifted by the trap itself. The Gaussian intensity profile of the dipole trap leads to a differential light-shift across the trap, affecting

the STIRAP efficiency. In order to avoid this, we conduct the scans for the STIRAP transitions and the STIRAP itself in free space. We switch the dipole trap off for the duration of STIRAP, and then pulse it on immediately after STIRAP. We are able to pulse the trap off for 600 μs at a time before we see any loss in molecule number.

Spectroscopy was first conducted on the pump beam as shown in Fig. 5.20 (a). When the pump beam is resonant with a transition from the Feshbach state $|F\rangle$ to an excited state $|E\rangle$, the molecules are transferred to the excited state, and then rapidly decay to other molecular states which we are unable to detect. After the Feshbach molecules are prepared in the trap, the pump beam is pulsed on using the AOM. For the initial measurements a pulse time of between 100 to 500 μs is used to easily identify the transition. Once the transition has been identified, and the fine adjustment of the beams is completed, we are able to use shorter pulse times of $\approx$ 1 μs , set by the Rabi frequency. At the correct frequency, we see a loss in molecules as the laser addresses the transition to the excited state. We note $\nu_{\text{offset}}^{\text{pump}} = 176.51 \pm 0.01$ MHz and a Lorentzian linewidth of 374 $\pm$ 19 kHz of the feature.

We then conduct two-photon spectroscopy to set the Stokes laser on the transition to the ground state of the molecule (Fig. 5.20 (b)). The Stokes power is set to the maximum available power of 40 mW, while the pump power is set to 100 μW and locked to the $|F\rangle$ to $|E\rangle$ transition. We then pulse both the pump and the Stokes beam on simultaneously for 300 μs, and scan the frequency of the Stokes beam by scanning $\omega_{\text{offset}}^{\text{Stokes}}$. With the Stokes light off resonance, we observe some loss in molecules as they are driven out by the resonant pump beam. When the Stokes beam is on resonance, and the Rabi frequency of the Stokes beam is significantly larger than that of the pump beam, the molecules are projected into a dark state (Sec. 2.3.2). These molecules are not lost to decays and return back to the Feshbach state when the STIRAP beams are turned off. So, when the Stokes laser is resonant to the $|E\rangle$ to ground state $|G\rangle$ transition, we do not see the loss in molecule number. We note parameters of $\omega_{\text{offset}}^{\text{Stokes}} = 490.7 \pm 0.6$ MHz and a Lorentzian linewidth of 2000 $\pm$ 200 kHz. The width of the two-photon spectroscopy feature is large when compared to the width of the STIRAP transition ($\approx$ 200 kHz when aligned). The

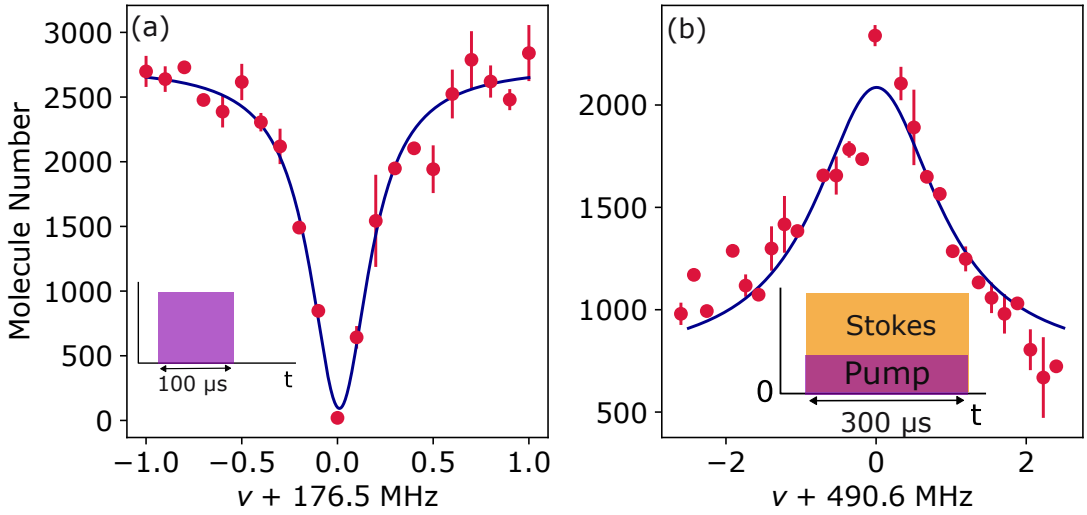

Figure 5.20: The initial scan to identify the STIRAP transitions in RbCs. (a) shows spectroscopy of the pump beam, where we see loss in the imaged molecule number when the beam is on resonance. We initially probe this with a long (compared to the Rabi frequency) 100 μs pulse of the pump (purple) light while varying the frequency. This allows us to find ν_{offset}, the offset frequency that we need to operate at to be locked onto transition. We note parameters of $\nu_{\text{offset}}^{\text{pump}} = 176.51 \pm 0.01$ MHz and a Lorentzian linewidth of 374 $\pm$ 19 kHz (b) shows the two-photon spectroscopy conducted to find the Stokes transition. With the pump beam locked to the transition, we reduce the power of the pump, and pulse both the pump and the Stokes beams on together for 300 μs . When the Stokes is on resonance with the $|E\rangle$ to ground state $|G\rangle$ transition, we see a peak in the molecule number. We note parameters of $\nu_{\text{offset}}^{\text{Stokes}} = 490.7 \pm 0.6$ MHz and a Lorentzian linewidth of 2.0 $\pm$ 0.2 MHz

uncertainty in centre frequency is relatively large (60 kHz) when compared to the width of the STIRAP feature. The two-photon spectroscopy signal thus mostly serves to give us an initial idea of where to set the Stokes frequency. A more accurate scan of the frequency is conducted using the STIRAP itself, as will be shown later[11].

With the beams all coarsely optimised here, we are able to attempt STIRAP with a $\cos^4$ pulse sequence of the pump and Stokes beams and see a signal of ground state RbCs molecules as shown in Fig. 5.21 (a). After the Feshbach molecules are trapped in the $|-6\rangle$ state, we pulse off the trap and pulse on the STIRAP beams in

[11]The STIRAP feature was only 30 kHz wide before the axial alignment of the beam was completed, and would have been tedious to find without the two-photon spectroscopy signal

a $\cos^4$ pulse shape. We must then transfer the molecules back to the Feshbach state for dissociation and imaging using a reversed STIRAP pulse. Figure 5.21 (c) shows the first signal of ∼1500 molecules imaged after a STIRAP round trip, from a trap of 2000 Feshbach molecules. Conducting the dissociation after only one-way STIRAP results in no signal being imaged as expected. The expected population in a given state is given by Eq. 2.3.2. Figure 5.21 (c) shows a measurement of the population in the Feshbach state at various points through the two-way STIRAP sequence, conducted by turning off both STIRAP beams partially through the sequence and then dissociating the molecules. The Feshbach molecules are dissociated to atoms and are imaged, while the ground state molecules are not imaged.

5.8 Optimisation of STIRAP

5.8.1 Rabi Frequency

For optimal STIRAP, the intensity of the STIRAP beams on the molecules should be maximised. We do this by measuring the Rabi frequency of transitions driven by both beams and perform the fine optimisation of the axial focal positions of the STIRAP beams. We find that the focal position is significantly different from what was optimised using the xODT method. We ascribe this to the optimal trapping parameters being different from the optimal alignment of the laser beam onto the atoms. When optimising for trapped atom number, the dipole trap has to balance the intensities of the beams and additionally is biased towards higher waists to increase the atom number that can be loaded into the trap. For STIRAP, we would like to maximise the intensity of the beams on the atoms, so want to minimise the beam size on the atoms.

We optimise the focal position of the beams by maximising the Rabi frequencies. For the pump beam, we use measure the Rabi frequency by measuring the molecule number after various pulse lengths of the pump beam on the Feshbach molecules. We adjust the position of the beam waist by adjusting the spacing between the fibre tip and the first lens. Figure 5.22 (a) shows the dependence of the pump Rabi frequency on the spacing between the lens and the collimator. For Stokes beam, the

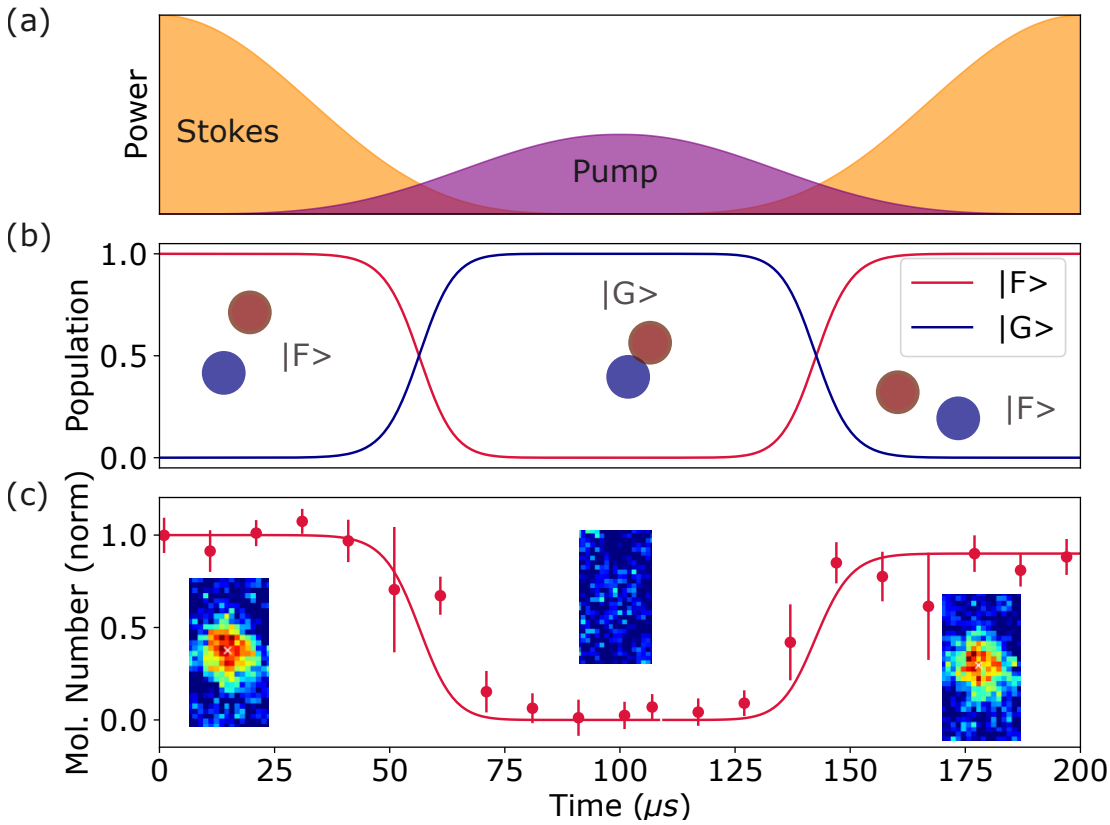

Figure 5.21: The STIRAP sequence. (a) Pulse sequence used for a two way STIRAP, where the Stokes and Pump beams are pulsed in a $\cos^4$ ramp. (b) shows the predicted population in the Feshbach state and ground state throughout the two way STIRAP sequence for a perfectly efficient STIRAP. (c) shows the measured atom from molecule number after dissociation at various points through the sequence. Only the Feshbach molecules are dissociated into atoms which are then imaged. Inset in (c) are images of the cloud before any STIRAP pulses, after one way STIRAP and after a return STIRAP.

optimisation is done in a similar manner. However, to measure the Rabi frequency, we must drive a transition out of the $|G\rangle$ state. So, we conduct a single STIRAP, transferring the molecules to the ground state, followed by a pulse of Stokes light. We perform a STIRAP pulse from $|G\rangle$ to $|F\rangle$ and then dissociate and image the molecules. The Rabi flop of the Stokes beam along with the microwave spectroscopy performed later (Sec. 7.1) are good indicators that we are indeed preparing ground state molecules.

The variation in intensity of the STIRAP beams along the cloud leads to a

dephasing effect due the variation of the Rabi frequency across the cloud. We follow the approach used in [139, 224] to fit the oscillation of molecule number (N) with time (t) to an equation of the form,

$$N = \frac{N_0}{2} e^{-\Gamma t/2} \left(1 + e^{-(t/t_d)^2} \cos(\Omega t)\right) + N_1,$$

where Γ is the excited state linewidth, t_d is the dephasing time due to the variation of Rabi frequency across the cloud, and N_1 is the number of molecules that are not addressed by the beam. Figure 5.22 (b) and (c) show Rabi flops on both the pump and the Stokes transitions respectively when the beams are aligned. We measure Rabi frequencies of $\Omega_{pump} = 374 \pm 17$ kHz and $\Omega_{Stokes} = 2150 \pm 40$ kHz.

We find that at the highest Rabi frequencies, the Rabi flops observed - particularly for the Stokes beam do not reach a minima of zero molecules. We are nevertheless able to remove all the Feshbach molecules with longer pulses (50 μs or more) and perform efficient STIRAP as is detailed below. We attribute this to the size of the STIRAP beam being comparable to the size of the cloud, so there is a significant variation of intensity of the beam across the cloud, and hence a dephasing phenomena where all the molecules in the cloud have spatially varying Rabi frequencies. The absorption imaging scheme doesn't allow us to resolve the spatial information of the molecular cloud, just the total molecule number. At larger beam waists obtained by adjusting the spacing between the fibre tip and the first lens, we observe a lower Rabi frequency, and greater of loss the molecules after a π pulse of the pump beam (see Fig 5.22 (d)). Future upgrades to the experiment to increase the available power in the STIRAP beams could provide an opportunity to redesign the system to have larger waists and address the whole cloud more uniformly without compromising much on the Rabi frequency.

5.8.2 Pulse Duration

The efficiency of STIRAP relates to the duration of the pulses, as discussed in Sec. 2.3.2. In order to optimise the STIRAP pulse time, we employ a sequence with two STIRAP pulses $|F\rangle$ to $|G\rangle$ and back, and then image the molecules for different

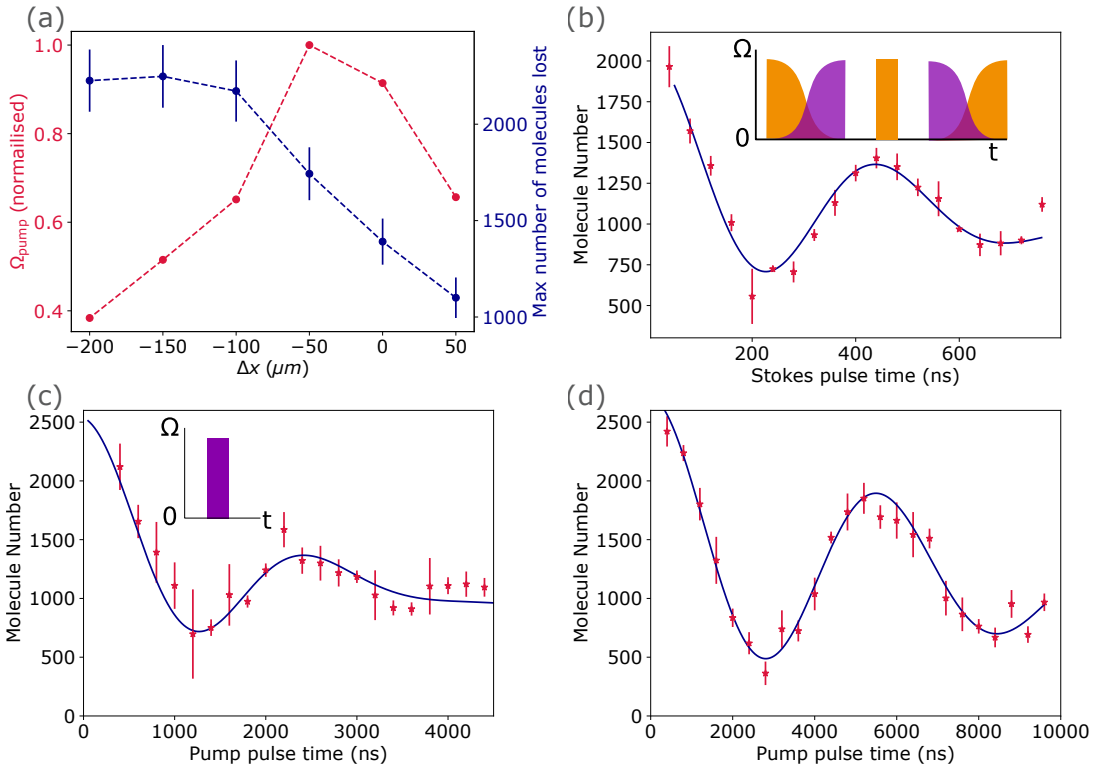

Figure 5.22: Measurement of the Rabi frequencies of the pump and the Stokes beams. (a) shows the dependence of the Rabi frequency, and the maximum number of molecules lost (the peak-to-peak amplitude of a Rabi oscillation) as a function of the spacing of the fibre and collimating lens. (b) and (c) show the Rabi flops on the Stokes and pump transitions respectively, at the highest measured Rabi frequencies. The inset plots represent the pump (purple) and Stokes (orange) beam pulse sequences during these measurements (d) demonstrates a Rabi flop at a lower Rabi frequency, with a bigger beam - showing a greater peak-to-peak oscillation amplitude.

pulse times. Figure 5.23 shows the variation of the imaged molecule number with the pulse time. We fit the efficiency η as a function of time (t) to an equation of the form,

$$\eta(t) = \exp\left(-\frac{\tau_{\text{adi}}}{t} - \frac{t}{\tau_{\text{deph}}}\right),$$

where τ_{adi} and τ_{deph} are the adiabatic and dephasing times respectively. The adiabatic time τ_{adi} is dependent on the Rabi frequency of the two STIRAP beams, and τ_{deph} predominantly on the frequency noise on the beams. We fit τ_{deph} of 900 $\pm$ 150 μs and τ_{adi} of 5.1 $\pm$ 0.4 μs from the data. This is consistent with the the

expectation that $\tau_{\text{adi}} = \pi^2\gamma/\Omega^2 = 4.6 \pm 0.4$ μs from our measurements of the Rabi frequencies of each beam. This implies an optimal pulse time ($t' = \sqrt{\tau_{\text{adi}} \times \tau_{\text{deph}}}$) of 67 ± 4 μs .

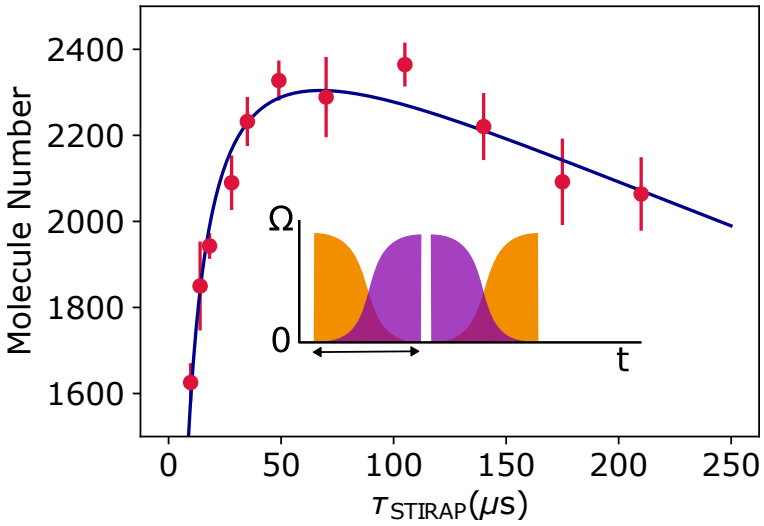

Figure 5.23: A measurement of the optimal pulse time τ_{STIRAP} of the STIRAP pulses. We vary the pulse time and measure the number of molecules after a round trip. Each data point is the average of 5 experimental runs. We then fit a curve of the form Eq. 5.8.2 to retrieve τ_{adi} and τ_{deph}.

With the other parameters optimised, we re-optimise the pump and Stokes frequencies to be on resonance. We are able to scan the pump beam at a pulse time of less than the π pulse time of the Rabi flop (so ≈ 1 μs). The Stokes beam is set on resonance by scanning the frequency while performing STIRAP. The number of molecules after a return STIRAP pulse is measured as a function of the frequency. Figure 5.24 shows such scans of the pump and the Stokes beams. We note a linewidth of 240 ± 17 kHz of the STIRAP feature when scanning the Stokes beam.

5.8.3 STIRAP efficiency

To measure the efficiency of the STIRAP, we perform multiple STIRAP sequences on the same atom cloud and measure the atom number as a function of the number of STIRAP pulses (N_{STIRAP}) as shown in Fig. 5.25. To image any molecules, the cloud has to be in the $|F\rangle$ state during the dissociation ramp, so the number of pulses

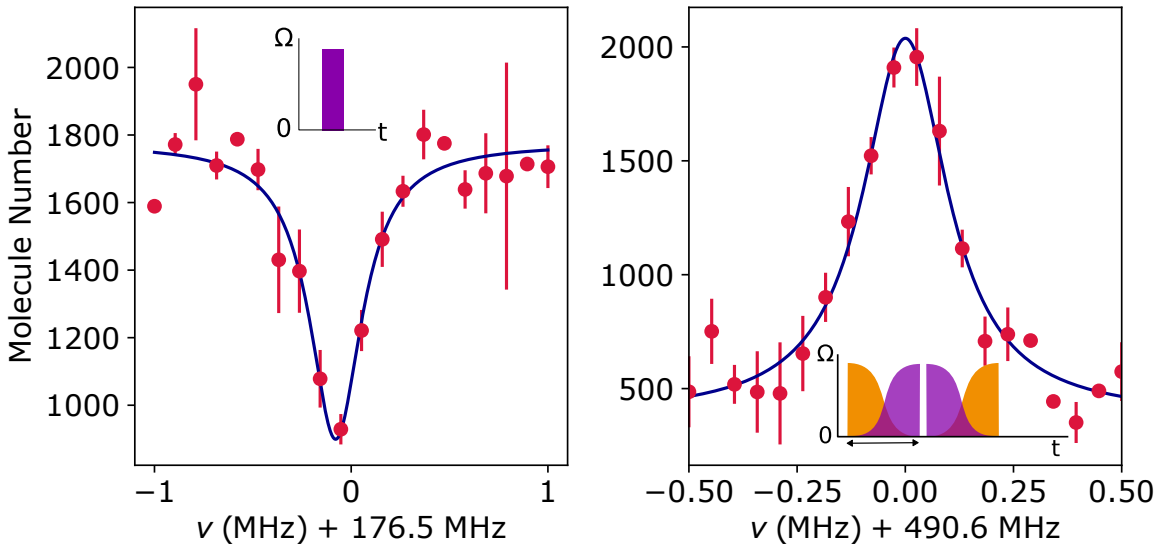

Figure 5.24: Scans of the pump and Stokes beams. (a) shows a scan of the pump beam, with a short pulse (less that a π pulse time) of 1 us around the central frequency ω_0^p. (b) shows a scan of the Stokes beam during a sequence with return STIRAP. We use this for the optimisation of the Stokes frequency to set it on resonance for STIRAP. The linewidth of 240 $\pm$ 17 kHz is significantly narrower than that of the two-photon spectroscopy

has to be even. For a pulse duration of 70 μs , we are able to have a maximum N_{STIRAP} of 8 (so 4 round trips) in free space, limited by the 600 μs we can leave the cloud in free space. For current purposes, $N_{\mathrm{STIRAP}} = 8$ is sufficient to measure the efficiency. If we choose to attempt this measurement with more STIRAP pulses (to perhaps measure efficiencies close to 99%), we could design a sequence where we alternate the STIRAP pulses with holds in the dipole trap to prevent the molecules from being lost. Here, we measure a STIRAP efficiency of 95.7 $\pm$ 0.2 % one-way, which means that we can successfully transfer and recover over 91% of the Feshbach molecules to the ground state.

5.8.4 Ground state molecule lifetime

We measure the lifetime of the molecules in the ground state in the dipole trap shown in Fig. 5.26. We assume that the lifetime of molecules is limited by loss due to two body inelastic 'sticky' collisions as detailed in [51]. We fit an exponential

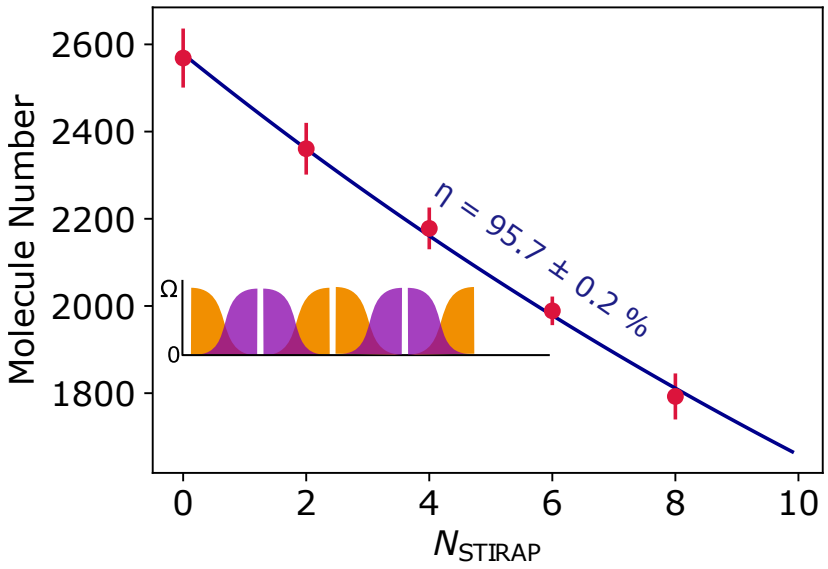

Figure 5.25: A measurement of the efficiency of STIRAP. We measure the efficiency by performing multiple STIRAP cycles (N_{STIRAP}) on a molecule cloud (represented in the inset), and measuring the number of molecules as a function of N_{STIRAP}. The molecule number plotted is the average of 5 experimental runs for each point. We measure a one-way STIRAP efficiency of 95.7 ± 0.2 %

decay to the molecule number, and measure a lifetime of 300 ± 20 ms of molecules in the dipole trap.

5.9 Optical feedforward

The work detailed in the rest of the chapter has been published in [144]. Some text and figures have been reproduced from the manuscript and the supplementary materials of the same

While the STIRAP efficiency is relatively insensitive to some experimental conditions like laser amplitude noise, it is inherently sensitive to laser phase noise as it relies on the adiabatic evolution of a dark state [140, 142], and requires narrow linewidth lasers. The path to improving STIRAP efficiencies involves the reduction of this phase noise. While we implement it to transfer associated molecules to the ground state, STIRAP is commonly used for quantum state transfer in many

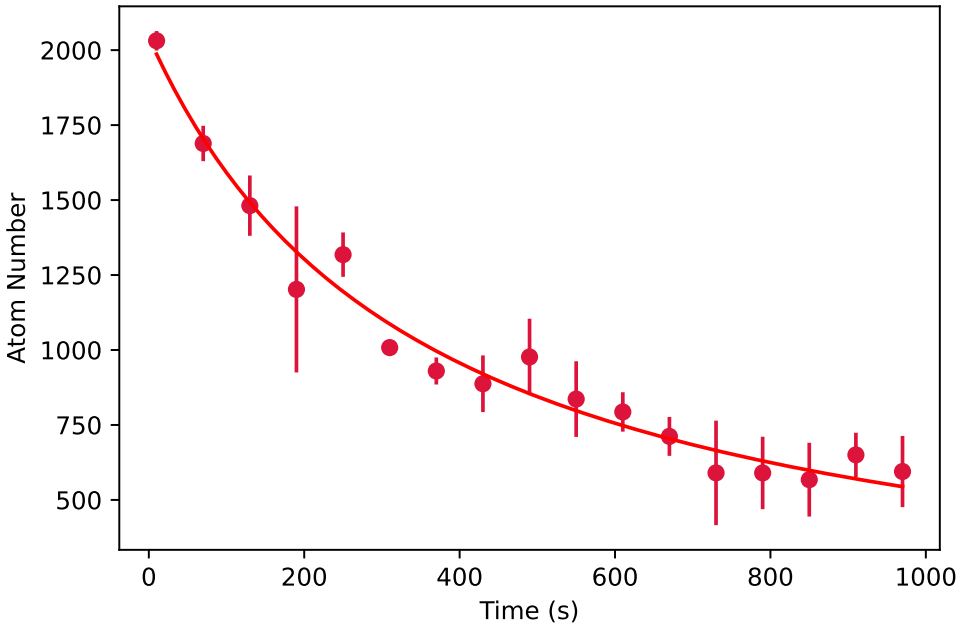

Figure 5.26: The lifetime of molecules in their ground state in the dipole trap. The main loss mechanism here is assumed to be two body loss from inelastic collisions. The fit in the figure is to a two-body loss function. We see a loss of approximately half the molecules in ≈ 300 ms. The decay timescale fits qualitatively with results seen in [51].

other experiments. Examples include experiments involving superconducting circuits [225], trapped ions [226], nitrogen-vacancy centres [227], optomechanical resonators [228], and optical waveguides [229].

The narrow linewidths required are often achieved by a stabilisation of the laser frequency to a stable reference, often using an active electronic stabilisation feedback loop. These feedback loops shift the low frequency phase noise to higher frequencies outside the bandwidth of the feedback loop. This leads to a significant amount of high frequency phase noise - often referred to as a *servo bump*. The servo bump is often at frequencies close to the Rabi frequency of the STIRAP. This often limits the STIRAP efficiency, as the STIRAP efficiency is most sensitive to noise at frequencies close to the Rabi frequency [142]. Some groups have filtered out this high frequency noise by passing the light through a second optical cavity [230–234]. This method while effective, leads to a large loss in optical power of the beam.

We instead opt for the method described in [235, 236], where the use of feedfor-

ward noise cancellation resulted in a reduction in high frequency phase noise without the use of a second cavity and without a significant loss in power. Even as we are unable to remove the high frequency phase noise with the feedback lock, we can measure the noise on the lock as shown in Fig. 5.30. The feedforward method relies on measuring the phase noise and correcting for it in real time by inserting the inverse of the measured noise onto the beam using an EOM[12]. Here, we show that the feedforward noise cancellation significantly reduces the magnitude of the phase noise at the servo bump, leading to improved STIRAP efficiencies, limited only by the available laser power.

This project was conducted in collaboration with another lab in Durham, where ultracold RbCs molecules are trapped in optical tweezers. This was done for two reasons - namely (i) the presence of fibre amplifiers in the other lab offering a higher Rabi frequency for the STIRAP and (ii) these experiments were conducted before we attempted STIRAP in our own lab. The STIRAP lasers used were present in the 'microscope lab', and the optical feedforward was done in the microscope lab. The narrow linewidth light with the phase noise reduced was fed into an optical fibre which carried it to the 'Tweezer lab'. The light was then fed into a fibre amplifier, before being used in for STIRAP. The STIRAP pathway used is identical to the one we have described earlier. Full details of the tweezer experiment can be found in [117, 211, 217, 237].

5.9.1 Setup of the feedfoward

The setup used for the noise reduction with feedforward is shown in Fig. 5.27. As before, the pump and Stokes lasers are locked to a cavity. Once locked, the error signal is split, with one component going to the PID loop for feedback, and the other being used for the optical feedforward. The error signal for feedforward is passed through a voltage controlled amplifier (VCA) in an inverting configuration (VCA810 Texas Instruments with a 3 dB bandwidth of 12 MHz). This signal then drives a fibre EOM[13] with the inverse of the noise profile. The VCA allows us to easily match

[12] A similar idea to noise cancelling headphones
[13] iXblue-NIR-MPX-LN-0.1 for the Stokes and iXblue-MPX-LN-0.1 for the pump

the magnitude of the noise for the feedforward. The light is passed through a 30 m delay fibre before it passes through the EOM. This is done to match the electronic delay of the error signal to that of the light to achieve optimal noise reduction at all frequencies [235]. Practically, it is difficult to adjust the exact size of an optical fibre, when compared to adjusting the size of an electronic cable, so we delay the light by some extra amount and match the delay using a delay line on the error signal. The EOM thus imprints the inverse of the phase noise profile onto the beam, cancelling it out. We are able to measure the noise spectrum of the laser using a self-heterodyne measurement, where we perform beat note measurement between the locked laser output after feedforward, and the transmission of the cavity. The low noise light is then fed into fibre amplifiers (Precilasers). The output of the fibre amplifiers is then coupled through an AOM, which is used for both amplitude control and frequency control. The pump and Stokes beams are then overlapped on a dichroic and used for STIRAP.

While previous demonstrations of this technique had used free space EOMs [235, 236], we elected to use a fibre EOM both for the comparatively low V_π, and for the overall ease of setup. We connect the delay fibre, the EOM the transfer fibre (to transfer the beam to the neighbouring lab) and the Fibre amplifiers using fibre mating sleeves, which is both convenient and offers high fibre coupling efficiencies. The magnitude of the phase noise is small relative to the peak intensity, so the applied modulation voltage to the EOM is actually quite small. For the feedforward to work effectively, the voltage response of the EOM should be uniform across the frequency span. The EOMs used are designed for near DC operation, and we observe a 15% change in V_π between 0 to 3 MHz modulation frequencies.

It is important to ascertain the electronic delay on the error signal in order to achieve optimal feedforward noise cancellation for all frequencies. To measure this delay time, we utilise a method described in [235]. When the delay time of the electronic error signal is not matched to the optical delay time, instead of broadband noise reduction, the noise reduction happens only at certain frequencies. The noise reduction here has peaks at the frequencies where the periodic noise undergoes an integer number of full cycles during the mismatched delay time. We use co-axial

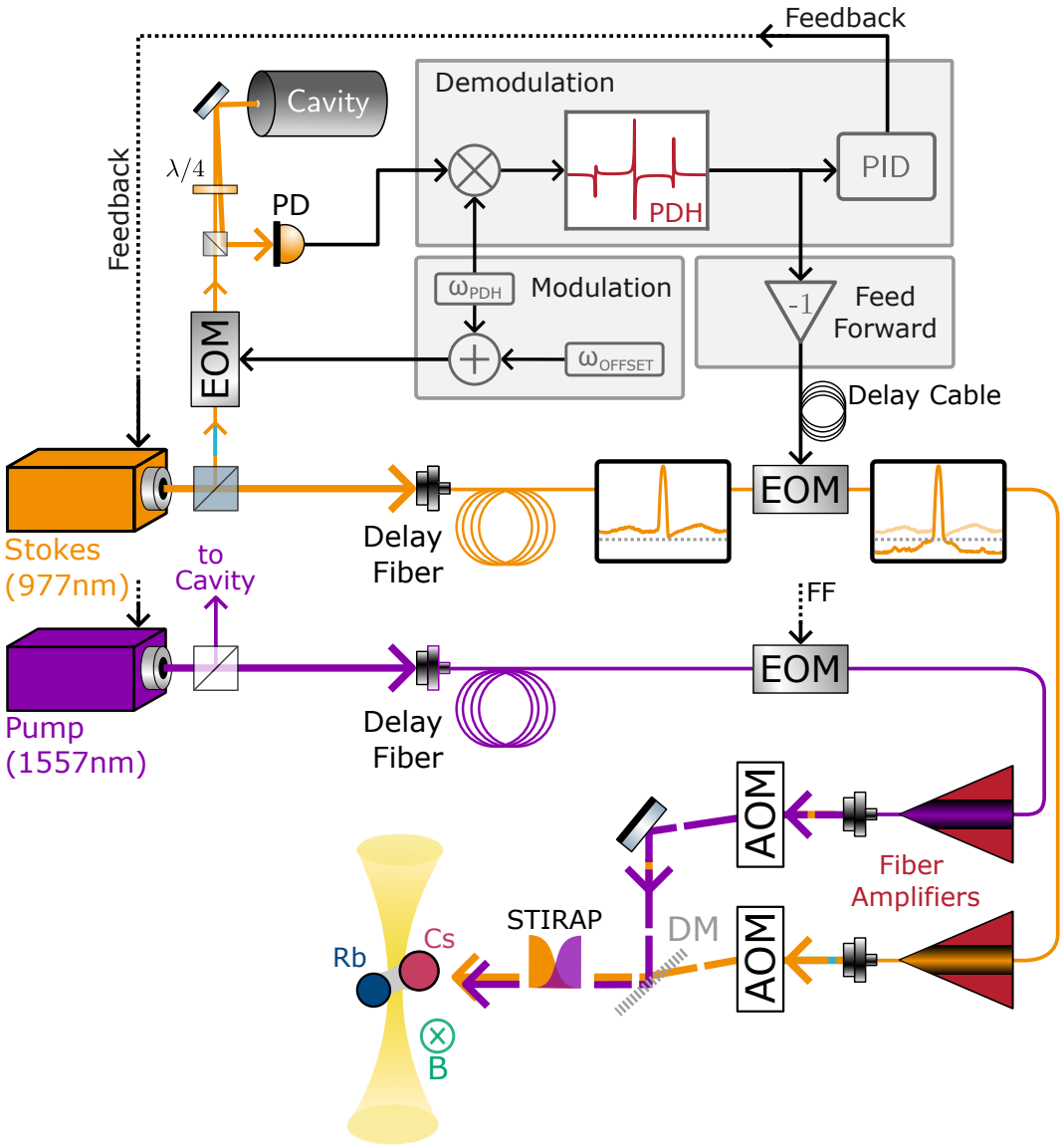

Figure 5.27: The setup of the optical feedforward in the experiment. The lasers are both locked to the ULE cavity as described earlier. The high frequency phase noise from this is fed into the AOM through an inverting amplifier. A delay fibre and a delay cable are used to match the optical and electronic delays. The beam is then passed through an EOm which applies the feedforward. We then amplify the power in both beams using Fibre amplifiers, before sending them to the experiment through an AOM. Figure reproduced from [144]

BNC cables of varying lengths to change the electronic delay time, and measure the frequency of the maximum noise cancellation. Figure 5.28 (a) shows the different noise cancellation peaks at different delay times, and (b) shows the position of the dip corresponding to the first cycle (2π as a function of the frequency. We are measuring reductions in the phase noise of a locked laser. Most of the noise we measure is in

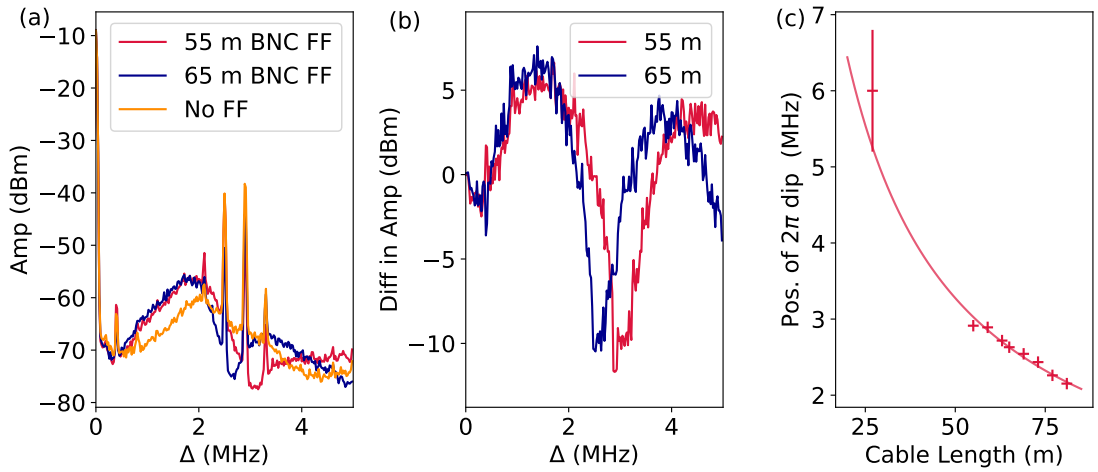

Figure 5.28: The measurements used to calculate the electronic delay on the error signal. (a) shows the noise spectra of the beat between the laser output and the cavity transmission without the feedforward, and with the feedforward for two different lengths of BNC cable. (b) shows the subtraction of the noise spectra of the FF signals from the signal without the FF. The peaks at $f_{2\pi}$ can be seen here (c) $f_{2\pi}$ as a function of the BNC cable length. We get $\tau_{elec} = 55 \pm 3$ ns

the 0.5 - 3 MHz range, so we choose BNC lengths where the 2π frequency ($f_{2\pi}$) corresponds to those frequencies. [14] We use the equation,

$$1/f_{2\pi} = 3L/2c + 1/\tau_{elec},$$

where $f_{2\pi}$ relates to the delay in the BNC cable 3L/2c (for a cable of length L, assuming the speed of the signal in the cable is 2c/3) and the intrinsic electronic delay time τ_{elec}. This gives us a delay time of 55 $\pm$ 3 ns, corresponding to a 11 $\pm$ 1 m optical delay fibre for no extra coaxial cable. We use a longer fibre however, and compensate for the extra optical delay with a longer co-axial cable for experimental practicality.

We measure the effectiveness of the FF noise cancellation using a self-heterodyne beat between the cavity transmission and the laser light out of the EOM. The two parameters of the setup that must be optimised are the BNC cable length and the

[14] It is difficult to take data at short cable lengths since there is very little noise to cancel at >5MHz. While we see significant noise in the 0.5 -2 kHz range, we were limited by the length of cable available.

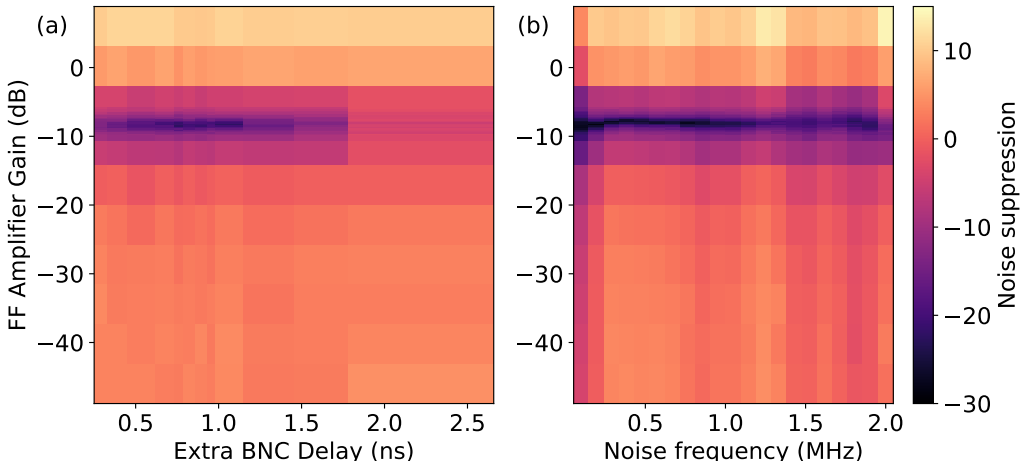

Figure 5.29: The optimisation of the parameters for the feedforward on the Stokes laser. Additional noise was injected into the system (detailed in the text), and the suppresion of that noise peak with the feedforward was measured while changing the setup parameters (a) show the suppression of an injected noise peak at 1 MHz as a function of the additional delay time (obtained by changing the length of the BNC co-axial cable) and the VGA gain. (b) is taken with the delay time set to 0.78 ns, and shows the the suppression of an injected noise peak as a function of the VGA gain and the frequency of the noise peak

VCA gain level. The feedback lock performs well enough that with the combination of feedback and feedforward, the laser noise quickly reduces to below the noise floor of the photodiode. So, we must introduce additional noise into the laser to properly characterise and optimise the feedforward performance. The Toptica lasers used allow us to inject noise into them after the feedback locking. This is done by introducing a sinusoidal modulation to the laser current at a given frequency. We then characterise the feedforward by scanning the VCA control voltage for different length of the BNC cable and measuring the suppression of the injected noise peak. Fig 5.29 (a) shows the noise suppression on the Stokes laser at 1 MHz as a function of VCA gain and the BNC length. We then set the BNC to the optimal length (4.2 m corresponding to a delay of 0.78 ns) and scan the VCA gain for different noise injection frequencies as shown in Fig 5.29 (b). The pump laser was optimised identically. The behaviour is as expected, with the level of noise suppression being relatively insensitive to the frequency of the noise. We note distinct peaks for the optimal BNC length and the VCA gain. The gain on the VCA must be tuned such

that the amplitude of the phase noise is matched by the amplitude of the feedforward. At too low gains, the phase noise is not suppressed, as the feedforward amplitude is far less than that of the noise signal. At overly large gains, the noise peak becomes larger with the feedforward on than with it off, as we start to overcompensate for the phase noise and inject extra noise into the laser. We note an optimal phase noise suppression of 29 dB.

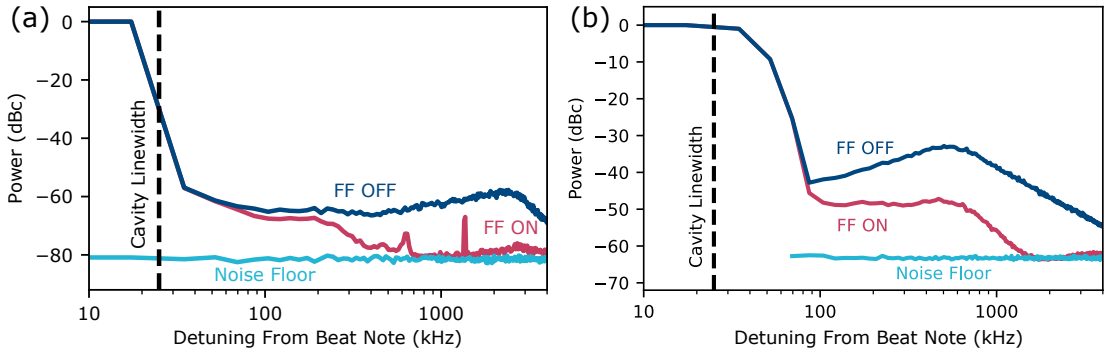

Figure 5.30: The performance of the feedforward using a self hetrodyne beat note measurement between the cavity transmission and the laser output. The noise power spectrum is shown for the (a) Stokes and (b) the pump laser, with and without the feedforward. The residual spikes in the spectra are attributed to noise pickup from neighbouring instruments. Figure adapted from [144]

Figure 5.30 (a) and (b) show self heterodyne beat measurements of the Stokes and pump beam respectively, with and without the feedforward. We see that we are able to reduce the magnitude of the servo bump for both lasers effectively, with a suppression of $\approx$ 20 dB. The light with noise suppression applied is then coupled into the fibre amplifiers and then to the main tweezer experiment for use in STIRAP.

5.10 STIRAP with Feedforward

The effect of the feedforward on STIRAP efficiency is investigated by performing STIRAP on an array of optical tweezers loaded with single RbCs molecules. Full details of the setup can be found in [117, 211, 217, 237]. Rb and Cs are loaded into species specific tweezers. The tweezers are imaged here to check for the presence of one atom of each species in the tweezer, and then the atoms are cooled to the

motional ground state. The tweezers are then merged, and the atoms are associated to Feshbach molecules, following a pathway similar to what we have discussed earlier. Errors in forming the molecule are measured by pulling out a Rb atom from the atom pair after attempting association. This atom is loaded into an error detection array. We then perform STIRAP on the Feshbach molecules to transfer them to the ground state. The ground state molecules are imaged by reversing the STIRAP and Feshbach association to leave an atom pair in the tweezer. The Cs and Rb atoms are then separated into different tweezers and imaged. Thus, we are able to distinguish between three cases (i) molecule formed and recovered, where the signal arrays of Rb and Cs both have an atom (ii) no molecule formed - where there is only an Rb atom in the error detection array (iii) molecule formed but not recovered - where there is no signal in any of the arrays. We are able to calculate a molecule recovery probability P_r as the probability of recovering a molecule given that it has been formed (or the probability of imaging Rb and Cs pairs when an atom is not imaged in the Rb error detection array). The probability P_r is effected by multiple factors, so to isolate the effect of STIRAP, we perform compare the effects of performing various numbers of STIRAPs on the same molecule before dissociation.

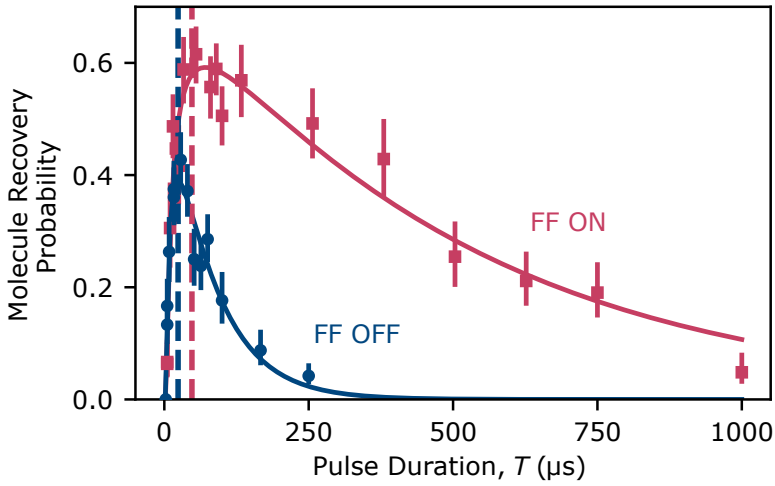

Figure 5.31: A measurement of the optimal pulse time for STIRAP with and without the optical feedforward. In both cases, the molecule recovery probability is measured for different pulse times, and τ_{adi} and τ_{deph} are obtained from a fit. We find a significant improvement in τ_{deph} when using the feedforward. Figure from [144].

We have 110 mW of pump light at a waist of 63 ± 3 μm and 272 mW of Stokes light at a waist of 72 ± 3 μm on the atoms. In a similar manner to that detailed earlier, we measure Rabi frequencies of $\Omega_{\text{Stokes}} = 1190 \pm 30$ kHz and $\Omega_{\text{pump}} = 1170 \pm 20$ kHz. As before, the intensity of the STIRAP pulses is modulated with an AOM before the fibre that couples the light into the experiment.

We then ascertain the optimal pulse time (T) for the STIRAP with and without the feedforward. We do this by measuring the molecule recovery probability as a function of the pulse time as shown in Fig. 5.31. For heightened contrast, P_r is measured after $N_{\text{STIRAP}} = 10$. The resultant data is fit to Eq. 5.8.2 to obtain τ_{adi} and τ_{deph} both with and without the feedforward. We measure τ_{adi} to be 1.0 ± 0.1 μs and τ_{deph} to be 0.73 ± 0.09 ms without the feedforward. With the feedforward, we measure τ_{adi} to be 0.9 ± 0.1 μs and τ_{deph} to be 5.0 ± 0.6 ms. As expected, the τ_{adi} is similar for both cases, being set by the Rabi frequency of the beams. We show that the feedforward greatly increases τ_{deph}, by nearly an order of magnitude - confirming that the phase noise was the major cause of dephasing. From this, we find optimal STIRAP pulse times of 23.85 μs (without feedforward) and 45 μs (with feedforward).

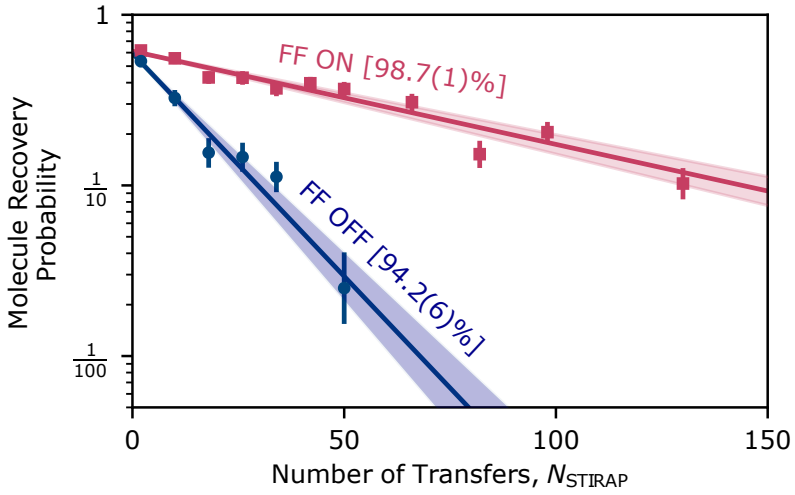

Figure 5.32: A measurement of the STIRAP efficiency with and without the feedforward implemented. The use of feedforward improves the STIRAP efficiency to 98.7 ±0.1%, a record high for RbCs. Figure adapted from [144].

We measure the STIRAP efficiency by performing STIRAP multiple times in

the same sequence at the optimal pulse time and measuring the molecule recovery probability as shown in Fig. 5.32 . The results are then analysed to determine the efficiency of STIRAP both with and without feedforward. We obtain STIRAP efficiencies of $\eta_{\mathrm{ON}} = 0.987 \pm 0.001$ and $\eta_{\mathrm{OFF}} = 0.942 \pm 0.006$ for STIRAP with and without the feedforward respectively. This shows a significant improvement in the efficiency. STIRAP efficiency is often the dominant error in detection of molecules, so this improvement is an important step in the control and use of molecules for quantum information science.

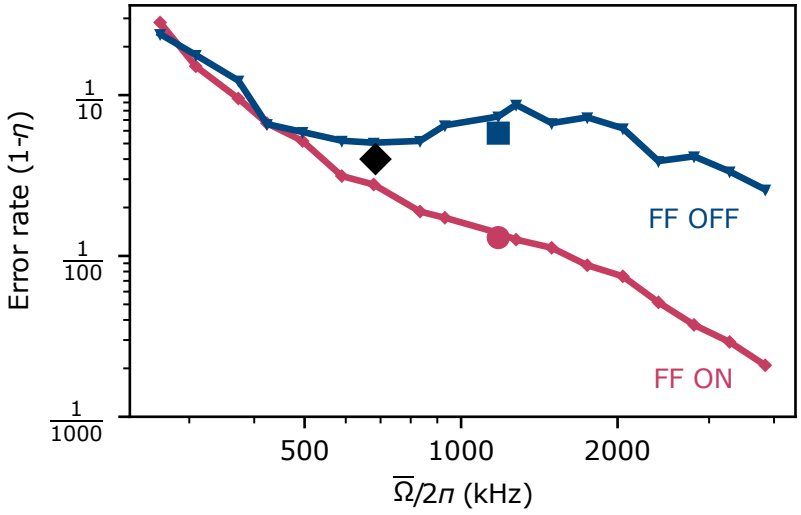

Figure 5.33: The modelled STIRAP efficiency for our system using the measured phase noise on the pump and Stokes lasers, with and without Feedforward. We find that the efficiency with feedforward is limited now by the Rabi frequency of the beams, and not the phase noise as it was without the feedforward. The black data point shows the previous peak STIRAP efficiency measured. The blue and crimson data points show the measurements without and with the feedforward implemented. Figure adapted from [144]

We would like to reduce the error even further as a high state transfer fidelity is crucial to many applications including high fidelity quantum simulation [238] and quantum information storage [239]. To better understand how we can improve the efficiency further, we conduct simulations on the STIRAP efficiency based on the 3-level model described in [141]. The model accounts for the major noise sources in our system. It takes in the phase noise on the lasers, obtained from the self-heterodyne beat note as shown earlier. It also accounts for low frequency noise

contributions, most significantly from the magnetic field drift and from the laser linewidth by including a randomised shot-to-shot two-photon detuning. Full details of the simulation can be found in [144] and Tom Hepworths upcoming thesis. We simulate the error rate of STIRAP $(1 - \eta)$ for different Rabi frequencies of the STIRAP beams.

Figure 5.33 shows the results of this simulation. As expected, we see that at low Rabi frequencies, the STIRAP efficiency is dominated by the magnetic field noise, and is similar with or without the feedforward. When the Rabi frequency increases towards the frequency of the servo bumps, we can see the reduction of efficiency without feedforward, with the efficiency showing the shape of the servo bumps. When the feedforward is employed, we see that the efficiency readily increases as a function of the Rabi frequencies. We simulate upto a Rabi frequency of 4 MHz, where the error rates area of order 10^{-3}. To implement this in the experiment would require a $\sim 20\times$ increase in intensity, which should be achievable by focusing the STIRAP beams down more and increasing the laser power further using an amplifier.

CHAPTER 6

Microscopy of Rb and Cs gases

The next step towards a molecular microscope is the realisation of an atomic microscope for both Rb and Cs. RbCs molecules can not be imaged directly due to the absence of a suitable cycling transition in the molecule. In order to image these molecules, we must split them apart as described in Chapter 4 and image the resultant atoms. While imaging of one species is enough to gain information, we aim to image both the atoms from a dissociated molecule.

In this chapter we present the setup and characterisation of our microscopy of both Rb and Cs in the experiment. We begin by introducing the optical lattice and the high resolution fluorescence imaging system, with the high NA objective. We detail the methods used to analyse the microscopy images to identify single atoms and the lattice parameters. We then proceed to the setup of the light sheet which allows us to image atoms in a single plane. We then discuss the optimisation and characterisation of the high resolution system for both Rb and Cs clouds. Finally, we demonstrate the ability to reconstruct the lattice occupancy from the fluorescence images.

6.1 The optical lattice setup

The optical setup for the 3D optical lattice is shown in Fig. 6.1. The horizontal (XY) lattice is originates from one of the Azurlight fibre amplifiers, and has four passes on the atoms in a bow-tie configuration used to generate the lattice potential. The vertical confinement and lattice potential for the Z (vertical) lattice is sourced from another Azurlight fibre amplifier (see Fig. 3.10). The resultant horizontal lattice has lattice sites spaced by 752 nm horizontally, oriented at 45 degrees to the incident angle of each of the 4 passes of the beam. The vertical lattice is reflected off of the objective lens itself, and has a lattice spacing of 532 nm.

We have redeveloped the horizontal lattice from the setup previously implemented in the lab and described in [148]. The horizontal lattice potential was previously made by two different perpendicular beams reflected back on each other. We have changed this setup to have a single beam reflected on itself in a bow-tie configuration as shown in Fig. 6.1 (a), with four total passes on the atoms. This offers some advantages. We have a more compact optical setup with a lower footprint on the optical table. There is also an increase in lattice depth per unit power - for a given beam waist, the current setup has a maximum intensity proportional to 16 times the power in the beam, a factor of two improvement a setup with two beams at the same power[1]. In addition, the lattice spacing is increased by a factor of $\sqrt{2}$, which makes resolving the atoms or molecules in the lattice easier as they are further apart from their nearest neighbour. However, the increase in lattice spacing does reduce the strength of dipolar interactions between adjacent molecules. In addition, we can now only control the horizontal lattice depth as a whole - rather than control the lattice depth in the two horizontal axes individually.

The light for the horizontal lattice originates from Fibre Amplifier 1. Full details of the origin of this beam and its orientation relative to other beams can be found in Fig. 3.6. It is coupled into a fibre after passing through an AOM, which is used to control the power of the beam. We are able to stabilise the beam power at low and

[1]With the bow-tie configuration, the maximum intensity for a given power (P_0) is proportional to $4^2 P_0 = 16 P_0$. For two separate lattice beams reflected on each other once, each with power (P_0), this is proportional to $(2 \times 2^2) P_0 = 8 P_0$

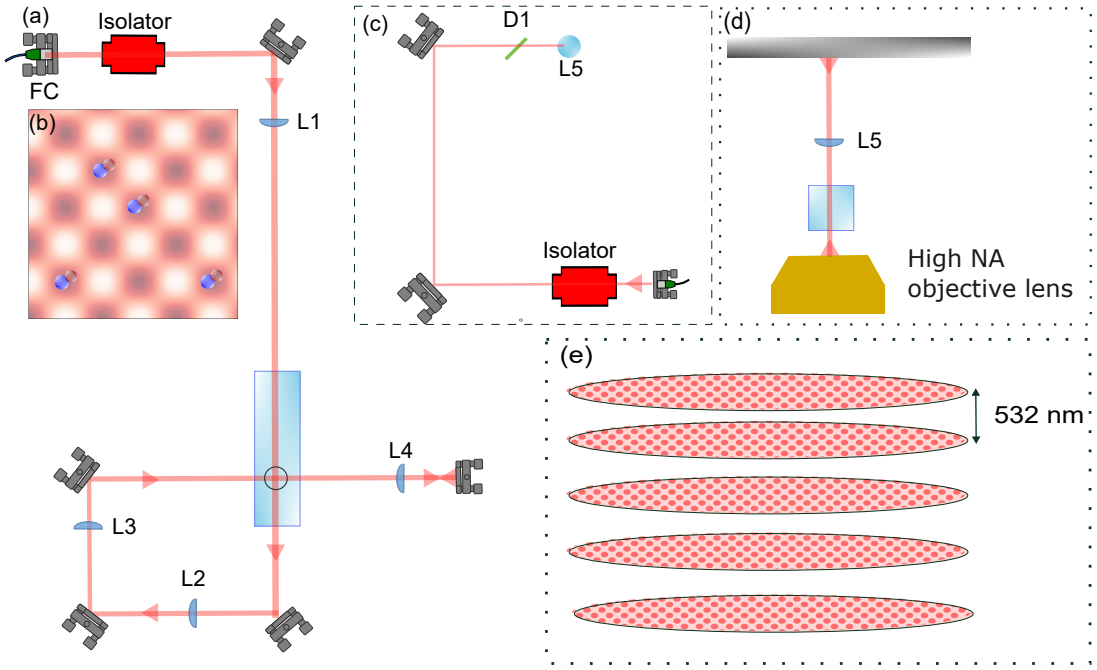

Figure 6.1: The setup of the 3D optical lattice. (a) shows the optical setup for the horizontal lattice as seen from above. We couple 1064 nm light from a fibre amplifier into a fibre to ensure we have a Gaussian beam out of the fibre. The power in the lattice is controlled by an AOM before the fibre. Further details are provided in the text. The four beams combine to produce a lattice with a lattice spacing of $\lambda/\sqrt{2} = 752$ nm oriented diagonal to the beams themselves as shown in (b). The vertical lattice setup (shown in c) is mounted above the science cell. The beam is focused onto the atoms using a lens (L5) mounted above the science cell. A side on view of the vertical lattice setup is shown in (d) This produces a lattice with spacing $\lambda/2 = 532$ nm in the vertical direction as shown in (e).

high optical powers using a logarithmic photodiode as the detector for the servoing (see Sec. 3.3.3). We couple the beam to a fibre to ensure we have a good Gaussian beam shape for the lattice beams. We use up to 5 W of light out of the fibre in the horizontal lattice, which corresponds to a lattice depth of $\approx 16,500 E_{\mathrm{Rec}}$ for Cs. An isolator is placed after the fibre output to prevent the reflection of the lattice beam damaging the fibre amplifier. The lenses (L1, L2, L3, L4 in Fig. 6.1 (a)) used are set up to focus the lattice beam on to the position of the atoms with the same waist on every pass. The beam initially co-propagates with the optical transport path through the main chamber, so the initial focusing lens - L1, placed before the main chamber - has a long focal length f=750 mm focuses the beam at to a size of

$\sim$ 100 μm. L2 and L3 are both f=200 mm lenses,arranged to focus the beam on the atoms to a waist of $\sim$ 100 μm as well. L4 (f = 200 mm) collimates the first pass and then focuses the reflection of the beam onto the atoms, again at a waist of $\sim$ 100 μm.

The vertical lattice consists of a beam from fibre amplifier #3, coupled through the fibre and focused onto the atoms by lens L5 (see Fig. 6.1 (c) and (d)). The high NA objective used for imaging was designed to be reflective at 1064 nm, so we are able to reflect the beam for the vertical lattice off of the objective lens itself.

The lattice beams were both aligned on the atoms via trap frequency measurements and Kaptiza-Dirac scattering, both detailed in Chapter 3. The first pass of the horizontal lattice (beam blocked before L2) was aligned to the atoms with a trap frequency measurement. The second pass was then aligned using Kapitza-Dirac scattering (beam blocked before L4) to maximise the lattice depth in the 1D lattice. The retro reflecting mirror was finally aligned using Kapitza-Dirac as well. The vertical lattice was aligned only using Kapitza-Dirac, using the lattice depth to optimise the focus position. Further details of the methodology used to align the lattice beams in our experiment can be found in [148]. From this, we find a calibration of 106 $\pm 3\mu$K /W. We are able to reach trap depths of about 500 μK for Cs at 5W in the lattice corresponding to $E_{\text{rec}} \approx$ 16,500. For Rb, the lower polarisability means that the trap depth is only around 300 μK at 5W, but the lower mass of Rb leads to an $E_{\text{rec}} \approx$ 16,000. The vertical lattice is able to reach depths of 350 μK for Cs.

6.2 The high resolution imaging setup

As in other quantum gas microscope experiments [14, 15, 20, 21, 83, 157], we image the fluorescence from the atoms while performing optical molasses cooling of the atoms trapped in a deep pinning lattice to image the atoms. To see correlations in the atoms and later molecules, it is advantageous that they are separated by short distances ($<$ 1 μm ideally). Our lattice, as previously described, has a nearest neighbour spacing of a_{lattice} =752 nm.

To image atoms to a sufficient resolution to be able to resolve atoms separated by a_{lattice}, we rely on a high NA objective lens[2] placed outside the cell. The objective was designed to correct for the 3 mm thick science cell window, and have a minimal chromatic focal length shift between 780 nm and 852 nm - the wavelengths used to image Rb and Cs respectively. The objective lens is designed to have a focal length of 35.2 mm, and a diffraction-limited NA of 0.7 - the maximum permitted by the cuboidal science cell. The objective lens is mounted on a kinematic mount with three piezo-actuated screws[3] with three piezo actuators, allowing for fine control of the tip-tilt of the lens and the vertical (Z) axis separation of the lens from the cell. We centre the lens in the horizontal plane (X-Y) by pushing it with screws and using a dial gauge for feedback. The objective lens was characterised using a test target as detailed in [148].

The magnification of the system is chosen by making a compromise between the size of each imaged atom and the signal from each atom on the camera. For our single atom resolved imaging, we choose a magnification such that a_{lattice} corresponds to ≈ 4 pixels on the camera (where we should be able to reconstruct the lattice well [240]). We initially used an Andor iXon 897 EMCCD camera, with a pixel size of 16×16 μm, and an area of 512×512 pixels. We later use a Hamamatsu Orca 1555-2-UP cMOS camera, which has a pixel size of 4.6 μm, and an area of 4096×2304 pixels. The data in this thesis was taken with one of three possible imaging setups - all shown in Fig. 6.2. When the Orca camera is used we only use a single 1000 mm lens after the objective to image the atoms onto the camera. The expected magnification of this two lens setup is given by $f_2/f_1 = 28.4$, which gives us an effective pixel size of 162 nm. This leads to a nominal field of view of $\approx$ 660×370 μm, and a_{lattice} projected to be to 4.6 pixels. This setup was used for most of the data taken in this thesis, as it offers the capability to (i) resolve the entire atom cloud (seen to be around 200 μm wide) trapped in the lattice and (ii) reliably image single atoms and resolve their lattice sites.

[2]Special Optics -Special Optics 54-51-36 custom part
[3]Custom made by Radiant Dyes, with Physik Instrumente PiezoMike actuators

The initial camera we used was the Andor iXon[4], which was used for some of the data presented in this thesis[5]. Due to its larger pixel size, we used a 4x *magnifying* telescope (for a total magnification of 114x) to have a_{lattice} be 4.2 pixels. However, this imaging method has a field of view of only 71 μm, so we are unable to image the full atom cloud. To be able to image the full atom cloud - useful for the initial alignment of the imaging to the atoms, and to image the entire atom cloud, we remove the telescope or use a 4x *demagnifying* telescope as shown in Fig. 6.2 (c). While this increases the field of view to 1.1 mm, we lose the single site resolution capability (with each lattice site now < 0.3 pixels on the 4x demagnified setup).

We use a optical molasses cooling beam to image both our Rb [14, 15]. and Cs atoms [154]. We currently use only one molasses beam, in a lin-$\perp$-lin configuration, with a quarter waveplate placed before a mirror that retro-reflects the beam. Figure 6.2 shows the setup of the molasses beam. The beam is a 1 mm waist beam that originated from our laser table. We note that with the beam waist being large compared to the atom cloud, the alignment of the beam to the atoms is not extremely sensitive (while still important). In our setup, we find that it is important to align the beam to pass in between the electrodes very well, as any part of the beam clipping on the electrodes leads to scattering of the molasses light on to our imaging camera, reducing the image quality dramatically. We initially used a second molasses beam, propagating from the other side of the cell, but found no significant improvement in molasses performance. We attribute this to the optical lattice likely being able to redistribute energy between spatial dimensions, allowing us to not directly cool in all dimensions. We are unsure as to why the addition of the second molasses beam did not aid the cooling, and this could perhaps indicate a technical issue with the setup. With the single beam molasses proving sufficient for good microscopy, we use it in our setup.

[4] used before we acquired the Orca

[5] We state that this camera was used in the relevant sections

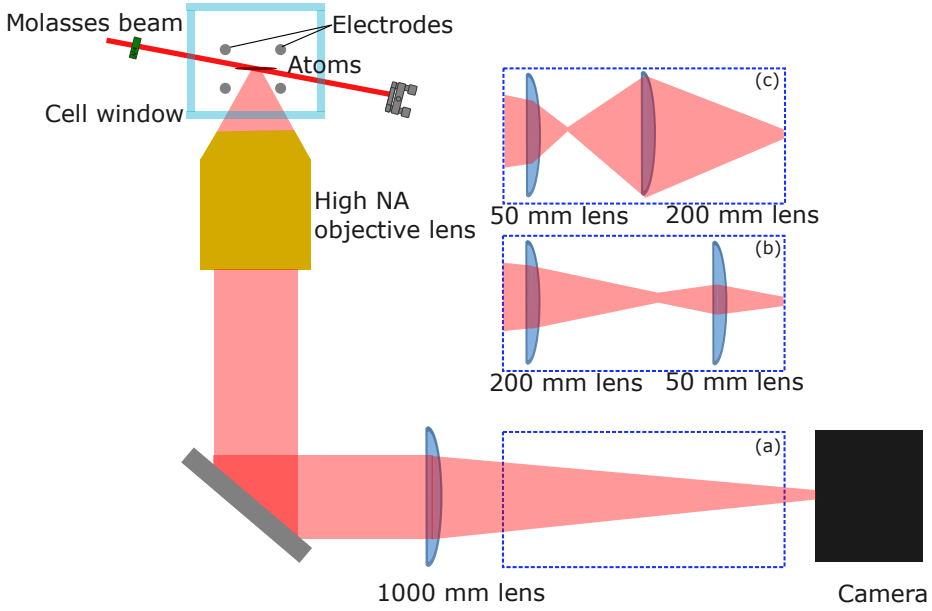

Figure 6.2: High resolution imaging setup. The atoms are laser cooled with the retro-reflected molasses beam. A portion of the fluorescence from the atoms is collected by the High NA objective and then imaged onto a camera. The molasses beam is aligned to pass between the electrodes as shown. The magnification of the system with just the objective lens and the 1000 mm lens as shown in (a) is . We have the options to demagnify or magnify the image by a factor 4 using a telescope system as shown in (b) and (c) respectively

6.3 The microscopy sequence

The sequence used for microscopy of atoms is shown in Fig. 6.3. An single species atomic cloud is loaded into a dipole trap in the science cell. Then, the optical lattice (and light sheet beam which is described later) is turned on to pin the atoms to their positions. The B-field coils are switched off, and any stray fields are nullified using the shim coils. After a 20 ms wait for eddy currents to dissipate, we begin the molasses imaging. With the atoms in the lattice being much colder ($\approx 1-5\ \mu$K) than the lattice depths typically used ($\approx 250-400\ \mu$K), we do not expect significant tunnelling in this time.

In the sequences used for the characterisation of the atomic microscopy for both

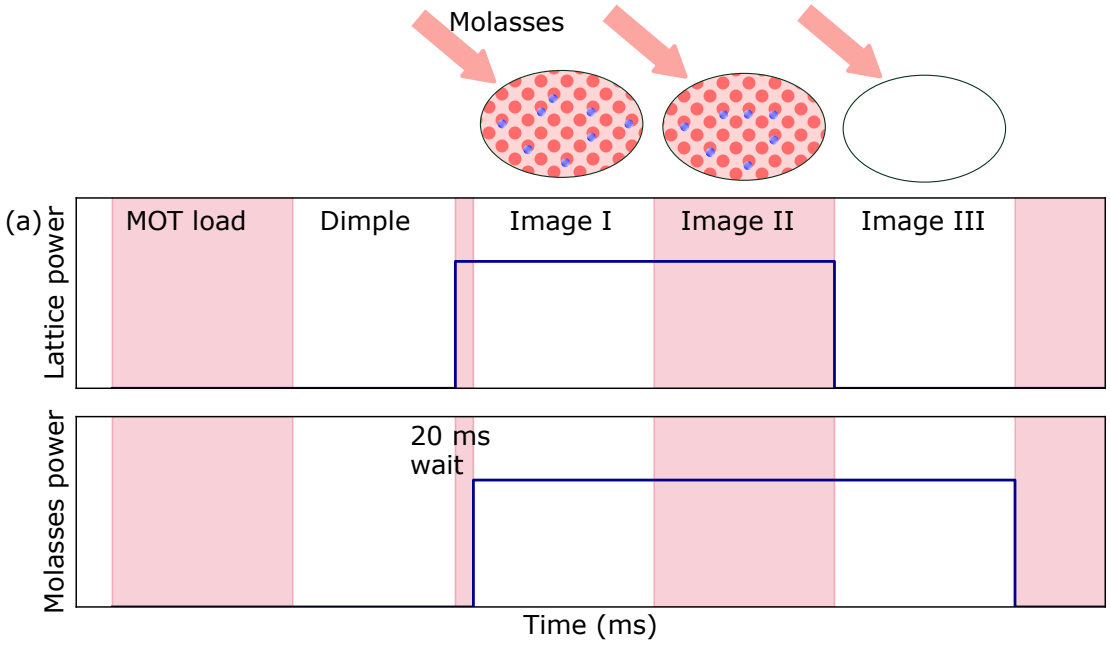

Figure 6.3: The sequence used for microscope imaging in the optical lattices. A cloud of Cs (or Rb) atoms is loaded into a dipole trap. The lattice is then ramped up to pin the atoms, and after a 20 ms wait, the molasses beam is turned on. We take three images (shown in Fig. 6.4) in each sequence. I and II are sequentially captured images of the atoms in the lattice with a 1 s exposure, while III is a background image, taken without the lattice on.

species, we take three different images sequentially, shown in Fig. 6.3. Each image has a 1 s exposure time. The first two images (I and II) are taken with the lattice beams (and light sheet beam) on, and the optical molasses light used for the fluorescence imaging also on. The third image (III) - a background image - is taken with just the molasses beam on, without any lattice beams on. The amount of trapping light that is incident on the camera is negligible, as we filter it out using two wavelength dependent filters. The majority of the background is attributed to scatter of the molasses light off of the electrodes and the science cell. The reason we take two sequential images of the atoms is to characterise the molasses. For a perfectly lossless molasses, these two images should be identical, as the atoms stay in the same position in the lattice, and scatter an identical number of photons. From these three camera images, we generate a *signal image*, subtracting the background from the first image (I - III) and a *loss image*, subtracting the second image from

the first (I - II). The *signal image* is what we use for identification of the atoms and the lattice. Fig. 6.4 (b) shows a sample signal image with the atoms identified. From this, we are able to count atoms in the region of interest of each image.

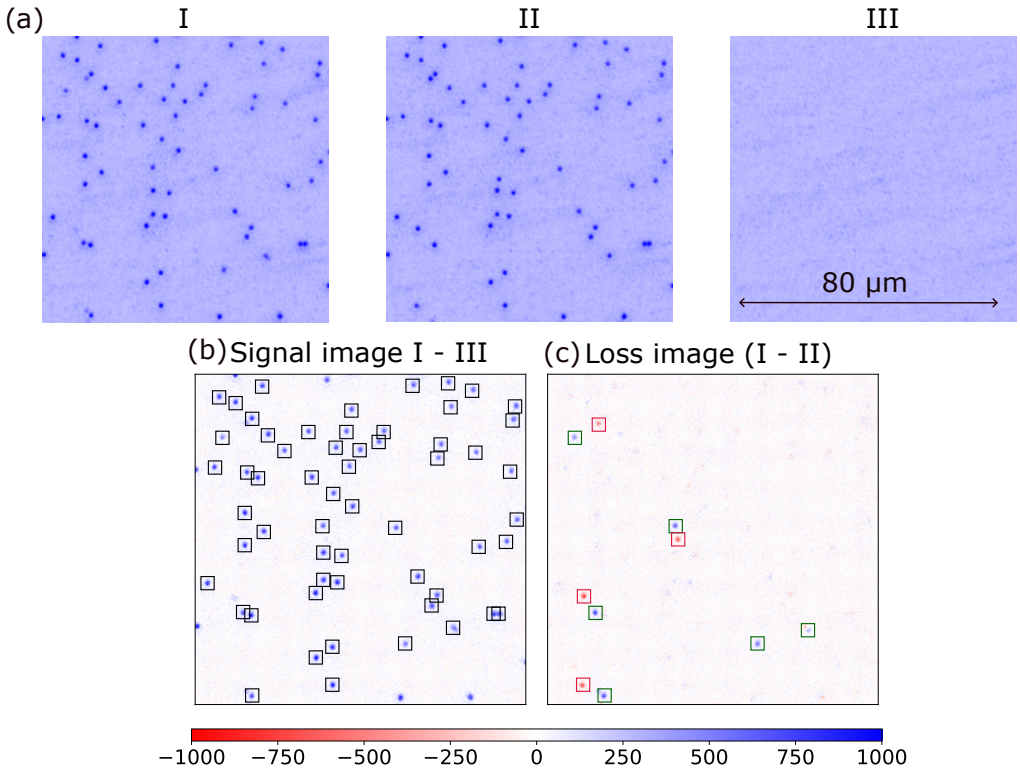

Figure 6.4: (a) shows sample images (I, II and III) taken in the sequence described in the text. (b) We identify and count the number of atoms in the first image I, subtracting the background (III) from it to improve the SNR. The number of atoms that have been lost from their initial site (blue dots in green squares) or hopped to a different site (red dots in red squares) in 1 s can be seen by considering the difference between images I and II as shown in (c). We intentionally do not count atoms at the edge of the image to avoid errors in identification and to ensure that the full PSF of the atoms is in atoms selected and analysed.

The *loss image* is used to characterise the molasses performance, by providing a measure of the loss of atoms during a fluorescence image. In the loss image, we see positive peaks where atoms were present in the first image but not the second image, and negative peaks where atoms were present in the second image but not the first. The negative peaks show atoms that have been lost from their initial site during the first molasses imaging, likely by tunnelling to a different lattice site.

We identify these peaks using the blob finding algorithm (with negative threshold values) and label them as 'hopped' atoms (see Sec. 6.4.1). The positive peaks are also identified. We expect to have more of these positive peaks than negative peaks, since they signify all the atoms from the first image that are no longer at their initial site (whether they have hopped to another lattice site, or been lost completely). We define our 'error' as the total number of atoms that are no longer on their initial site. The 'lost' atoms are defined as the difference between the 'error' and the 'hopped' atoms - signifying the number of atoms that have been completely lost from the lattice and the image. Figure 6.4 (c) shows a *loss image* with the hopped atoms and the errors identified.

6.4 Atom identification in the microscope

We first present the details of the code and method used to analyse the images from the quantum gas microscope to identify individual atoms. Details of how the images were obtained, and the optimisation of the microscope using these images will be provided later in the chapter. We are able to fit the lattice onto the atoms, with the lattice spacing and angle being free parameters. We note that most of the images presented were taken using the light sheet, and not the 3D optical lattice. The setup of the light sheet is detailed below, but, we find it useful to start with a description of the image analysis methods before introducing the light sheet. The fit lattice spacing is used to calibrate our imaging size. Once we optimised the microscope imaging we use a neural network to deconvolve the lattice and identify which sites are occupied. Details of the methods used here are in Section 6.9.

For the initial identification of single atoms in the lattice, and characterisation of the molasses imaging, we find it instructive to image sparse clouds of atoms in the optical lattice. With sparse clouds, it is significantly easier to visually identify the signal from individual atoms, and perform the initial optimisation of the signal. Without the imaging system aligned to optimise the PSF, and the molasses optimised to maximise the signal, it is a significant challenge to identify any visible structure in images with densely loaded lattices. The sparsely loaded lattices are

realised by reducing the MOT load in the sequence to 50 ms, in order to load a low number of atoms into the MOT and later the dipole trap. The rest of the sequence (DRSC, transport and loading into the dimple trap) is done as before. This allows us to load the lattice with <1% filling, in order to generate shots with a collection of well spaced single atoms for analysis. Sequences with densely filled lattices typically use a 2 s MOT load.

6.4.1 Identification of single atoms

Figure. 6.4 (b) shows a sample microscope image of a sparse cloud of Cs loaded into the microscope and images with the fluorescence imaging system. The atoms positions here have been identified and are highlighted (blue squares). To identify the atoms, we use a blob detection algorithm [241] (Scikit-Image Blob LoG), which searches the image for any peaks that are above a defined threshold and are of a reasonable size[6].

We take the identified atoms positions and define a square zone (usually 3 μm wide) around them. This zone is used to identify the PSF of a single atom and to evaluate the number of counts per atom. It is also used to isolate the PSF of a single atom for analysis. To avoid the inclusion of multiple atoms in a single zone when performing the analysis, we filter out atoms that are within 3 μm of another atom. While we are able to image the entire cloud when using the Orca Camera, we generally define a 70 μm wide square region of interest within which we analyse the images. The lattice beams themselves have a radius of $\sim$100 μm, so atoms outside the region of interest (ROI) start to see a significantly weaker optical lattice, which leads to increased loss and worse imaging. We discard any atoms that are less than 3 μm from an edge of the ROI to avoid including clipped or incomplete PSFs in our analysis.

6.4.2 Fitting the lattice

With the atom positions identified, we are able to fit the optical lattice to the atoms, following the approach used in [146, 242]. The full details of the code and methods

[6]Specifying limits on the Gaussian waists in the different axes

used for this fitting can be found in [148]. The fitting of the lattice to the atoms involves fitting the angle of each lattice beam, and the spacing between two lattice sites, and the lattice offset or phase.

For atoms in an optical lattice, we expect the list of atom positions (x_i,y_i) in our image to lie along to the lattice axes x' and y'. We can transform from the image axes (x, y) to the lattice axes (x', y') using a rotation of the form,

$$x' = x\cos\theta_y + y\sin\theta_x \qquad\qquad y' = -x\sin\theta_y + y\cos\theta_x. \tag{6.1}$$

We want to identify the rotation angles θ_x and θ_y so that (x', y') coincide with the lattice axes. At the optimal rotational angles, the distances of the atoms positions, x_i' and y_i' are periodic in that coordinate system, and a histogram of the distances can be plotted as shown in Fig. 6.5 (c). To fit the lattice spacing to the image, we perform a Fourier transform of the data, and find the fundamental peak in the spectrum (Fig. 6.5 (d)). We can then determine the lattice angle more accurately by searching for the maxima of the height of this peak as a function of the lattice angle (Fig. 6.5 (e)).

From these fits, we obtain lattice angles of 44.62 $\pm$0.02° and 134.58 $\pm$0.03°, close to our expected values of 45° and 135° from the lattice geometry. The lattice spacing (a_{lattice}) is found to correspond to 4.59 $\pm$0.15 pixels, in good agreement with our expectation of 4.6 pixels (with a magnification of 28.4) on the Orca camera from the design of the imaging setup. We note that the lattice angle and spacing (and magnification) are ascertainable from a few sparse images (even without an optimal molasses sequence)

To deconvolve the lattice, the initial phase of the lattice is calculated and the occupancy of each site is ascertained, as shown in Sec. 6.9 This is left for the end of the chapter.[7].

[7]The author is partial to including these images at the conclusion of the chapter for some dramatic flair

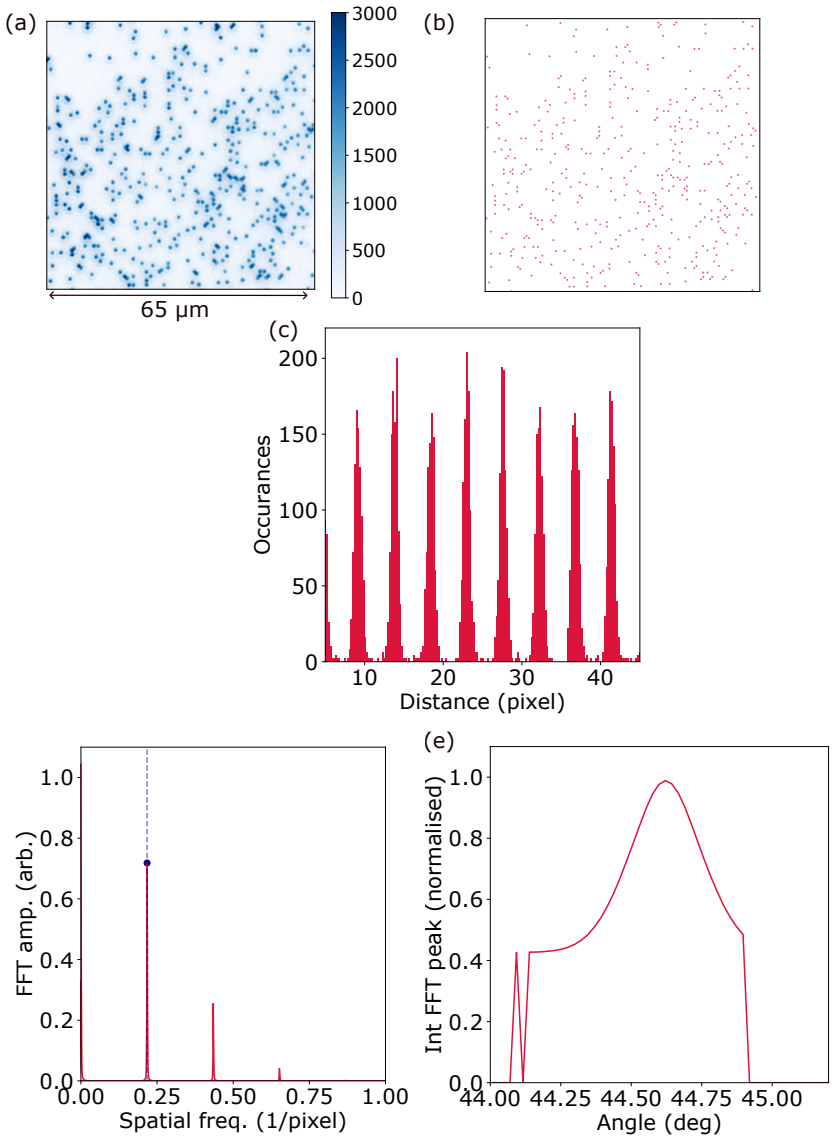

Figure 6.5: Finding the optical lattice from microscope images. (a) shows a microscope image of the Cs atom cloud, loaded at $\approx 3\%$ filling. The atom positions are identified as shown in (b) using a peak finding algorithm. (c) shows the distribution of distances between atoms measured along one of the lattice axes. The angle was varied, and the angle with the maximum contrast in the signal (so the most prominent peaks) is the lattice angle. (d) shows the spatial spectrum of the atom positions at the fit lattice angle, and (e) the variation of the principle peak height of the spatial spectrum as a function of the lattice angle (which is used to precisely define the lattice angle). The lattice offset is found and the image is deconvolved later, as shown in Sec. 6.9

6.5 Atoms in the 3D optical lattice

Our initial attempts at microscopy were performed by loading atoms into the 3D optical lattice and using the Andor camera. We have previously investigated atoms trapped and imaged in a 3D lattice[8], probing the Mott insulator-superfluid transition, the efficacy of the molasses cooling, and conducted some single atom imaging [148]. We were unable to perform single layer selection, likely due to the presence of too much magnetic field noise (Sec. 2.4.1). Our images taken with the 3D lattice setup have atoms loaded into various lattice planes, so it is not possible to resolve the atoms in densely loaded images, and difficult to resolve them faithfully, even in the sparse images. However, we were able to use the 3D lattice to trap clouds of atoms or molecules and resolve small clouds of molecules via florescence imaging. Fig. 6.6 shows images of the atom cloud taken using the Z-lattice. While there are some bright in-focus atoms, it is apparent that there are a significant number of atoms present on out of focus planes of the image in Fig. 6.6 (a). The 3D lattice can be used to trap and image the entire atom cloud if the optical setup used is set to a magnification where the entire atom cloud is visible as shown in Fig. 6.6 (b). While for us the inability to prepare a single layer in the lattice is a major issue, we note that recently, progress has been made in imaging atoms across multiple lattice planes [243].

6.6 The light sheet

To generate a clear reconstruction of the system under investigation, we must image only a single plane in the vertical direction. After initial attempts at spectroscopic layer selection in the 3D lattice using a microwave pulse for Cs atoms failed, we decided to use a light sheet to load atoms into a single plane for imaging. Fig. 6.7 (a) shows the optical setup of the light sheet. The setup consists of light from a fibre (sourced from Fibre Amp 2), followed by a lens system to shape it into a beam of horizontal waist ≈ 150 μm and vertical waist ≈ 8 μm. This is done using

[8] With a cubic lattice geometry in that case

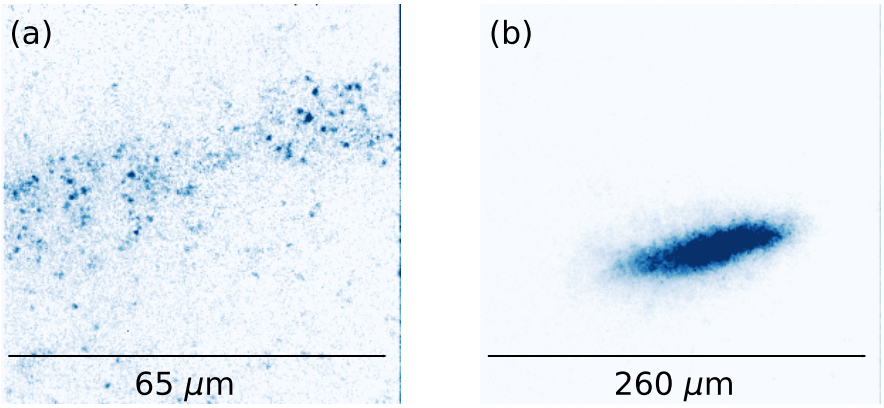

Figure 6.6: Fluorescence images of atoms taken in the 3D optical lattice. (a) shows an image of a sparse cloud of atoms loaded in the 3D lattice. We see that while some of the atoms are in focus, there are many atoms that are out of focus, as they are loaded into different planes of the lattice. (b) shows an image of a denser cloud in the optical lattice taken using the Andor Camera with the demagnifying setup, where we are able to image the entire cloud trapped in the lattice. In these images, we do not have single site resolution, due to the limited size of the Andor camera. With the Hamamatsu camera we currently use, we are able to resolve the entire cloud and have single atom resolution.

a cylindrical telescope to shape the beam to be cylindrical in shape, followed by a focusing lens (L1) that focuses the beam onto the atoms. With the light sheet and the horizontal lattice both on, we expect the resultant potential to resemble a 2D array of tubes, with the light sheet providing vertical confinement, and the horizontal lattice providing the horizontal confinement.

We align the light sheet to the atoms by optimising for the number of atoms that can be trapped in a xODT between the light sheet and the Cs dimple. The axial position of the focus is optimised by translating the lens L1, which is mounted on a linear translation stage, along the beam path. We confirm the alignment of the beam using a trap frequency measurement, shown in Fig. 6.7 (b). We measure the horizontal waist of 145± 3 μm on a camera and fit for the vertical waist of 7.2± 0.2 μm (from the trap frequency), which agrees with the expectation of the

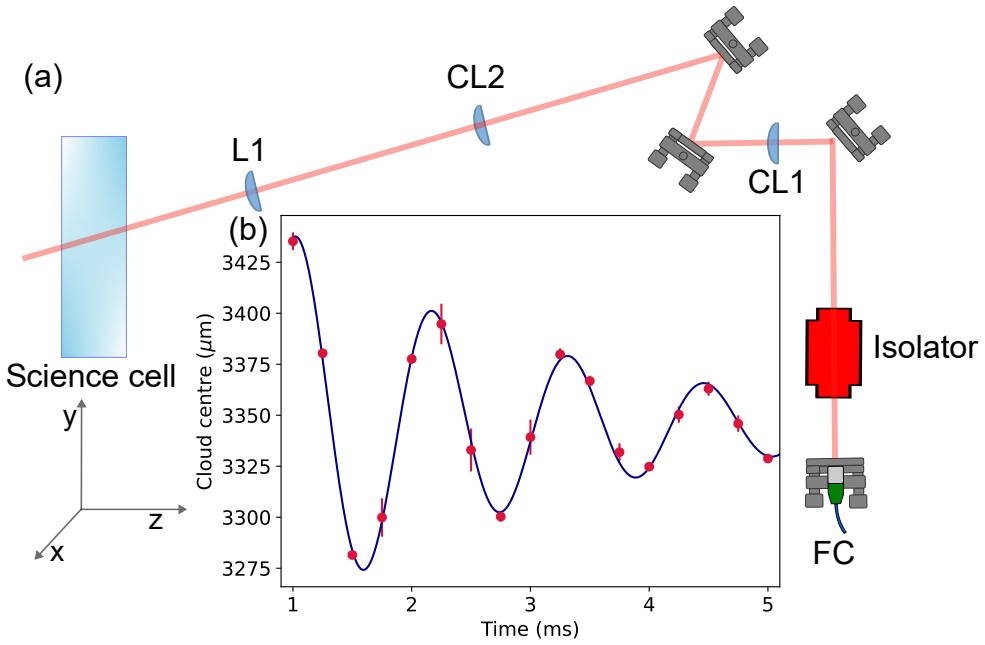

Figure 6.7: The light sheet setup (a) shows the optical setup of the light sheet. After emerging from the fibre collimator (FC), the beam is shaped using two cylindrical lenses CL1 (f = 15 mm) and CL2 (f = 300 mm) before b eing focused on the atoms by a spherical lens L3 (f=150 mm) This results in a beam of horizontal waist 145 μm and vertical waist 7.2 $\pm$ 0.2 μm. (b) shows the measurement of the waist using the trap frequency of the light sheet on the atoms, as we ensure that beam is well aligned to the atoms in the axial direction

beam waist from our design. It is important that the beam must be aligned to be flat with relation to the imaging plane (and the science cell window). A tilt of even 1° in the beam is sufficient to change the height of the atoms from the objective by around 2 μm across the cloud (which is around 100 μm wide), which will then cause significant aberrations as shown in Fig. 6.8 (b). To align the beam to be sufficiently flat on the axis of rotation around the X-axis (as depicted in Fig. 6.7), we have mounted L1 on a rotation stage, which we can use to adjust the beam to be flat. It is considerably more challenging[9] to align the beam to be flat in the Z-axis. We achieve this by aligning the beam to the atoms, and then using a camera, realigning all the optics in the beam path to be centred on this position. After alignment, we

[9] a week of pain

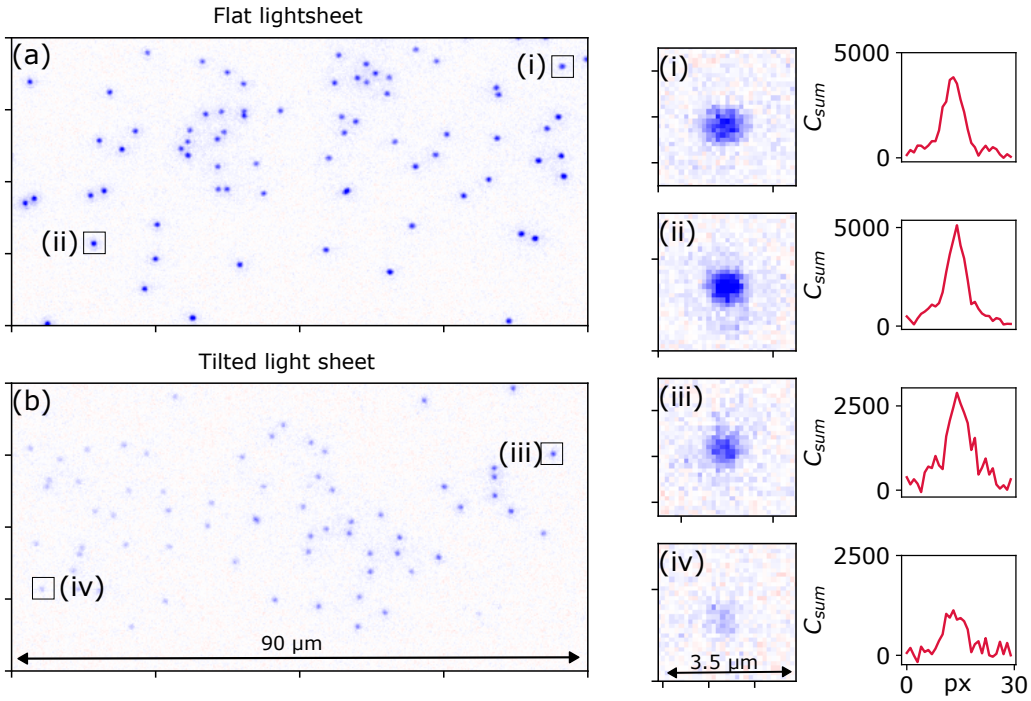

Figure 6.8: It is important to carefully align the light sheet beam to be flat and parallel to the objective, to ensure homogeneous PSF across the atom cloud. (a) is an image of the light sheet aligned to be flat, with (i) and (ii) showcasing atoms from opposite sides of the atomic cloud (with integrated cross cuts of the PSF plotted to the right). A tilt of even a few degrees results in the inability to bring the entire cloud into focus at the same time as shown in (b). Here, we estimate the light sheet was tilted by about 1°, and there is a large change in the PSF of atoms across the clouds - as shown in (iii) and (iv). We are able to align the light sheet to be flat to the level where the difference in PSF height of atoms varies by less than 20% across the cloud.

are able to capture images of single atoms in the optical lattice with a low ($< 20\%$ variation in peak height) spatially dependant variation of the PSF throughout the the atom cloud as shown in Fig. 6.8 (a).

A depiction of the sequence using the light sheet for microscopy is shown in Fig. 6.9. With some atoms in the dipole trap, we simply turn on the light sheet and the horizontal lattice together to similar depths of to pin the atoms in place. The light sheet is able to reach trap depths of 400 μK for Cs with 4 W of power (250 μK for Rb). This is sufficient to keep the atoms pinned during the molasses cooling. In addition to the sparse clouds used to characterise the setup, we image dense clouds as well, albeit with a maximum imaged filling factor of 0.5. This is because in a

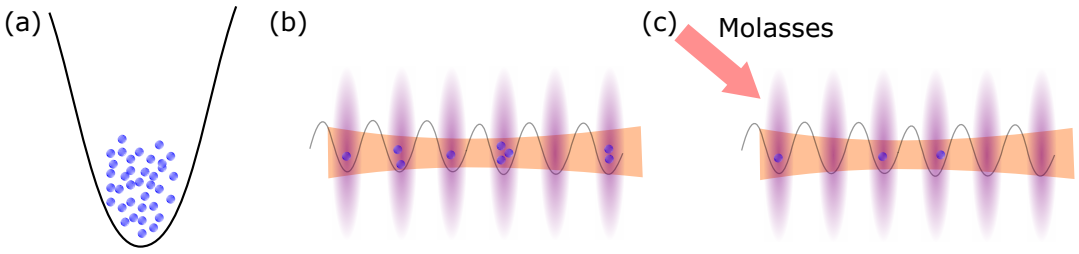

Figure 6.9: A cartoon showing how the imaging in the light sheet works. (a) we start with a cloud of atoms in an optical dipole trap. (b) the horizontal lattice (purple) and light sheet (orange) are turned on, and trap atoms in their potential. (c) when the optical molasses cooling happens we image a the parity of the cloud that was loaded into the lattice, as pairs of atoms are ejected from light-assisted collisions

dense cloud, though the number of atoms loaded into any one site of the lattice may be greater than 1, rapid light-assisted collisions occur during the molasses imaging, causing pairwise ejection of atoms and emptying the sites with even occupancies. In the future, to image highly filled lattices of atoms, we would have to prepare the atoms in a Mott insulating state in the lattice with an occupancy of 1 in the centre of the lattice.

6.7 Optimisation of the Microscope imaging

Now that single atoms in a single plane can be resolved, we move onto optimising the atom fluorescence signal from the individual atomic microscopes. We would like to optimise for three factors namely (a) an unabberated Point Spread Function (PSF) of narrow radius (b) maximum signal to noise of individual atom signal and (c) a low error rate/loss rate during imaging.

Optimisation of the PSF is the most straightforward - and decoupled from the rest, as it solely depends on the alignment of the optical system. For a given position of the camera and the 1000 mm lens, the atoms can be brought into focus by translating the objective lens using the piezo adjusters. We take images of sparsely loaded lattices and plot the PSF as a function of objective lens optima as shown in 6.10. The camera position was also translated, but the imaging is far less sensitive to this [148].

The optimisation of the signal-to-noise ratio (SNR) and loss rate is less straightforward. The level of signal from each atom depends on the scattering rate of the molasses, which is a function of the molasses intensity and detuning - as given in Eq. 2.9. We measure the error rate as the total number of atoms lost from their lattice site during a molasses imaging cycle. The loss of atoms entirely from the lattice or hopping of atoms between the lattice site is predominantly driven by the molasses itself, given the finite molasses temperature. [244]. The noise in an image is related to the molasses power, due to a small fraction of the molasses imaging light being scattered into the imaging path.

Finally, the horizontal lattice and light sheet powers both must be sufficient to keep the atoms pinned to the lattice for the duration of imaging. For Cs, we are comfortably able to pin the atoms, although this is a bit more challenging for Rb due to the lower polarisability of Rb at 1064 nm. It should be noted that the lattice and light sheet both detune the cooling transition a significant amount due to the AC Stark shift.

We chose to optimise our molasses for a 70 x 70 μm area (so about 8500 lattice sites) in the center of the image. The lattice beam (light sheet) has a waist of 100 μm (145 μm). Beyond this distance, we find that the molasses performance changes significantly, both due to the lattice becoming weaker and less able to trap the atoms, and due to the light shift from the lattice reducing the molasses detuning, causing a 'hotter' molasses. More details of this are presented in Sec. 6.7.2

6.7.1 PSF optimisation

With the atoms separated horizontally by only 752 nm, it is important to align the imaging well, so that the PSF of the atoms is narrow, unaberrated, and has a high peak height. A large PSF or an Airy ring around the atoms would significantly complicate the identification of the lattice and resolution of atoms on neighbouring sites. Ideally, given the $a_{lattice}$ of 752 nm, we would like the radius of the PSF to be under the Sparrow limit [245, 246] ($\approx 1.3\ a_{lattice}$), so 977 nm. However, we can resolve atoms in lattice sites that have larger PSFs, since we have information about the structure of the atomic distribution and the individual PSFs themselves.

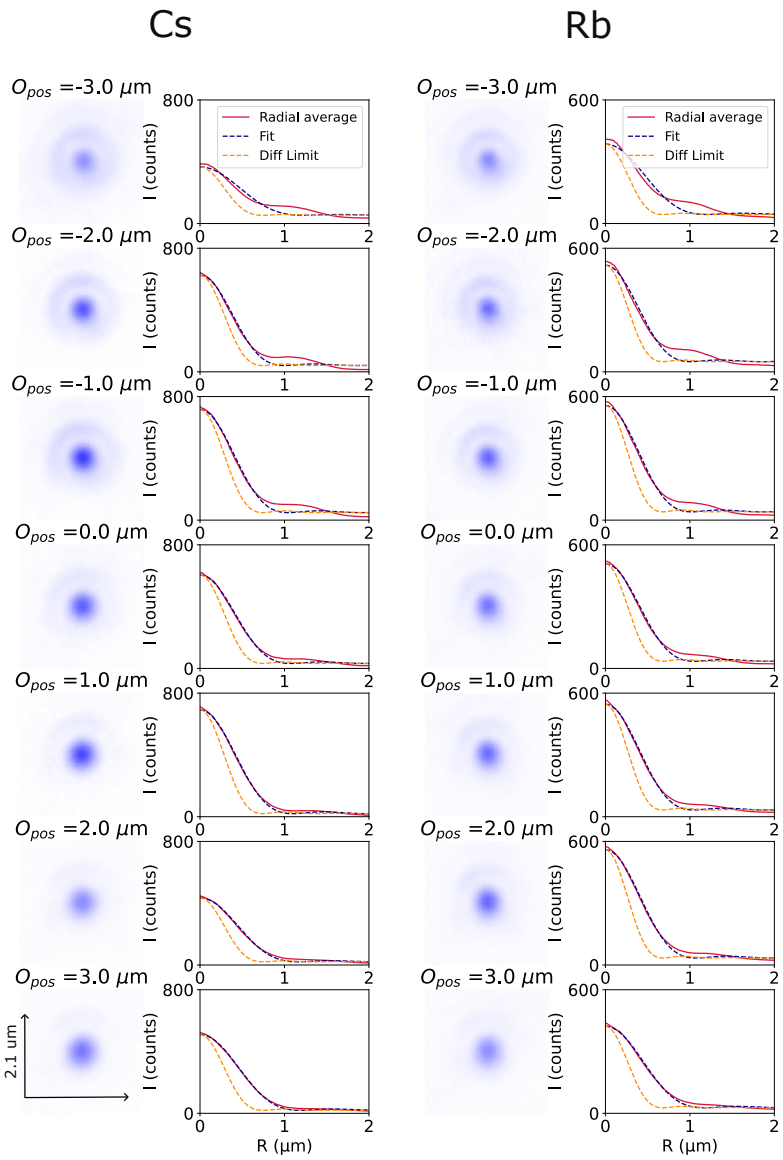

Figure 6.10: Optimisation of the distance of the objective lens from the atoms. O_{pos} refers to the distance of the objective from the optima further away from the atoms (negative O_{pos} corresponds to moving closer to the atoms). The value of O_{pos} at the optima we find was retroactively set to zero for these plots. The value on the piezo controller includes an arbitrary offset. We are unable to measure the exact distance between the objective and the cell.. We image sparse clouds and identify the single atoms in the clouds while varying the distance of the objective from the atoms. The PSF of all the individual atoms in four images (≈ 40 per image) in the centre of the cloud are averaged to to give the averaged PSF displayed for Cs (Rb) in the second (fourth) column. The fit height and waist were optimised as discussed in the text and Fig. 6.11.

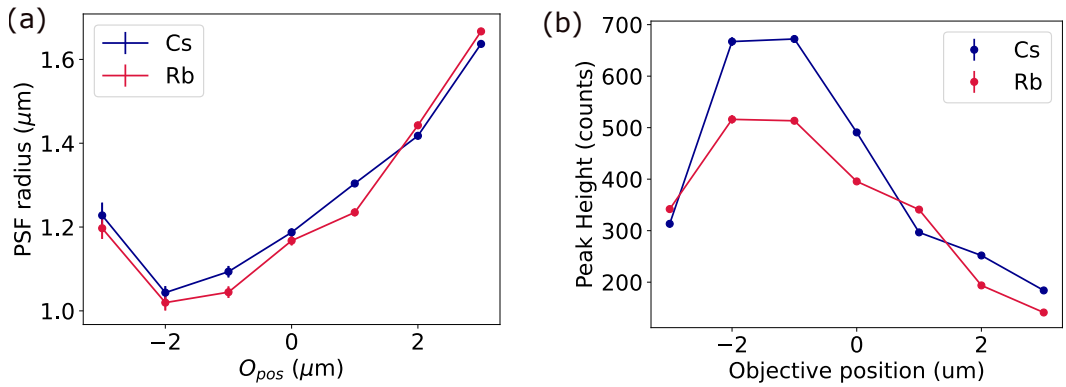

Figure 6.11: Plots of the waist and peak height during the optimisation of the distance of the objective lens from the atoms. We set the objective to optimise for (i) a Gaussian PSF (ii) a minimal PSF radius - as shown in (a) and (iii) a maximum PSF height - as shown in (b). We find that the lens and imaging system works as designed, with no significant chromatic shift in the position seen when imaging Rb and Cs. The error on these points is the fit error of the average, and does not reflect the error between shots, or the variance in peak heights in a single image. The Rb and Cs points at the same objective position were taken grouped together to avoid backlash error.

The imaging system relies on the atoms being at the focal plane of the objective lens, (to a tolerance given by the depth of field) and the camera being at the focal point of the system. For the full optimisation of the imaging setup, we scan the objective position, using the piezo adjuster, through the focal point with the camera at different positions. Fig. 6.10 and 6.11 show scans of the objective lens, imaging both Rb and Cs. We are able to narrow the PSF of the Cs (Rb) atoms to have Airy radii of 1.09 ± 0.12 (1.04 ± 0.10) μm, which while slightly over the Sparrow limit is easily small enough for our deconvolution algorithms to work [21, 240][10]. We see that the imaging system does not suffer any considerable chromatic shift, making it possible to have Rb and Cs imaged simultaneously. We notice that the imaging system is stable throughout the course of the day, with the objective requiring

[10]This is also worse than the quoted NA, but given that we have sufficient resolution and quality, we don't worry too much.

some re-optimisation every few days[11]). We note that the molasses parameters were optimised after the PSF was optimised. This should just effect the peak height of the signal and not any other focusing parameters.

6.7.2 Molasses cooling parameters

The next set of parameters to optimise is the molasses power and detuning. Once sufficient repump light is incident on the atoms, we optimise for the molasses cooling power and detuning together. The aim of this optimisation is to maximise the signal (or scattered photons) from each atom, while still maintaining a low error rate. To be able to reconstruct the lattice with high fidelity, we would like a SNR > 4 [240], and a low error rate of $\approx 1\%$ for both species. The signal (or number of photons collected) depends on the scattering rate (Eq. 2.9). The efficiency of the molasses has been attributed to the temperature $T \propto s_0/\Delta$ of the molasses [152], so we look for a point that balances the scattering rate and the molasses temperature. In our setup, the molasses beam is a source of background noise, with some scatter off of the cell and electrodes ending up incident on the camera. So, for the maximum SNR, we favour lower molasses intensities for the same scattering rate.

We optimise the molasses using the metric of the error rate - as described in Section 6.3. We take 10 sets of images of a sparsely loaded lattice (≈ 40 molecules per image out of the 8500 lattice cite ROI) for each set of parameters. We use the *signal image* to count the total number of atoms in a shot, and the *loss image* to count the number of errors, the atoms that have hopped sites, and those that have been lost from the lattice. These are then normalised by the total number of atoms measured in the first image to give a *hopping rate*, *loss rate*, and *error rate*.

The data for Cs was taken using the Andor iXon 897 EMCCD camera, with the EM gain on, while the Rb data was taken after replacing the camera with the Hamamatsu Orca camera. The reported values of scattering rate have been calculated accordingly. With a measured NA of 0.49, 9% of the emitted photons are collected by the objective lens. The quantum efficiency of the Hamamatsu Orca

[11] It moves by around 2-3 microns over the course of a week

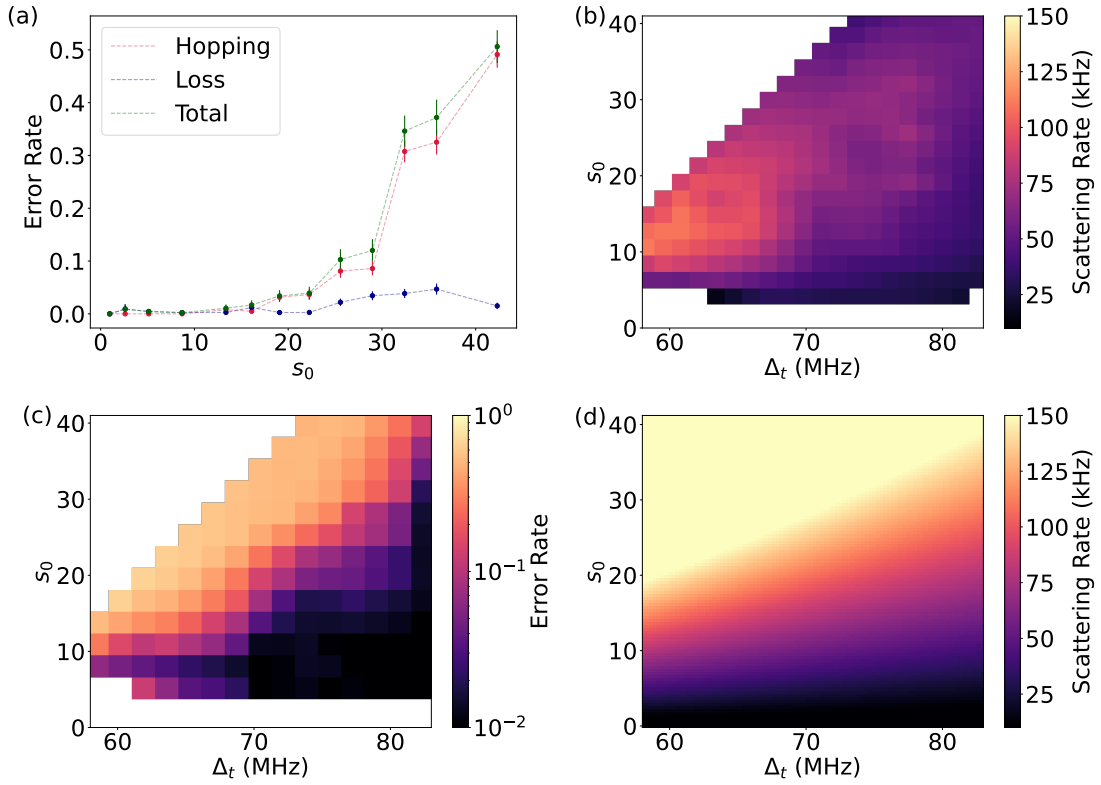

Figure 6.12: Characterisation of the optical molasses cooling parameters, the molasses intensity s_0 and detuning Δ_t for Cs. For a given Δ_t, 10 images with ≈ 40 atoms per image were taken, and the number of atoms, the hopping rate, loss rate, and error rate were calculated. For Cs, (a) shows the loss rate when changing s_0 at Δ_t of 73 MHz. (b) shows the scattering rate as a function of the molasses parameters, and (c) the error rate. We set our molasses cooling at $\Delta_t = 73$ MHz and $s_0 = 18.5$ for Cs. (d) shows the calculated scattering rate.

camera is 45% at 852 nm and 55% at 780 nm. The Andor iXon has quantum efficiencies of 55% at 852 nm and 85% at 780 nm, and was operated at an EM gain of 200. Finally, the Hamamatsu Orca has a photon response of 11 counts per photon. Accounting for a 4% loss of light on the optics in the system we are able to convert between counts and scattering rate for each atom. The counts of each atom are taken by summing the counts in a *signal image* in a 8x8 pixel region centred on the atom.

Figure 6.12 shows the characterisation of the molasses parameters for Cs and Fig. 6.13 the same for Rb, done at lattice depths of approximately 400 (250) μK , and light sheet depths of approximately 450 (275) μK for Cs (Rb). Fig. 6.12 (a) and

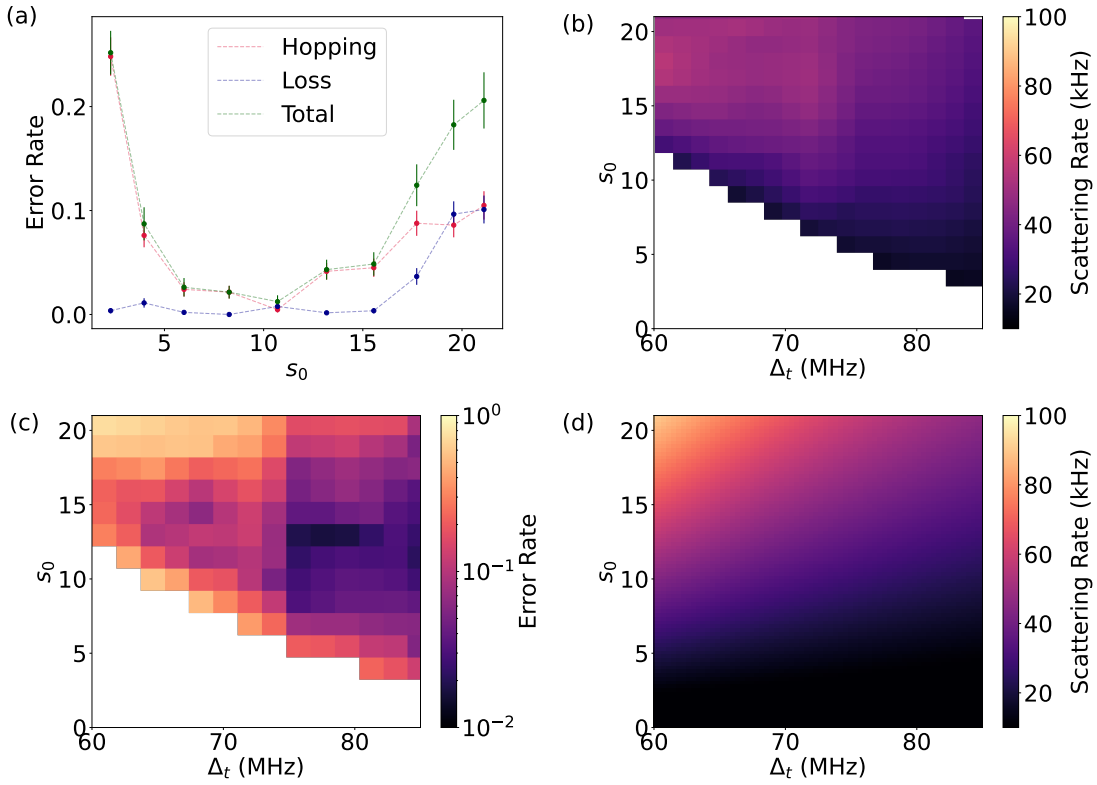

Figure 6.13: A characterisation of the Rb molasses, performed in the same manner as the Cs characterisation. (a) Shows a scan of s_0 at $\Delta_t = 79\,\text{MHz}$ for Rb imaged in the microscope (b) and (c) show the scattering rate and error rate as a function of molasses parameters for Rb. (d) shows the calculated scattering rate. We set our molasses cooling for Rb at $s_0 = 11\,\text{MHz}$ and $\Delta_t = 79\,\text{MHz}$.

Fig. 6.13 (a) show scans of power for a given molasses detuning (Δ_t) for Cs and Rb respectively, including the points we find as optimal. Here, Δ_t is the total molasses detuning, and includes the light shift from the lattice and light sheet beams (36 MHz total). Even though the AOMs that are used to change the frequency are double passed, we notice a variation in power of the beam as the frequency is changed, attributed to the beam moving slightly off the fibre it is coupled into after the AOM. This makes it difficult to take a regularly spaced grid of data. So, we scan the power (and measure it) at different molasses detunings and then use a linear interpolation to plot the data on a grid[12]. Fig 6.12 and 6.13 (c) show the error

[12]The interpolation works by triangulating each grid point to the three nearest data points and then using linear weights to predict the value of the specific grid point

rates for Rb and Cs as a function of molasses intensity and detuning parameters. As expected we see the error rate increase as both power and detuning increase. In addition, for Rb, which is less strongly trapped, we see the error rate increase at low power - where the molasses cooling becomes ineffective. Fig. 6.12 (b) and Fig. 6.13 (b) show the scattering rate as a function of power and detuning for Cs and Rb respectively, interpolated from a grid of points as before. The scattering rate increases with increase in power and reduction of detuning as expected. The observed scattering rates for both Rb and Cs are almost a factor 2 lower than the predicted values, which are plotted in Fig. 6.12 (d) and Fig. 6.13 (d) for the two species. We ascribe this discrepancy to an error in estimating the intensity of the molasses beam at the atoms. We have estimated the intensity (and hence the saturation parameter s_0) by measuring the beam power and assuming that the beam is centred on the atoms, and has a waist of 1 mm on both passes. However, the molasses beam has been aligned to pass between the electrodes - rather than centred on the atoms - to minimise scatter. In addition, the molasses beam is not the same size on both passes, since we do not have a 1:1 telescope or any other similar optical setup in usage here. So, the actual intensity of trapping light on the atoms may also be lower than the value used in the plots. The light shift was calculated using the polarisability values presented in [247,248], assuming no loss of light as it propagates along the system.

For Cs, we find an optimal molasses value of $s_0 = 18.5$, $\Delta_t = 72$ MHz and $\Gamma_{scat} = 66 \pm 6$ kHz, and an error rate of $0.006 \pm 0.004\ s^{-1}$. For Rb, we find an optimal molasses value of $s_0 = 11$, $\Delta_t = 79$ MHz and $\Gamma_{scat} = 36 \pm 3$ kHz, and an error rate of $0.016 \pm 0.004\ \mathrm{s}^{-1}$.

The Rb scattering rate is about 25% of what has previously achieved in atomic microscopes of Rb [151, 152]. We attribute our lower molasses scattering rate at the optima to our one beam molasses, rather than the more complicated schemes employed by the other experiments. Cs microscopes are less common, although some preliminary results on the molasses optimisation in a Cs microscope were reported in [154]. For both species, we take images in the regime where we are able to resolve the atoms well with our blob finding algorithm and stop at intensities and

detunings where our error rate nears one. We are able to image Cs for a broader range of parameters, since the atoms are trapped at a higher depth than Rb, so are more robust to the molasses.

6.7.3 Lattice depth

The lattice and light sheet depths play an important role, as atoms are less likely to suffer loss in deeper lattices. Generally, lattice depths of roughly 300 μK [15] are required to pin the atoms to their sites and keep them there for the molasses imaging. We reach these lattice depths using high power 1064 nm beams for our lattice as described earlier. We are limited to about 5 W in the horizontal lattice beam, for a trap depth of about 500 μK for Cs and 300 μK for Rb, though we often run at setpoints slightly below this for experimental reliability reasons. For Cs we are able to use molasses with a larger scattering rate, and still image nearly the entire atom cloud with a low error rate, whereas the Rb scattering rate optima is lower and we see significant loss on the edges of the atom cloud. Fig. 6.14 shows a *signal image* and a *loss image* of both the Rb and Cs cloud with dense loading (so around 50% filling due to light assisted collisions).

We find it instructive to investigate the effect changing the lattice depth has on the Rb imaging. Fig. 6.15(a) shows the *signal images* for different molasses detunings and lattice powers, while Fig. 6.15 (b) shows the *loss images* for the same. As expected, we see the scattering rate is dependent on the molasses detuning - and the effect of the light shift can be starkly observed here. In a given *signal image*, we observe that the atoms are brighter towards the edges of the cloud than the centre. We attribute this to the differential light shift of atoms in the cloud from the lattice. The cloud radius is similar to the waist of the lattice beams, so the light shift will be significant. In addition, for the same free space detuning, the fluorescence signal reduces when increasing the lattice power. For our optimum setpoints, we are looking for regions where the signal image has a high positive signal (blue) and the loss image is zero (white). At low lattice powers, we are unable to effectively cool, and the atoms are lost, even for high detunings. As we increase the lattice power, we are able to image more successfully. An increase in lattice power and

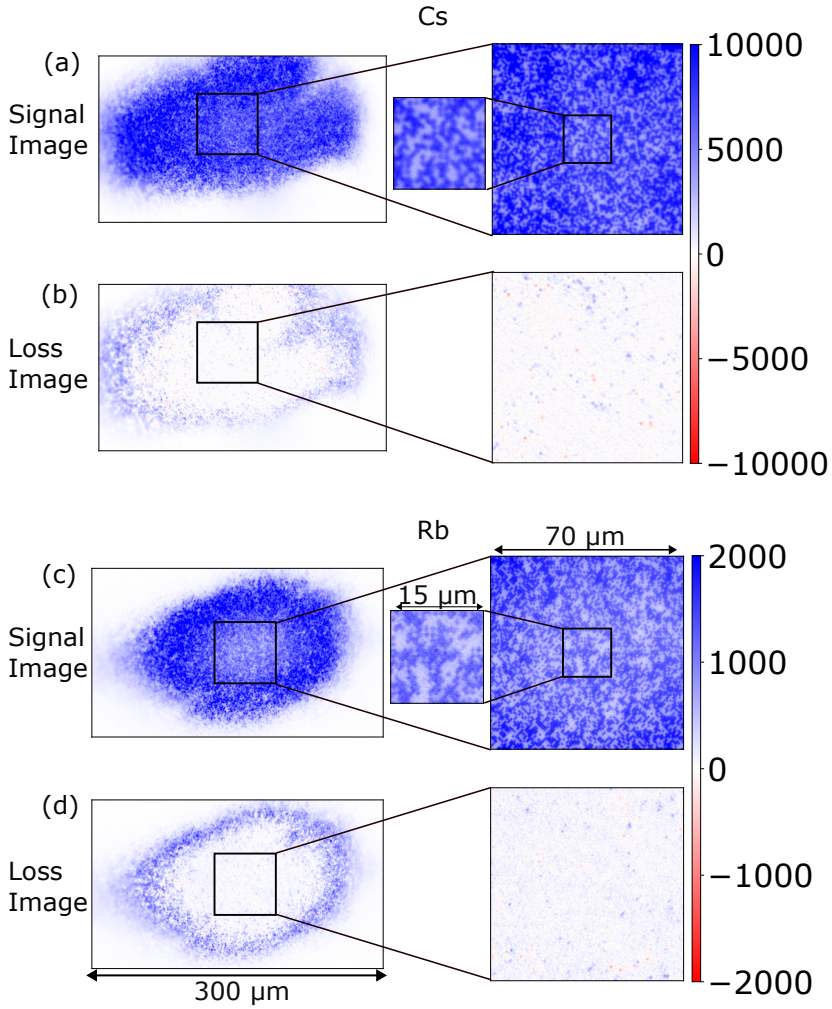

Figure 6.14: Images of Cs and Rb loaded and imaged in the light sheet and horizontal lattice. We are able to see the entire cloud that is being imaged with the camera for both species. (a) is a signal image for Cs, with a MOT load of 2s, and a mean occupancy of roughly 50% due to light assisted collisions. Adjacent panels show a 70 x 70 μm cross section and a 15 x 15 μm cross section of the cloud, where the single atoms can be identified even by visual inspection (b) shows a loss image for Cs. We see that the centre of the cloud is well trapped through the molasses, whereas the edges are lost during the molasses cycle. (c) and (d) show the corresponding images for Rb.

an increase in detuning both allow us to successfully image a larger region of the cloud (the central white area in the *loss images* becomes larger). While currently we have enough power to comfortably image both species with the microscope, we plan to upgrade the 1064 nm lattice and light sheet to in a 1146 nm (the 'magic' wavelength [67, 249] for molecules) in the near future. We expect to have less power

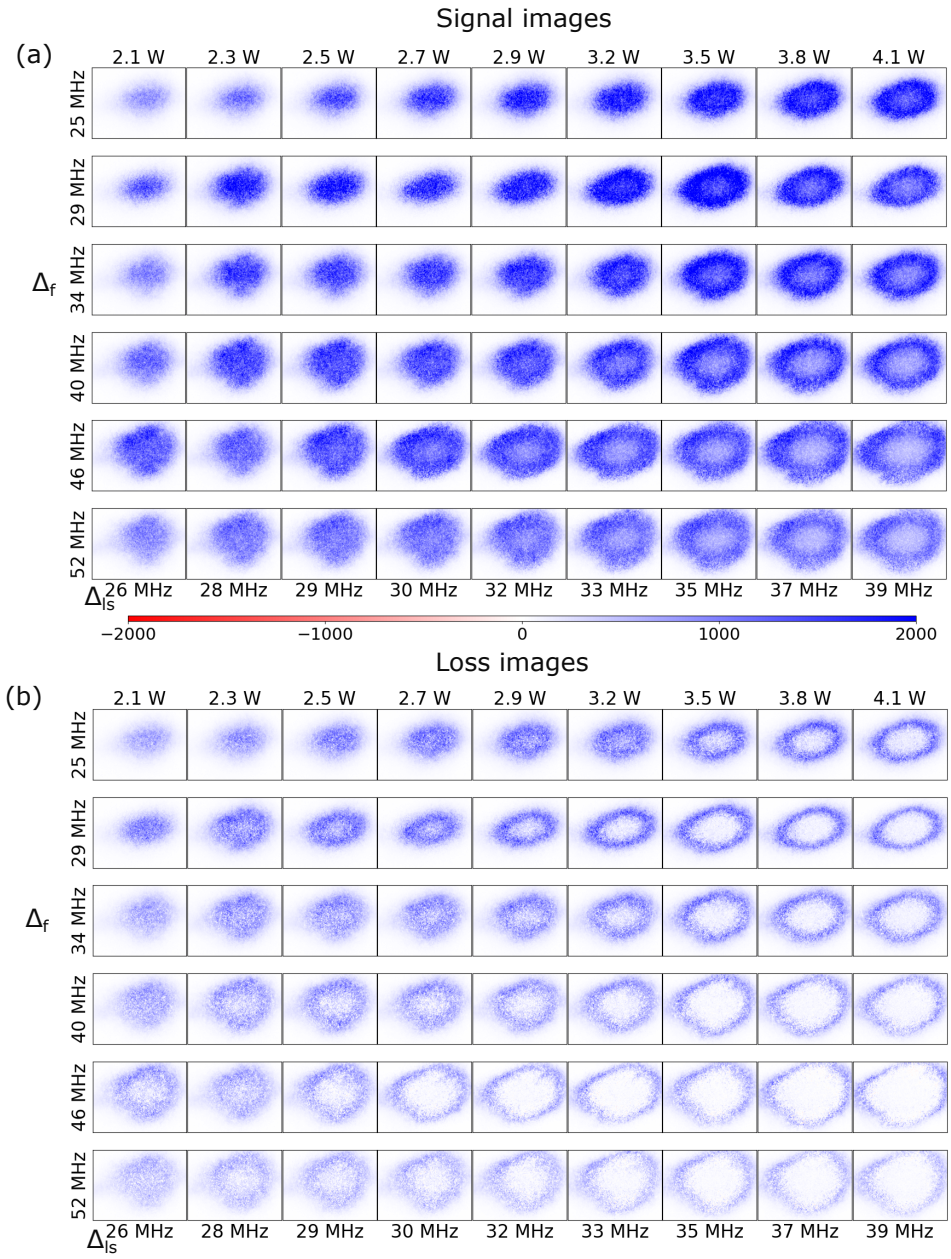

Figure 6.15: Images of the Rb cloud taken with the quantum gas microscope for different lattice powers and molasses detunings. Different lattice powers are plotted horizontally, with the resultant light shift (Δ_{ls}) in frequency noted underneath. The vertical axis labels (Δ_f) correspond to different field free detunings set by an AOM. The molasses intensity used corresponded to 14 s_0. (a) shows the signal images, with the scattering rate decreasing with an increase in molasses detunings and lattice powers as expected. (b) shows the loss images, where blue regions on these plots indicate lost atoms. For low lattice powers and low detunings, the entire cloud is lost during the molasses imaging. As the lattice powers increase, we see a central region with low loss develop and expand.

available, and would have to design the lattice beams to trap sufficiently well for good microscope imaging.

6.8 Characterisation of the microscope

With the molasses imaging optimised, we perform a characterisation of the imaging in the lattice. To make the reconstruction of the lattice easier, we would like to have a high SNR. We define the SNR as,

$$\mathrm{SNR} = \frac{\mu_{\mathrm{atom}} - \mu_{\mathrm{back}}}{\sigma_{\mathrm{atom}} - \sigma_{\mathrm{back}}}, \tag{6.2}$$

where the difference between mean signal from an atom (μ_{atom}) and the signal from the background (μ_{back}) is divided by the widths of the two distributions (σ_{atom} and σ_{back}). We assume a Gaussian broadening of the signal from the atoms and the background. We attribute the finite width of the measured signal from the atoms to intensity fluctuations, both spatial and temporal. The spatial variations could be due to uneven illumination of the cloud by the molasses beam as well as the spatial variation in lattice depth (and hence detuning of the molasses beam). The temporal fluctuations could originate from fluctuations in the beam power over time (as it is not servoed). The fluctuations in the background can be attributed to dark counts on the camera as well as scatter of the molasses beam off the cell and electrodes incident on the camera. While the subtraction of the background image removes some of the noise, some remains due to mechanical vibrations of the experiment and fluctuations in optical power between the signal images and the background images.

Figure 6.16 shows a measurement of the SNR for microscope imaging of both Rb and Cs. The measurement was conducted by taking around 300 images of Rb and 100 of Cs, and identifying the positions of atoms in each image. The analysis was restricted to a 70 x 70 μm area in the centre of the cloud. A 3 μm wide square ROI centered around each atom is considered, and the sum of the counts on the pixels in that area is taken as the counts for an atom. We plot a histogram showing the distribution of counts per atom for both species. The background counts are measured by measuring the counts on the pixels in 3 μm wide square ROIs which

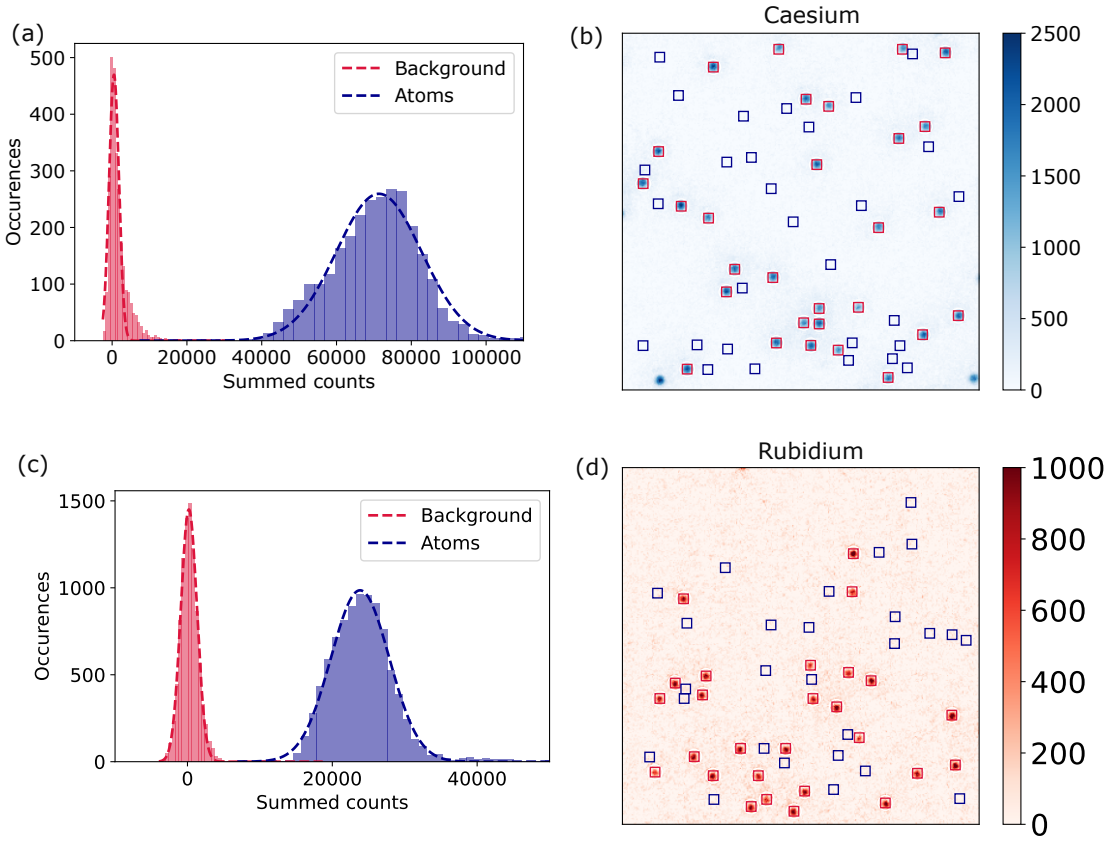

Figure 6.16: Identification of single Rb and Cs atoms in a sparsely loaded cloud. The atoms are identified by searching for peaks above a certain threshold in a *signal image*. The counts in a 3 μm wide square around each of these atoms is summed and plotted on a histogram in blue. to get a measure for the background, we randomly select points that are at least 3 μm away from any other atom and sum the counts in a 3 μm wide square around them as well. The histograms show the distribution of summed counts in the boxes which we have identified as containing atoms, and the boxes which contain the background samples. (a) shows the the histogram of counts in these boxes summed over 100 Cs images. (b) shows a sample Cs image with the atoms and background areas highlighted. (c) shows the corresponding histogram for Rb over 300 images and (d) the corresponding picture of the atoms

do not contain atoms in the same images.

The background points were selected to be at least 3 μm away from any atom. This was done by randomly generating points throughout the image, and then removing any points that were within 3 μm of any atom. Similarly, atom separated by less than 3 μm are not considered to avoid the fluorescence of multiple atoms being counted in the signal for a single atom. For computational efficiency, this was

done by assigning the points in each image to a k-dimensional tree (k-d tree) [250] and then conducting a nearest neighbour search on the points[13].

We measure a SNR of 4.6 for Rb and 6.2 for Cs in our imaging, comparable to what has been previously observed in other microscope experiments [146, 251]. This should be sufficiently high that we can reconstruct the lattice with high fidelity [240]. We note that the shape of the distributions, both of the background and the atom signal are slightly asymmetric. The background signal in particular, has a significant 'tail', which we attribute to some fluorescence signal from the atoms making it into the ROIs used to select the background.

6.9 Reconstruction of the lattice using a neural network

We now can superimpose the lattice onto the image of our atoms, and proceed to reconstruct the lattice. We utilise a neural network (NN) based approach, based on previous work in [252] to identify which sites are occupied and which sites are not to reconstruct the lattice. Full details of the NN used and its training have been presented in [148].

The reconstruction of the lattice is detailed in Fig. 6.17. To recreate the occupancy of the lattice, we take a 20 x 20 pixel region centred around each lattice site. The signal from each of these regions is deconvolved by scaling by an array of weights generated by the neural network (which was trained using simulated data). Figure 6.17 (a) and (b) shows a histogram of the counts in the 20 x 20 pixel region with and without the deconvolution for a sparsely filled lattice. We apply a threshold to the weighted sum, labelling lattice sites with a deconvolved sum above the threshold as *occupied*. Fig. 6.17 (c) shows a sample fluorescence image of Cs atoms and and the NN output for each lattice site. Fig. 6.17 (d) shows an overlay of the two plots in (c) along with a reconstruction of the lattice. We see a clear separation in the histograms of the unoccupied and occupied lattice sites for theses

[13] This method scales as $\log(N)$ in complexity

sparse images, implying a very good reconstruction fidelity[14]. The lattice offset (or phase) was optimised to maximise the separation of these two distributions.

Reconstruction of a more densely filled lattice is more challenging. Each atom is more likely to have neighbours, leading to a greater variation in signal in the 20 x 20 pixel bin around each atom. As shown in Fig. 6.18 (a), it is difficult to even see a bimodal distribution of counts in a region around each lattice site. The application of the NN deconvolution greatly helps here, and we have a clear bimodal distribution again, which we are able to threshold. Fig. 6.18 (b) shows the reconstruction of a lattice with occupancy ≈ 0.4. As seen from the histograms, there is no longer a clear gap at the threshold. However, the error rate from reconstruction remains small (0.6 $\pm$0.3% in this image) when compared to the molasses loss rate. Future upgrades to this system could involve using an unsupervised deep-learning algorithm, similar to [21].

[14]The fidelity is limited by the molasses cooling efficiency rather than the reconstruction.

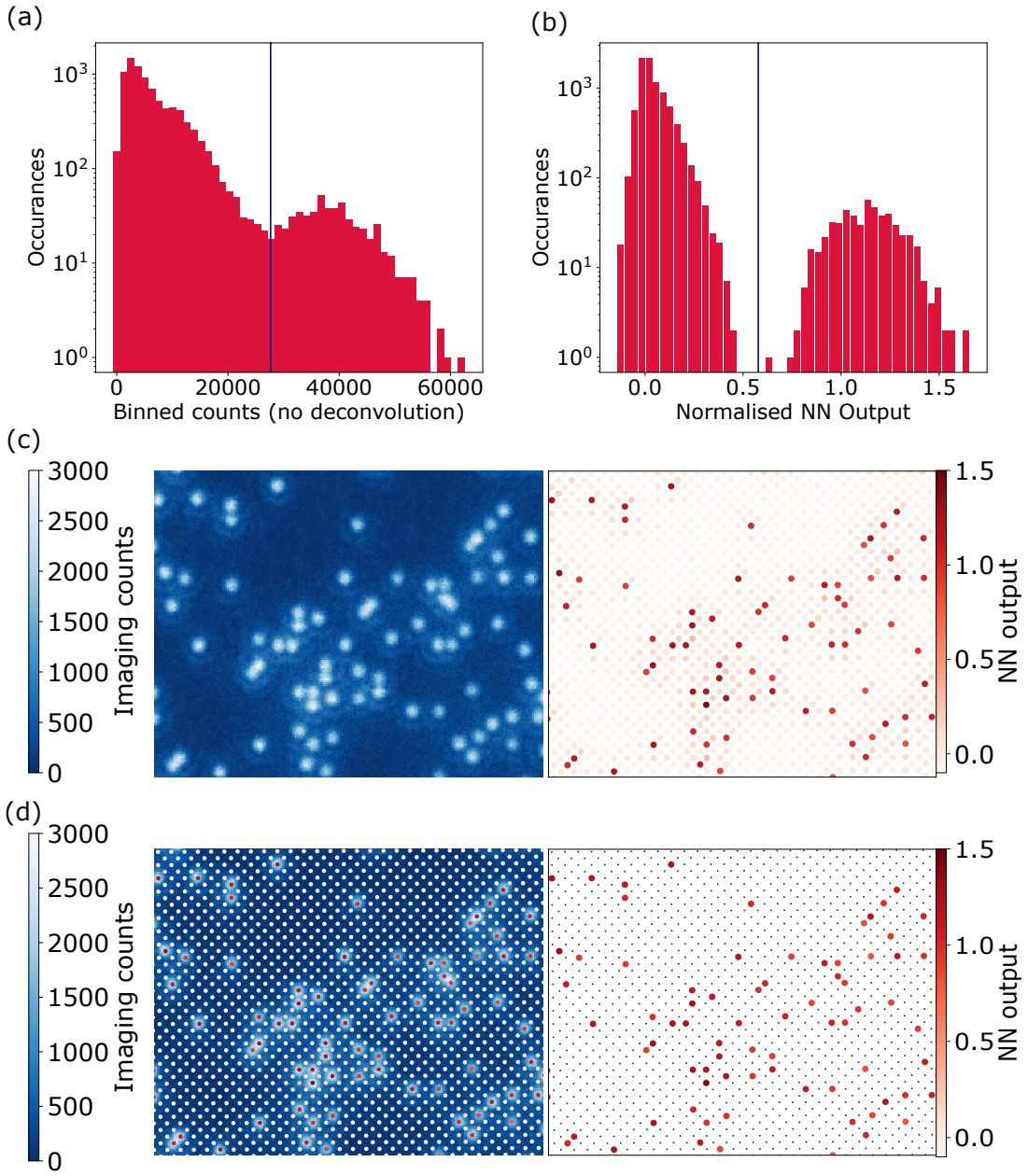

Figure 6.17: The reconstruction of the occupancy of a sparse Cs lattice by deconvolving with a Neural network. (a) the non deconvolved summed counts in a 20 x 20 pixel square region centred on each lattice site. (b) the deconvolved and scaled counts in the same region around each lattice site, showing a binomial distribution of occupied an unoccupied sites. (c) a fluorescence image, and the weighed sum of each lattice site. (d) the weighed sum of the NN of each occupied lattice site overlaid with the lattice, and a reconstruction of the lattice with occupied sites in red.

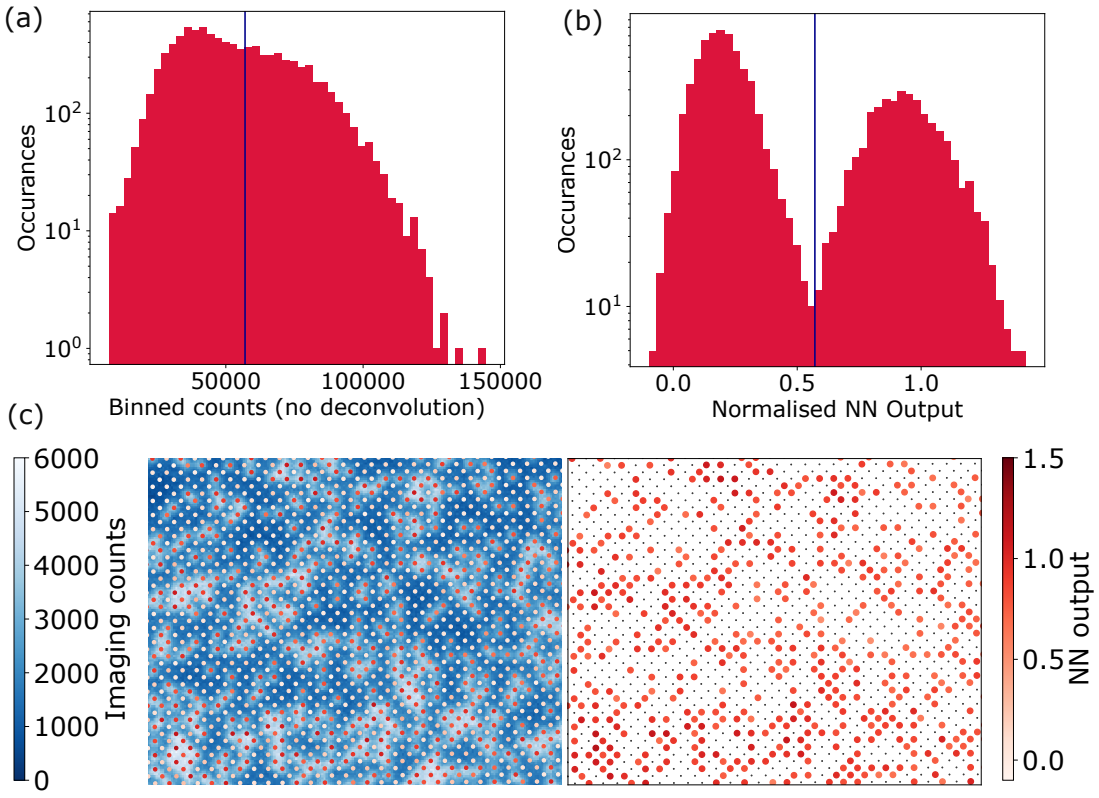

Figure 6.18: Reconstruction of a lattice with 35% filling. (a) and (b) show the histograms of counts on the ROI around each lattice site without and with the deconvolution applied respectively. (c) shows the reconstruction of the lattice.

CHAPTER 7

Spin resolved imaging of single RbCs molecules

The work detailed in the rest of the chapter is a part of a manuscript in preparation at the time of writing [253]. Some text and figures have been reproduced from early drafts of the manuscript and the supplementary materials of the same. We refer the reader to the same for further details about our spin-resolved microscopy.

In this chapter, we describe our work towards spin resolved imaging of clouds of RbCs molecules with single molecule resolution using the optical lattice. We begin by detailing the microwave spectroscopy we have performed of the $N = 1$ and $N = 2$ rotational levels of the molecule. We highlight the process behind imaging single molecules in the lattice, including the implementation of the blast beam, which acts to remove atoms from the molecular gas, as well as prevent light-assisted collisions (LACs) between the two atoms in the molecule during imaging. We then offer an overview of the sequence used to conduct spin resolved imaging, by mapping two different spin states of the molecule onto the two different constituent atoms of the molecule. Much of this work is in progress as this thesis is being written, and further details can be found in [253]

7.1 Microwave spectroscopy of RbCs molecules

With ground state molecules associated, we move on to driving molecular transitions to the different rotational levels. The RbCs ground state is the $|N, M_F\rangle = |0, 5\rangle$ state. We are able to drive transitions to the states $|1, 4\rangle$, $|1, 5\rangle$, and $|1, 6\rangle$. We further explore driving transitions to higher levels by driving the $|1, 5\rangle$ to $|2, 5\rangle$ transition.

The initial microwave spectroscopy of molecules was performed before the light sheet was in place, but when we were able to perform fluorescence imaging of Cs atoms in the 3D optical lattice (Fig. 6.6). We extract an atom number from the fluorescence with a linear fit, calibrated to the absorption imaging. This is done as the signal from the ≈ 2000 atoms imaged is relatively faint with absorption imaging, but is much brighter with fluorescence imaging - even without the ability to resolve individual atoms.[1]

As before, we dissociate the molecule back to its constituent atoms and image the atoms, with each atom acting as an indicator for the presence of a molecule. After preparing the molecules in a dipole trap as detailed before, we utilised a microwave pulse to change their state. STIRAP is a state selective process, so when the STIRAP from the $|G\rangle$ to $|F\rangle$ is performed, only molecules in the $|0, 5\rangle$ were transferred to the Feshbach state, and later dissociated into atoms. The lattice was then turned on to pin the atoms and fluorescence imaging is performed in the lattice.

Figure 7.1 shows the results from driving the various $N = 0$ to $N = 1$ transitions, located close to 980 MHz. We find each of the transitions utilising a short (less than the expected π pulse time), low-power (about 20 dBm into the antenna for a reasonable Rabi frequency and to avoid off resonant coupling to the other M_F states) microwave pulse onto the molecules, and measuring the number of molecules still in $N = 0$ by dissociating and imaging the atoms. Once the three expected transitions are observed, we perform Rabi flops on all the transitions to characterise the polarisation of the microwave antenna used. We make use of a microwave am-

[1] As we have shown, later upgrades involved the introduction of the light sheet and use of a larger camera, which allow for good single molecule resolved imaging of the whole cloud.

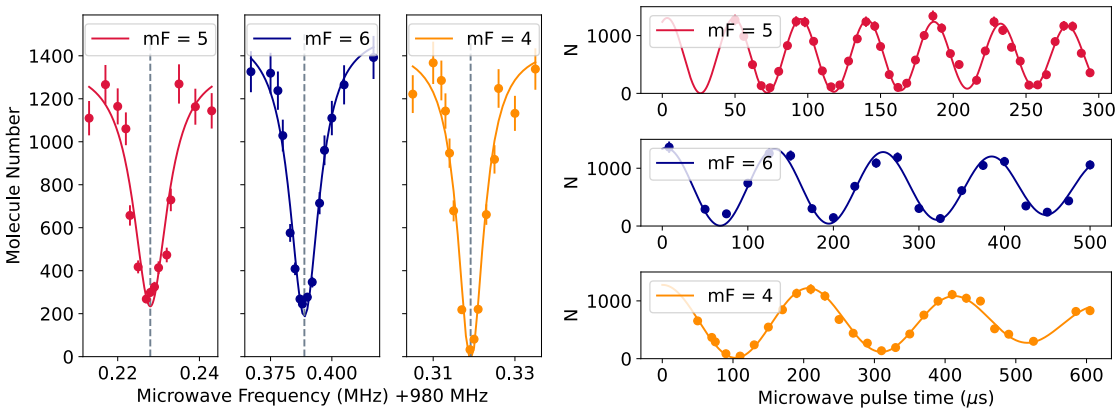

Figure 7.1: We perform microwave spectroscopy of all the $N = 0$ to $N = 1$ transitions available in RbCs from the ground state, and measure the Rabi frequencies of each of the transitions at a fixed power to characterise the polarisation of the microwaves emitted by our antenna (see Table 7.1)

plifier (MiniCircuits TVA-4W-422A+) here. The Rabi flops are shown in Fig. 7.1 for times starting at 50 μs[2].

Given the ratio of the Rabi frequencies of the transitions and the known transition dipole moments (TDMs), we are able to establish the polarisation of light out of the antenna (see Table 7.1). The TDMs were calculated using diatomic-py [254]. We find a ratio of approximately 4.9:2.7:1 for the electric field components that drive the π:σ^-:σ^+ transitions.

Transitions	$\|0,5\rangle$ to $\|1,4\rangle$	$\|0,5\rangle$ to $\|1,6\rangle$	$\|0,5\rangle$ to $\|1,5\rangle$
Calc. Freq. (MHz)	980.384	980.322	980.233
Measured Freq. (MHz)	980.387(1)	980.319(1)	980.228(1)
TDM ($\times 10^{-30}$ Cm^{-1})	1.60	2.36	2.18
Rabi Freq. (kHz)	7.84(8)	4.84(6)	21.8(1)
$\frac{E_i}{E_\pi}$	0.558	0.204	1

Table 7.1: A list of the measured $N = 0$ to $N = 1$ transitions in RbCs, with their Rabi frequencies when driven by the same antenna at the same power. We are able to calculate the polarisation of the electric field (from the components $E_{\sigma_+/\pi/\sigma_-}$) out of the antenna from this.

We then investigate transfer to $N = 2$ from $N = 1$. This is done using another microwave pulse, utilising the same antenna. With the transfer to $N = 1$ charac-

[2]Typical microwave amplifiers take 5-10 μs to ramp up the output power.

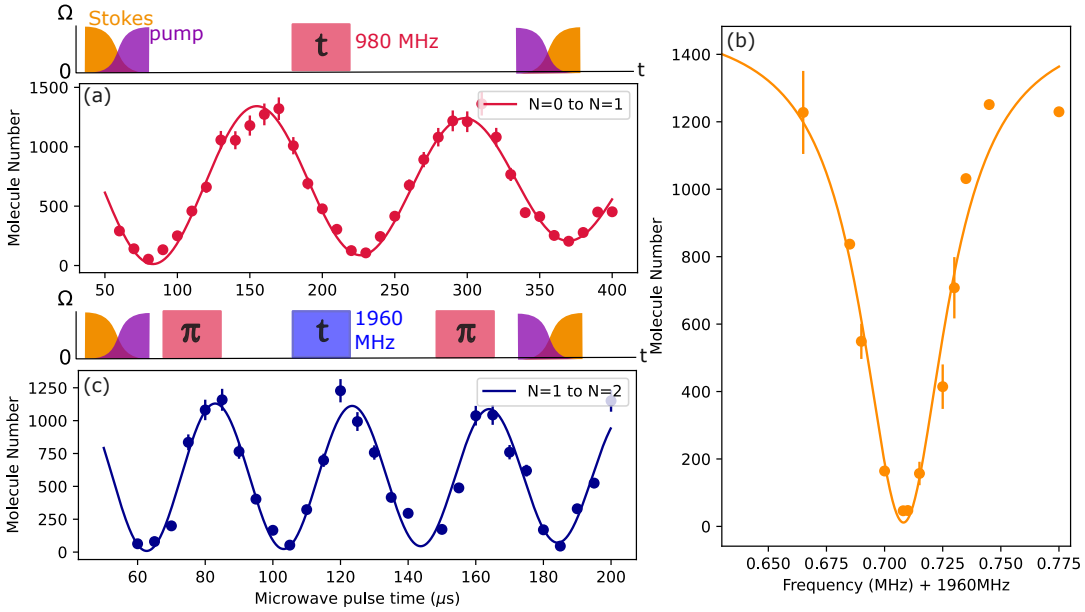

Figure 7.2: We perform microwave spectroscopy of the $|1,6\rangle$ to $|2,7\rangle$ transition, transferring molecules first to $N = 1$ with a π pulse, and then to $N = 2$. (a) shows a Rabi flop of the $|0,5\rangle$ to $|1,6\rangle$ transition along with the sequence used (above). After preparing the molecules in $|1,6\rangle$, we use another microwave pulse to transfer them to $|2,7\rangle$. (b) shows a scan of the microwave frequency for the $|1,6\rangle$ to $|2,7\rangle$ transition. (c) shows a Rabi flop on the $|1,6\rangle$ to $|2,7\rangle$. The atoms are transferred back to $|0,5\rangle$ with a π pulse for readout.

terised, we are able to use a microwave π pulse to transfer the molecular population to the $N = 1$ state. The population in the $N = 1$ state can be imaged by performing another π pulse (to transfer it to $N = 0$) and then dissociating. We transfer the molecule population to $N = 1$ and then scan for the stretched $|1,6\rangle$ to $|2,7\rangle$ transition as shown in Fig. 7.2. This is done in a similar manner to before, but imaging the $N = 1$ state instead, looking for a loss in $N = 1$ molecules when they are transferred to $N = 2$. From here, we are able to drive a Rabi flop between the $N = 1$ and $N = 2$ levels as well. With these transitions successfully addressed, we should be able to prepare the molecules in arbitrary mixtures of $N = 0$, $N = 1$ and $N = 2$ to investigate their collisional dynamics in the future.

7.2 Single molecule imaging in the optical lattice

7.2.1 Loading the lattice

Figure 7.3 shows the number of molecules measured as a function of the hold time in the lattice. We see a fast initial loss, followed by a slower loss rate of molecules. Similar dynamics have been seen before for molecules in lattices, for example in [255]. There, it was suggested that this initial fast loss of some molecules could be due to collisions. We currently are unsure of the exact mechanism behind this loss, and tentatively attribute it to a combination of collisional loss and evaporative loss with some molecules suffering a rapid loss as they are not captured by the trapping potential. The slower loss throughout this hold time is attributed to loss from scattering of trapping photons [117, 256]. In the future, preparation of colder gases should enable the use of lower optical power in the lattice.

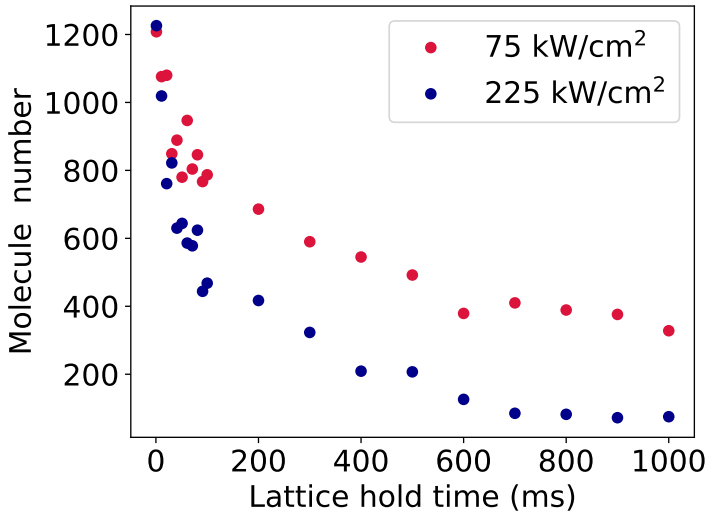

Figure 7.3: Lifetime of molecules in the lattice. We measure the lifetime of molecules in the optical lattice for different peak lattice intensities. We suspect the loss to be due to a combination of evaporative loss as the molecules are loaded into the lattice, and loss from scattering lattice photons. We must balance the two loss mechanisms. As can be seen, turning the lattice up high to prevent all evaporative loss does not work, as the molecules are lost rapidly due to scattering of the lattice photons.

7.2.2 The blast beam

With the light sheet in place and imaging characterised for both species, we proceed to attempt imaging molecules with single molecule resolution. In our initial attempts at imaging Feshbach molecules and ground state molecules, we proceeded as was described in the previous section, by dissociating the molecules and then trapping the atoms in the optical lattice and imaging the two species. While we were able to image molecules successfully this way, we noted a background signal of up to 50 atoms that were not removed successfully during the magnetic purification step, and remained trapped with the molecules. As we image the molecules by imaging the constituent atoms, this significantly limits the capabilities of the experiment to resolve low molecule numbers.

As shown in Fig. 7.4 (a) and (b), we implemented a high field resonant 'blast' beam to remove all atoms from the trap, and have a pure molecular gas. The blast beam is sourced from the cooling light used for the $2D^+$ MOTs for both Rb and Cs. The light is modulated with an EOM, with sidebands added at the appropriate frequencies to tune the beam to address the F=3 to F'=4 transition at 181 G. The light for both blast beams is combined and directed at the atoms in the science cell. We find that the blast is very effective for both species. We test this by loading an initial sample of $\approx 10^5$ atoms of each species and then removing them away with the appropriate blast beam. We utilise a 100 μs pulse of light, with ≈ 2 mW of light on the atoms. We then image the remnants of the cloud after the blast and see that we are left with a mean atom number of <3 atoms for both species. Fig. 7.4 (a) shows Cs atoms imaged without dissociating the molecule cloud, and Fig. 7.4 (b) shows the same sequence with the addition of a blast beam. As expected, when the atoms are blasted, we see no signal.

7.2.3 Single molecule resolved images

We are now able to attempt imaging single ground state molecules in the optical lattice[3]. Figure 7.5 (a) shows a schematic overview of the sequence used. As before,

[3]Dramatic music plays as we thank the reader for their patience

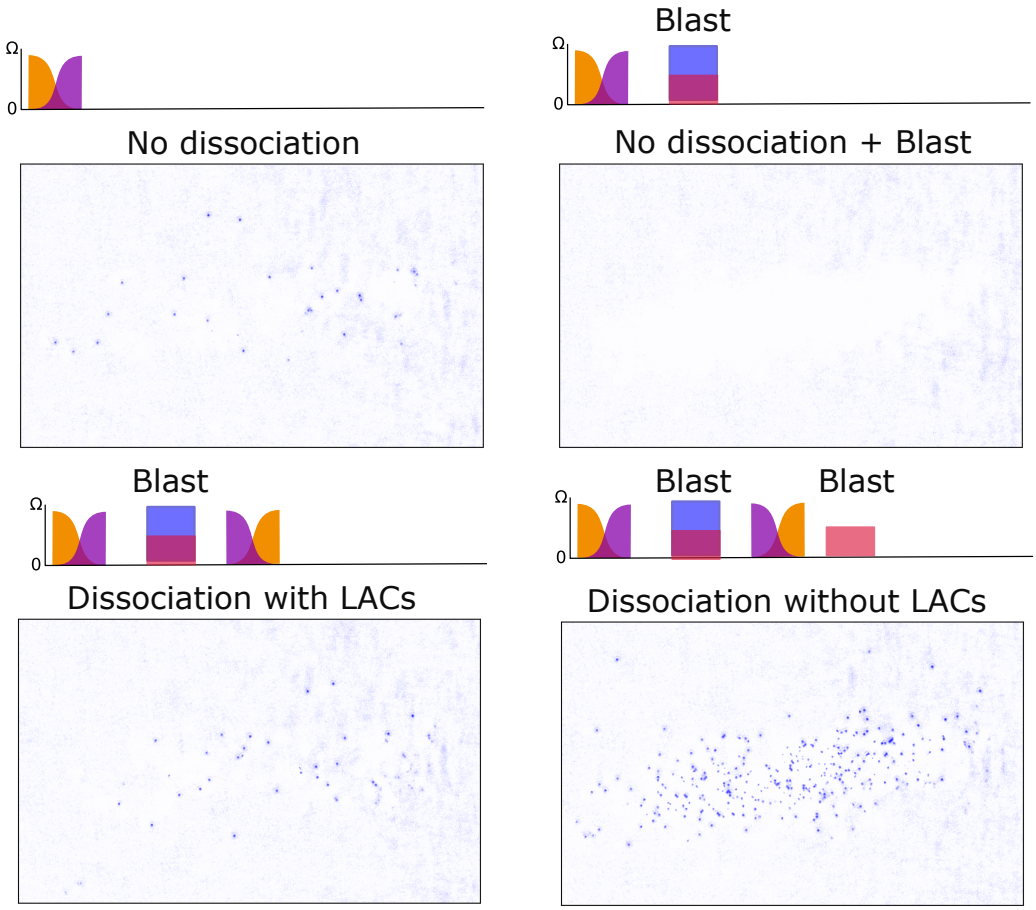

Figure 7.4: Images of atoms from the molecular cloud (taken by imaging Cs) with and without the blast beam. (a) shows the molecular cloud imaged without dissociating the molecule. We expect no signal, but still see some signal due to incomplete purification, which means that some Cs atoms are still present in the molecular gas. Introducing a blast beam leads to a removal of all the atoms. In (c) we blast atoms before loading the molecules into a lattice, and then image the molecular cloud after the molecules are dissociated in the lattice. We see very few atoms imaged due to LACs between Rb and Cs from the same molecule on the same site. (d) shows the same sequence imaging Cs, after Rb atoms are blasted out after dissociation. We see an increase in the measured molecule number, as atoms are no longer lost to LACs.

we prepare ground state molecules in a dipole trap. We blast out any remaining free atoms in the trap to leave a pure molecular cloud. The molecules are then loaded into the horizontal lattice and light sheet before they are dissociated in the lattice into

their constituent atoms[4]. The STIRAP to transfer to the $|F\rangle$ state is performed in a weak optical lattice (of depth $\approx 50\ E_{\mathrm{rec}}$). STIRAP must be performed in a relatively weak lattice to avoid any light shifts from the lattice beams. The lattice is then ramped up to a higher depth to pin the molecules ($\approx 5000\ E_{\mathrm{rec}}$) and the molecules are dissociated into the atoms. We then are left with an atom pair on each site corresponding to each former molecule.

If two atoms are trapped on the same site are imaged using the optical molasses, we expect fast light-assisted collisions (LACs) to lead to a loss of the atoms during the molasses imaging. So, we must blast away one atomic species, and image the other. Figure 7.4 shows the difference in imaged Cs atoms with and without the removal of all Rb atoms (using the blast beam) after the dissociation. Comparing measured atom numbers with and without the blast beam, we see that $\approx 85\%$ of the Cs atoms are lost to LACs if imaged without a Rb blast beam. Further details of the LACs in the experiment are discussed in [253].

Figure 7.5 shows images of a cloud of molecules imaged with single molecule resolution, imaged using both Rb and Cs (in different sequences). We perform the microscopy as before, and are able to reconstruct the optical lattice and determine the occupancy of each site and the number of molecules present. With our imaging system, we are able to image the entire molecular cloud, with single molecule resolution. In the images shown we image either Rb or Cs from every molecule in the cloud.

We note that using our current experimental scheme, we do not have the capability to experimentally confirm that all our molecules are loaded and then imaged on the same site. Over the hold time in the lattice, the molecules may tunnel in the lattice, particularly as they are not prepared in the lattice ground band [257]. The molecules temperature is estimated from the atomic temperatures to be $\approx 1\ \mu$K , while the lattice depth should be $\approx 50\ \mu$K during the hold time, which should minimise tunnelling. So, we expect this tunnelling to be minimal given the difference in depths of the lattice and the molecule temperature.

[4]Note that we now dissociate the molecules in the lattice, so we form an atom pair that should be confined to a single lattice site (rather than dissociate first and then ramp up the lattice)

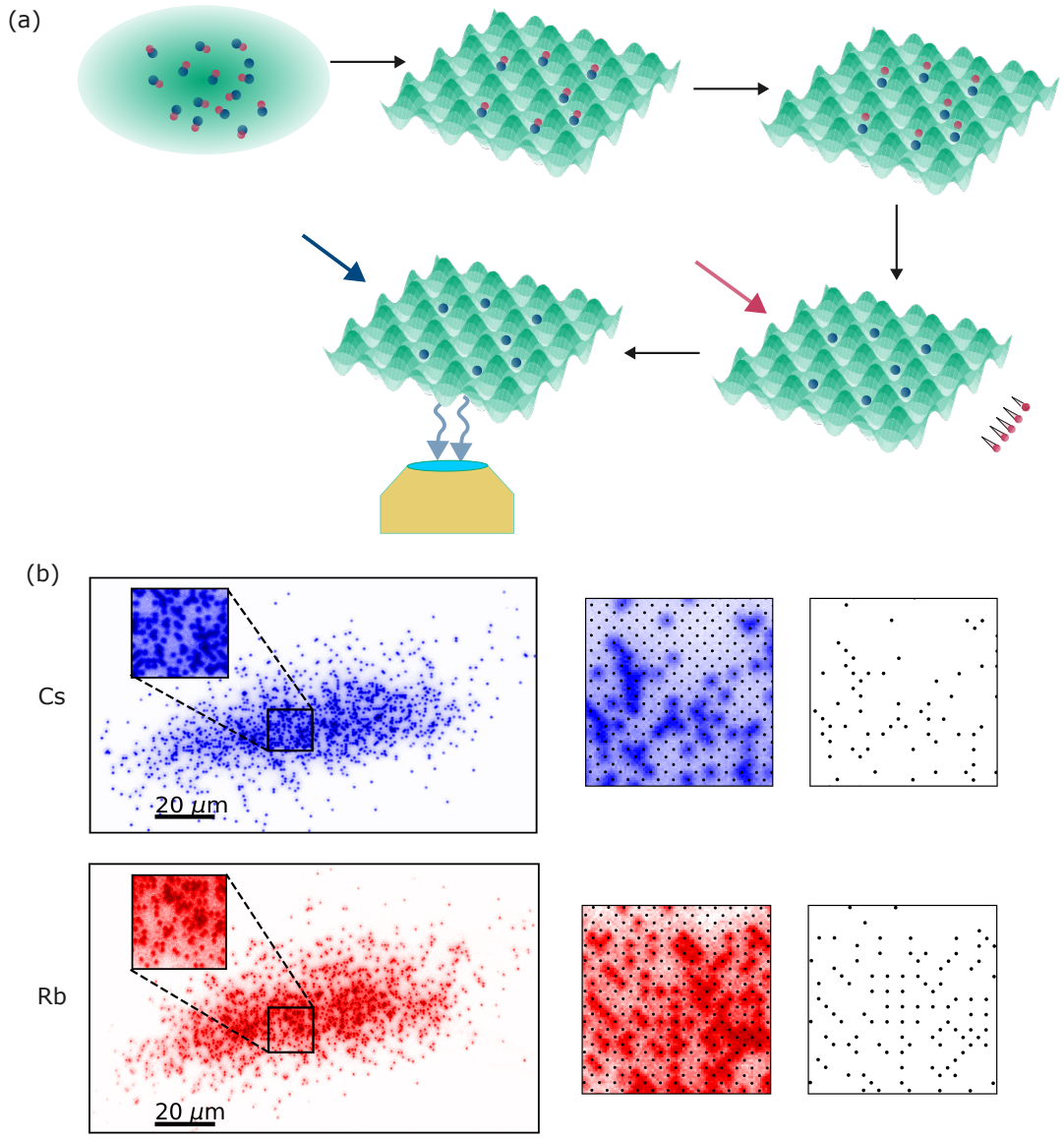

Figure 7.5: Single molecule resolved imaging in the optical lattice. Cs is shown in blue, and Rb in red. As shown in (a), we form molecules in the dipole trap, load them into the lattice and then dissociate in the lattice. We remove one atomic species from the lattice with a blast beam, and then image the other. We expect the remaining atoms to tag the lattice sites the molecules were on. As we are able to image both Rb and Cs in the microscope, we can image the molecules by blasting Rb and imaging Cs, or by blasting Cs and then imaging Rb as shown in (b). We get a similar molecule number in both cases (≈ 1300 for the images displayed here) after reconstructing the lattice.

While it is difficult to directly confirm that the atoms do not tunnel during the lattice hold, we are able to place some bounds on the tunnelling. The loss of $\approx 85\%$ of the atoms to LACs when one species is not blasted out implies that the majority

of atoms remain on the same lattice site they were dissociated in. While the loss to the LACs sets an upper bound on the fraction of atoms that are tunnelling in the lattice, we should consider that atoms could be recaptured in the lattice onto an empty site after being ejected from their initial site by a LAC. Note that the tunnelling of atoms we refer to here occurs during the hold in the lattice before imaging occurs. The tunnelling/loss during the imaging itself should be minimal as was optimised for earlier.

We should be able to easily quantify the molecular and atomic confinement and tunnelling in the lattice by associating molecules in the lattice and imaging both atoms from the same molecule in one sequence, plans for which are briefly detailed in the Outlook (Sec. 8.3).

7.3 Spin resolved imaging of RbCs

We utilise the method proposed in [84] to map the rotational state of the molecule to the species to be imaged. This relies on a series of state manipulations detailed below. The state selectivity of the STIRAP is crucial, where only molecules in $N = 0$ are transferred to $|F\rangle$, while molecules in other rotational levels are unaffected.

Figure 7.6 details the sequence used to map the different rotational states of the molecule onto different species. First, we prepare molecules in a dipole trap and prepare them in some mixture of $N = 0$ and $N = 1$ using a microwave pulse. We then conduct STIRAP to transfer the molecules in $N = 0$ to $|F\rangle$ ($N = 1$ molecules are not affected). After this we perform a microwave π pulse to transfer $N = 1$ molecules to $N = 0$[5]. The molecules in $|F\rangle$ are then dissociated to atom pairs of Rb in $|1, 1\rangle$ and Cs in $|3, 3\rangle$ by ramping the magnetic field up over the Feshbach resonance. The Cs atoms in the atom pairs are then blasted away using the Cs blast beam. The molecules in $N = 0$ (originally $N = 1$) are unaffected by the field ramps and the Cs blast. The molecules originally in $N = 0$ have now been converted to Rb atoms in the state $|1, 1\rangle$. The magnetic field is then reduced to 5 G[6], and the

[5]This is done to avoid molecules in $N = 1$ changing state as the field is ramped down, as an avoided crossing is reached.

[6]While theoretically we do not need to do this, practically magnetic field noise at the high field

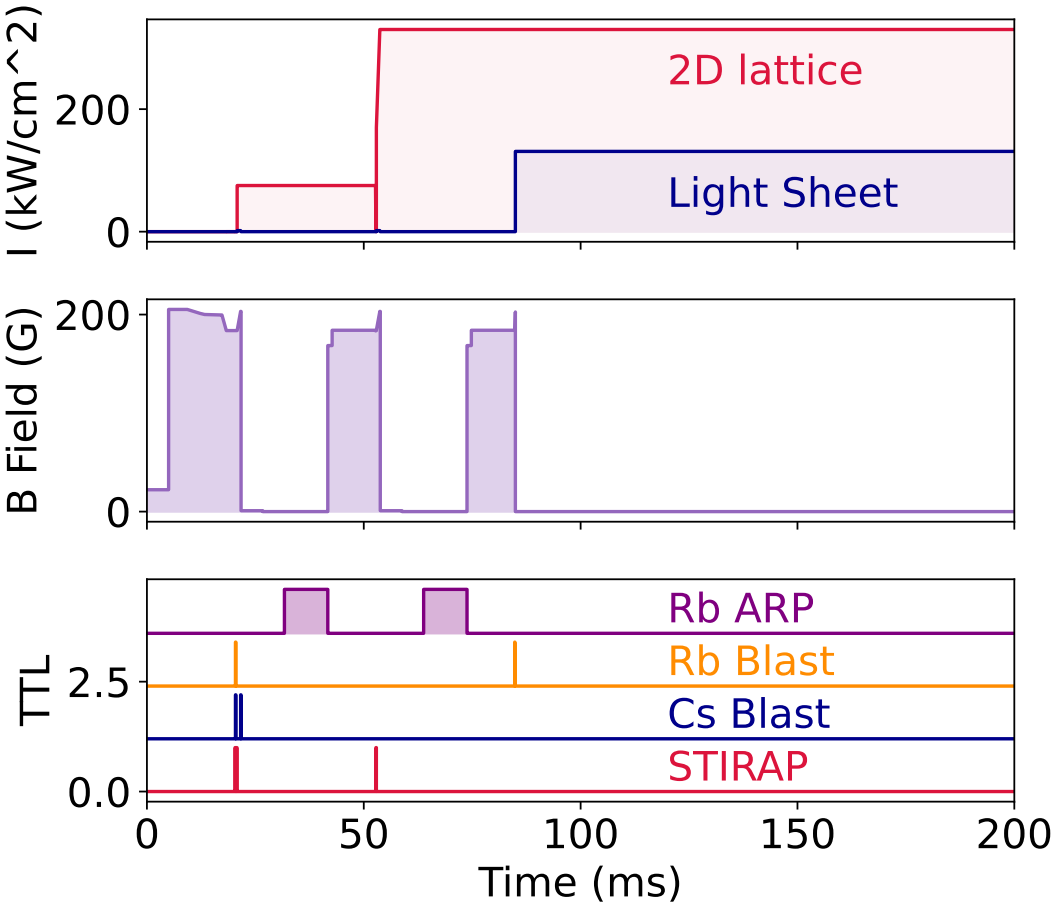

Figure 7.6: The sequence used for spin resolved microscopy of the molecules. The top panel shows the depth of the lattice and the light sheet. The middle panel shows the magnetic field. The lower panel shows the status of the TTLs used to set the ARP, the blast pulses and the STIRAP.

Rb atoms are transferred to the state $|2,2\rangle$ using microwave adiabatic rapid passage (ARP). We then return to a magnetic field of 181.5 G and perform another STIRAP pulse followed by a magnetic field ramp to convert the molecules in $N = 0$ to atom pairs. Molecules initially in $N = 0$ have now been converted to Rb atoms in $|2,2\rangle$, while molecules in $N = 0$ are now atom pairs of Rb in $|1,1\rangle$ and Cs in $|3,3\rangle$. We then return to a magnetic field of 5 G and perform another ARP pulse on Rb. This transfers the Rb atoms in $|1,1\rangle$ to $|2,2\rangle$, and crucially transfers the atoms in $|2,2\rangle$ to $|1,1\rangle$. The ARP pulses take 10 ms. We then blast *only* the Rb atoms in $|2,2\rangle$ using

reduced the ARP efficiency, so we go to low fields

the blast beam. So, we are left with Rb atoms in $|1,1\rangle$ tagging $N = 0$ molecules were and Cs atoms in $|3,3\rangle$ tagging $N = 1$ molecules. These atoms can then be imaged sequentially using the microscope, and the image deconvolved to count the atoms.

As shown in Fig. 7.7, we then implement the scheme to map the $N = 0$ state to Rb and the $N = 1$ state to Cs and drive a Rabi flop between the two states, measuring the number of atoms of each species in each shot (and hence the number of atoms in each rotational state in each shot). We are able to see a clear Rabi flop, which shows that the sequence works as expected.

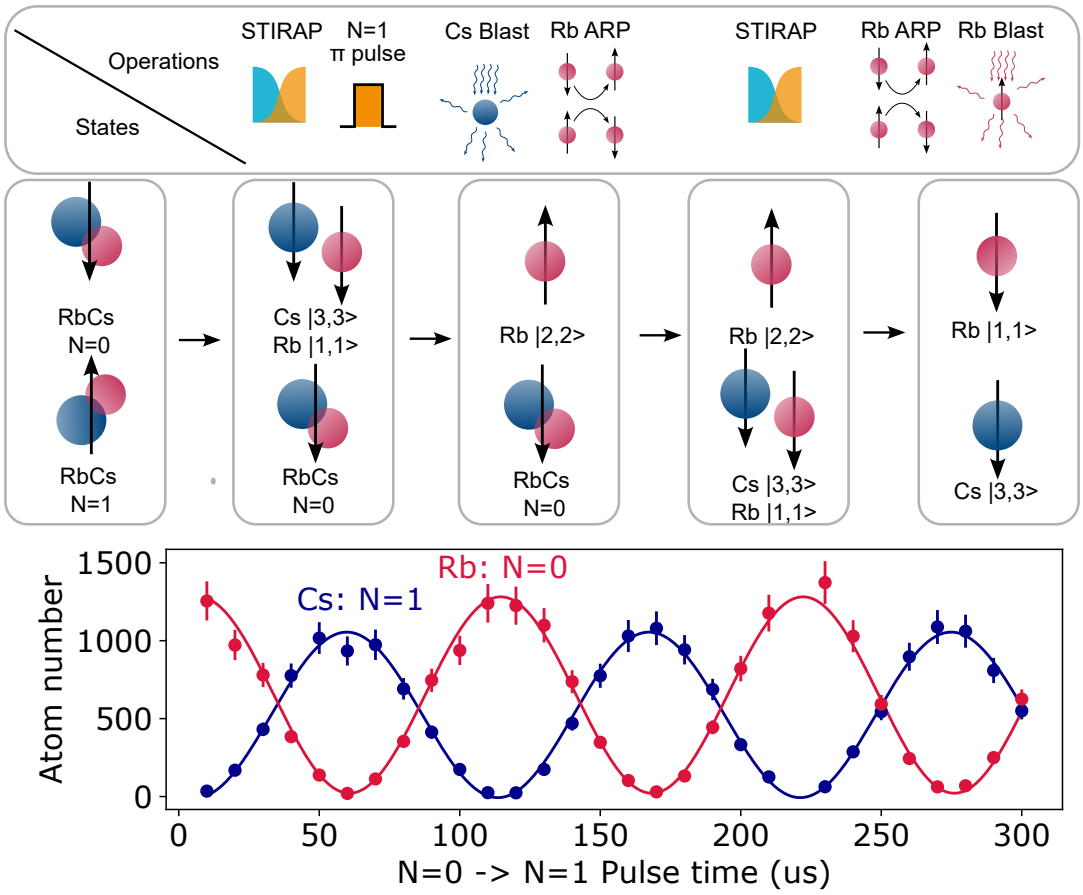

Figure 7.7: Spin resolved microscopy of molecules. (a) shows how molecules in the $N = 0$ state are mapped onto Rb and molecules in the $N = 1$ state are mapped onto Cs. (b) shows a Rabi flop driven between $N = 0$ and $N = 1$, where the molecules are imaged using the spin resolved sequence. We see a clear Rabi flop with Rb ($N = 0$) and Cs ($N = 1$) oscillating as expected.

With such an involved sequence, we must be careful about the prorogation of errors through the sequence. We find that our state detection fidelities are limited by the STIRAP efficiency, the ARP efficiency and the lifetime of the ground state molecules in the lattice. In addition, the parity projection where sites with 2 molecules (or more) suffer loss leads to a reduction in the measured molecule number.

We have measured these sources of error. The predominant source of loss is the loss of the molecules during the $\approx$ 50ms it is held in the lattice before it is dissociated (initially $N = 1$, but in $N = 0$ when the loss happens). This is the time required to ramp the magnetic field down, perform ARP on Rb and then ramp the field back up to 181 G to dissociate the remainder of the molecules. We measure a loss of $22 \pm 4\%$ of the molecules in this time. This would propagate forward as an asymmetric loss in Cs atoms imaged (tagging $N = 1$). The STIRAP efficiency for both STIRAP pulses in the lattice is measured to be $95 \pm 1\%$, consistent with our previous measurements of STIRAP in free space. The ARP efficiency was measured to be $98.9 \pm 0.4\%$. While errors from STIRAP appear equally in the measurement of $N = 1$ and $N = 0$, the asymmetric error caused by the molecule loss in the lattice dominates, and is visible in the measurement of a Rabi flop as the height of the $N = 0$ signal is larger than that of the $N = 1$ signal.

The proof of principle measurement of a Rabi flop of an ultracold molecule with the spin-species mapping sequence demonstrates the efficacy of this method, and that the molecule microscope apparatus functions as expected. We hope to now utilise the experiment investigating the dynamics of ultracold molecules in optical lattices.

CHAPTER 8

Conclusions and outlook

In this thesis I have described the work done in the past few years, as we have constructed an apparatus that can image ultracold molecules of RbCs with single molecule resolution. To conclude the thesis, we present a short summary of the work described here, and a brief outlook on the future of the experiment.

8.1 Summary

In this thesis, we have described the association and subsequent microscopy of an ultracold molecular gas of RbCs. We utilise a sequential loading scheme to evaporatively cool Rb and Cs to degeneracy in separate traps. We merge the atomic clouds and associate them using magneto-association, followed by state transfer to the ground state via STIRAP, resulting in a cloud of about 2500 molecules. We describe the setup and optimisation of the apparatus for the magneto-association and for the STIRAP, as well as the implementation of an optical feedforward scheme to improve the STIRAP efficiency to 98.7 $\pm$ 0.1%. We then conducted microscopy of both Rb and Cs, and described the setup and characterisation of the sequence for the same. Finally, we discussed our early results in the microscopy of ground state

molecules, including the spin-resolved sequence.

8.2 Investigating collisions of molecules

Typical bulk gas ultracold molecule experiments which use absorption imaging are only able to resolve molecule numbers of ≈ 100. With the experiment in its current state, we are able to image molecular clouds with single molecule resolution. This allows us the opportunity to investigate the dynamics of impurity states of $< 10\%$ in the molecules. We initially plan to investigate the rotational state dependant collisions of the molecules in greater detail. Currently, the plan is to prepare a mixture of ≈ 100 molecules in a state $|A\rangle$ and ≈ 1000 molecules in a state $|B\rangle$. Here, the loss of molecules in state $|B\rangle$ should be dominated by their collisions with those in state $|A\rangle$. It has been theorised that the loss rates between $|N=0\rangle + |N=0\rangle$, $|N=0\rangle + |N=1\rangle$ and $|N=0\rangle + |N=2\rangle$ vary by more than an order of magnitude [258], which we hope to see with such an experiment.

8.3 Associating molecules in the lattice

In our current experimental scheme, we produce our molecules in a dipole trap from non-degenerate atomic mixtures of Rb and Cs. The association efficiency is limited to $\approx 5\%$, and the molecules produced are at fairly high temperatures (200 nK if we assume that they are the same temperature as the atoms used to associate them), and are thus not able to be prepared in the ground band of the lattice easily. In order to mitigate these two situations, we plan to produce molecules in an optical lattice from a dual Mott-insulator of Rb and Cs, as described in [113].

We plan to evaporate Rb and Cs to a BEC simultaneously (As we have shown to be capable of) and then ramp on the lattice to where Cs in a Mott insulting state with mean occupancy N=1 per lattice site. At this time, Rb is still in the superfluid state (as it has a lower polarisability than Cs, so the lattice depth is lower). We then plan to merge the Rb superfluid with the Cs Mott insulator, at a field where the Rb-Cs three-body loss is minimised (near the 352 G resonance). Cs-Cs-Cs three-

body loss is no longer an issue here since Cs is in a Mott insulating state. With an Rb superfluid overlapped over the Cs Mott insulator, we increase the lattice depth to put Rb into a Mott insulating state as well. We now hope to have a dual-species Mott insulator with one Rb atom and one Cs atom, both in the lattice ground band on the same site. Feshbach association can then be performed as before, and we expect to see near unity association probabilities. We hope that this leads to an improvement in molecule number and PSD, with all the molecules prepared in the ground band. This should help us realise a densely populated lattice.

Further improvements to this sequence envisioned include the use of a shallow angle lattice to separate the Rb and the Cs atoms. The lattice will be at a wavelength that is attractive to Rb and repulsive to Cs (say 817 nm). The plan here is to super impose a shallow angle lattice, with vertical lattice spacing of ≈ 1 μm onto the horizontal lattice and light sheet. This will be done before the species are merged. We then expect to have a dual-species Mott insulator, with Rb and Cs separated vertically (as Rb is present in the shallow angle lattice nodes, and Cs in the anti-nodes). We merge the Mott insulators by ramping down the lattice power. When imaging, instead of using a blast beam, we will be able to turn this shallow angle lattice back on, separating the Rb and Cs, while still pinning them in the lattice. We should then be able to avoid LACs and image both Rb and Cs from the *same* atom, at the same horizontal position giving us a definite confirmation of the spatial resolution of the microscope. The shallow angle lattice has currently been designed, tested and implemented in the experiment, but we find that the current molasses temperature is too hot to preserve the site resolution. So, this would have to be coupled with improvements to our molasses, perhaps using a 2-beam molasses, a gray molasses, or even a Raman sideband cooling for a colder imaging.

8.4 A magic wavelength optical lattice

Currently, we utilise a lattice with 1064 nm light. We expect the rotational coherence time to be too small to resolve any dipole-dipole interactions directly in this lattice. We instead plan to use a 'magic' wavelength lattice, where we utilise a wave-

length (1146 nm) selected to eliminate the state dependant differential light shift between the rotational states, and allow for longer coherence times. Recent work from the other RbCs experiments in Durham has shown long rotational coherences for RbCs both in an optical lattice [67], and in optical tweezers [68], with the latter demonstrating coherence times of ≈15 s. Work is currently underway to setup a laser at the magic wavelength to be used for both the optical lattice and the light sheet beam

8.5 Dipole-dipole interactions of molecules

After these upgrades, a magic wavelength lattice with densely loaded molecules is in reach, and we will be able to resolve dipole-dipole interactions in the lattice. We plan to initially investigate correlations between molecules and molecular chains in adjacent lattice sites, perhaps comparing results with similar experiments done in the neighbouring tweezer lab. Then we will move on to investigating lattice physics phenomena, as were mentioned in the introduction. Examples of future research include the simulation of anisotropic Hamiltonians such as XXZ Hubbard models, quantum magnetism, with potential for realisation of the t-J-V-W model and exotic phases of matter, including spin liquids, and spin glasses [43–46, 48, 49, 78].

8.6 Concluding remarks

The work presented in this thesis, where we have presented the association of molecules, their transfer to the ground state and their subsequent microscopy draws to an end the first stage of the experiment. Building on the previous work [118, 148, 160, 222], the construction of the experiment is now complete[1], and we are on the cusp of utilising it to investigate molecular and lattice dynamics with dipolar interactions. The future is bright[2] in the microscope lab. With the realisation of a microscope for RbCs molecules, we now can move forward to investigating in-

[1] To first order
[2] As long as all the lasers keep working

teractions between the molecules and dipping our toes into the seas[3] of quantum simulation.

[3] or Cs

Bibliography

[1] S. Chu, J. E. Bjorkholm, A. Ashkin, and A. Cable, "Experimental Observation of Optically Trapped Atoms," *Physical Review Letters*, vol. 57, pp. 314–317, July 1986. Publisher: American Physical Society. 1.1, 3.2.3

[2] A. L. Migdall, J. V. Prodan, W. D. Phillips, T. H. Bergeman, and H. J. Metcalf, "First Observation of Magnetically Trapped Neutral Atoms," *Physical Review Letters*, vol. 54, pp. 2596–2599, June 1985. Publisher: American Physical Society. 1.1

[3] P. D. Lett, R. N. Watts, C. I. Westbrook, W. D. Phillips, P. L. Gould, and H. J. Metcalf, "Observation of Atoms Laser Cooled below the Doppler Limit," *Physical Review Letters*, vol. 61, pp. 169–172, July 1988. Publisher: American Physical Society. 1.1

[4] M. H. Anderson, J. R. Ensher, M. R. Matthews, C. E. Wieman, and E. A. Cornell, "Observation of Bose-Einstein Condensation in a Dilute Atomic Vapor," *Science*, vol. 269, pp. 198–201, July 1995. Publisher: American Association for the Advancement of Science. 1.1, 2.1.1

[5] K. B. Davis, M. O. Mewes, M. R. Andrews, N. J. van Druten, D. S. Durfee, D. M. Kurn, and W. Ketterle, "Bose-Einstein Condensation in a Gas of Sodium Atoms," *Physical Review Letters*, vol. 75, pp. 3969–3973, Nov. 1995. Publisher: American Physical Society. 1.1, 2.1.1

[6] C. C. Bradley, C. A. Sackett, J. J. Tollett, and R. G. Hulet, "Evidence of Bose-Einstein Condensation in an Atomic Gas with Attractive Interactions," *Physical Review Letters*, vol. 75, pp. 1687–1690, Aug. 1995. Publisher: American Physical Society. 1.1

[7] B. DeMarco and D. S. Jin, "Onset of Fermi Degeneracy in a Trapped Atomic Gas," *Science*, vol. 285, pp. 1703–1706, Sept. 1999. Publisher: American Association for the Advancement of Science. 1.1

[8] F. Schreck, L. Khaykovich, K. L. Corwin, G. Ferrari, T. Bourdel, J. Cubizolles, and C. Salomon, "Quasipure Bose-Einstein Condensate Immersed in a Fermi Sea," *Physical Review Letters*, vol. 87, p. 080403, Aug. 2001. Publisher: American Physical Society. 1.1

[9] B. W. Reichardt, A. Paetznick, D. Aasen, I. Basov, J. M. Bello-Rivas, P. Bonderson, R. Chao, W. v. Dam, M. B. Hastings, A. Paz, M. P. d. Silva, A. Sundaram, K. M. Svore, A. Vaschillo, Z. Wang, M. Zanner, W. B. Cairncross, C.-A. Chen, D. Crow, H. Kim, J. M. Kindem, J. King, M. McDonald, M. A. Norcia, A. Ryou, M. Stone, L. Wadleigh, K. Barnes, P. Battaglino, T. C. Bohdanowicz, G. Booth, A. Brown, M. O. Brown, K. Cassella, R. Coxe, J. M. Epstein, M. Feldkamp, C. Griger, E. Halperin, A. Heinz, F. Hummel, M. Jaffe, A. M. W. Jones, E. Kapit, K. Kotru, J. Lauigan, M. Li, J. Marjanovic, E. Megidish, M. Meredith, R. Morshead, J. A. Muniz, S. Narayanaswami, C. Nishiguchi, T. Paule, K. A. Pawlak, K. L. Pudenz, D. R. Pérez, J. Simon, A. Smull, D. Stack, M. Urbanek, R. J. M. v. d. Veerdonk, Z. Vendeiro, R. T. Weverka, T. Wilkason, T.-Y. Wu, X. Xie, E. Zalys-Geller, X. Zhang, and B. J. Bloom, "Logical computation demonstrated with a neutral atom quantum processor," Nov. 2024. arXiv:2411.11822 [quant-ph]. 1.1, 1.2

[10] S. J. Evered, D. Bluvstein, M. Kalinowski, S. Ebadi, T. Manovitz, H. Zhou, S. H. Li, A. A. Geim, T. T. Wang, N. Maskara, H. Levine, G. Semeghini, M. Greiner, V. Vuletić, and M. D. Lukin, "High-fidelity parallel entangling gates on a neutral-atom quantum computer," *Nature*, vol. 622, pp. 268–272, Oct. 2023. Publisher: Nature Publishing Group. 1.1, 1.2

[11] P. Scholl, M. Schuler, H. J. Williams, A. A. Eberharter, D. Barredo, K.-N. Schymik, V. Lienhard, L.-P. Henry, T. C. Lang, T. Lahaye, A. M. Läuchli, and A. Browaeys, "Quantum simulation of 2D antiferromagnets with hundreds of Rydberg atoms," *Nature*, vol. 595, pp. 233–238, July 2021. Publisher: Nature Publishing Group. 1.1, 1.2

[12] S. Ebadi, T. T. Wang, H. Levine, A. Keesling, G. Semeghini, A. Omran, D. Bluvstein, R. Samajdar, H. Pichler, W. W. Ho, S. Choi, S. Sachdev, M. Greiner, V. Vuletić, and M. D. Lukin, "Quantum phases of matter on a 256-atom programmable quantum simulator," *Nature (London)*, vol. 595, July 2021. Institution: Harvard Univ., Cambridge, MA (United States) Publisher: Nature Publishing Group. 1.1, 1.2

[13] C. Gross and W. S. Bakr, "Quantum gas microscopy for single atom and spin detection," *Nature Physics*, vol. 17, pp. 1316–1323, Dec. 2021. Publisher: Nature Publishing Group. 1.1.1

[14] W. S. Bakr, J. I. Gillen, A. Peng, S. Fölling, and M. Greiner, "A quantum gas microscope for detecting single atoms in a Hubbard-regime optical lattice," *Nature*, vol. 462, pp. 74–77, Nov. 2009. 1.1.1, 2.5, 3.1, 6.2, 6.2

[15] J. F. Sherson, C. Weitenberg, M. Endres, M. Cheneau, I. Bloch, and S. Kuhr, "Single-atom-resolved fluorescence imaging of an atomic Mott insulator," *Na-*

ture, vol. 467, pp. 68–72, Sept. 2010. Publisher: Nature Publishing Group. 1.1.1, 2.5, 3.1, 6.2, 6.2, 6.7.3

[16] E. Haller, J. Hudson, A. Kelly, D. A. Cotta, B. Peaudecerf, G. D. Bruce, and S. Kuhr, "Single-atom imaging of fermions in a quantum-gas microscope," *Nature Physics*, vol. 11, pp. 738–742, Sept. 2015. Publisher: Nature Publishing Group. 1.1.1, 2.5, 3.1

[17] L. W. Cheuk, M. A. Nichols, M. Okan, T. Gersdorf, V. V. Ramasesh, W. S. Bakr, T. Lompe, and M. W. Zwierlein, "Quantum-Gas Microscope for Fermionic Atoms," *Physical Review Letters*, vol. 114, p. 193001, May 2015. Publisher: American Physical Society. 1.1.1, 2.5, 3.1

[18] M. F. Parsons, F. Huber, A. Mazurenko, C. S. Chiu, W. Setiawan, K. Wooley-Brown, S. Blatt, and M. Greiner, "Site-Resolved Imaging of Fermionic 6Li in an Optical Lattice," *Physical Review Letters*, vol. 114, p. 213002, May 2015. Publisher: American Physical Society. 1.1.1, 2.4.1, 2.5

[19] A. Omran, M. Boll, T. A. Hilker, K. Kleinlein, G. Salomon, I. Bloch, and C. Gross, "Microscopic Observation of Pauli Blocking in Degenerate Fermionic Lattice Gases," *Physical Review Letters*, vol. 115, p. 263001, Dec. 2015. Publisher: American Physical Society. 1.1.1, 2.4.1, 2.5, 3.1

[20] O. Elíasson, J. S. Laustsen, R. Heck, R. Müller, J. J. Arlt, C. A. Weidner, and J. F. Sherson, "Spatial tomography of individual atoms in a quantum gas microscope," *Physical Review A*, vol. 102, p. 053311, Nov. 2020. Publisher: American Physical Society. 1.1.1, 2.5, 6.2

[21] A. Impertro, J. F. Wienand, S. Häfele, H. von Raven, S. Hubele, T. Klostermann, C. R. Cabrera, I. Bloch, and M. Aidelsburger, "An unsupervised deep learning algorithm for single-site reconstruction in quantum gas microscopes," *Communications Physics*, vol. 6, pp. 1–8, July 2023. Number: 1 Publisher: Nature Publishing Group. 1.1.1, 2.4.1, 2.5, 6.2, 6.7.1, 6.9

[22] G. J. A. Edge, R. Anderson, D. Jervis, D. C. McKay, R. Day, S. Trotzky, and J. H. Thywissen, "Imaging and addressing of individual fermionic atoms in an optical lattice," *Physical Review A*, vol. 92, p. 063406, Dec. 2015. Publisher: American Physical Society. 1.1.1, 2.5, 3.1

[23] M. S. Miranda, *Quantum gas microscope for ytterbium atoms*. PhD thesis, Tokyo Institute of Technology, March 2016. 1.1.1, 3.3.1

[24] R. Yamamoto, J. Kobayashi, T. Kuno, K. Kato, and Y. Takahashi, "An ytterbium quantum gas microscope with narrow-line laser cooling," *New Journal of Physics*, vol. 18, p. 023016, Feb. 2016. Publisher: IOP Publishing. 1.1.1, 2.4.1, 3.1

[25] L. Su, A. Douglas, M. Szurek, R. Groth, S. F. Ozturk, A. Krahn, A. H. Hébert, G. A. Phelps, S. Ebadi, S. Dickerson, F. Ferlaino, O. Marković, and M. Greiner, "Dipolar quantum solids emerging in a Hubbard quantum simulator," *Nature*, vol. 622, pp. 724–729, Oct. 2023. Publisher: Nature Publishing Group. 1.1.1

[26] S. Buob, J. Höschele, V. Makhalov, A. Rubio-Abadal, and L. Tarruell, "A Strontium Quantum-Gas Microscope," *PRX Quantum*, vol. 5, p. 020316, Apr. 2024. Publisher: American Physical Society. 1.1.1, 2.5

[27] D. Greif, M. F. Parsons, A. Mazurenko, C. S. Chiu, S. Blatt, F. Huber, G. Ji, and M. Greiner, "Site-resolved imaging of a fermionic Mott insulator," *Science*, vol. 351, pp. 953–957, Feb. 2016. Publisher: American Association for the Advancement of Science. 1.1.1

[28] L. W. Cheuk, M. A. Nichols, K. R. Lawrence, M. Okan, H. Zhang, E. Khatami, N. Trivedi, T. Paiva, M. Rigol, and M. W. Zwierlein, "Observation of spatial charge and spin correlations in the 2D Fermi-Hubbard model," *Science*, vol. 353, pp. 1260–1264, Sept. 2016. Publisher: American Association for the Advancement of Science. 1.1.1

[29] L. W. Cheuk, M. A. Nichols, K. R. Lawrence, M. Okan, H. Zhang, and M. W. Zwierlein, "Observation of 2D Fermionic Mott Insulators of 40K with Single-Site Resolution," *Physical Review Letters*, vol. 116, p. 235301, June 2016. Publisher: American Physical Society. 1.1.1

[30] M. Boll, T. A. Hilker, G. Salomon, A. Omran, J. Nespolo, L. Pollet, I. Bloch, and C. Gross, "Spin- and density-resolved microscopy of antiferromagnetic correlations in Fermi-Hubbard chains," *Science (New York, N.Y.)*, vol. 353, pp. 1257–1260, Sept. 2016. 1.1.1

[31] T. A. Hilker, G. Salomon, F. Grusdt, A. Omran, M. Boll, E. Demler, I. Bloch, and C. Gross, "Revealing hidden antiferromagnetic correlations in doped Hubbard chains via string correlators," *Science*, vol. 357, pp. 484–487, Aug. 2017. Publisher: American Association for the Advancement of Science. 1.1.1

[32] R. Islam, R. Ma, P. M. Preiss, M. Eric Tai, A. Lukin, M. Rispoli, and M. Greiner, "Measuring entanglement entropy in a quantum many-body system," *Nature*, vol. 528, pp. 77–83, Dec. 2015. Publisher: Nature Publishing Group. 1.1.1

[33] J. Koepsell, J. Vijayan, P. Sompet, F. Grusdt, T. A. Hilker, E. Demler, G. Salomon, I. Bloch, and C. Gross, "Imaging magnetic polarons in the doped Fermi–Hubbard model," *Nature*, vol. 572, pp. 358–362, Aug. 2019. Publisher: Nature Publishing Group. 1.1.1

[34] C. Gross and I. Bloch, "Quantum simulations with ultracold atoms in optical lattices," *Science*, vol. 357, pp. 995–1001, Sept. 2017. 1.1.1

[35] L. Chomaz, I. Ferrier-Barbut, F. Ferlaino, B. Laburthe-Tolra, B. L. Lev, and T. Pfau, "Dipolar physics: a review of experiments with magnetic quantum gases," *Reports on Progress in Physics*, vol. 86, p. 026401, Dec. 2022. Publisher: IOP Publishing. 1.2

[36] K. Aikawa, D. Akamatsu, J. Kobayashi, M. Ueda, T. Kishimoto, and S. Inouye, "Toward the production of quantum degenerate bosonic polar molecules, 41K87Rb," *New Journal of Physics*, vol. 11, p. 055035, May 2009. 1.2

[37] A. Griesmaier, J. Werner, S. Hensler, J. Stuhler, and T. Pfau, "Bose-Einstein Condensation of Chromium," *Physical Review Letters*, vol. 94, p. 160401, Apr. 2005. Publisher: American Physical Society. 1.2

[38] M. Lu, N. Q. Burdick, S. H. Youn, and B. L. Lev, "Strongly Dipolar Bose-Einstein Condensate of Dysprosium," *Physical Review Letters*, vol. 107, p. 190401, Oct. 2011. Publisher: American Physical Society. 1.2

[39] C. S. Adams, J. D. Pritchard, and J. P. Shaffer, "Rydberg atom quantum technologies," *Journal of Physics B: Atomic, Molecular and Optical Physics*, vol. 53, p. 012002, Dec. 2019. Publisher: IOP Publishing. 1.2

[40] D. DeMille, "Quantum Computation with Trapped Polar Molecules," *Physical Review Letters*, vol. 88, p. 067901, Jan. 2002. 1.2

[41] S. F. Yelin, K. Kirby, and R. Côté, "Schemes for robust quantum computation with polar molecules," *Physical Review A*, vol. 74, p. 050301, Nov. 2006. 1.2

[42] T. Langen, G. Valtolina, D. Wang, and J. Ye, "Quantum state manipulation and cooling of ultracold molecules," *Nature Physics*, vol. 20, pp. 702–712, May 2024. Publisher: Nature Publishing Group. 1.2, 1.3

[43] S. L. Cornish, M. R. Tarbutt, and K. R. A. Hazzard, "Quantum computation and quantum simulation with ultracold molecules," *Nature Physics*, vol. 20, pp. 730–740, May 2024. ADS Bibcode: 2024NatPh..20..730C. 1.2, 1.3, 2.4, 8.5

[44] A. Micheli, G. K. Brennen, and P. Zoller, "A toolbox for lattice-spin models with polar molecules," *Nature Physics*, vol. 2, pp. 341–347, May 2006. Publisher: Nature Publishing Group. 1.2, 1.3, 8.5

[45] S. R. Manmana, E. M. Stoudenmire, K. R. A. Hazzard, A. M. Rey, and A. V. Gorshkov, "Topological phases in ultracold polar-molecule quantum magnets," *Physical Review B*, vol. 87, p. 081106, Feb. 2013. Publisher: American Physical Society. 1.2, 1.3, 8.5

[46] A. V. Gorshkov, S. R. Manmana, G. Chen, J. Ye, E. Demler, M. D. Lukin, and A. M. Rey, "Tunable Superfluidity and Quantum Magnetism with Ultracold Polar Molecules," *Physical Review Letters*, vol. 107, p. 115301, Sept. 2011. Publisher: American Physical Society. 1.2, 1.3, 8.5

[47] R. Barnett, D. Petrov, M. Lukin, and E. Demler, "Quantum Magnetism with Multicomponent Dipolar Molecules in an Optical Lattice," *Physical Review Letters*, vol. 96, p. 190401, May 2006. Publisher: American Physical Society. 1.2

[48] N. Y. Yao, M. P. Zaletel, D. M. Stamper-Kurn, and A. Vishwanath, "A quantum dipolar spin liquid," *Nature Physics*, vol. 14, pp. 405–410, Apr. 2018. Publisher: Nature Publishing Group. 1.2, 1.3, 8.5

[49] W. Lechner and P. Zoller, "From classical to quantum glasses with ultracold polar molecules," *Physical review letters*, vol. 111, p. 185306, 11 2013. 1.2, 1.3, 8.5

[50] T. P. Softley, "Cold and ultracold molecules in the twenties," *Proceedings of the Royal Society A: Mathematical, Physical and Engineering Sciences*, vol. 479, p. 20220806, June 2023. 1.2

[51] P. D. Gregory, M. D. Frye, J. A. Blackmore, E. M. Bridge, R. Sawant, J. M. Hutson, and S. L. Cornish, "Sticky collisions of ultracold RbCs molecules," *Nature Communications*, vol. 10, p. 3104, July 2019. Publisher: Nature Publishing Group. 1.2, 1.3.2, 2.1, 5.8.4, 5.26

[52] R. Bause, A. Schindewolf, R. Tao, M. Duda, X.-Y. Chen, G. Quéméner, T. Karman, A. Christianen, I. Bloch, and X.-Y. Luo, "Collisions of ultracold molecules in bright and dark optical dipole traps," *Physical Review Research*, vol. 3, p. 033013, July 2021. Publisher: American Physical Society. 1.2

[53] J. A. Blackmore, L. Caldwell, P. D. Gregory, E. M. Bridge, R. Sawant, J. Aldegunde, J. Mur-Petit, D. Jaksch, J. M. Hutson, B. E. Sauer, M. R. Tarbutt, and S. L. Cornish, "Ultracold molecules for quantum simulation: rotational coherences in CaF and RbCs," *Quantum Science and Technology*, vol. 4, p. 014010, Dec. 2018. Publisher: IOP Publishing. 1.2

[54] G. Quéméner and J. L. Bohn, "Shielding $^{2}\mathrm{\ensuremath{\Sigma}}$ ultracold dipolar molecular collisions with electric fields," *Physical Review A*, vol. 93, p. 012704, Jan. 2016. Publisher: American Physical Society. 1.2

[55] G. Wang and G. Quéméner, "Tuning ultracold collisions of excited rotational dipolar molecules," *New Journal of Physics*, vol. 17, p. 035015, Mar. 2015. Publisher: IOP Publishing. 1.2

[56] K. Matsuda, L. De Marco, J.-R. Li, W. G. Tobias, G. Valtolina, G. Quéméner, and J. Ye, "Resonant collisional shielding of reactive molecules using electric fields," *Science*, vol. 370, pp. 1324–1327, Dec. 2020. Publisher: American Association for the Advancement of Science. 1.2

[57] T. Karman and J. M. Hutson, "Microwave Shielding of Ultracold Polar Molecules," *Physical Review Letters*, vol. 121, p. 163401, Oct. 2018. Publisher: American Physical Society. 1.2

[58] T. Karman and J. M. Hutson, "Microwave shielding of ultracold polar molecules with imperfectly circular polarization," *Physical Review A*, vol. 100, p. 052704, Nov. 2019. Publisher: American Physical Society. 1.2, 1.3.2

[59] A. Schindewolf, R. Bause, X.-Y. Chen, M. Duda, T. Karman, I. Bloch, and X.-Y. Luo, "Evaporation of microwave-shielded polar molecules to quantum degeneracy," *Nature*, vol. 607, pp. 677–681, July 2022. 1.2, 1.3.2

[60] L. Anderegg, S. Burchesky, Y. Bao, S. S. Yu, T. Karman, E. Chae, K.-K. Ni, W. Ketterle, and J. M. Doyle, "Observation of microwave shielding of ultracold molecules," *Science*, vol. 373, pp. 779–782, Aug. 2021. Publisher: American Association for the Advancement of Science. 1.2, 1.3.2

[61] J. Lin, G. Chen, M. Jin, Z. Shi, F. Deng, W. Zhang, G. Quéméner, T. Shi, S. Yi, and D. Wang, "Microwave Shielding of Bosonic NaRb Molecules," *Physical Review X*, vol. 13, p. 031032, Sept. 2023. Publisher: American Physical Society. 1.2, 1.3.2

[62] N. Bigagli, W. Yuan, S. Zhang, B. Bulatovic, T. Karman, I. Stevenson, and S. Will, "Observation of Bose–Einstein condensation of dipolar molecules," *Nature*, pp. 1–5, June 2024. 1.2, 1.3.2

[63] L. De Marco, G. Valtolina, K. Matsuda, W. G. Tobias, J. P. Covey, and J. Ye, "A degenerate Fermi gas of polar molecules," *Science*, vol. 363, pp. 853–856, Feb. 2019. 1.2, 1.3.2

[64] W. G. Tobias, K. Matsuda, G. Valtolina, L. De Marco, J.-R. Li, and J. Ye, "Thermalization and Sub-Poissonian Density Fluctuations in a Degenerate Molecular Fermi Gas," *Physical Review Letters*, vol. 124, p. 033401, Jan. 2020. Publisher: American Physical Society. 1.2

[65] S. Burchesky, L. Anderegg, Y. Bao, S. S. Yu, E. Chae, W. Ketterle, K.-K. Ni, and J. M. Doyle, "Rotational Coherence Times of Polar Molecules in Optical Tweezers," *Physical Review Letters*, vol. 127, p. 123202, Sept. 2021. Publisher: American Physical Society. 1.2, 1.3.2

[66] A. J. Park, L. R. Picard, G. E. Patenotte, J. T. Zhang, T. Rosenband, and K.-K. Ni, "Extended Rotational Coherence of Polar Molecules in an Elliptically Polarized Trap," *Physical Review Letters*, vol. 131, p. 183401, Oct. 2023. Publisher: American Physical Society. 1.2, 1.3.2

[67] P. D. Gregory, "Second-scale rotational coherence and dipolar interactions in a gas of ultracold polar molecules | Nature Physics," 2024. 1.2, 1.3.2, 6.7.3, 8.4

[68] D. K. Ruttley, T. R. Hepworth, A. Guttridge, and S. L. Cornish, "Long-lived entanglement of molecules in magic-wavelength optical tweezers," *Nature*, vol. 637, pp. 827–832, Jan. 2025. Publisher: Nature Publishing Group. 1.2, 1.3.2, 8.4

[69] L. R. B. Picard, A. J. Park, G. E. Patenotte, S. Gebretsadkan, D. Wellnitz, A. M. Rey, and K.-K. Ni, "Entanglement and iSWAP gate between molecular qubits," *Nature*, vol. 637, pp. 821–826, Jan. 2025. Publisher: Nature Publishing Group. 1.2

[70] Y. Bao, S. S. Yu, L. Anderegg, E. Chae, W. Ketterle, K.-K. Ni, and J. M. Doyle, "Dipolar spin-exchange and entanglement between molecules in an optical tweezer array," *Science*, vol. 382, pp. 1138–1143, Dec. 2023. Publisher: American Association for the Advancement of Science. 1.2

[71] C. M. Holland, Y. Lu, and L. W. Cheuk, "On-demand entanglement of molecules in a reconfigurable optical tweezer array," *Science*, vol. 382, pp. 1143–1147, Dec. 2023. Publisher: American Association for the Advancement of Science. 1.2

[72] R. Sawant, J. A. Blackmore, P. D. Gregory, J. Mur-Petit, D. Jaksch, J. Aldegunde, J. M. Hutson, M. R. Tarbutt, and S. L. Cornish, "Ultracold polar molecules as qudits," *New Journal of Physics*, vol. 22, p. 013027, Jan. 2020. 1.2

[73] V. V. Albert, J. P. Covey, and J. Preskill, "Robust Encoding of a Qubit in a Molecule," *Physical Review X*, vol. 10, p. 031050, Sept. 2020. Publisher: American Physical Society. 1.2

[74] K. R. A. Hazzard and B. Gadway, "Synthetic dimensions," *Physics Today*, vol. 76, pp. 62–63, Apr. 2023. 1.2

[75] ACME Collaboration, "Improved limit on the electric dipole moment of the electron," *Nature*, vol. 562, pp. 355–360, Oct. 2018. 1.2

[76] "Improved measurement of the shape of the electron | Nature." 1.2

[77] T. S. Roussy, L. Caldwell, T. Wright, W. B. Cairncross, Y. Shagam, K. B. Ng, N. Schlossberger, S. Y. Park, A. Wang, J. Ye, and E. A. Cornell, "An improved bound on the electron's electric dipole moment," *Science*, vol. 381, pp. 46–50, July 2023. Publisher: American Association for the Advancement of Science. 1.2

[78] R. Barnett, D. Petrov, M. Lukin, and E. Demler, "Quantum magnetism with multicomponent dipolar molecules in an optical lattice," *Phys. Rev. Lett.*, vol. 96, p. 190401, 2006. 1.3, 8.5

[79] J.-R. Li, K. Matsuda, C. Miller, A. N. Carroll, W. G. Tobias, J. S. Higgins, and J. Ye, "Tunable itinerant spin dynamics with polar molecules," *Nature*, vol. 614, pp. 70–74, Feb. 2023. 1.3

[80] C. Miller, A. N. Carroll, J. Lin, H. Hirzler, H. Gao, H. Zhou, M. D. Lukin, and J. Ye, "Two-axis twisting using Floquet-engineered XYZ spin models with polar molecules," *Nature*, vol. 633, pp. 332–337, Sept. 2024. Publisher: Nature Publishing Group. 1.3

[81] A. N. Carroll, H. Hirzler, C. Miller, D. Wellnitz, S. R. Muleady, J. Lin, K. P. Zamarski, R. R. W. Wang, J. L. Bohn, A. M. Rey, and J. Ye, "Observation of Generalized t-J Spin Dynamics with Tunable Dipolar Interactions," Apr. 2024. arXiv:2404.18916 [cond-mat]. 1.3

[82] J. S. Rosenberg, L. Christakis, E. Guardado-Sanchez, Z. Z. Yan, and W. S. Bakr, "Observation of the Hanbury Brown–Twiss effect with ultracold molecules," *Nature Physics*, vol. 18, pp. 1062–1066, Sept. 2022. 1.3, 1.3.1, 2.4.1

[83] L. Christakis, J. S. Rosenberg, R. Raj, S. Chi, A. Morningstar, D. A. Huse, Z. Z. Yan, and W. S. Bakr, "Probing site-resolved correlations in a spin system of ultracold molecules," *Nature*, vol. 614, pp. 64–69, Feb. 2023. 1.3, 2.5, 6.2

[84] J. P. Covey, L. D. Marco, L. Acevedo, A. M. Rey, and J. Ye, "An approach to spin-resolved molecular gas microscopy," *New Journal of Physics*, vol. 20, p. 043031, Apr. 2018. Publisher: IOP Publishing. 1.3, 7.3

[85] H. J. Williams, S. Truppe, M. Hambach, L. Caldwell, N. J. Fitch, E. A. Hinds, B. E. Sauer, and M. R. Tarbutt, "Characteristics of a magneto-optical trap of molecules," *New Journal of Physics*, vol. 19, p. 113035, Nov. 2017. Publisher: IOP Publishing. 1.3.1

[86] J. F. Barry, D. J. McCarron, E. B. Norrgard, M. H. Steinecker, and D. DeMille, "Magneto-optical trapping of a diatomic molecule," *Nature*, vol. 512, pp. 286–289, Aug. 2014. Publisher: Nature Publishing Group. 1.3.1

[87] L. Anderegg, B. L. Augenbraun, E. Chae, B. Hemmerling, N. R. Hutzler, A. Ravi, A. Collopy, J. Ye, W. Ketterle, and J. M. Doyle, "Radio Frequency Magneto-Optical Trapping of CaF with High Density," *Physical Review Letters*, vol. 119, p. 103201, Sept. 2017. Publisher: American Physical Society. 1.3.1

[88] R. L. McNally, I. Kozyryev, S. Vazquez-Carson, K. Wenz, T. Wang, and T. Zelevinsky, "Optical cycling, radiative deflection and laser cooling of barium monohydride (138Ba1H)," *New Journal of Physics*, vol. 22, p. 083047, Aug. 2020. Publisher: IOP Publishing. 1.3.1

[89] S. Truppe, H. J. Williams, M. Hambach, L. Caldwell, N. J. Fitch, E. A. Hinds, B. E. Sauer, and M. R. Tarbutt, "Molecules cooled below the Doppler limit," *Nature Physics*, vol. 13, pp. 1173–1176, Dec. 2017. Publisher: Nature Publishing Group. 1.3.1

[90] B. L. Augenbraun, L. Anderegg, C. Hallas, Z. D. Lasner, N. B. Vilas, and J. M. Doyle, "Chapter Two - Direct laser cooling of polyatomic molecules," in *Advances In Atomic, Molecular, and Optical Physics* (L. F. DiMauro, H. Perrin, and S. F. Yelin, eds.), vol. 72 of *Advances in Atomic, Molecular, and Optical Physics*, pp. 89–182, Academic Press, Jan. 2023. 1.3.1

[91] M. T. Bell and T. P. Softley, "Ultracold molecules and ultracold chemistry," *Molecular Physics*, Jan. 2009. Publisher: Taylor & Francis Group. 1.3.1

[92] C. A. Regal, C. Ticknor, J. L. Bohn, and D. S. Jin, "Creation of ultracold molecules from a Fermi gas of atoms," *Nature*, vol. 424, pp. 47–50, July 2003. 1.3.1

[93] C. Ospelkaus, S. Ospelkaus, L. Humbert, P. Ernst, K. Sengstock, and K. Bongs, "Ultracold Heteronuclear Molecules in a 3D Optical Lattice," *Physical Review Letters*, vol. 97, p. 120402, Sept. 2006. Publisher: American Physical Society. 1.3.1

[94] K.-K. Ni, S. Ospelkaus, M. H. G. de Miranda, A. Pe'er, B. Neyenhuis, J. J. Zirbel, S. Kotochigova, P. S. Julienne, D. S. Jin, and J. Ye, "A High Phase-Space-Density Gas of Polar Molecules," *Science*, vol. 322, pp. 231–235, Oct. 2008. 1.3.1

[95] M.-G. Hu, Y. Liu, D. D. Grimes, Y.-W. Lin, A. H. Gheorghe, R. Vexiau, N. Bouloufa-Maafa, O. Dulieu, T. Rosenband, and K.-K. Ni, "Direct observation of bimolecular reactions of ultracold KRb molecules," *Science (New York, N.Y.)*, vol. 366, pp. 1111–1115, Nov. 2019. 1.3.1

[96] T. Takekoshi, M. Debatin, R. Rameshan, F. Ferlaino, R. Grimm, H.-C. Nägerl, C. R. Le Sueur, J. M. Hutson, P. S. Julienne, S. Kotochigova, and E. Tiemann, "Towards the production of ultracold ground-state RbCs molecules: Feshbach resonances, weakly bound states, and the coupled-channel model," *Physical Review A*, vol. 85, p. 032506, Mar. 2012. 1.3.1

[97] P. K. Molony, P. D. Gregory, Z. Ji, B. Lu, M. P. Köppinger, C. R. Le Sueur, C. L. Blackley, J. M. Hutson, and S. L. Cornish, "{Creation of Ultracold $^{87}\mathrm{Rb}^{133}\mathrm{Cs}$ Molecules in the Rovibrational Ground State}," *Physical Review Letters*, vol. 113, p. 255301, Dec. 2014. 1.3.1, 1.3.2, 2.2, 2.3.1, 2.3.2, 5.4

[98] J. W. Park, S. A. Will, and M. W. Zwierlein, "Ultracold Dipolar Gas of Fermionic $^{23}Na^{40}K$ Molecules in Their Absolute Ground State," *Phys. Rev. Lett.*, vol. 114, p. 205302, May 2015. 1.3.1

[99] F. Seeßelberg, N. Buchheim, Z.-K. Lu, T. Schneider, X.-Y. Luo, E. Tiemann, I. Bloch, and C. Gohle, "Modeling the adiabatic creation of ultracold polar $^{23}Na^{40}K$ molecules," *Phys. Rev. A*, vol. 97, p. 013405, Jan. 2018. 1.3.1

[100] H. Yang, D.-C. Zhang, L. Liu, Y.-X. Liu, J. Nan, B. Zhao, and J.-W. Pan, "Observation of magnetically tunable Feshbach resonances in ultracold 23Na40K + 40K collisions," *Science*, vol. 363, pp. 261–264, Jan. 2019. 1.3.1

[101] K. K. Voges, P. Gersema, M. Meyer zum Alten Borgloh, T. A. Schulze, T. Hartmann, A. Zenesini, and S. Ospelkaus, "Ultracold Gas of Bosonic $^{23}\mathrm{Na}^{39}\mathrm{K}$ Ground-State Molecules," *Physical Review Letters*, vol. 125, p. 083401, Aug. 2020. 1.3.1

[102] W. B. Cairncross, J. T. Zhang, L. R. Picard, Y. Yu, K. Wang, and K.-K. Ni, "Assembly of a Rovibrational Ground State Molecule in an Optical Tweezer," *Physical Review Letters*, vol. 126, p. 123402, Mar. 2021. 1.3.1

[103] I. Stevenson, A. Z. Lam, N. Bigagli, C. Warner, W. Yuan, S. Zhang, and S. Will, "Ultracold Gas of Dipolar NaCs Ground State Molecules," *Physical Review Letters*, vol. 130, p. 113002, Mar. 2023. 1.3.1

[104] M. Guo, B. Zhu, B. Lu, X. Ye, F. Wang, R. Vexiau, N. Bouloufa-Maafa, G. Quéméner, O. Dulieu, and D. Wang, "Creation of an Ultracold Gas of Ground-State Dipolar $^{23}\mathrm{Na}^{87}\mathrm{Rb}$ Molecules," *Physical Review Letters*, vol. 116, p. 205303, May 2016. 1.3.1

[105] T. M. Rvachov, H. Son, A. T. Sommer, S. Ebadi, J. J. Park, M. W. Zwierlein, W. Ketterle, and A. O. Jamison, "Long-Lived Ultracold Molecules with Electric and Magnetic Dipole Moments," *Physical Review Letters*, vol. 119, p. 143001, Oct. 2017. 1.3.1

[106] C. He, X. Nie, V. Avalos, S. Botsi, S. Kumar, A. Yang, and K. Dieckmann, "Efficient Creation of Ultracold Ground State $\^{6}\textrm{Li}\^{40}\textrm{K}$ Polar Molecules," Oct. 2023. arXiv:2310.03300. 1.3.1

[107] Z.-X. Sun, Y. Hai, B.-K. Lyu, G.-R. Wang, and S.-L. Cong, "Formation of ultracold ground-state CsYb molecules via Feshbach-optimized photoassociation," *Journal of Physics B: Atomic, Molecular and Optical Physics*, vol. 53, p. 205204, Sept. 2020. Publisher: IOP Publishing. 1.3.1

[108] A. Ciamei, J. Szczepkowski, A. Bayerle, V. Barbé, L. Reichsöllner, S. M. Tzanova, C.-C. Chen, B. Pasquiou, A. Grochola, P. Kowalczyk, W. Jastrzebski, and F. Schreck, "The RbSr 2+ ground state investigated via spectroscopy of hot and ultracold molecules," *Physical Chemistry Chemical Physics*, vol. 20, pp. 26221–26240, Oct. 2018. Publisher: The Royal Society of Chemistry. 1.3.1

[109] A. GUTTRIDGE, *Photoassociation of Ultracold CsYb Molecules and Determination of Interspecies Scattering Lengths*. Doctoral, Durham University, 2018. 1.3.1, 3.2.3

[110] S. Finelli, A. Ciamei, B. Restivo, M. Schemmer, A. Cosco, M. Inguscio, A. Trenkwalder, K. Zaremba-Kopczyk, M. Gronowski, M. Tomza, and M. Zaccanti, "Ultracold $\mathrm{Li}\mathrm{Cr}$: A New Pathway to Quantum Gases of Paramagnetic Polar Molecules," *PRX Quantum*, vol. 5, p. 020358, June 2024. Publisher: American Physical Society. 1.3.1

[111] C. D. Bruzewicz, M. Gustavsson, T. Shimasaki, and D. DeMille, "Continuous formation of vibronic ground state RbCs molecules via photoassociation," *New Journal of Physics*, vol. 16, p. 023018, Feb. 2014. Publisher: IOP Publishing. 1.3.1

[112] A. D. Lercher, T. Takekoshi, M. Debatin, B. Schuster, R. Rameshan, F. Ferlaino, R. Grimm, and H. C. Nägerl, "Production of a dual-species Bose-Einstein condensate of Rb and Cs atoms," *The European Physical Journal D*, vol. 65, pp. 3–9, Nov. 2011. 1.3.2, 2.2, 4.1, 4.2.1, 4.3

[113] L. Reichsöllner, A. Schindewolf, T. Takekoshi, R. Grimm, and H.-C. Nägerl, "Quantum Engineering of a Low-Entropy Gas of Heteronuclear Bosonic Molecules in an Optical Lattice," *Physical Review Letters*, vol. 118, p. 073201, Feb. 2017. Publisher: American Physical Society. 1.3.2, 2.2, 5, 4.1, 4.2, 4.2.1, 4.5, 8.3

[114] A. G. A. Schindewolf, *Quantum engineering of a low-entropy sample of RbCs molecules in an optical lattice / by Andreas Schindewolf*. Oct. 2018. 1.3.2, 2.2, 4.5

[115] T. Takekoshi, M. Debatin, R. Rameshan, F. Ferlaino, R. Grimm, H.-C. Nägerl, C. R. Le Sueur, J. M. Hutson, P. S. Julienne, S. Kotochigova, and E. Tiemann, "Towards the production of ultracold ground-state RbCs molecules: Feshbach resonances, weakly bound states, and the coupled-channel model," *Physical Review A*, vol. 85, p. 032506, Mar. 2012. Publisher: American Physical Society. 1.3.2, 2.2, 2.3.1, 2.3, 5.2.2, 5.3.1

[116] M. P. Köppinger, D. J. McCarron, D. L. Jenkin, P. K. Molony, H.-W. Cho, S. L. Cornish, C. R. Le Sueur, C. L. Blackley, and J. M. Hutson, "Production of optically trapped $^{87}\mathrm{RbCs}$ Feshbach molecules," *Physical Review A*, vol. 89, p. 033604, Mar. 2014. Publisher: American Physical Society. 1.3.2, 2.2, 2.3.1, 2.3.1, 3.1

[117] D. K. Ruttley, A. Guttridge, T. R. Hepworth, and S. L. Cornish, "Enhanced Quantum Control of Individual Ultracold Molecules Using Optical Tweezer Arrays," *PRX Quantum*, vol. 5, p. 020333, May 2024. 1.3.2, 5.9, 5.10, 7.2.1

[118] A. J. Matthies, J. M. Mortlock, L. A. McArd, A. P. Raghuram, A. D. Innes, P. D. Gregory, S. L. Bromley, and S. L. Cornish, "Long-distance optical-conveyor-belt transport of ultracold $^{133}\mathrm{Cs}$ and $^{87}\mathrm{Rb}$ atoms," *Physical Review A*, vol. 109, p. 023321, Feb. 2024. Publisher: American Physical Society. 1.3.2, 3.2.4, 3.2.4, 4.1, 8.6

[119] T. Takekoshi, L. Reichsöllner, A. Schindewolf, J. M. Hutson, C. R. Le Sueur, O. Dulieu, F. Ferlaino, R. Grimm, and H.-C. Nägerl, "Ultracold Dense Samples of Dipolar RbCs Molecules in the Rovibrational and Hyperfine Ground State," *Physical Review Letters*, vol. 113, p. 205301, Nov. 2014. Publisher: American Physical Society. 1.3.2, 2.3.1

[120] P. GREGORY, *Coherent Control of Ultracold Polar Molecules*. Doctoral, Durham University, 2018. 1.3.2, 3.1

[121] J. A. Blackmore, L. Caldwell, P. D. Gregory, E. M. Bridge, R. Sawant, J. Aldegunde, J. Mur-Petit, D. Jaksch, J. M. Hutson, B. E. Sauer, M. R. Tarbutt, and S. L. Cornish, "Ultracold molecules for quantum simulation: rotational coherences in CaF and RbCs," *Quantum Sci. Technol.*, vol. 4, p. 014010, Dec. 2018. 1.3.2

[122] A. Guttridge, D. K. Ruttley, A. C. Baldock, R. González-Férez, H. Sadeghpour, C. Adams, and S. L. Cornish, "Observation of Rydberg Blockade Due to the Charge-Dipole Interaction between an Atom and a Polar Molecule," *Physical Review Letters*, vol. 131, p. 013401, July 2023. Publisher: American Physical Society. 1.3.2

[123] B. Mukherjee, M. D. Frye, C. R. Le Sueur, M. R. Tarbutt, and J. M. Hutson, "Shielding collisions of ultracold CaF molecules with static electric fields," *Physical Review Research*, vol. 5, p. 033097, Aug. 2023. 1.3.2

[124] R. Bause, M. Li, A. Schindewolf, X. Y. Chen, M. Duda, S. Kotochigova, I. Bloch, and X. Y. Luo, "Tune-Out and Magic Wavelengths for Ground-State

Na 23 K 40 Molecules," *Physical Review Letters*, vol. 125, no. 2, pp. 1–11, 2020. 5

[125] C. J. Foot and C. J. Foot, *Atomic Physics*. Oxford Master Series in Physics, Oxford, New York: Oxford University Press, Nov. 2004. 2

[126] H. J. Metcalf and P. Van Der Straten, *Laser Cooling and Trapping*. Graduate Texts in Contemporary Physics, New York, NY: Springer, 1999. 2

[127] R. Grimm, M. Weidemüller, and Y. B. Ovchinnikov, "Optical dipole traps for neutral atoms," vol. 42, pp. 95–170, 2000. 2, 2.1

[128] M. S. Safronova, B. Arora, and C. W. Clark, "Frequency-dependent polarizabilities of alkali-metal atoms from ultraviolet through infrared spectral regions," *Physical Review A*, vol. 73, p. 022505, Feb. 2006. 2.1

[129] W. Ketterle and N. J. V. Druten, "Evaporative Cooling of Trapped Atoms," in *Advances In Atomic, Molecular, and Optical Physics* (B. Bederson and H. Walther, eds.), vol. 37, pp. 181–236, Academic Press, Jan. 1996. 2.1.1

[130] C. Cohen-Tannoudji and D. Gury-Odelin, *Advances in Atomic Physics: An Overview*. World Scientific, 2011. Google-Books-ID: 3SVpDQAAQBAJ. 2.1.1

[131] M. Berninger, "Feshbach resonances, weakly bound molecular states, and coupled-channel potentials for cesium at high magnetic fields | Phys. Rev. A." 2.2, 5.1, 5.2.1

[132] T. Weber, J. Herbig, M. Mark, H.-C. Nägerl, and R. Grimm, "Three-Body Recombination at Large Scattering Lengths in an Ultracold Atomic Gas," *Physical Review Letters*, vol. 91, p. 123201, Sept. 2003. Publisher: American Physical Society. 2.2

[133] V. Efimov, "Energy levels arising from resonant two-body forces in a three-body system," *Physics Letters B*, vol. 33, pp. 563–564, Dec. 1970. 2.2

[134] T. Kraemer, "Few-body interactions in an ultracold gas of Cesium atoms," 2.2

[135] J. Söding, D. Guéry-Odelin, P. Desbiolles, F. Chevy, H. Inamori, and J. Dalibard, "Three-body decay of a rubidium Bose–Einstein condensate," *Applied Physics B*, vol. 69, pp. 257–261, Oct. 1999. 2.2

[136] D. J. McCarron, H. W. Cho, D. L. Jenkin, M. P. Köppinger, and S. L. Cornish, "Dual-species Bose-Einstein condensate of $^{87}\mathrm{Rb}$ and $^{133}\mathrm{Cs}$," *Physical Review A*, vol. 84, p. 011603, July 2011. Publisher: American Physical Society. 2.2

[137] L. K. Reichsöllner, "A general quantum-engineering technique for efficient production of ultracold dipolar molecules," 2.3.1

[138] K. Bergmann, H. Theuer, and B. W. Shore, "Coherent population transfer among quantum states of atoms and molecules," *Reviews of Modern Physics*, vol. 70, pp. 1003–1025, July 1998. 2.3.2, 2.4

[139] P. K. Molony, P. D. Gregory, A. Kumar, C. R. Le Sueur, J. M. Hutson, and S. L. Cornish, "Production of Ultracold ^{87}Rb133Cs in the Absolute Ground State: Complete Characterisation of the Stimulated Raman Adiabatic Passage Transfer," *ChemPhysChem*, vol. 17, no. 22, pp. 3811–3817, 2016. 2.3.2, 5.8.1

[140] N. V. Vitanov, A. A. Rangelov, B. W. Shore, and K. Bergmann, "Stimulated Raman adiabatic passage in physics, chemistry, and beyond," *Reviews of Modern Physics*, vol. 89, p. 015006, Mar. 2017. 2.3.2, 5.9

[141] L. P. Yatsenko, V. I. Romanenko, B. W. Shore, and K. Bergmann, "Stimulated Raman adiabatic passage with partially coherent laser fields," *Physical Review A*, vol. 65, p. 043409, Apr. 2002. 2.3.2, 2.3.2, 5.10

[142] L. P. Yatsenko, B. W. Shore, and K. Bergmann, "Detrimental consequences of small rapid laser fluctuations on stimulated Raman adiabatic passage," *Physical Review A*, vol. 89, p. 013831, Jan. 2014. 2.3.2, 2.3.2, 5.4, 5.9

[143] D. K. Ruttley, A. Guttridge, T. R. Hepworth, and S. L. Cornish, "Enhanced quantum control of individual ultracold molecules using optical tweezer arrays," Jan. 2024. arXiv:2401.13593. 2.3.2

[144] B. P. Maddox, "Enhanced Quantum State Transfer via Feedforward Cancellation of Optical Phase Noise | Phys. Rev. Lett.," 2024. 2.3.2, 5, 5.4, 5.9, 5.27, 5.30, 5.31, 5.32, 5.33, 5.10

[145] M. Greiner, *Ultracold quantum gases in three-dimensional optical lattice potentials*. Text.PhDThesis, Ludwig-Maximilians-Universität München, Apr. 2003. 2.4

[146] C. Weitenberg, "Single-Atom Resolved Imaging and Manipulation in an Atomic Mott Insulator," 2011. 2.4, 6.4.2, 6.8

[147] U. Scheider, *Interacting Fermionic Atoms in Optical Lattices - A Qantum Simulator for Condensed Matter Physics*. PhD thesis, Johannes Gutenberg-Universit, 2010. 2.4

[148] J. MORTLOCK, *Towards Quantum Gas Microscopy of Ultracold Molecules*. Doctoral, Durham University, 2024. 2.4, 3, 3.2.2, 3.2.3, 3.2.4, 3.2.7, 3.3.2, 3.3.3, 4.1, 4.3, 6.1, 6.1, 6.2, 6.4.2, 6.5, 6.7, 6.9, 8.6

[149] M. Melchner Von Dydiowa, "Quantum simulation with an optical kagome lattice," July 2022. 2.4

[150] D. Jaksch, C. Bruder, J. I. Cirac, C. W. Gardiner, and P. Zoller, "Cold Bosonic Atoms in Optical Lattices," *Physical Review Letters*, vol. 81, pp. 3108–3111, Oct. 1998. Publisher: American Physical Society. 2.4

[151] W. S. Bakr, "A quantum gas microscope for detecting single atoms in a Hubbard-regime optical lattice | Nature," 2009. 2.4.1, 6.7.2

[152] C. Weitenberg, "Single-Atom Resolved Imaging and Manipulation in an Atomic Mott Insulator," 2011. 2.4.1, 6.7.2, 6.7.2

[153] I. Despard, "The construction of a bosonic quantum-gas microscope." 2.4.1

[154] T. M. Klostermann, "Construction of a Caesium Quantum Gas Microscope," 2.4.1, 6.2, 6.7.2

[155] P. T. Brown, D. Mitra, E. Guardado-Sanchez, P. Schauß, S. S. Kondov, E. Khatami, T. Paiva, N. Trivedi, D. A. Huse, and W. S. Bakr, "Spin-imbalance in a 2D Fermi-Hubbard system," *Science*, vol. 357, pp. 1385–1388, Sept. 2017. Publisher: American Association for the Advancement of Science. 2.4.1, 2.5

[156] J. Yang, L. Liu, J. Mongkolkiattichai, and P. Schauss, "Site-Resolved Imaging of Ultracold Fermions in a Triangular-Lattice Quantum Gas Microscope," *PRX Quantum*, vol. 2, p. 020344, June 2021. Publisher: American Physical Society. 2.4.1

[157] M.-D. Li, W. Lin, A. Luo, W.-Y. Zhang, H. Sun, B. Xiao, Y.-G. Zheng, Z.-S. Yuan, and J.-W. Pan, "High-powered optical superlattice with robust phase stability for quantum gas microscopy," *Optics Express*, vol. 29, pp. 13876–13886, Apr. 2021. Publisher: Optica Publishing Group. 2.5, 6.2

[158] J. Trisnadi, M. Zhang, L. Weiss, and C. Chin, "Design and construction of a quantum matter synthesizer," *Review of Scientific Instruments*, vol. 93, p. 083203, Aug. 2022. 2.5, 3.1, 3.2.4

[159] K. Kwon, K. Kim, J. Hur, S. Huh, and J.-y. Choi, "Site-resolved imaging of a bosonic mott insulator of ^{7}Li atoms," *Phys. Rev. A*, vol. 105, p. 033323, Mar 2022. 2.5, 3.3.1

[160] A. RATKATA, *Towards Quantum gas microscope for 87Rb133Cs molecules*. Doctoral, Durham University, 2024. 3, 3.2.2, 3.3, 3.2.3, 3.2.7, 3.3.2, 8.6

[161] A. MATTHIES, *Optical Conveyor-Belt Transport of Cs and Rb Atoms*. Doctoral, Durham University, 2023. 3, 3.2.4, 3.3.2, 4.3

[162] A. P. Raghuram, J. M. Mortlock, S. L. Bromley, and S. L. Cornish, "A motorized rotation mount for the switching of an optical beam path in under 20 ms using polarization control," *Review of Scientific Instruments*, vol. 94, p. 063201, June 2023. 3, 3.11, 3.12, 3.13, 12, 3.14

[163] P. K. Molony, "Creation of ultracold polar ground-state RbCs molecules - Durham e-Theses." 3.1, 5, 5.5, 5.6.4

[164] A. J. Matthies, J. M. Mortlock, L. A. McArd, A. P. Raghuram, A. D. Innes, P. D. Gregory, S. L. Bromley, and S. L. Cornish, "Long-distance optical-conveyor-belt transport of ultracold $^{133}\mathrm{Cs}$ and $^{87}\mathrm{Rb}$ atoms," *Physical Review A*, vol. 109, p. 023321, Feb. 2024. Publisher: American Physical Society. 3.2.3

[165] A. Gozzini, F. Mango, J. H. Xu, G. Alzetta, F. Maccarrone, and R. A. Bernheim, "Light-induced ejection of alkali atoms in polysiloxane coated cells," *Il Nuovo Cimento D*, vol. 15, pp. 709–722, May 1993. 2

[166] C. N. Cohen-Tannoudji and W. D. Phillips, "New Mechanisms for Laser Cooling," *Physics Today*, vol. 43, pp. 33–40, Oct. 1990. 3.2.3

[167] A. J. Kerman, *Raman sideband cooling and cold atomic collisions in optical lattices*. PhD thesis, Jan. 2002. Publication Title: Ph.D. Thesis ADS Bibcode: 2002PhDT.....146K. 3.2.3, 3.2.3

[168] A. J. Kerman, V. Vuletić, C. Chin, and S. Chu, "Beyond Optical Molasses: 3D Raman Sideband Cooling of Atomic Cesium to High Phase-Space Density," *Physical Review Letters*, vol. 84, pp. 439–442, Jan. 2000. Publisher: American Physical Society. 3.2.3

[169] H. J. Lewandowski, D. M. Harber, D. L. Whitaker, and E. A. Cornell, "Observation of Anomalous Spin-State Segregation in a Trapped Ultracold Vapor," *Phys. Rev. Lett.*, vol. 88, p. 070403, Jan. 2002. 3.2.4

[170] K. Nakagawa, Y. Suzuki, M. Horikoshi, and J. Kim, "Simple and efficient magnetic transport of cold atoms using moving coils for the production of Bose–Einstein condensation," *Appl. Phys. B*, vol. 81, pp. 791–794, Oct. 2005. 3.2.4

[171] D. Pertot, D. Greif, S. Albert, B. Gadway, and D. Schneble, "Versatile transporter apparatus for experiments with optically trapped Bose–Einstein condensates," *J. Phys. B: At., Mol. Opt. Phys.*, vol. 42, no. 21, p. 215305, 2009. 3.2.4

[172] S. Händel, T. P. Wiles, A. L. Marchant, S. A. Hopkins, C. S. Adams, and S. L. Cornish, "Magnetic merging of ultracold atomic gases of ^{85}Rb and ^{87}Rb," *Phys. Rev. A*, vol. 83, p. 053633, May 2011. 3.2.4

[173] M. Greiner, I. Bloch, T. W. Hänsch, and T. Esslinger, "Magnetic transport of trapped cold atoms over a large distance," *Phys. Rev. A*, vol. 63, no. 3, p. 031401, 2001. 3.2.4

[174] W. Hänsel, J. Reichel, P. Hommelhoff, and T. W. Hänsch, "Magnetic conveyor belt for transporting and merging trapped atom clouds," *Phys. Rev. Lett.*, vol. 86, no. 4, pp. 608–611, 2001. 3.2.4

[175] S. Minniberger, F. Diorico, S. Haslinger, C. Hufnagel, C. Novotny, N. Lippok, J. Majer, C. Koller, S. Schneider, and J. Schmiedmayer, "Magnetic conveyor belt transport of ultracold atoms to a superconducting atomchip," *Appl. Phys. B*, vol. 116, pp. 1017–1021, Sept. 2014. 3.2.4

[176] T. L. Gustavson, A. P. Chikkatur, A. E. Leanhardt, A. Görlitz, S. Gupta, D. E. Pritchard, and W. Ketterle, "Transport of Bose-Einstein Condensates with optical tweezers," *Phys. Rev. Lett.*, vol. 88, no. 2, p. 020401, 2001. 3.2.4

[177] A. Couvert, T. Kawalec, G. Reinaudi, and D. Guéry-Odelin, "Optimal transport of ultracold atoms in the non-adiabatic regime," *EPL*, vol. 83, no. 1, p. 13001, 2008. 3.2.4

[178] M. A. Naides, R. W. Turner, R. A. Lai, J. M. DiSciacca, and B. L. Lev, "Trapping ultracold gases near cryogenic materials with rapid reconfigurability," *Appl. Phys. Lett.*, vol. 103, p. 251112, Dec. 2013. 3.2.4

[179] J. Léonard, M. Lee, A. Morales, T. M. Karg, T. Esslinger, and T. Donner, "Optical transport and manipulation of an ultracold atomic cloud using focus-tunable lenses," *New J. Phys.*, vol. 16, no. 9, p. 093028, 2014. 3.2.4

[180] G. Unnikrishnan, C. Beulenkamp, D. Zhang, K. P. Zamarski, M. Landini, and H.-C. Nägerl, "Long distance optical transport of ultracold atoms: A compact setup using a Moiré lens," *Rev. Sci. Instrum.*, vol. 92, p. 063205, June 2021. 3.2.4

[181] C. Gross, H. C. J. Gan, and K. Dieckmann, "All-optical production and transport of a large ^{6}Li quantum gas in a crossed optical dipole trap," *Phys. Rev. A*, vol. 93, p. 053424, May 2016. 3.2.4

[182] T. Middelmann, S. Falke, C. Lisdat, and U. Sterr, "Long-range transport of ultracold atoms in a far-detuned one-dimensional optical lattice," *New J. Phys.*, vol. 14, p. 073020, July 2012. 3.2.4

[183] D. Schrader, S. Kuhr, W. Alt, M. Müller, V. Gomer, and D. Meschede, "An optical conveyor belt for single neutral atoms," *Appl. Phys. B*, vol. 73, no. 8, pp. 819–824, 2001. 3.2.4

[184] S. Schmid, G. Thalhammer, K. Winkler, F. Lang, and J. H. Denschlag, "Long distance transport of ultracold atoms using a 1D optical lattice," *New J. Phys.*, vol. 8, no. 8, pp. 159–159, 2006. 3.2.4

[185] F. Sorrentino, A. Alberti, G. Ferrari, V. V. Ivanov, N. Poli, M. Schioppo, and G. M. Tino, "Quantum sensor for atom-surface interactions below 10 μm," *Physical Review A*, vol. 79, p. 013409, Jan. 2009. 3.2.4

[186] I. Ushijima, M. Takamoto, M. Das, T. Ohkubo, and H. Katori, "Cryogenic optical lattice clocks," *Nature Photonics*, vol. 9, pp. 185–189, Mar. 2015. 3.2.4

[187] T. Klostermann, C. R. Cabrera, H. von Raven, J. F. Wienand, C. Schweizer, I. Bloch, and M. Aidelsburger, "Fast long-distance transport of cold cesium atoms," *Phys. Rev. A*, vol. 105, p. 043319, Apr. 2022. 3.2.4

[188] Y. Bao, S. S. Yu, L. Anderegg, S. Burchesky, D. Gonzalez-Acevedo, E. Chae, W. Ketterle, K.-K. Ni, and J. M. Doyle, "Fast optical transport of ultracold molecules over long distances," *New J. Phys.*, vol. 24, p. 093028, Sept. 2022. 3.2.4

[189] J. Trisnadi, M. Zhang, L. Weiss, and C. Chin, "Design and construction of a quantum matter synthesizer," *Review of Scientific Instruments*, vol. 93, p. 083203, 08 2022. 3.2.4

[190] D. M. Stamper-Kurn, H.-J. Miesner, A. P. Chikkatur, S. Inouye, J. Stenger, and W. Ketterle, "Reversible Formation of a Bose-Einstein Condensate," *Physical Review Letters*, vol. 81, pp. 2194–2197, Sept. 1998. Publisher: American Physical Society. 3.2.5

[191] W. Ketterle, D. S. Durfee, and D. M. Stamper-Kurn, "Making, probing and understanding Bose-Einstein condensates," Apr. 1999. arXiv:cond-mat/9904034. 3.2.6, 4.3

[192] C. F. Ockeloen, A. F. Tauschinsky, R. J. C. Spreeuw, and S. Whitlock, "Detection of small atom numbers through image processing," *Physical Review A*, vol. 82, p. 061606, Dec. 2010. Publisher: American Physical Society. 3.2.6

[193] T. Franzen, "A new RbYb ultracold mixture machine - from room temperature to 2-photon-photoassociation on the intercombination line," 3.2.6

[194] A. P. Raghuram, J. M. Mortlock, S. L. Bromley, and S. L. Cornish, "A motorized rotation mount for the switching of an optical beam path in under 20 ms using polarization control," *Review of Scientific Instruments*, vol. 94, no. 6, p. 063201, 2023. 3.3.1

[195] K. Nagano, A. Perreca, K. Arai, and R. X. Adhikari, "External quantum efficiency enhancement by photon recycling with backscatter evasion," *Appl. Opt.*, vol. 57, pp. 3372–3376, May 2018. 3.3.1

[196] I. L. Dimitrova, *Realizing quantum spin models with* ^{7}Li *atoms in an optical lattice*. PhD thesis, Massachusetts Institute of Technology, February 2020. 3.3.1

[197] F. Fueten, "A computer-controlled rotating polarizer stage for the petrographic microscope," *Computers & Geosciences*, vol. 23, no. 2, pp. 203–208, 1997. 3.3.1

[198] D. P. Shelton, W. M. O'Donnell, and J. L. Norton, "Note: Fast, small, accurate 90° rotator for a polarizer," *Review of Scientific Instruments*, vol. 82, no. 3, p. 036103, 2011. 3.3.1

[199] A. Rakonjac, K. O. Roberts, A. B. Deb, and N. Kjærgaard, "Note: Computer controlled rotation mount for large diameter optics," *Review of Scientific Instruments*, vol. 84, p. 026107, feb 2013. 3.3.1

[200] D. Nilsson, T. Dahlberg, and M. Andersson, "Step-by-step guide to 3d print motorized rotation mounts for optical applications.," *Applied optics*, vol. 60, pp. 3764–3771, 2021. 3.3.1

[201] M. McCauley. http://www.airspayce.com/mikem/arduino/AccelStepper/. 3.3.1

[202] T. Kenjo, *Stepping motors and their microprocessor controls*. Monographs in electrical and electronic engineering, Oxford: Clarendon, 1984. 3.3.1, 3.3.1

[203] P. P. Acarnley, *Stepping motors : a guide to modern theory and practice*. IEE control engineering series ; 19, 1982. 3.3.1

[204] Trinamic Motion Control, "Application note 15." https://www.trinamic.com/fileadmin/assets/Support/AppNotes/AN015-StealthChop_Performance.pdf. 3.3.1

[205] J. L. Roberts, "The First Experiments with 85Rb BECs," 3.3.2

[206] S. B. Papp, "Experiments with a two-species Bose-Einstein condensate utilizing widely tunable interparticle interactions," 3.3.2

[207] D. Steck, "Cesium d line data," 01 2010. 3.4.2, 3.4.2

[208] R. Grimm, M. Weidemüller, and Y. B. Ovchinnikov, *Optical Dipole Traps for Neutral Atoms*, vol. 42 of *Advances In Atomic, Molecular, and Optical Physics*, pp. 95 – 170. Academic Press, 2000. 3.4.3

[209] P. L. Kapitza and P. a. M. Dirac, "The reflection of electrons from standing light waves," *Mathematical Proceedings of the Cambridge Philosophical Society*, vol. 29, pp. 297–300, May 1933. 3.4.4

[210] A. Ratkata, P. D. Gregory, A. D. Innes, A. J. Matthies, L. A. McArd, J. M. Mortlock, M. S. Safronova, S. L. Bromley, and S. L. Cornish, "Measurement of the tune-out wavelength for ^{133}Cs at 880 nm," *Phys. Rev. A*, vol. 104, p. 052813, Nov. 2021. 3.4.4

[211] D. K. Ruttley, "A Hybrid Quantum System of Ultracold Polar Molecules and Rydberg Atoms," 5, 5.6.4, 5.9, 5.10

[212] C. Chin, V. Vuletić, A. J. Kerman, S. Chu, E. Tiesinga, P. J. Leo, and C. J. Williams, "Precision Feshbach spectroscopy of ultracold Cs2," *Physical Review A*, vol. 70, p. 032701, Sept. 2004. Publisher: American Physical Society. 5.1, 5.2.1

[213] M. P. Köppinger, P. D. Gregory, D. L. Jenkin, D. J. McCarron, A. L. Marchant, and S. L. Cornish, "Repeated output coupling of ultracold Feshbach molecules from a Cs BEC," *New Journal of Physics*, vol. 16, p. 115016, Nov. 2014. Publisher: IOP Publishing. 5.2.1

[214] K. Pilch, A. D. Lange, A. Prantner, G. Kerner, F. Ferlaino, H.-C. Nägerl, and R. Grimm, "Observation of interspecies Feshbach resonances in an ultracold Rb-Cs mixture," *Physical Review A*, vol. 79, p. 042718, Apr. 2009. Publisher: American Physical Society. 5.3.1

[215] M. P. Köppinger, D. J. McCarron, D. L. Jenkin, P. K. Molony, H.-W. Cho, S. L. Cornish, C. R. L. Sueur, C. L. Blackley, and J. M. Hutson, "Production of optically trapped ^{87}RbCs Feshbach molecules," *Physical Review A*, vol. 89, p. 033604, Mar. 2014. arXiv:1312.3551. 5.3.1, 5.3.2, 5.3.3, 5.13

[216] S. SPENCE, *Assembling Single RbCs Molecules with Optical Tweezers*. Doctoral, Durham University, 2023. 5.3.3

[217] D. K. Ruttley, A. Guttridge, S. Spence, R. C. Bird, C. R. Le Sueur, J. M. Hutson, and S. L. Cornish, "Formation of Ultracold Molecules by Merging Optical Tweezers," *Physical Review Letters*, vol. 130, p. 223401, May 2023. 5.4, 5.9, 5.10

[218] P. D. Gregory, P. K. Molony, M. P. Köppinger, A. Kumar, Z. Ji, B. Lu, A. L. Marchant, and S. L. Cornish, "A simple, versatile laser system for the creation of ultracold ground state molecules," *New Journal of Physics*, vol. 17, p. 055006, May 2015. 5.5

[219] G. S. Vasilev, A. Kuhn, and N. V. Vitanov, "Optimum pulse shapes for stimulated Raman adiabatic passage," *Physical Review A*, vol. 80, p. 013417, July 2009. Publisher: American Physical Society. 5.5

[220] E. D. Black, "An introduction to Pound–Drever–Hall laser frequency stabilization," *American Journal of Physics*, vol. 69, pp. 79–87, Jan. 2001. 5.6

[221] thorpe, "Laser frequency stabilization and control through offset sideband locking to optical cavities." 5.6

[222] A. INNES, *Towards a novel platform for imaging molecules in an optical lattice*. Doctoral, Durham University, 2023. 5.6.1, 8.6

[223] E. D. Black, "An introduction to Pound–Drever–Hall laser frequency stabilization," *American Journal of Physics*, vol. 69, pp. 79–87, Jan. 2001. 5.6.2

[224] A. Daniel, R. Agou, O. Amit, D. Groswasser, Y. Japha, and R. Folman, "Damping of local Rabi oscillations in the presence of thermal motion," *Physical Review A*, vol. 87, p. 063402, June 2013. 5.8.1

[225] K. S. Kumar, A. Vepsäläinen, S. Danilin, and G. S. Paraoanu, "Stimulated Raman adiabatic passage in a three-level superconducting circuit," *Nature Communications*, vol. 7, p. 10628, Feb. 2016. 5.9

[226] D. Møller, J. L. Sørensen, J. B. Thomsen, and M. Drewsen, "Efficient qubit detection using alkaline-earth-metal ions and a double stimulated Raman adiabatic process," *Physical Review A*, vol. 76, p. 062321, Dec. 2007. 5.9

[227] D. A. Golter and H. Wang, "Optically Driven Rabi Oscillations and Adiabatic Passage of Single Electron Spins in Diamond," *Physical Review Letters*, vol. 112, p. 116403, Mar. 2014. 5.9

[228] V. Fedoseev, F. Luna, I. Hedgepeth, W. Löffler, and D. Bouwmeester, "Stimulated Raman Adiabatic Passage in Optomechanics," *Physical Review Letters*, vol. 126, p. 113601, Mar. 2021. 5.9

[229] S. Longhi, G. Della Valle, M. Ornigotti, and P. Laporta, "Coherent tunneling by adiabatic passage in an optical waveguide system," *Physical Review B*, vol. 76, p. 201101, Nov. 2007. 5.9

[230] J. Hald and V. Ruseva, "Efficient suppression of diode-laser phase noise by optical filtering," *JOSA B*, vol. 22, pp. 2338–2344, Nov. 2005. 5.9

[231] T. Nazarova, C. Lisdat, F. Riehle, and U. Sterr, "Low-frequency-noise diode laser for atom interferometry," *JOSA B*, vol. 25, pp. 1632–1638, Oct. 2008. 5.9

[232] N. Akerman, N. Navon, S. Kotler, Y. Glickman, and R. Ozeri, "Universal gate-set for trapped-ion qubits using a narrow linewidth diode laser," *New Journal of Physics*, vol. 17, p. 113060, Nov. 2015. 5.9

[233] H. Levine, A. Keesling, A. Omran, H. Bernien, S. Schwartz, A. S. Zibrov, M. Endres, M. Greiner, V. Vuletić, and M. D. Lukin, "High-Fidelity Control and Entanglement of Rydberg-Atom Qubits," *Physical Review Letters*, vol. 121, p. 123603, Sept. 2018. 5.9

[234] R. Bause, A. Kamijo, X.-Y. Chen, M. Duda, A. Schindewolf, I. Bloch, and X.-Y. Luo, "{Efficient conversion of closed-channel-dominated Feshbach molecules of $^{23}\mathrm{Na}^{40}\mathrm{K}$ to their absolute ground state}," *Physical Review A*, vol. 104, p. 043321, Oct. 2021. 5.9

[235] L. Li, W. Huie, N. Chen, B. DeMarco, and J. P. Covey, "Active Cancellation of Servo-Induced Noise on Stabilized Lasers via Feedforward," *Physical Review Applied*, vol. 18, p. 064005, Dec. 2022. Publisher: American Physical Society. 5.9, 5.9.1, 5.9.1, 5.9.1

[236] W.-C. Ji, B.-W. Wang, Y. Hu, X.-Y. Cui, P. Xu, X. Jiang, H.-N. Dai, and Y.-A. Chen, "Characterization of the Pound-Drever-Hall Feedback Loop in an Ultra-Stable Laser System," in *CLEO 2024 (2024), paper JTu2A.21*, p. JTu2A.21, Optica Publishing Group, May 2024. 5.9, 5.9.1

[237] S. Spence, R. V. Brooks, D. K. Ruttley, A. Guttridge, and S. L. Cornish, "Preparation of 87Rb and 133Cs in the motional ground state of a single optical tweezer," *New Journal of Physics*, vol. 24, p. 103022, Oct. 2022. Publisher: IOP Publishing. 5.9, 5.10

[238] A. J. Daley, I. Bloch, C. Kokail, S. Flannigan, N. Pearson, M. Troyer, and P. Zoller, "Practical quantum advantage in quantum simulation," *Nature*, vol. 607, pp. 667–676, July 2022. 5.10

[239] C. Zhang and M. R. Tarbutt, "Quantum computation in a hybrid array of molecules and Rydberg atoms," *PRX Quantum*, vol. 3, no. 3, p. 030340, 2022. 5.10

[240] A. La Rooij, C. Ulm, E. Haller, and S. Kuhr, "A comparative study of deconvolution techniques for quantum-gas microscope images," *New Journal of Physics*, vol. 25, p. 083036, Aug. 2023. Publisher: IOP Publishing. 6.2, 6.7.1, 6.7.2, 6.8

[241] S. v. d. Walt, J. L. Schönberger, J. Nunez-Iglesias, F. Boulogne, J. D. Warner, N. Yager, E. Gouillart, and T. Yu, "scikit-image: image processing in Python," *PeerJ*, vol. 2, p. e453, June 2014. Publisher: PeerJ Inc. 6.4.1

[242] L. W. Cheuk, *Quantum gas microscopy of strongly correlated fermions*. Thesis, Massachusetts Institute of Technology, 2017. Accepted: 2017-10-30T15:30:33Z. 6.4.2

[243] T. Legrand, F.-R. Winkelmann, W. Alt, D. Meschede, A. Alberti, and C. A. Weidner, "Three-dimensional imaging of single atoms in an optical lattice via helical point-spread-function engineering," *Physical Review A*, vol. 109, p. 033304, Mar. 2024. Publisher: American Physical Society. 6.5

[244] J. Dalibard, "Laser cooling below the Doppler limit by polarization gradients: simple theoretical models," 2023. 6.7

[245] C. M. Sparrow, "On Spectroscopic Resolving Power," *The Astrophysical Journal*, vol. 44, p. 76, Sept. 1916. Publisher: IOP ADS Bibcode: 1916ApJ....44...76S. 6.7.1

[246] E. Hecht, *Optics*. Pearson Education, Incorporated, 2017. Google-Books-ID: ZarLoQEACAAJ. 6.7.1

[247] M. S. Safronova and U. I. Safronova, "Critically evaluated theoretical energies, lifetimes, hyperfine constants, and multipole polarizabilities in $^{87}\mathrm{Rb}$," *Physical Review A*, vol. 83, p. 052508, May 2011. Publisher: American Physical Society. 6.7.2

[248] M. S. Safronova, U. I. Safronova, and C. W. Clark, "Magic wavelengths, matrix elements, polarizabilities, and lifetimes of Cs," *Physical Review A*, vol. 94, p. 012505, July 2016. Publisher: American Physical Society. 6.7.2

[249] Q. Guan, S. L. Cornish, and S. Kotochigova, "Magic conditions for multiple rotational states of bialkali molecules in optical lattices," *Physical Review A*, vol. 103, p. 043311, Apr. 2021. Publisher: American Physical Society. 6.7.3

[250] "cKDTree — SciPy v1.15.1 Manual." 6.8

[251] H. von Raven, "A new Caesium quantum gas microscope with precise magnetic field control," 6.8

[252] L. R. B. Picard, M. J. Mark, F. Ferlaino, and R. van Bijnen, "Deep learning-assisted classification of site-resolved quantum gas microscope images," *Measurement Science and Technology*, vol. 31, p. 025201, Nov. 2019. Publisher: IOP Publishing. 6.9

[253] J. M. Mortlock, A. P. Raghuram, B. P. Maddox, P. D. Gregory, and S. L. Cornish, "Multi-state detection and spatial addressing in a microscope for ultracold molecules," June 2025. arXiv:2506.12329 [cond-mat]. 7, 7.2.3

[254] J. A. Blackmore, P. D. Gregory, J. M. Hutson, and S. L. Cornish, "Diatomic-py: A Python module for calculating the rotational and hyperfine structure of 1 molecules," *Computer Physics Communications*, vol. 282, p. 108512, Jan. 2023. 7.1

[255] A. Chotia, B. Neyenhuis, S. A. Moses, B. Yan, J. P. Covey, M. Foss-Feig, A. M. Rey, D. S. Jin, and J. Ye, "Long-Lived Dipolar Molecules and Feshbach Molecules in a 3D Optical Lattice," *Physical Review Letters*, vol. 108, p. 080405, Feb. 2012. Publisher: American Physical Society. 7.2.1

[256] J. A. Blackmore, R. Sawant, P. D. Gregory, S. L. Bromley, J. Aldegunde, J. M. Hutson, and S. L. Cornish, "Controlling the ac Stark effect of RbCs with dc electric and magnetic fields," *Physical Review A*, vol. 102, pp. 1–15, July 2020. 7.2.1

[257] B. Neyenhuis, "Ultracold Polar KRb Molecules in Optical Lattices," 7.2.3

[258] E. F. Walraven and T. Karman, "Rotational-state dependence of interactions between polar molecules," *Physical Review A*, vol. 109, p. 043310, Apr. 2024. Publisher: American Physical Society. 8.2